

# Controlled Growth and Application of Highly Oriented Surface-Mounted Metal-Organic Frameworks (SURMOFs)

Dissertation

zur Erlangung des Doktorgrades

der Naturwissenschaften

vorgelegt beim Fachbereich Biochemie, Chemie und Pharmazie

der Goethe-Universität Frankfurt am Main

von

Xiujun Yu

Frankfurt am Main

2016

(D30)

Vom Fachbereich Biochemie, Chemie und Pharmazie  
der Goethe-Universität Frankfurt am Main als Dissertation angenommen.

Dekan: Prof. Dr. Michael Karas

Gutachter: (1) Prof. Dr. Andreas Terfort

(2) Prof. Dr. Norbert Auner

Datum der Disputation:

*To my parents  
Zihua Yu and Guiying Wang  
And my wife  
Man He*

---

Die vorliegende Arbeit wurde im Zeitraum von September 2012 bis März 2016 unter der Anleitung von Herrn Professor Dr. Andreas Terfort am Institut für Anorganische und Analytische Chemie der Goethe-Universität Frankfurt am Main angefertigt.

---

<b>Abstract</b> .....	I
<b>Zusammenfassung</b> .....	V
<b>1 Introduction</b> .....	1
1.1 Metal-organic frameworks (MOFs) .....	1
1.1.1 Introduction to MOFs .....	1
1.1.2 Synthesis of MOFs .....	4
1.1.3 Applications of MOFs .....	7
1.2 Surface-mounted metal-organic frameworks (SURMOFs) .....	11
1.2.1 Introduction to SURMOFs .....	11
1.2.2 Self-assembled monolayers (SAMs) .....	12
1.2.2.1 Introduction to SAMs .....	12
1.2.2.2 Preparation and structure of thiolate SAMs on gold.....	13
1.2.2.3 Applications of SAMs.....	14
1.2.3 Growth protocols of SURMOFs.....	14
1.2.3.1 Direct solvothermal growth of SURMOFs .....	15
1.2.3.2 Growth of SURMOFs from aged mother solutions.....	16
1.2.3.3 Gel-layer growth of SURMOFs.....	17
1.2.3.4 Stepwise layer-by-layer (LbL) growth of SURMOFs .....	18
1.2.3.5 Spray-assisted LbL growth of SURMOFs .....	23
1.2.3.6 Langmuir-Blodgett LbL deposition of SURMOFs .....	25
1.2.3.7 Evaporation/solvent induced growth of SURMOFs .....	26
1.2.4 Applications of SURMOFs .....	28
1.3 Common methods for SURMOF characterization .....	31
1.4 Task and outline .....	32
<b>2 Experimental section</b> .....	35
2.1 Materials and general preparation.....	35
2.2 Experimental details of chapter 3 .....	36
2.3 Experimental details of chapter 4 .....	36
2.4 Experimental details of chapter 5 .....	37
2.5 Experimental details of chapter 6 .....	39

---

2.6 Characterization .....	40
<b>3 Temperature dependent crystallographic orientation and growth mechanism of a [Cu<sub>2</sub>(sdb)<sub>2</sub>(bipy)] SURMOF .....</b>	<b>43</b>
3.1 Introduction.....	43
3.2 Results and discussion .....	44
3.2.1 LbL growth of orientation controlled [Cu <sub>2</sub> (sdb) <sub>2</sub> (bipy)] SURMOFs .....	44
3.2.2 First-layer study and growth mechanism of [Cu <sub>2</sub> (sdb) <sub>2</sub> (bipy)] SURMOFs .....	48
3.2.3 Pore-orientation dependent adsorption capacities of volatile organic compounds (VOCs) .....	52
3.3 Conclusions.....	54
<b>4 Multifunctional SURMOFs: The effects of linker acidity (<i>pK<sub>a</sub></i>) on the orientational quality .....</b>	<b>57</b>
4.1 Introduction.....	57
4.2 Results and discussion .....	59
4.2.1 Linker <i>pK<sub>a</sub></i> effect on [Cu <sub>2</sub> L <sub>2</sub> (dabco)] SURMOFs containing a single kind of linker .....	59
4.2.2 Linker <i>pK<sub>a</sub></i> effect on [Cu <sub>2</sub> Lm <sub>2</sub> (dabco)] SURMOFs containing two linkers.....	61
4.2.3 Linker <i>pK<sub>a</sub></i> effect on [Cu <sub>2</sub> Lm <sub>2</sub> (dabco)] SURMOFs containing more linkers.....	65
4.2.4 Effect of the linker ratio in [Cu <sub>2</sub> {(bdc) <sub>x</sub> +(f <sub>4</sub> bdc) <sub>1-x</sub> } <sub>2</sub> (dabco)] (0≤x≤1) SURMOFs on the orientation.....	66
4.2.5 Adsorption capacities of [Cu <sub>2</sub> {(bdc) <sub>x</sub> +(f <sub>4</sub> bdc) <sub>1-x</sub> } <sub>2</sub> (dabco)] (0≤x≤1) SURMOFs ..	68
4.3 Conclusions.....	69
<b>5 LbL deposition and pore-size limited charge transfer of SURMOFs containing redox-active species .....</b>	<b>71</b>
5.1 Introduction.....	71
5.2 Results and discussion .....	73
5.2.1 LbL growth of [Cu <sub>2</sub> (bpdc-amide-Fc) <sub>2</sub> (dabco)] (Fc-SURMOF) and [Cu <sub>2</sub> (bpdc-amide-Me <sub>2</sub> Fc) <sub>2</sub> (dabco)] (Me <sub>2</sub> Fc-SURMOF) SURMOFs .....	73
5.2.2 Charge transfer properties of Fc- and Me <sub>2</sub> Fc-SURMOFs.....	75
5.2.3 Electrochemical property tuning of the SURMOFs containing redox-active species	

---

.....	77
5.3 Conclusions.....	79
<b>6 Polyoxometalate loaded HKUST-1 (POM@HKUST-1) SURMOFs: POM dependent crystallite orientation and electrochemical application .....</b>	<b>81</b>
6.1 Introduction.....	81
6.2 Results and discussion .....	82
6.2.1 Growth and orientation tuning of POM@HKUST-1 SURMOFs .....	82
6.2.2 Adsorption capacities and redox properties of POM@HKUST-1 SURMOFs.....	84
6.2.3 Selective methylene blue (MB) dye loading and enhanced electrochemical properties of POM@HKUST-1 SURMOFs .....	85
6.3 Conclusions.....	88
<b>7 Summary .....</b>	<b>89</b>
<b>8 Appendix.....</b>	<b>91</b>
8.1 Appendix of chapter 3.....	91
8.2 Appendix of chapter 4.....	95
8.3 Appendix of chapter 5.....	102
8.4 Appendix of chapter 6.....	106
8.5 List of abbreviations .....	108
<b>9 References .....</b>	<b>113</b>
<b>10 Curriculum Vitae.....</b>	<b>131</b>
<b>11 Acknowledgements .....</b>	<b>133</b>
<b>12 Erklärung über frühere Promotionsverfahren und Eidesstattliche Versicherung .</b>	<b>135</b>





## Abstract

Metal-organic frameworks (MOFs) have emerged as a promising class of crystalline porous inorganic-organic hybrid materials showing a wide range of applications. In order to realize the integration of MOFs into specific devices, this thesis mainly focuses on the controlled growth and the properties of highly oriented surface-mounted metal-organic frameworks (SURMOFs).

The stepwise layer-by-layer (LbL) growth method (also known as liquid phase epitaxial growth, LPE) exhibits vast advantages for the controllable growth of SURMOFs regarding the crystallite orientation, film thickness and homogeneity. However, up to date, only a few MOFs, such as HKUST-1, the tetragonal  $[M_2L_2P]$  ( $M = Cu^{2+}$  or  $Zn^{2+}$ ;  $L =$  rigid dicarboxylate;  $P =$  dinitrogen pillar) system and the  $[M_2L_2]$  ( $M = Cu^{2+}$  or  $Zn^{2+}$ ;  $L =$  rigid dicarboxylate) system, have been demonstrated to be suited for this protocol. So the first project of this thesis was designed to extend the applicability of the LbL growth. To this end, a semi-rigid linker based  $[M_2L_2P]$  SURMOF, namely  $[Cu_2(sdb)_2(bipy)]$  ( $sdb = 4,4'$ -sulfonylbiphenyl dicarboxylate;  $bipy = 4,4'$ -bipyridine) was chosen. Employing the stepwise LbL growth,  $[Cu_2(sdb)_2(bipy)]$  SURMOFs were successfully grown onto both monodentate pyridyl- and bidentate carboxyl-terminated surfaces at the temperature range of 15-65 °C. Interestingly, the orientation of the SURMOFs largely depends on the deposition temperature on both surfaces. At low deposition temperatures (below 40 °C), either on pyridyl- or carboxyl-terminated surfaces, exclusively [010] oriented  $[Cu_2(sdb)_2(bipy)]$  SURMOFs are obtained. In contrast, at high temperatures (40-65 °C), [001] oriented SURMOF growth is favored. Based on the results from X-ray diffraction (XRD), infrared reflection-absorption spectroscopy (IRRAS), scanning electron microscopy (SEM) and atomic force microscopy (AFM), we proposed a novel growth mode of the  $[Cu_2(sdb)_2(bipy)]$  system. That is, instead of the surface chemistry (template effects, defined by the functional groups of SAMs), the temperature-induced ripening processes and the tendency to minimize surface energies can dominate the SURMOF growth. The pore-orientation dependent dynamic adsorption capacities of oriented  $[Cu_2(sdb)_2(bipy)]$  SURMOFs, which are investigated by a quartz crystal microbalance (QCM), indicate that, indeed, the crystallites all have the same quality regardless of their genesis and orientation.

Inspired by the advantage of controllable LbL deposition of isorecticular  $[M_2L_2P]$  SURMOFs, the second project of this thesis was conceived to grow multivariate SURMOFs (MTV-SURMOFs) using mixed dicarboxylate linkers of the same type but bearing different functionalities. We advance a hypothesis that the linker acidity (expressed by the  $pK_a$  values) may have an influence on the oriented growth of MTV-SURMOFs. In order to test the hypothesis, seven isorecticular  $[Cu_2L_2(dabco)]$  ( $L$  = single kind of dicarboxylate linker; dabco = 1,4-diazabicyclo[2.2.2]octane) SURMOFs were grown onto pyridyl-terminated surfaces at 60 °C. The results from XRD and IRRAS show that the quality of [001] orientation is greatly affected by the acidity of the linkers. If the linker  $pK_a$  value raises above a certain value (4.3) or falls below a certain value (2.7), unexpected [100] orientation is visible in  $[Cu_2L_2(dabco)]$  SURMOFs. With this observation in mind, we deposited a series of  $[Cu_2Lm_2(dabco)]$  ( $Lm$  = mixed dicarboxylate linkers) SURMOFs, which contain two to five linkers, under the same conditions and the quality of [001] orientation in the MTV-SURMOFs was controlled by adjusting the linker category and the molar ratios.  $[Cu_2Lm_2(dabco)]$  SURMOFs with exclusive [001] orientation are obtained when the growth solution contains two linkers of relatively high  $pK_a$  value or more than two kinds of dicarboxylate linkers (independent of the  $pK_a$  values of linkers), while the mixtures of ligands with relatively low  $pK_a$  values or a high content of low  $pK_a$  valued linkers can result in mis-oriented growth of  $[Cu_2Lm_2(dabco)]$  SURMOFs with unexpected [100] crystallite orientation. In addition, the adsorption capacity and selectivity of  $[Cu_2Lm_2(dabco)]$  SURMOFs towards benzene ( $C_6H_6$ ) and hexafluorobenzene ( $C_6F_6$ ) are tunable by varying the molar ratios of linkers in a binary mixture as demonstrated for the  $[Cu_2\{(bdc)_x+(f_4bdc)_{1-x}\}_2(dabco)]$  SURMOFs ( $0 \leq x \leq 1$ ; bdc = 1,4-benzenedicarboxylate;  $f_4bdc$  = tetrafluorobenzene-1,4-dicarboxylate).

Moreover, the LbL growth shows enormous potential in the rational construction of functional  $[M_2L_2P]$  SURMOFs following the bottom-up principle. Therefore, the third project of this thesis was devised to deposit functional SURMOFs containing redox-active species. For this, the 4,4'-biphenyldicarboxylic acid ( $H_2(bpdc)$ ) linker was functionalized with ferrocene (Fc) and dimethyl ferrocene ( $Me_2Fc$ ) moieties and then employed for the LbL deposition. For the sake of the oriented growth, a novel pyrazole-terminated SAM (based on (4-(1*H*-pyrazol-4-yl)) phenylmethanethiol, PyzP1) was utilized to functionalize the substrates. As supported by

the out-of-plane XRD patterns,  $[\text{Cu}_2(\text{bpdc-amide-Fc})_2(\text{dabco})]$  SURMOF (Fc-SURMOF) is perfectly grown along the [100] direction, while the mis-oriented growth of  $[\text{Cu}_2(\text{bpdc-amide-Me}_2\text{Fc})_2(\text{dabco})]$  SURMOF ( $\text{Me}_2\text{Fc-SURMOF}$ ) was observed, as indicated by the appearance of (101), (210) and (310) diffraction peaks. Surprisingly, the electrochemical properties of the two SURMOFs exhibit a vast difference. The Fc-SURMOF shows excellent electrochemical properties due to the reversible oxidation and reduction of the ferrocene moieties in the oriented pores, while the  $\text{Me}_2\text{Fc-SURMOF}$  was found to be a closely packed insulating layer since no extensive charge transfer is observed. A diffusion controlled mechanism of redox reaction is proposed, where the diffusion of the counter anions in the pores limits the current. Moreover, the insulating  $\text{H}_2(\text{bpdc-amide-Me}_2\text{Fc})$  ligand can be further employed to tune the electrochemical properties of mixed SURMOFs and MOF-on-MOF heterostructures.

Besides the LbL growth protocol, the spin-coating technique is also promising for the oriented growth of SURMOFs. Driven by the specific applications, the fourth project of this thesis was planned to grow functional SURMOFs containing catalytically active units. The Keggin-type polyoxometalates (POMs) with high catalytic activities were chosen to functionalize the HKUST-1 SURMOFs. Combining the technique with methanol vapor induced growth, a series of highly oriented, POM functionalized HKUST-1 SURMOFs (denoted as POM@HKUST-1 SURMOFs) were controllably deposited onto pyridyl-terminated surfaces. No POM leaching was observed. Moreover, the crystallite orientation of the SURMOFs can be tuned by altering the POM category. The POM@HKUST-1 SURMOFs exhibit great potential as electrocatalyst in electrochemical devices due to the excellent redox properties of Keggin-type POMs. In addition, the PTA@HKUST-1 (PTA = phosphotungstic acid) SURMOF can be employed as an ideal platform for the selective loading of methylene blue (MB) dye with high efficiency. Remarkably, the MB dye cannot be desorbed by ion exchange owing to the strong binding between the dye molecules and the framework. The MB loaded PTA@HKUST-1 SURMOF shows reliable redox properties under inert conditions, further confirming the application potential of SURMOFs in electrochemical devices. Additionally, the MB dye can be released without affecting the SURMOF during the CV measurements under UV irradiation and the resulting empty SURMOF can be reused for dye loading.



## Zusammenfassung

Metall-organische Gerüstverbindungen (engl. metal-organic frameworks, MOFs) haben sich als eine vielversprechende Klasse kristalliner, poröser anorganisch-organischer Hybridverbindungen etabliert. Ihre strukturelle Vielfalt und ihre Durchstimbarkeit eröffnen MOFs eine große Zahl von Anwendungsmöglichkeiten. Für spezifische Anwendungen wie chemische Sensoren, Membranen, katalytisch wirksame Beschichtungen und viele andere nanotechnologische Verfahren müssen MOFs auf verschiedene Arten von Oberflächen als Filme aufgebracht werden. Um die Integrierung von MOFs in nanotechnologische Verfahren zu ermöglichen, beschäftigt sich die vorliegende Arbeit mit dem kontrollierten Aufwachsen von hochorientierten Oberflächen-gebundenen MOFs (engl. surface-mounted MOFs, SURMOFs) und deren Eigenschaften. Zum kontrollierten Aufwachsen von SURMOFs wurden unterschiedliche Techniken verwendet: Das stufenweise Lage-für-Lage (engl. layer-by-layer, LbL) Verfahren, auch epitaktisches Aufwachsen aus flüssiger Phase (engl. liquid epitaxial growth, LPE) genannt, wurde eingesetzt, um SURMOFs mit niedrig-symmetrischer Kristallstruktur, mit multiplen funktionellen Gruppen und mit Redox-aktiven Eigenschaften herzustellen. Mittels Aufschleudern wurden katalytisch aktive SURMOFs produziert. Die Eigenschaften dieser SURMOFs wie Adsorptionsverhalten, Ladungstransfer und katalytische Wirkung wurden erforscht. Hinsichtlich der einheitlichen Orientierung der Kristallite, der Schichtdicke und der Homogenität der erhaltenen Filme ist die LbL-Methode unerreicht. Jedoch konnten bis jetzt mittels LbL nur wenige SURMOFs hergestellt werden, wie z.B. HKUST-1, tetragonale  $M_2L_2P$  ( $M = Cu^{2+}$  oder  $Zn^{2+}$ ;  $L =$  starre Dicarboxylate;  $P =$  Distickstoff-funktionalisierte Verbindungen) Systeme, oder  $[M_2L_2]$  ( $M = Cu^{2+}$  oder  $Zn^{2+}$ ;  $L =$  starre Dicarboxylate) Systeme.

Weil SURMOFs die Kernstücke vieler Anwendungen geworden sind, ist ein tiefgreifendes Verständnis ihres Aufwachsverhaltens notwendig. Daher wurde im ersten Projekt der vorliegenden Arbeit die Ausweitung des LbL Verfahrens auf neue Systeme untersucht, um so ein tiefgreifenderes Verständnis des mit diesem Verfahren verbundenen Aufwachsmodus zu erlangen. Zu diesem Zweck wurde ein  $[M_2L_2P]$  MOF mit geringer Symmetrie und einem halbstarren Linker ausgewählt, nämlich  $[Cu_2(sdb)_2(bipy)]$  ( $sdb = 4,4'$ -Sulfonylbiphenyl-

dicarboxylat; bipy = 4,4'-Bipyridin). Mittels LbL Verfahren konnten  $[\text{Cu}_2(\text{sdb})_2(\text{bipy})]$  SURMOFs auf ein- und zwei-phasigen, Pyridyl-terminierten und zwei-phasigen, Carboxyl-terminierten Oberflächen in einem Temperaturbereich von 15 bis 65 °C abgeschieden werden. Interessanterweise ist die Orientierung der SURMOF-Kristallite auf beiden Oberflächen ausschließlich von der Abscheidungstemperatur abhängig. Bei niedrigen Temperaturen (unterhalb 40 °C) werden auf beiden Oberflächen  $[\text{Cu}_2(\text{sdb})_2(\text{bipy})]$  SURMOFs erhalten, die exklusiv entlang der [010]-Achse orientiert sind. Im Gegensatz dazu ist bei hohen Temperaturen (40-65 °C) ein SURMOF-Wachstum entlang der [001]-Achse bevorzugt. Anhand der Resultate aus Röntgenbeugungsmessungen, Infrarot-Reflexions-Absorptions-Spektroskopie (IRRAS), Rasterelektronenmikroskopie (REM) und Rasterkraftmikroskopie (engl. atomic force microscopy, AFM) wurde für den Aufwachsmechanismus von  $[\text{Cu}_2(\text{sdb})_2(\text{bipy})]$  ein neuer Mechanismus gefunden. Anstatt der exponierten funktionellen Oberflächen-Gruppen dominieren temperaturinduzierte Reifungsprozesse und die Minimierung der Oberflächenenergie das Aufwachsen der SURMOFs. Die von der Porenrichtung abhängige, dynamische Adsorptionskapazität der unterschiedlich orientierten  $[\text{Cu}_2(\text{sdb})_2(\text{bipy})]$  SURMOFs wurde mittels Quarzkristall-Mikrowaage untersucht, wodurch bestätigt werden konnte, dass die Kristallite unabhängig von ihrer Entstehung und ihrer Orientierung dieselbe Qualität aufweisen.

Die Funktionalisierung von SURMOFs ist eine wichtige Voraussetzung für viele spezifische Anwendungen. Eine Strategie ist der Einbau gleich mehrerer verschiedener Funktionalitäten, mit denen man multivariante (MTV-) SURMOFs erhalten kann. Tetragonale  $[\text{M}_2\text{L}_2\text{P}]$  SURMOFs sind ideale Modellsysteme für die Herstellung von MTV-SURMOFs, weil die Dicarboxylat-Linkermoleküle einfach durch andere Linker desselben Typs ersetzt werden können. Weiterhin sind isoretikuläre  $[\text{M}_2\text{L}_2\text{P}]$  SURMOFs gut geeignet für das LbL-Aufwachs-Protokoll. Daher sollten im zweiten Projekt dieser Arbeit MTV-SURMOFs mit gemischten Dicarboxylat-Linkern desselben Typs, aber mit verschiedenen funktionellen Gruppen, hergestellt werden. Es wurde die Hypothese aufgestellt, dass die Acidität der Linkermoleküle (ausgedrückt durch deren  $pK_S$ -Werte) das orientierte Aufwachsen der MTV-SURMOFs beeinflusst. Um diese Hypothese zu überprüfen, wurden sieben isoretikuläre  $[\text{Cu}_2\text{L}_2(\text{dabco})]$  (L = sortenreiner Dicarboxylat-Linker; dabco = 1,4-Diazabicyclo[2.2.2]octan) SURMOFs bei

60 °C auf Pyridyl-terminierte Oberflächen aufgebracht. Die Resultate von Röntgenbeugungs- und Infrarotexperimenten zeigen, dass die Qualität der [001]-Ausrichtung deutlich durch die Acidität der Linkermoleküle beeinflusst wird. Bei kleinen  $pK_S$ -Werten konnten Kristallite mit der unerwünschten [100] Orientierung in den  $[\text{Cu}_2\text{L}_2(\text{dabco})]$  SURMOFs beobachtet werden. Aufgrund dieser Beobachtung wurde unter denselben Bedingungen eine Serie von  $[\text{Cu}_2\text{L}_m(\text{dabco})]$  SURMOFs auf Pyridyl-terminierte Oberflächen aufgewachsen. Die Bezeichnung Lm steht für Mischungen von zwei bis zu fünf verschiedenen Linker-Molekülen. Das Ausmaß der [001]-Orientierung dieser MTV-SURMOFs kann durch Auswahl der Linker und deren Molenbrüche kontrolliert werden.  $[\text{Cu}_2\text{L}_m(\text{dabco})]$  SURMOFs, die ausschließlich [001]-Orientierung aufweisen, wurden erhalten, wenn die Abscheidung zwei Linkermoleküle mit verhältnismäßig hohen  $pK_S$ -Werten enthält, oder mehr als zwei Arten von Dicarboxylat-Linkern mit beliebigen  $pK_S$ -Werten, während Lösungen von Liganden mit ausschließlich oder mehrheitlich niedrigen  $pK_S$ -Werten zur Bildung von fehlorientierten  $[\text{Cu}_2\text{L}_m(\text{dabco})]$  SURMOFs führen. Ferner stellte sich heraus, dass die Adsorptionskapazität und die Adsorptionsselektivität der  $[\text{Cu}_2\text{L}_m(\text{dabco})]$  SURMOFs bezüglich Benzol und Hexafluorbenzol durch Änderung des Molenbruches der Linker in binären Mischungen einstellbar sind. Dies konnte anhand des  $[\text{Cu}_2\{(\text{bdc})_x+(\text{f}_4\text{bdc})_{1-x}\}_2(\text{dabco})]$  ( $0 \leq x \leq 1$ ; bdc = 1,4-Benzoldicarboxylat;  $\text{f}_4\text{bdc}$  = Tetrafluorbenzol-1,4-dicarboxylat) SURMOFs demonstriert werden. Mit steigendem Anteil an  $\text{H}_2(\text{bdc})$ -Linker weisen die SURMOFs eine bessere Selektivität für Hexafluorbenzol auf, was der Wechselwirkung von fluorierten und nicht-fluorierten Aromaten zugeschrieben wird.

In Anbetracht der Tatsache, dass die weit überwiegende Mehrheit aller MOFs elektrische Isolatoren sind, ist es eine enorme Herausforderung, eine elektronische / elektrochemische Funktionalisierung von SURMOFs zu erreichen. Der Einbau redox-aktiver, organischer Linkermoleküle stellt ein effektives Mittel zur Verbesserung des Ladungstransports in SURMOFs dar. Das dritte Projekt dieser Arbeit verfolgt die Verwirklichung eines rationalen Designs von SURMOFs mit intrinsischer elektrischer Leitfähigkeit durch den Einsatz von Linkern mit redox-aktiven Funktionalitäten. Dazu wurden 4,4'-Biphenyldicarbonsäure ( $\text{H}_2(\text{bpdc})$ ) mit Ferrocen (Fc)- und Dimethylferrocen ( $\text{Me}_2\text{Fc}$ )-Einheiten über Amidbrücken funktionalisiert und anschließend im LbL-Verfahren zu Herstellung von SURMOFs benutzt.

Auch hier wurden tetragonale  $[M_2L_2P]$  SURMOFs hergestellt, weil sich diese Systeme besonders gut für die LbL-Methode eignen. Um ein orientiertes Wachstum zu erreichen, wurde der SURMOF auf einer neuartigen SAM aus 4-(1*H*-Pyrazol-4-yl)phenylmethanthiolat abgeschieden. Wie Röntgenbeugung und REM-Bilder zeigten, sind sowohl der  $[Cu_2(bpdc-amid-Fc)_2(dabco)]$  SURMOF (Fc-SURMOF) als auch der  $Cu_2(bpdc-amid-Me_2Fc)_2(dabco)$  SURMOF ( $Me_2Fc$ -SURMOF) dicht gepackt und bevorzugt entlang der  $[100]$ -Richtung orientiert. Es wurden jedoch Fehlorientierungen im  $Me_2Fc$ -SURMOF gefunden, wie das unerwartete Vorhandensein von  $(101)$ -,  $(210)$ - und  $(310)$ -Röntgenbeugungssignalen zeigt. Erstaunlicherweise sind die beiden SURMOFs elektrochemisch äußerst verschieden. Der Fc-SURMOF weist aufgrund der reversiblen Oxidierbarkeit/Reduzierbarkeit der Ferrocen-Einheiten exzellente elektrochemische Eigenschaften auf. Dagegen erwies sich der  $Me_2Fc$ -SURMOF als dicht gepackter, isolierender Film, bei dem kein Ladungstransfer beobachtet werden konnte. Als Erklärung wird ein diffusions-kontrollierter Mechanismus der in den SURMOFs stattfindenden Redoxreaktion vorgeschlagen. Der den Ladungstransfer begrenzende Faktor ist hierbei die Diffusion der Gegenanionen in den Poren. Ferner kann der isolierende  $H_2(bpdc-Me_2Fc)$ -Ligand eingesetzt werden, um die elektrochemischen Eigenschaften von gemischten SURMOFs oder MOF-auf-MOF-Heterostrukturen durchzustimmen.

Ein weiterer Ansatz, SURMOFs zu funktionalisieren, ist die Beladung der Poren mit funktionstragenden Spezies. Die Herstellung derartiger Systeme für die (Elektro-)Katalyse war das vierte Projekt in der vorliegenden Arbeit. Dazu wurden Keggin-artige Polyoxometallate (POMs) mit hoher katalytischer Aktivität in HKUST-1 SURMOFs integriert. HKUST-1 wurde wegen seiner zu den POMs passenden Porengröße ausgewählt. Anstelle des LbL-Protokolls wurde in diesem Projekt das Aufschleudern verwendet, das für das gerichtete Aufwachsen von HKUST-1 ebenfalls gut geeignet ist. Durch Kombination des Aufschleuderns mit einer Methanol-Dampf-induzierten Kristallisation wurde auf Pyridyl-terminierten Oberflächen eine Serie hochorientierter POM-funktionalisierter HKUST-1 SURMOFs (POM@HKUST-1 SURMOFs) abgeschieden. Die Beladung der POMs stellte sich als hocheffizient heraus. Eine Auslaugung der POMs konnte nicht festgestellt werden. Weiterhin zeigte sich, dass die Orientierung der POM@HKUST-1 SURMOFs Kristallite durch



Variation der POM-Kategorie beeinflusst werden kann. Aufgrund der exzellenten Redox-Eigenschaften der POMs weisen POM@HKUST-1 SURMOFs ein großes Potenzial als Elektrokatalysatoren in elektrochemischen Anwendungen auf. Darüber hinaus ist PTA@HKUST-1 (PTA = Wolframatophosphorsäure, engl. phosphotungstic acid) eine ideale Plattform für die hocheffiziente, selektive Absorption des Farbstoffs Methylenblau (MB). Bemerkenswerterweise kann MB wegen seiner starken Bindung zu diesem SURMOF durch Ionenaustausch nicht wieder desorbiert werden. Mit MB geladene PTA@HKUST-1 SURMOFs zeigen unter inerten Bedingungen verlässliche Redox Eigenschaften, eine weitere Bestätigung für die Anwendung von SURMOFs in elektrochemischen Geräten. Unter UV-Bestrahlung kann MB aus dem SURMOF freigesetzt werden, ohne Letzteren zu beeinträchtigen. Der leere SURMOF kann anschließend erneut mit MB beladen werden.



# 1 Introduction

## 1.1 Metal-organic frameworks (MOFs)

### 1.1.1 Introduction to MOFs

Metal-organic frameworks (MOFs, also known as porous coordination polymers or PCPs) have emerged as a promising class of porous crystalline materials with ultrahigh porosity and tremendous internal surface areas (beyond  $6000 \text{ m}^2/\text{g}$ ).<sup>1-7</sup> On a fundamental level, MOFs are organic-inorganic hybrid solids with infinite and uniform framework structures, which are constructed from metal-containing nodes (secondary building units, SBUs) and organic linkers combined by strong chemical bonds producing open crystalline frameworks with permanent porosity.<sup>2,5,8</sup> Due to many possibilities of the combination and the coordination manners of the metal nodes and the organic linkers, various MOF structures (more than  $20,000^5$ ) have been created. The typical crystal structures of the four most famous MOFs, HKUST-1<sup>9</sup> (a), ZIF-8<sup>10</sup> (b), MOF-5<sup>11</sup> (c) and MIL-101-Cr<sup>12</sup> (d) are depicted in Figure 1.1. Since the 1990s, promoted by Yaghi (USA), Férey (France) and Kitagawa (Japan), the research area of MOFs has become one of the fastest growing fields in chemistry as supported by the very large number of reported MOF structures, tens of thousands of published research papers and expanding research scopes within the past two decades.

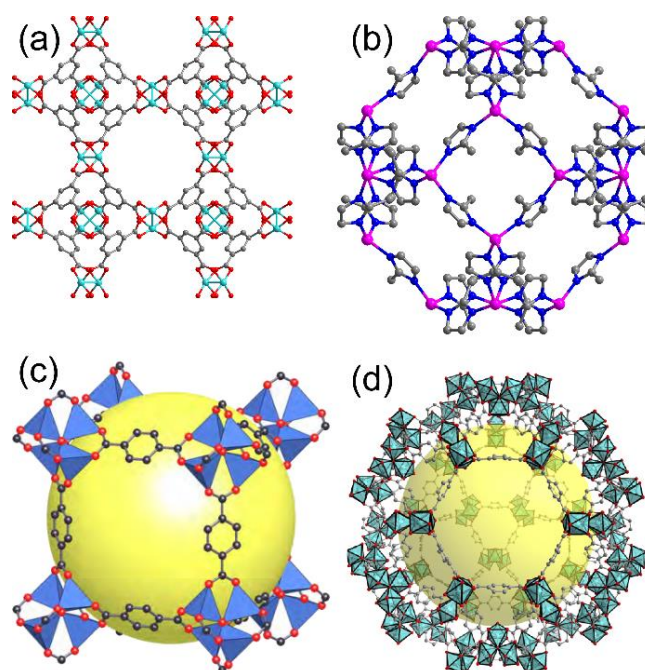


**Figure 1.1** Crystal structures of HKUST-1<sup>9</sup> (a), ZIF-8<sup>10</sup> (b), MOF-5<sup>11</sup> (c) and MIL-101-Cr<sup>12,13</sup> (d).

The inorganic part of MOFs, the metal nodes/SBUs, plays an important role in the rationalized design of MOF structures and the improvement of porosity and stability.<sup>14–18</sup> The concept of SBUs has been successfully applied in rationally designing the topologies of MOF structures, and more importantly, it has allowed the synthesis and use of a large number of SBUs with varying geometries (see Figure 1.2).<sup>2,5,11,19–23</sup> By considering the geometries and chemical attributes of SBUs and organic linkers, the topology of the network can be predicted. For example, in MOF-5, a preferred cubic network topology is formed by the coordination of the  $\text{Zn}_4\text{O}(\text{CO}_2)_6$  octahedral SBUs and rigid terephthalate linkers (Figure 1.1c). Moreover, MOFs with open metal sites, which are important for specific applications (e.g., selective adsorption and catalysis), can be obtained by judicious selection of SBUs.<sup>2</sup>

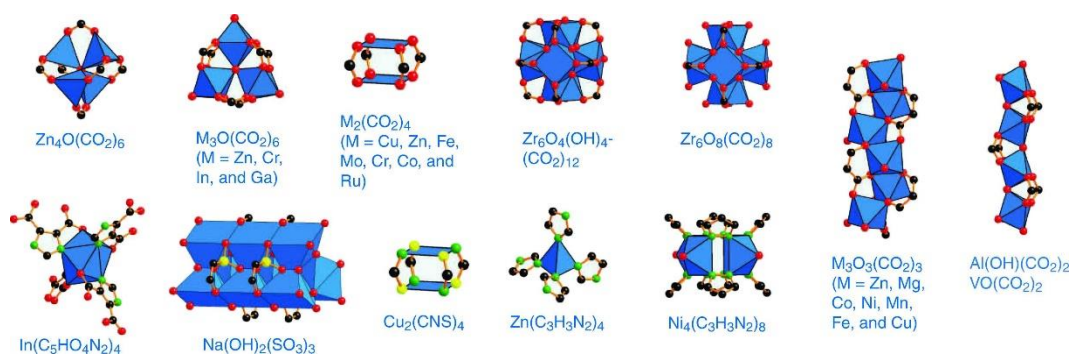


**Figure 1.2** Typical inorganic SBUs employed in the construction of MOF structures. Color code: metal ions, signified by blue polyhedra; C, black; O, red; N, green; and S, yellow. Adapted from ref. 5.

The organic part of MOFs, that is the linkers, is also crucial for the construction of MOFs with varied pore sizes and surface areas. Based on the structures, the ditopic or polytopic organic linkers can be classified into carboxylates, imidazoles, pyridines and pyrazolates (Figure 1.3). Through the judicious design and selection of organic linkers, MOFs with ultrahigh surface area (ultrahigh porosity) can be prepared. Usually, longer organic linkers provide larger pores and a greater number of adsorption sites (leading to the increase of surface area) within a given material.<sup>5</sup> Based on this idea, a novel synthetic strategy of MOFs, which is called “isorecticular expansion” (maintaining the same topology), has been developed by Yaghi et al.<sup>24–26</sup> Using this strategy, the group designed and synthesized a series of 16 IRMOFs (the isorecticular (IR) series) with the same underlying topology (the same cubic topology as MOF-5) employing expanded and variously functionalized organic linkers.<sup>24</sup>

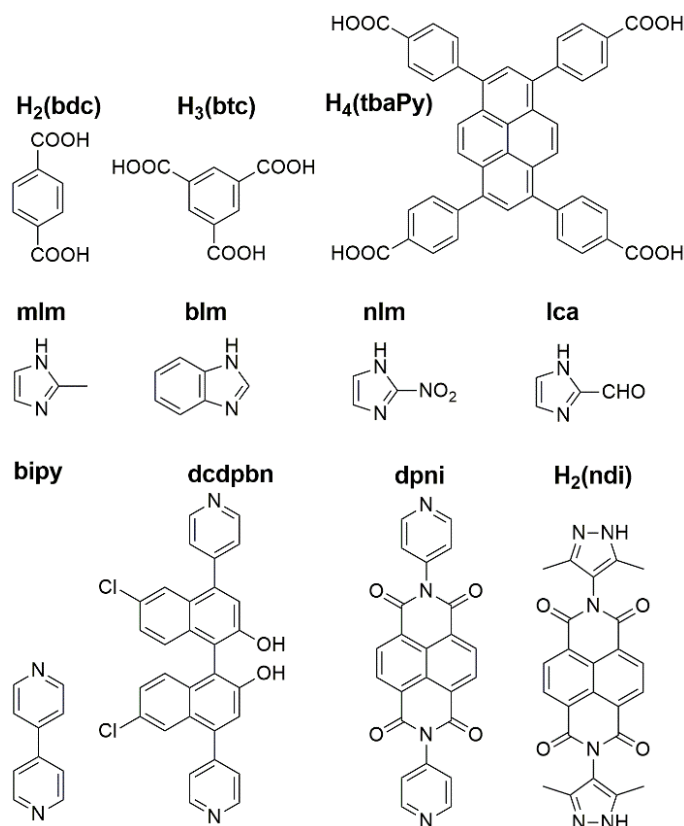


**Figure 1.3** Representative organic linkers such as carboxylates (upper), imidazoles (middle), pyridines and pyrazolates (bottom) used for the fabrication of MOF structures.

Another example is the isorecticular expansion of MOF-74.<sup>27</sup> The series of porous structures (from IRMOF-74-I to -XI) with pore apertures ranging from 14 Å to 98 Å were synthesized based on the topology of MOF-74.<sup>26</sup> The pore apertures of IRMOF-74-IX are large enough to allow the entrance of green fluorescent protein (barrel structure with a diameter of 34 Å and a height of 45 Å) without unfolding and the surface modification of pores with various functionalities does not alter the porosity significantly.<sup>26</sup> Moreover, the concept has also been applied for the isorecticular expansion of MOF-177<sup>28</sup> ( $Zn_4O(\text{btb})_2$ ; btb = 4,4',4''-benzene-1,3,5-triyl-tribenzoate) to generate MOF-180<sup>29</sup> ( $Zn_4O(\text{bte})_2$ ; bte = 4,4',4''-benzene-1,3,5-triyl-tris(ethyne-2,1-diyl) tribenzoate) and MOF-200<sup>29</sup> ( $Zn_4O(\text{bbc})_2$ ; bbc = 4,4',4''-benzene-1,3,5-triyl-tris(benzene-4,1-diyl) tribenzoate), utilizing larger tritopic linkers (Figure 1.4a). Using the same strategy, several isorecticular structures of HKUST-1 have also been obtained by the expansion with ttca (triphenylene-2,6,10-tricarboxylate), tatb (4,4',4''-s-triazine-2,4,6-triyltribenzoate), tatab (4,4',4''-s-triazine-1,3,5-triyltri-*p*-aminobenzoate), htb (4,4',4''-

(1,3,4,6,7,9,9b-heptaazaphenylene-2,5,8-triyl)tribenzoate) and bbc linkers (Figure 1.4b).<sup>25,30–33</sup> The cell volume for MOF-399 ( $\text{Cu}_3(\text{bbc})_2$ ), which has the highest void fraction (94%) and the lowest density ( $0.126 \text{ g/cm}^3$ ) of any MOF reported to date, is 17.4 times larger than that of HKUST-1.<sup>25</sup> The listed examples exhibit that, in principle, a great number of topologically identical but functionally distinctive MOF structures can be created through isorecticular expansion.

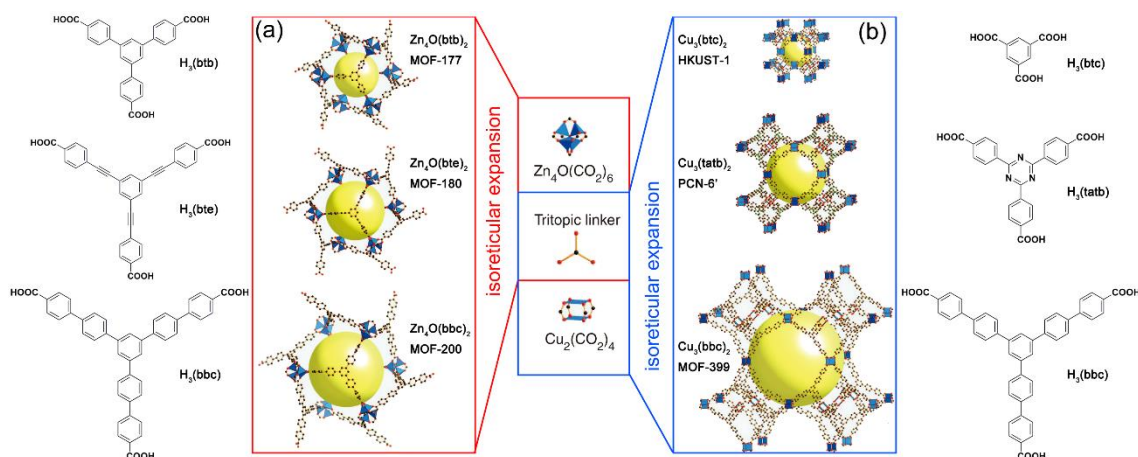


**Figure 1.4** The isorecticular expansion of archetypal MOFs built from  $\text{Zn}_4\text{O}(\text{CO}_2)_6$  (a) and  $\text{Cu}_2(\text{CO}_2)_4$  (b) SBUs, in which the linkers differ in functionality and length. The yellow spheres present the internal void space. Adapted from ref. 5.

However, the large empty space caused by the large linkers within the crystal framework makes it prone to the filling with interpenetrating structures (two or more frameworks grow and mutually intertwine together).<sup>5</sup> In order to prevent interpenetration, the topology design is an effective way.<sup>5,28</sup> Recently, the mixed-linker strategy (the two kinds of linkers have different topologies) has been used to prevent interpenetration and create ultrahigh porosity. Following this strategy, several novel MOFs with noninterpenetrating structures and ultrahigh porosities have been developed, such as UMCM-2<sup>34</sup> ( $(\text{Zn}_4\text{O})(\text{btb})_4(\text{t}^2\text{dc})_2$ ;  $\text{t}^2\text{dc}$  = thieno[3,2-b]thiophene-2,5-dicarboxylate; surface area =  $5200 \text{ m}^2/\text{g}$ ) and MOF-210<sup>29</sup> ( $(\text{Zn}_4\text{O})_3(\text{bte})_4(\text{bpdc})_3$ ;  $\text{bpdc}$  = biphenyl-4,4'-dicarboxylate; surface area =  $6240 \text{ m}^2/\text{g}$ ).

### 1.1.2 Synthesis of MOFs

The synthesis of MOFs has attracted immense attention during the last two decades due to the

possibility to obtain a large variety of aesthetically interesting structures that could lead to fascinating properties.<sup>35–40</sup> Conventionally, MOFs are synthesized by the hydro/solvothermal technique. This classic route involves mixing all the reactants (metal salts, ligands and solvents) together in sealed vessels and then heating them to an elevated temperature (ranging from room temperature to approximately 250 °C). After several hours or days, crystalline products can be generated.

For the conventional hydro/solvothermal synthesis, energy is generally transferred from a heat source, the oven, through convection.<sup>37</sup> As alternatives, other means, e.g., electrical current, electromagnetic radiation and mechanical waves (ultrasound), can also be utilized to introduce energy for the synthesis.<sup>37</sup> Accordingly, a series of newly established methods, including the microwave-assisted method,<sup>41–44</sup> the sonochemical synthesis,<sup>45,46</sup> the mechanochemical synthesis<sup>47–49</sup> and the electrochemical synthesis,<sup>50–52</sup> have been developed for the synthesis of MOFs. In addition, several novel methods, such as the surfactant-assisted method,<sup>53–56</sup> the microemulsion method,<sup>57,58</sup> the coordination modulation method<sup>59–61</sup> and the solvent-induced precipitation<sup>62–64</sup> have also been reported. These strategies exhibit certain advantages over the conventional hydro/solvothermal synthesis. For instance, the microwave-assisted synthesis is a time-saving method due to the high heating efficiency and the electrochemical synthesis method makes the large-scale production possible. Additionally, the new routes can produce MOF crystals with controllable particle size, size distribution and morphology as well as defect concentration, which can greatly affect the properties of the MOF material.<sup>37</sup>

Besides the synthesis routes, the process parameters, such as solvent, reactant concentration, reaction time, temperature programs and additives, are also of great importance for the size control and uniformity adjustment of the MOF crystals in the micro/nano regimes. Generally, solvent, reactant concentration, reaction time and temperature programs can strongly influence the relative nucleation and crystal growth rates. It has already been demonstrated that additives can be used to efficiently modulate the crystal growth. For example, molecular blocking agents and polymers can slow down the nucleation rate and the crystal growth by adsorption onto certain crystal faces, while capping agents can be used to stop crystal growth. Modulators are usually employed to control the size and morphology by competing with the organic linkers to coordinate with the metal ions during nucleation and crystal growth. Mostly, monodentate

ligands, which have the same chemical functionality as the multidentate linkers, are chosen as modulators. By following these strategies, micro/nanoscale MOFs with various morphologies (e.g., cubes, octahedra, hexagonal rods and bipyramidal hexagonal prisms; Figure 1.5) and unique properties have been reported.<sup>56,61,65–69</sup>

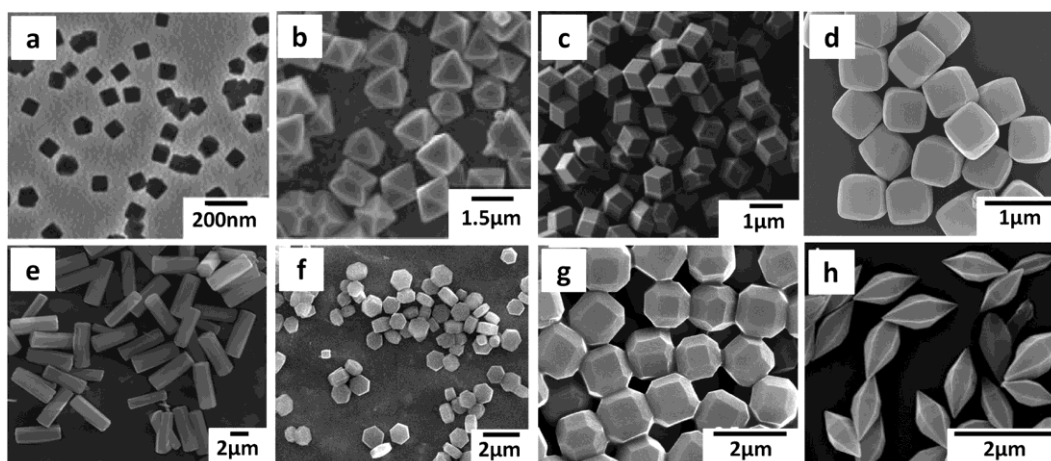


**Figure 1.5** Representative SEM images of MOF micro/nanostructures with various morphologies: (a) cubes<sup>68</sup>; (b) octahedra<sup>61</sup>; (c) rhombic dodecahedra<sup>67</sup>; (d) truncated cubes<sup>66</sup>; (e) hexagonal rods<sup>69</sup>; (f) hexagonal discs<sup>69</sup>; (g) truncated rhombic dodecahedra<sup>56</sup>; (h) bipyramidal hexagonal prisms<sup>65</sup>. Taken from ref. 35.

In addition, significant advances have been made to create MOF superstructures composed of nanocrystals as building blocks at the mesoscopic/macroscale. MOF superstructures with hierarchical orders have been fabricated to enrich the material performance and various applications.<sup>66,70,71</sup> Generally, such hierarchical MOF structures can be categorized into four dimensionalities, which are zero-dimensional architectures including hollow microspheres or capsules, one-dimensional architectures such as nanorods or nanofibers, two-dimensional architectures characterized as thin films or membranes (will be discussed in 1.2) and three-dimensional architectures consisting of continuous and extended systems (see Figure 1.6).<sup>72</sup> Accordingly, several strategies, including the use of hard (macrostructural) templates<sup>73–77</sup>, soft (molecular) templates<sup>78–82</sup>, reaction confinement (evaporation)<sup>70,83,84</sup>, liquid-solid interfacial reaction<sup>85</sup>, liquid-liquid interfacial reaction<sup>86–88</sup> and top-down processing<sup>66,89–92</sup>, have been reported for the synthesis of MOF superstructures.

Remarkably, a spray-drying method was demonstrated to produce hollow superstructures of a



variety of MOFs, including HKUST-1,  $[\text{Cu}_2(\text{bdc})_2]$  ( $\text{bdc} = 1,4\text{-benzenedicarboxylate}$ ), MOF-14 ( $\text{Cu}_3(\text{btb})_2$ ), MOF-505 ( $\text{Cu}_2(\text{bptc})$ ,  $\text{bptc} = 3,3',5,5'\text{-biphenyltetracarboxylate}$ ), MOF-74 ( $\text{M}_2(\text{dhbdc})$ ,  $\text{M} = \text{Zn}^{2+}$ ,  $\text{Mg}^{2+}$  and  $\text{Ni}^{2+}$ ,  $\text{dhbdc} = 2,5\text{-dihydroxy-1,4-benzenedicarboxylate}$ ), MIL-88A ( $\text{Fe}_3\text{O}(\text{fumarate})_3$ ), MIL-88B-NH<sub>2</sub> ( $\text{Fe}_3\text{O}(\text{bdc-NH}_2)_3$ ,  $\text{bdc-NH}_2 = 2\text{-amino-1,4-benzenedicarboxylate}$ ), UiO-66, ZIF-8, MOF-5 and IRMOF-3 ( $\text{Zn}_4\text{O}(\text{bdc-NH}_2)_3$ ).<sup>70</sup> Granick and coworkers<sup>66</sup> have reported the facet-to-facet assembly of polyhedral ZIF-8 crystals under an electrical field. For this, micrometer-sized ZIF-8 crystals with a narrow size distribution and well-defined polyhedral morphology were synthesized using coordination modulators and functionalized with a fluorescent dye to allow the confocal microscopic visualization. After application of the external electric field, the well-defined rhombic dodecahedral crystals reoriented to form almost perfect (110) facet-to-facet contacts in linear chains, which remained locked into place even after the external field was removed. Additionally, an elegant strategy employing the direct conversion of a structured metal oxide parent material into a MOF superstructure with the retention of the porous structure (coordination replication), has been demonstrated by the Kitagawa group,<sup>71</sup> who fabricated three-dimensional  $\text{Al}(\text{OH})(\text{ndc})$  ( $\text{ndc} = 1,4\text{-naphthalenedicarboxylate}$ ) superstructures with macro- and meso-pores produced from amorphous  $\text{Al}_2\text{O}_3$  templates.

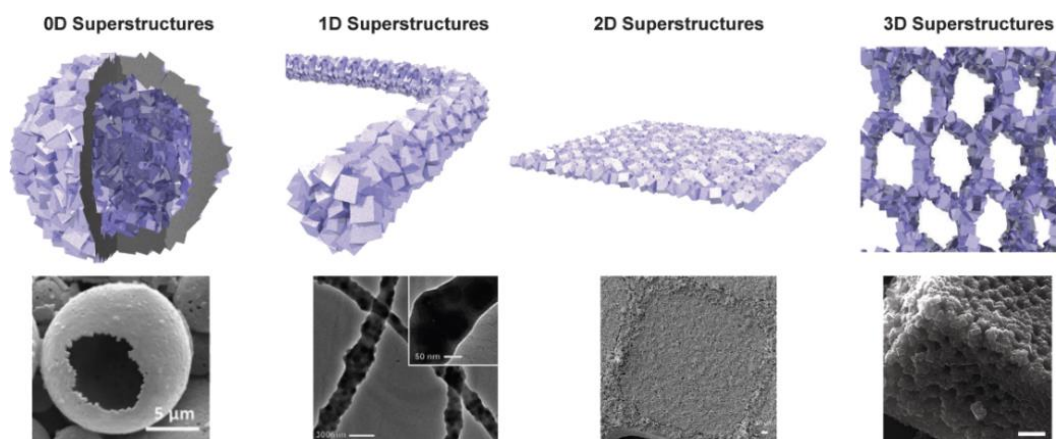


**Figure 1.6** MOF superstructures with different dimensionalities structured at the microscopic/mesoscopic scales. Adapted from ref. 72.

### 1.1.3 Applications of MOFs

MOFs as a new class of porous materials have exhibited many advantages over the traditional

porous materials, such as zeolites, mesoporous silica and activated carbon, due to the designability and versatility in correlation with fascinating properties. Traditionally, MOFs have been well documented for applications in gas storage and absorption (hydrogen and methane), separation and CO<sub>2</sub> capture.<sup>24,93–100</sup> Newly expanded applications in chemical and biological sensing, heterogeneous catalysis, ion conductivity and biomedical imaging are increasingly gaining importance.<sup>101–106</sup>

Hydrogen and methane are considered to be the best alternative fuels to fossil resources due to their high energy density and clean nature.<sup>95,97</sup> Much attention is being paid to improving the storage of these fuel gases under practical conditions.<sup>24,96,98</sup> Recently, numerous studies have demonstrated that the functionalities of the organic linkers have little influence on the hydrogen and methane absorption and the total gravimetric hydrogen and methane uptake capacities are generally proportional to the pore volume of MOFs.<sup>107</sup> To this end, various MOFs with large pore apertures have been developed. For example, at 56 bar and 77 K, hydrogen absorption capacities are 7.9 and 9.0 wt% for NU-100 and MOF-210, while at 80 bar, MOF-210 exhibits hydrogen absorption as high as 15 wt%.<sup>29,108</sup> Moreover, the total uptake of methane for MOF-200 and MOF-210 are 234 mg/g and 264 mg/g, respectively, at 80 bar and 298 K.<sup>29</sup> Another effective strategy for increasing the volumetric adsorption is the generation of open metal sites (or unsaturated metal sites).<sup>109</sup> The best known SBU exposing open metal sites is the paddle-wheel [Cu<sub>2</sub>COO<sub>4</sub>] SBU (the prototype MOF is HKUST-1). By using both effects (pore volumes and open metal sites), several Cu-MOFs with large pore volumes and high hydrogen uptake capacities have been reported.<sup>110–112</sup>

Reducing CO<sub>2</sub> emission and lowering the concentration of greenhouse gases in the atmosphere has become one of the most urgent environmental issues around the world.<sup>99,100,113</sup> MOFs have been documented as promising materials for the adsorption and selective capture of CO<sub>2</sub> from the atmosphere and flue gas.<sup>114,115</sup> The best CO<sub>2</sub> uptake reported to date was observed in MOF-200 with ultrahigh porosity (2437 mg/g at 50 bar and 298 K).<sup>29</sup> Furthermore, MOFs with open metal sites were also found to offer enhanced CO<sub>2</sub> uptake and selectivity at low pressures.<sup>116,117</sup> For instance, Mg-MOF-74 exhibits selective adsorption of CO<sub>2</sub> from CO<sub>2</sub>-CH<sub>4</sub> mixtures, with a dynamic uptake capacity of 8.9 wt%.<sup>118</sup> Additionally, chemical binding of CO<sub>2</sub> in MOFs by reversible formation and decomposition of organic carbonates at room temperature is a

promising approach to enhance the selectivity for CO<sub>2</sub> capture from flue and combustion gases in the presence of water.<sup>119</sup> Besides fuel gases and greenhouse gases, MOFs are also investigated as adsorbents for hazardous gases and volatile organic compounds (e.g., H<sub>2</sub>S, SO<sub>2</sub>, Cl<sub>2</sub>, ClCN, NH<sub>3</sub>, NO<sub>x</sub>, CO, C<sub>2</sub>H<sub>2</sub>, ethylene oxide, octane, tetrahydrothiophene and benzene vapor).<sup>120–123</sup>

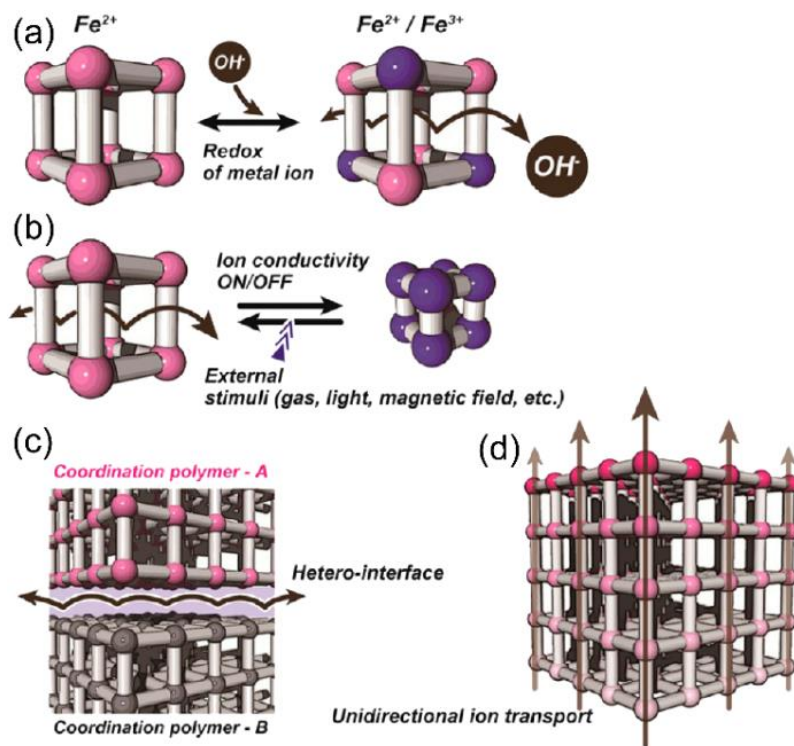


**Figure 1.7** Schematic illustrations of some new ideas for ion conductivity. (a) Conductivity of various ions by use of redox properties; (b) Control of ion conductivity by applying external stimuli; (c) Development of ionics at heterointerfaces; (d) Unidirectional ion transportation from one side to the other side of crystals. Image adapted from ref. 124.

The use of MOFs as new class of ion conductors and transporters is also a promising area of MOF research. MOF structures tend to have high hydrophilicity and guest-accessible voids and several kinds of ion conductivities (mainly proton conductivity) have been reported.<sup>124–133</sup> Early results demonstrated that the water-mediated proton conductivity of MOFs can be improved by the addition of acid functionalities, such as carboxylic, phosphonic or sulfonic acids.<sup>126,128</sup> However, for the practical application of MOFs as proton conductors they must be able to function under quite harsh conditions, such as relatively high operating temperatures (120–180 °C) and in anhydrous conditions.<sup>134</sup> Alternatively, the incorporation of protic guests

such as imidazole and 1,2,4-triazole into the microchannels of MOFs can result in high proton conduction under anhydrous conditions.<sup>135</sup> In addition, lithium ( $\text{Li}^+$ ) and other ions can also be transported in the MOF structures.<sup>136,137</sup> If new concepts and strategies are applied to the design of novel MOF structures (Figure 1.7) and the crystal structures of MOFs are optimized, further improvements in both conductivity and the working temperature range are expected.<sup>124</sup> The application of MOFs as a versatile supramolecular platform to develop heterogeneous catalysts for organic reactions represents a new direction in MOF research.<sup>103,104,138–140</sup> Catalytic properties of MOFs can be achieved by active sites in the structures, including coordinatively unsaturated metal sites, metalloligands, functional organic sites, as well as active metal nanoparticles embedded in the cavities.<sup>102,141–148</sup> The Allendorf group<sup>102</sup> has recently demonstrated that Mg-IRMOF-74 (I and II) with its high density of open metal sites is stable under reducing conditions and can cleave phenyl ethers to the corresponding hydrocarbons and phenols. Significantly, a series of metalloporphyrin-based (Mn, Co, Pd, Fe etc.) MOFs have been synthesized and their catalytic performances in oxidation reactions have been illustrated by the groups of Hupp, Ma, Wu and Zhou.<sup>149–157</sup> In order to create functional organic sites in MOFs, several methods, such as functionalization of organic linkers, grafting of active groups onto coordinatively unsaturated metal centers and post-covalent modification of organic ligands, have been employed. In addition, several catalytically active metals (e.g., Cu, Ru, Au, Pd, Pt) have been incorporated into the MOF cavities in the form of nanoparticles. These metal@MOF composites always show enhanced catalytic performance compared to the parent MOFs.<sup>146–148,158–162</sup> Furthermore, MOFs can also be applied as photocatalysts in energy transfer, light-harvesting, photocatalytic proton and  $\text{CO}_2$  reduction, water oxidation, and degradation of model organic pollutants.<sup>104,163,164</sup>

Another very interesting and well-investigated topic of MOFs are their optical properties and related applications in lighting, display, sensing, and detection. A large number of luminescent MOFs have been designed and reported.<sup>165–172</sup> Apart from the aforementioned fields, several other applications of MOFs, including drug delivery and controlled release, biomedical imaging, magnetism and electrochemistry, are also gaining momentum.<sup>105,106,173–175</sup>

## 1.2 Surface-mounted metal-organic frameworks (SURMOFs)

### 1.2.1 Introduction to SURMOFs

Although MOFs have various potential applications in form of bulk powders or single crystals, some extended applications, such as chemical sensors, smart membranes, catalytic coatings and many other nanotechnological devices, demand the integration of MOFs onto specific surfaces like thin films or coatings with defined thickness and high homogeneity as well as tunable chemical functionality.<sup>176–184</sup> Surface-mounted metal-organic frameworks (denoted as SURMOFs), which physically or chemically adhere to the (functionalized) substrates as continuous thin films and, in an ideal case, have a low roughness and high homogeneity, are ideal to fulfill the needs.<sup>181,183–185</sup> Additionally, SURMOFs present an opportunity to exploit the functionality of the materials' electrical, mechanical, optical or magnetic properties and to serve as effective platforms for loading the pores with functional molecules, such as metallic nanoparticles, redox-active species and luminescent compounds.<sup>186–194</sup> To fully control the properties of SURMOFs, several features including morphology, crystallographic orientation, surface roughness, film thickness, homogeneity, adhesion to the substrate and mechanical properties as well as stability need to be taken into account. For instance, for application in electrochemistry, pin-hole free layers with well-defined thickness are required to avoid direct contact of the metal substrate with the electrolyte.<sup>184</sup> Moreover, the judicious choice of substrates for the deposition of SURMOFs is crucial to meet specific applications. Transparent substrates are mandatory for optical devices built from SURMOFs, whereas conductive substrates are required in devices where electrical properties play a central role. Moreover, for the application of SURMOFs in flexible electronic devices, flexible substrates like plastic films are needed.

A key to spatially controlled deposition of SURMOFs is the functionalization of the substrates that allows to control the effective adhesion and growth along specified crystallographic directions. Self-assembled monolayers (SAMs), which are ordered molecular assemblies spontaneously formed by the chemisorption of suitably functionalized molecules onto the surface of substrates,<sup>195–198</sup> are a useful tool to functionalize the substrates and can be further employed as templates to direct the growth of SURMOFs.<sup>199–201</sup> Generally, well-ordered

monolayers carrying various functional groups can provide coordinating sites for initiating the growth of SURMOFs. Therefore, SAMs will be discussed in the following part.

## 1.2.2 Self-assembled monolayers (SAMs)

### 1.2.2.1 Introduction to SAMs

SAMs are ordered arrangements of molecules (or atoms) adsorbed on solid surfaces, in which intermolecular forces play a key role and which can be spontaneously formed from solution or from vapor phase.<sup>196,197,202</sup> As demonstrated in Figure 1.8, the molecules which form SAMs can be divided into three different parts: the anchor group, the spacer (backbone or main chain) and the functional group (end group). The anchor group is a chemical functionality with a specific affinity for a certain type of substrate and guides the self-assembly process, linking the molecules (of variable length) to the substrate through a strong bond.<sup>195,197</sup> The interactions among the spacers (typically van der Waals forces) can ensure an efficient packing of the monolayer and contribute to the stabilization of structures with increasing molecular size.<sup>197</sup> The functional group confers specific properties, such as hydrophilicity, hydrophobicity, bio-resistance and redox properties, to the surface and can be used to anchor different molecules, biomolecules or nanostructures by weak interactions or covalent bonds.<sup>196,197,203</sup> The diversity of the functional groups makes the SAMs one of the most flexible tools to tune the surface chemistry of substrates such as metals, metal oxides and semiconductors.<sup>196,197</sup>

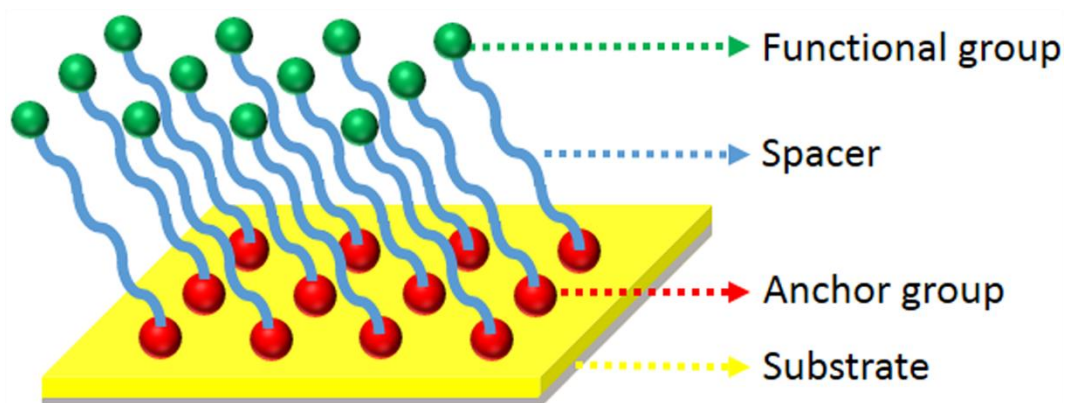


**Figure 1.8** Schematic illustration of a SAM formed on the surface of a substrate.

SAMs can be regarded as the interface between “two worlds”: inorganic compounds (metals

and semiconductors), on one hand, and organic and biological materials (organic compounds, polymers, complex biomolecules, and even cells) on the other.<sup>197</sup> By tuning the properties of SAMs, materials with totally different physical and chemical properties can be easily linked together. In the next section, the preparation and structure of the most extensively studied system of thiolate SAMs on gold will be discussed.

#### 1.2.2.2 Preparation and structure of thiolate SAMs on gold

Thiolate SAMs on coinage metals, particularly on gold, have attracted considerable attention due to their easy preparation from gas phase or, even more importantly, from solution, and their relatively high stability mediated by the strength of the S-Au bond and van der Waals interactions between the neighboring molecules in the monolayer.<sup>196,197</sup> The simple immersion of a clean gold substrate into an ethanolic solution of the corresponding thiols (typical concentration range: 10  $\mu$ M-1 mM) for a certain period (normally 12-18 h at room temperature) is the most widely used protocol for preparing SAMs on gold. Dense coverages of molecules are obtained quickly from dilute solutions, but a slow reorganization process requires times on the order of hours to maximize the density of molecules and minimize the defects in the SAM.<sup>196</sup> However, a number of experimental factors may have significant influence on the quality of the resulting SAMs, including solvent, temperature, concentration of the adsorbate, immersion time, concentration of oxygen in solution, cleanliness of the substrate, functional groups and length of the spacer.<sup>196</sup>

Structural information on thiolate SAMs has been widely gathered by many different and complementary surface science techniques, including scanning probe microscopy techniques (atomic force microscopy (AFM) and scanning tunneling microscopy (STM)), diffraction techniques (electron, neutron, atom, ion and X-ray diffraction), vibrational spectroscopies (infrared reflection/absorption spectroscopy (IRRAS), sum frequency generation (SFG), high resolution electron energy loss spectroscopy (HREELS) and surface enhanced Raman spectroscopy (SERS)), electron-based spectroscopies (such as Auger electron spectroscopy (AES), X-ray photoelectron spectroscopy (XPS), ultraviolet photoelectron spectroscopy (UPS) and X-ray absorption near edge structure (XANES)) as well as ellipsometry. According to

numerous studies on SAM formation, the generally accepted fact is that the reaction can be considered as an oxidative addition of S-H bonds to the gold surface, followed by a reductive elimination of hydrogen.<sup>195</sup> However, owing to some internal and external factors, several types of structural defects might be created in thiolate SAMs during the self-assembly process, that can have an important influence on the efficiency of some applications. To minimize the appearance of structural defects and improve the structural quality of the SAMs, several strategies can be employed. For instance, a careful choice of the solvent and the deposition temperature can yield thiolate SAMs with lower defect density and better chain order.<sup>204–207</sup>

### 1.2.2.3 Applications of SAMs

The unique abilities in tailoring the interfacial properties of various surfaces allow the use of SAMs for a broad range of applications, ranging from coatings, where the SAM might play an essentially passive role, up to SAMs as active elements in sensors.<sup>198,208–215</sup> As ultrathin layers or coatings, SAMs can be used for corrosion prevention, friction reduction, and lubrication in material protection.<sup>198,210</sup> In the area of device fabrication, SAMs are utilized as building blocks in sensors, biosensors, actuators, molecular motors; as active or passive elements in electronic devices, transistors, switches and as “nano alligator clips” in single molecule circuits.<sup>211–213</sup> In micro/nanofabrication, SAMs are employed as inks in microcontact printing ( $\mu$ CP) and dip pen lithography; as resists in photolithography and shave lithography and as anti-adherent layers in nanomolding and nanoreplication.<sup>214</sup> In biology and medicine, SAMs are used as building blocks for the design of biomolecule carriers and biorecognition assays and for the immobilization of cells, bacteria, and DNA.<sup>208,209,215</sup> More importantly, SAMs carrying various functional groups can functionalize surfaces as templates for initiating the growth of SURMOFs while controlling their lateral structure as well as their crystallite orientation.<sup>181,201,216</sup>

### 1.2.3 Growth protocols of SURMOFs

Since SURMOFs have become a centerpiece of materials science during the last decade, a number of innovative approaches have been developed for their fabrication. The commonly



employed methods include the direct solvothermal growth,<sup>217,218</sup> the gel-layer deposition,<sup>219</sup> crystallization from mother solutions,<sup>199,220</sup> secondary growth on seeding layers,<sup>221,222</sup> stepwise layer-by-layer growth (or liquid phase epitaxial growth),<sup>185,200,201,216,223</sup> spray-assisted layer-by-layer growth,<sup>224</sup> Langmuir-Blodgett layer-by-layer deposition,<sup>180,225</sup> microwave-induced thermal deposition,<sup>226</sup> evaporation or solvent induced crystallization,<sup>62,227</sup> colloidal dip coating deposition,<sup>228,229</sup> electrochemical deposition<sup>51,52</sup> and the morphological replacement method.<sup>230</sup> Of these methods, several representative approaches will be discussed in more detail in the following section.

### 1.2.3.1 Direct solvothermal growth of SURMOFs

Direct solvothermal growth is the simplest and most straightforward approach for the deposition of MOF thin films. The SURMOF growth can be easily attained by just putting the respective substrates into solutions of the SBUs and the linkers during the solvothermal syntheses. Usually, this method is powerful for the preparation of polycrystalline MOF films with micrometer thickness on varied substrates, such as metals, textiles, fibers and porous alumina.<sup>217,218,231,232</sup> In addition, surface functionalization of substrates with SAMs bearing particular functional groups, which should allow for a direct binding of the MOF material, has been demonstrated to improve the quality of the deposited MOF films.<sup>232,233</sup>

Through surface functionalization, Zacher et al. deposited HKUST-1 films on SiO<sub>2</sub> substrates, which were pretreated with 10-undecenyltrichlorosilane followed by an oxidation step.<sup>234</sup> Similarly, Huang et al.<sup>235,236</sup> utilized 3-aminopropyltriethoxysilane (APTES) to functionalize TiO<sub>2</sub> and Al<sub>2</sub>O<sub>3</sub> substrates onto which dense, well-intergrown ZIF-22 and ZIF-90 membranes with thicknesses of 40 μm and 20 μm were deposited under different solvothermal conditions. Interestingly, in both cases, the surface-bound amino groups react directly with the aldehyde groups of the imidazole derivatives instead of the Zn ions, so that the ZIFs are covalently bound to the supports via imine bonds. Additionally, Van Gough et al.<sup>237</sup> have shown that by modifying Si and TiO<sub>2</sub> surfaces with diazonium and catechol groups, respectively, the direct solvothermal growth of PPF-5 (porphyrin paddlewheel framework) was possible on such carboxylate-terminated surfaces, but only non-densely packed MOF films were produced.

These examples suggest that, with very few exceptions, the MOFs films obtained by direct solvothermal growth are typically randomly oriented and typically do not cover surface of the substrates completely, in particular when the thickness of the film is small (tens of nanometers).

#### 1.2.3.2 Growth of SURMOFs from aged mother solutions

The major problem of the direct solvothermal growth described in the previous section is that solvothermal reactions usually require relatively high temperatures (generally above 100 °C). At such temperatures, most of the SAMs (particularly the commonly used thiolate SAMs) are not stable, what hampers the controlled nucleation and growth of the MOF films.<sup>238</sup> To address this issue, the crystallization from the aged mother solutions at room temperature has been developed as an alternative. Generally, the aged mother solution is prepared as follows: after solvothermal synthesis for a short time, the reaction solution is cooled down to room temperature and filtered. The resultant solution, which still contains enough starting material to slowly generate more of the MOF product, is called “aged mother solution”. For the deposition of SURMOFs, the SAM-functionalized substrates are immersed into the mother solution for a certain period (hours or days).

The first successful example for the formation of SURMOFs by this method was reported by Hermes and coworkers.<sup>199</sup> MOF-5 was selectively grown onto the -COOH terminated areas after immersing the substrate patterned with -COOH/-CF<sub>3</sub>-functionalized SAMs into the filtered MOF-5 mother solution for 24 h. Later, the Bein group<sup>220</sup> extended this protocol to show that SAMs not only provide nucleation centers required for the growth of SURMOFs, but can also control the crystallite orientation when SAMs carrying appropriate functional groups were used. For example, HKUST-1 crystallites grown on -COOH terminated SAMs preferred [100] orientation, as shown in Figure 1.9, while [111] orientation dominated growth was observed on -OH terminated SAMs, as indicated by out-of-plane XRD data. Interestingly, they observed that HKUST-1 crystallites also grew onto a chemically inactive SAM, -CH<sub>3</sub> terminated SAM, although without preferred orientation. The authors suggested that this phenomenon is due to the dispersive forces between the organically terminated crystal faces and the alkyl-terminated SAM.

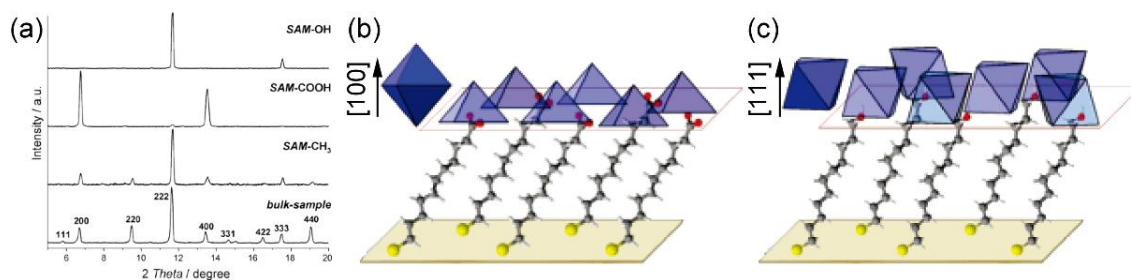


**Figure 1.9** (a) Out-of-plane XRD patterns of HKUST-1 films grown on different SAM functionalized surfaces; (b) [100] oriented growth of HKUST-1 on -COOH terminated surface; (c) [111] oriented growth of HKUST-1 on -OH terminated surface. Adapted from ref. 220.

Using the same method, this group also reported the deposition of highly oriented MIL-88B, chemically functionalized Fe-MIL-88B-NH<sub>2</sub>, Fe-MIL-101-NH<sub>2</sub>, UiO-68-NH<sub>2</sub> as well as CAU-1 on SAM-modified surfaces besides HKUST-1.<sup>239–241</sup> In addition, this protocol is also mild enough to allow *in situ* studies of the SURMOF growth, which would be helpful for a fundamental understanding of SURMOF growth in general.

### 1.2.3.3 Gel-layer growth of SURMOFs

Gel-layer growth is a kind of slow diffusion method. The Bein group<sup>219</sup> has demonstrated that highly oriented SURMOFs can also be deposited by utilizing this protocol. To this end, a polyethylene glycol (PEG) gel loaded with metal-ion precursor (Cu<sup>2+</sup> or Fe<sup>3+</sup>) was brought into contact with substrates modified either by a -COOH or a -OH terminated alkanethiolate SAM before the linker solution (H<sub>3</sub>(btc) or H<sub>2</sub>(bdc-NH<sub>2</sub>)) was carefully added. Since a high local concentration of metal ions was achieved near the surface, a relatively high heterogeneous nucleation rate was attained at that interface (Figure 1.10a). The morphology and thickness of the final films could be further controlled by altering the parameters of the procedure such as the chain length of the PEG and the concentration of metal ions in the gel. In the case of HKUST-1, a perfect [111] crystallite orientation was observed, which was independent of the functionality of the underlying SAM (-COOH or -OH, Figure 1.10b). The results are different from the HKUST-1 films grown in an aged mother solution at room temperature where -COOH and -OH SAM functionalities lead to distinct orientations. In the case of the flexible Fe-MIL-88B-NH<sub>2</sub>, highly [001] oriented films were obtained on -COOH terminated SAMs,

whereas for the films grown on the -OH terminated SAM, both (001) and (101) diffraction peaks were observed in out-of-plane XRD data, meaning no preferred growth direction could be attained (Figure 1.10c).

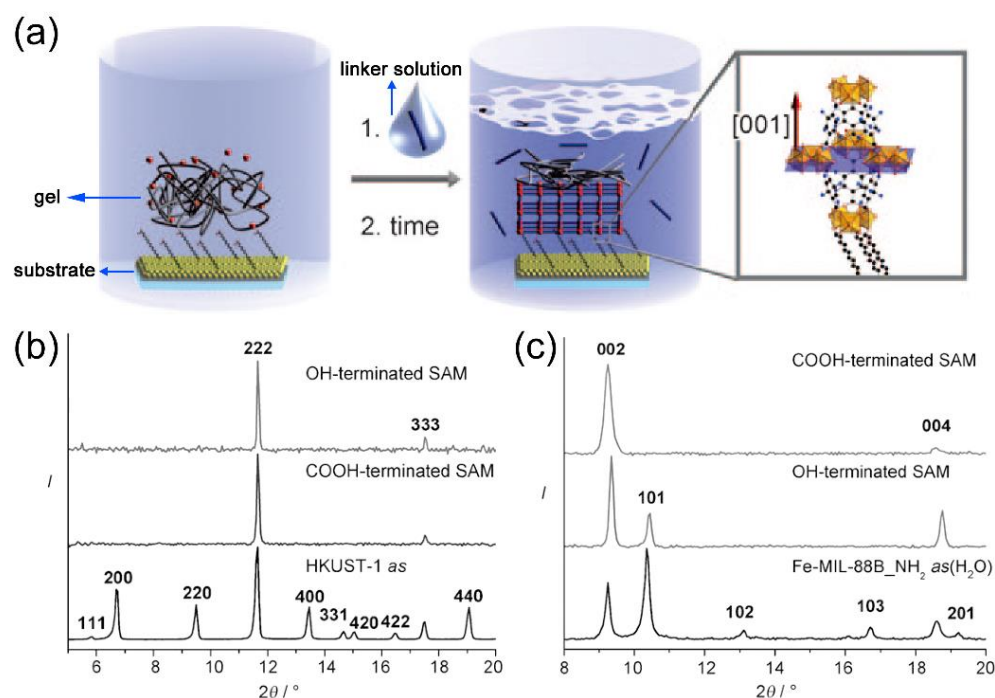


**Figure 1.10** (a) Outline of the gel-layer SURMOF growth process: the SAM surface becomes covered with a gel, which contains the metal ions, and the linker is provided as an external solution. By diffusion of the linkers to the surface, a SURMOF is formed. (b) XRD patterns of HKUST-1 and (c) XRD patterns of Fe-MIL-88B-NH<sub>2</sub> films grown on -OH and -COOH terminated SAMs. Adapted from Ref. 219.

#### 1.2.3.4 Stepwise layer-by-layer (LbL) growth of SURMOFs

Another straightforward method, the so-called stepwise layer-by-layer (LbL) or the liquid phase epitaxial (LPE) growth method, which allows for the growth of SURMOFs, has been introduced by Fischer, Wöll and their coworkers in 2007 (Figure 1.11a).<sup>200</sup> In contrast to the direct solvothermal growth and mother solution strategies in which the reactants are mixed, crystal nucleation and growth are separated in the LbL protocol by sequentially exposing a SAM-functionalized substrate to two or more solutions. Typically, one solution contains the metal SBUs, while the other solution contains the linker or linker mixture. When immersed into a metal precursor solution, the exposed functional groups on the surface first coordinate the metal SBUs. Physically adsorbed metal SBUs are subsequently removed *via* rinsing with

pure solvent (e.g., ethanol). In an ideal case, a monolayer of metal SBUs is formed on the surface. Further exposure to an organic linker solution leads to coordination of the organic linkers at the prefixed metal units and the process is determined by the coordination geometry of them. After removing unreacted species, the upward-facing and unoccupied sites serve as new active sites for the next cycle of metal precursor deposition. Finally, a SURMOF with low roughness and high homogeneity is formed by repeating the exposure procedure. The thickness and crystallite orientation of SURMOFs can be precisely tuned by adjusting the number of deposition cycles and the functional groups of SAMs.<sup>177,178,181,185,201,216,242</sup>

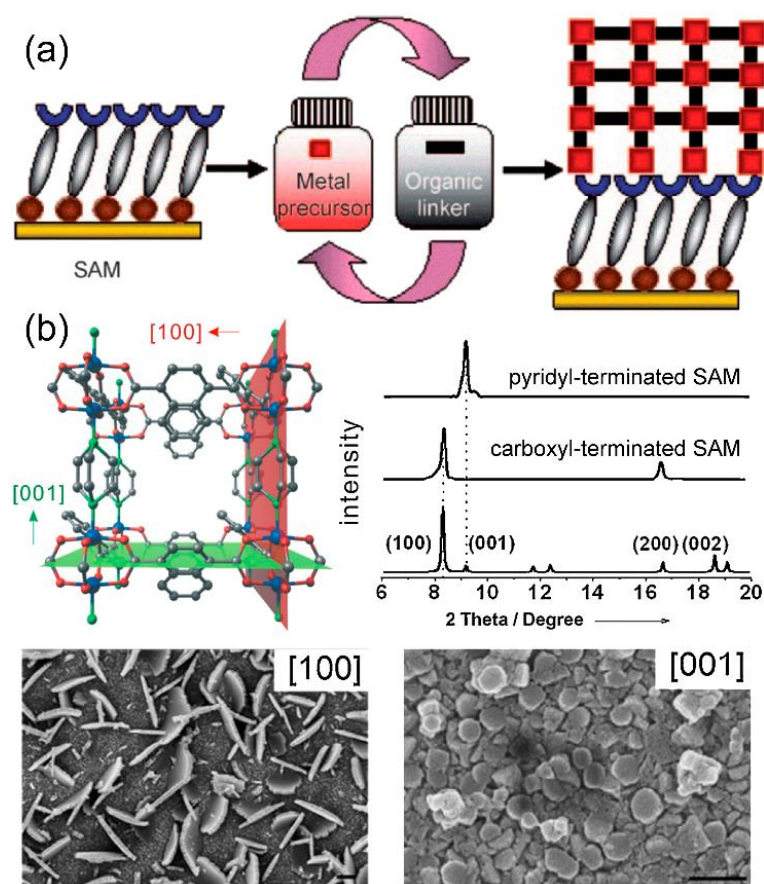


**Figure 1.11** (a) Illustration of LbL growth of SURMOFs on SAM functionalized surfaces; (b) The oriented growth of a tetragonal  $[\text{Cu}_2(\text{ndc}_2)(\text{dabco})]$  SURMOF is determined by the surface chemistry (monodentate pyridyl SAMs mostly induce MOF growth along the [001] direction; bidentate  $-\text{COOH}$  SAMs induce MOF growth along the [100] direction) and can be detected by out-of-plane XRD as well as SEM. Image taken from Refs. 216 and 243.

The first demonstration of the LbL technique was the growth of a highly [100] oriented

HKUST-1 SURMOF on a carboxyl-terminated SAM.<sup>200</sup> Later, the same group demonstrated that the crystallite orientation of HKUST-1 SURMOFs obtained by the LbL method depends on the nature of the exposed functional groups as supported by the preferred [111] and [100] orientation on -OH and -COOH terminated SAMs, respectively.<sup>216</sup> Recently, Shekhah et al.<sup>244,245</sup> have reported that the LbL protocol can be applied to deposit [110] oriented ZIF-8 SURMOFs onto OH-terminated gold surfaces as well as onto porous Al<sub>2</sub>O<sub>3</sub> membranes under optimized synthesis conditions. It is worthy to point out that in this process methanol was used as a solvent instead of the commonly used ethanol.

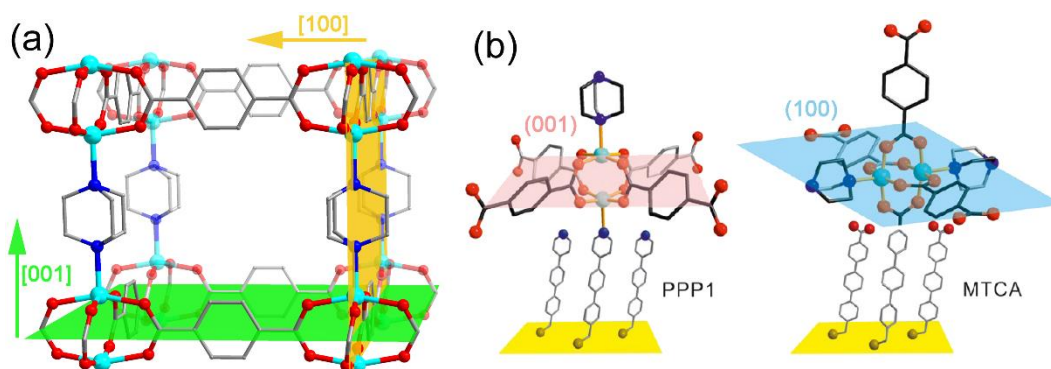


**Figure 1.12** (a) The two principal growth directions of a [M<sub>2</sub>L<sub>2</sub>P] SURMOF, e.g., [Cu(bdc)<sub>2</sub>(dabco)<sub>2</sub>], on a pyridyl or carboxyl-terminated surface. (b) Concept for the directed growth of [M<sub>2</sub>L<sub>2</sub>P] SURMOFs based on the different coordination sites in the paddle wheel SBU. The use of monodentate pyridyl-terminated SAM (PPP1) typically results in [001] orientation (left), while the use of a carboxyl-terminated SAM (MTCA) tilts the crystallographic growth direction by 90 °(right). Adapted from Ref. 247.

Additionally, the LbL deposition of SURMOFs is not limited to binary MOF systems containing the metal centers and one kind of ligand. Pillared-layer [M<sub>2</sub>L<sub>2</sub>P] MOFs, which contain two kinds of ligands (M = Zn<sup>2+</sup>, Cu<sup>2+</sup>..., L = dicarboxylate linkers, P = dinitrogen pillars), have been well proven to be suitable for LbL deposition.<sup>184,185,201,243,246</sup> Similar to the binary systems, the crystallite orientation of tetragonal [M<sub>2</sub>L<sub>2</sub>P] SURMOFs is also highly dependent on the surface chemistry, which can be modified by SAMs bearing various functional groups.<sup>201,243</sup> On pyridyl-terminated surfaces, a preferred growth along the [001] direction was observed, whereas highly [100] oriented SURMOFs were obtained on carboxyl-terminated SAMs (Figure 1.11b).<sup>243</sup> This varied orientation led to different film morphologies as could be observed by SEM. The [Cu<sub>2</sub>(ndc)<sub>2</sub>(dabco)] (dabco = 1,4-diazabicyclo[2.2.2]octane)

crystallites with [100] orientation were sheet-like and stood upright on the carboxyl SAM, while crystallites laying down parallel to the surface were observed on the pyridyl-terminated surface ([001] orientation).

On the other hand, the LbL approach also allows for the investigation of growth kinetics and mechanisms. As demonstrated by the Wöll group,<sup>216</sup> a successful LbL growth of HKUST-1 SURMOFs requires the employment of preformed tetrakis- $\mu$ -carboxylatodimetal clusters (e.g.,  $\text{Cu}_2(\text{CH}_3\text{COO})_4$ , so-called copper paddle-wheels), since no significant growth was observed when copper nitrate was applied which does not have the copper paddle-wheel units. Moreover, the LbL growth can also be employed to understand the growth mechanisms of layer-based tetragonal  $[\text{M}_2\text{L}_2\text{P}]$  systems. In general, the  $[\text{M}_2\text{L}_2\text{P}]$  systems consist of 2D layers of  $[\text{M}_2\text{L}_2]$  which are connected by dinitrogen pillar ligands to form 3D network structures, such as dabco and 4,4'-bipyridine (bipy), through the apical positions at the metal (normally  $\text{Cu}^{2+}$ ) centers.<sup>248</sup> As demonstrated in Figure 1.12a, the two principal growth directions, [100] and [001], are orthogonal. The orthogonality of the functionalities in the tetragonal system should make the growth direction tunable by altering the surface chemistry of substrates. Ideally, a substrate terminated by monodentate Lewis bases with high affinity to the axial coordination sites (e.g., pyridyl) should promote the growth in the [001] direction, whereas [100] orientation should be favored by termination with bidentate Lewis bases (e.g., carboxylate) (Figure 1.12b).<sup>247</sup> However, the first exception from this assumption about LbL growth of a  $[\text{Cu}_2(\text{ndc})_2(\text{dabco})]$  SURMOF was reported by Zacher et al.<sup>201</sup> They stated that a  $[\text{Cu}_2(\text{ndc})_2(\text{dabco})]$  SURMOF with exclusive [001] orientation (expected) could be deposited onto pyridyl-terminated substrates. However, on -COOH terminated SAMs, crystallite orientation and crystallinity of the  $[\text{Cu}_2(\text{ndc})_2(\text{dabco})]$  SURMOFs were greatly influenced by the LbL deposition fashion (two-step process ( $\text{M} \rightarrow (\text{L}+\text{P})$ ) vs. three-step process ( $\text{M} \rightarrow \text{L} \rightarrow \text{P}$ )) as well as the molar ratio of linker (L) and dinitrogen pillar (P). When the three-step LbL process was used, SURMOFs of the expected [100] orientation were obtained, but the crystal quality depended critically on the deposition order: the sequence ( $\text{M} \rightarrow \text{L} \rightarrow \text{P}$ ) resulted in much better crystallinity as compared to the ( $\text{M} \rightarrow \text{P} \rightarrow \text{L}$ ) one. By changing the molar ratio of L/P from 1:1 to 2:1, surprisingly, perfectly oriented SURMOFs were deposited, however, the crystallite orientation was [001] instead of [100]. Recently, our group has reported that an interplay of surface

functionalities, deposition temperature and first layer order together determine the orientation and crystal quality of a  $[\text{Cu}_2(\text{f}_4\text{bdc})_2(\text{dabco})]$  SURMOF.<sup>247</sup> By using the two-step LbL process, the growth of the SURMOF on carboxyl-terminated and pyridyl-terminated substrates was studied in detail. It was found that rearrangement processes in the very first layer determine the final orientation distribution of the growing crystals. Based on the experimental results, the authors proposed that the substitution at the apical position of the  $\text{Cu}_2$  SBUs is surprisingly hampered and requires significant thermal activation for attaining a complete reaction and a correct orientation. With this information, it was possible to obtain almost perfectly [001] oriented  $[\text{Cu}_2(\text{f}_4\text{bdc})_2(\text{dabco})]$  SURMOFs on the pyridyl-terminated SAMs at high temperature (60 °C), while on the carboxyl-terminated surfaces, the expected [100] crystallite orientation could be best achieved at low deposition temperature (5 °C). These findings suggest that the growth of tetragonal  $[\text{M}_2\text{L}_2\text{P}]$  type SURMOFs might be more complicated than anticipated and several parameters, such as surface chemistry, deposition conditions and temperature, need to be taken into consideration.

The stepwise LbL approach also allows to grow different SURMOFs on top of one another, yielding MOF-on-MOF heterostructures.<sup>201,249–253</sup> Spatial functionalization and hybridization of SURMOFs can be achieved with integration of multiple properties into one thin film sample using the outer surface of a preformed MOF as a templating substrate for the growth of a second type of MOF. Isoreticular tetragonal  $[\text{M}_2\text{L}_2\text{P}]$  MOFs with comparable linker sizes are suitable for the fabrication of MOF-on-MOF heterostructures because the linkers or the metal SBUs can be varied without changing the original tetragonal topology as depicted in Figure 1.13.<sup>201,249</sup> Following this strategy, Shekhah et al. reported the growth of highly oriented  $[\text{Zn}_2(\text{ndc})_2(\text{dabco})]$  SURMOF on top of an isostructural  $[\text{Cu}_2(\text{ndc})_2(\text{dabco})]$  SURMOF. These heterostructured SURMOFs exhibited a preferred [001] crystallite orientation.<sup>249</sup> Zacher et al. fabricated a  $[\text{Cu}_2(\text{f}_4\text{bdc})_2(\text{dabco})]/[\text{Cu}_2(\text{ndc})_2(\text{dabco})]$  heterostructure by changing linkers and keeping metal precursors the same.<sup>201</sup> Moreover, by altering both the metal clusters and the linkers, they grew  $[\text{Zn}_2(\text{bdc-BME})_2(\text{dabco})]/[\text{Cu}_2(\text{ndc})_2(\text{dabco})]$  heterostructures. Additionally, playing with this sophisticated strategy, the synthesis of Janus-SURMOFs (binary SURMOFs with reversible order, A-on-B or B-on-A) and photoswitchable  $[\text{Cu}_2(\text{azo-bpdc})_2(\text{dabco})]/[\text{Cu}_2(\text{bpdc})_2(\text{dabco})]$  heterostructure were reported.<sup>253,254</sup> The strategy also shows potential for



the fabrication of multifunctional core-shell or core-shell-shell heterostructures when the first layer consists of discrete crystals instead of a closed film. Liu et al.<sup>251</sup> deposited a series of A-B and A-B-C heterostructured SURMOFs, where A =  $[\text{Cu}_2(\text{bdc})_2(\text{dabco})]$ , B =  $[\text{Cu}_2(\text{bdc-NH}_2)_2(\text{dabco})]$ , C =  $[\text{Cu}_2(\text{ndc})_2(\text{dabco})]$ , with a preferred [001] oriented growth on pyridyl-terminated SAMs. The spatial distribution of functionalities can be precisely controlled by the number of LbL deposition cycles as demonstrated by post-synthetic modification (PSM) of the amino groups with isothiocyanates. Additionally, the LbL growth method can be applied to fabricate heterostructured SURMOFs with large structural differences. As demonstrated by the same group,<sup>250</sup> a heterostructure with a [111] oriented HKUST-1 layer on top of a highly [001] oriented  $[\text{Cu}_2(\text{ndc})_2(\text{dabco})]$  SURMOF was deposited onto quartz crystal microbalance (QCM) substrates. The [111] orientation of the HKUST-1 layer suggests that the dangling dabco ligands of the  $[\text{Cu}_2(\text{ndc})_2(\text{dabco})]$  layer act as monodentate ligands very similar to the situation on pyridyl-terminated SAMs.

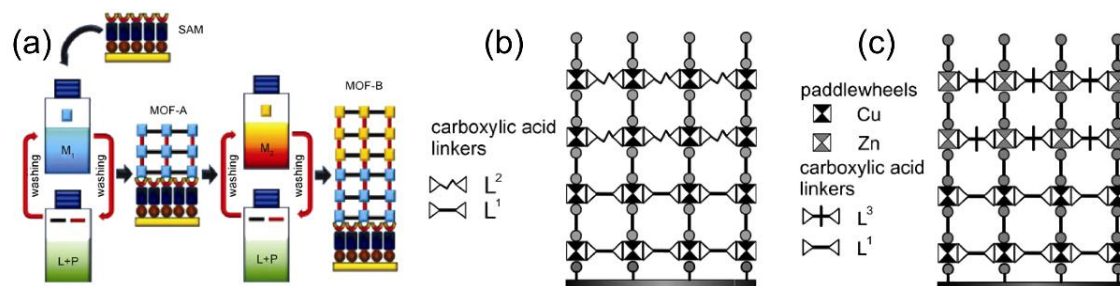


**Figure 1.13** Schematic representation of LbL deposition of MOF-on-MOF heterostructures. (a) The metal clusters are changed; (b) The linkers are altered; (c) Both metal clusters and linkers are varied. Adapted from Ref. 249 and 201.

### 1.2.3.5 Spray-assisted LbL growth of SURMOFs

Although the computer-assisted pump-method and the robot method are already applied in the LbL growth of SURMOFs, it remains very time consuming.<sup>188,193,245,246,251</sup> For example, at least one hundred deposition cycles are required for the growth of MOF thin films with a thickness of 100-200 nm. The recently established spray-assisted LbL growth protocol (Figure 1.14a) has been documented as an efficient alternative and time-saving method to deposit SURMOFs.<sup>224</sup> HKUST-1 was employed as the first example to demonstrate the efficiency of

this method.<sup>224</sup> In the seminal paper of Arslan et al., -COOH terminated substrates were alternatively exposed to aerosols containing  $\text{Cu}(\text{OAc})_2$  (10 s) or  $\text{H}_3\text{btc}$  (20 s) produced by spray nozzles.<sup>224</sup> In between, a rinsing step by exposing the substrates to an aerosol of the pure solvent (in most cases ethanol) for 5 s was sufficient to remove the residual reactants (metal source and organic linkers). A HKUST-1 SURMOF of 100 nm can be grown in 30 min, which is much faster than the conventional LbL process (usually 72 hours are needed for the same thickness). The growth rate of the spray-assisted deposition of HKUST-1 was 10 nm/cycle, which is much larger than the conventional LbL growth rate (1.3 nm/cycle).<sup>224</sup> In addition, the same authors broadened the application of the spray method for the deposition of SURMOFs of other systems, such as 2D layer systems of the general formula  $[(\text{M}_2\text{L}_2(\text{H}_2\text{O})_2)]$ , namely  $[(\text{Zn}/\text{Cu})_2(\text{bdc})_2(\text{H}_2\text{O})_2]$ , and 3D tetragonal  $[\text{M}_2\text{L}_2\text{P}]$  MOFs, namely  $[\text{Cu}_2(\text{ndc})_2(\text{dabco})]$ . Later, employing the same deposition protocol, Liu et al. reported the fabrication of a  $\text{Cu}^{2+}$ -based isorecticular SURMOF-2 series using dicarboxylate linkers with varied length as well as  $\text{Zn}^{2+}$ -based SURMOF-2 with a porphyrin core.<sup>255,256</sup>

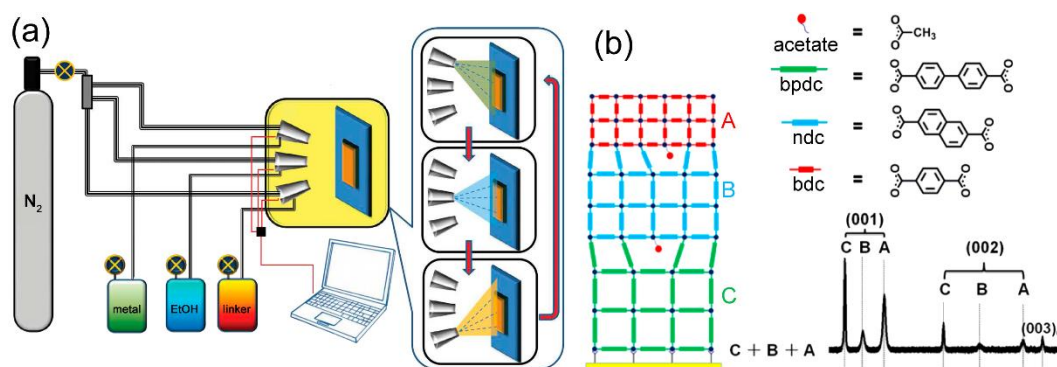


**Figure 1.14** (a) Outline of the spray-assisted layer-by-layer growth of SURMOFs; (b) Deposition of hetero-SURMOF-2 with [001] orientation even if the lattice constants do not match, as confirmed by XRD. The defect sites presumably are occupied by acetate ligands. Adapted from Ref. 224 and 190.

The spray-assisted LbL method can also be used to fabricate MOF-on-MOF heterostructures. As reported by the Wöll group,<sup>190</sup> despite large (20%) lattice mismatches, heterostructured SURMOFs with high crystallinity and exclusive [001] orientation can be achieved (Figure 1.14b). The authors proposed that the unexpected tolerance of the large lattice mismatch was caused by the capping of vacancies with acetate groups and the low elastic constant of the MOF materials. The hypothesis was further supported by a detailed theoretical analysis using

*ab-initio* methods.

### 1.2.3.6 Langmuir-Blodgett LbL deposition of SURMOFs

As an alternative method, the Langmuir-Blodgett (LB) approach has been adopted by the Kitagawa group for the growth of MOF monolayers.<sup>180,225,257</sup> By using the LB-LbL method, NAFS-1, which is composed of cobalt-containing porphyrin units (Co-tcpp, tcpp = 5,10,15,20-tetrakis (4-carboxyphenyl) porphyrin) linked together by binuclear copper paddle-wheel units in a 2D array of Cu-Cotcpp-bipy, was successfully transferred to a silicon substrate in a layer-by-layer fashion (Figure 1.15), yielding nanofilms.<sup>225</sup> By repeating the transfer, the overall thickness of the film could be precisely controlled and adjusted. Both out-of-plane and in-plane XRD measurements indicated that the NAFS-1 films have a high crystalline order along the growth direction. Here, the rarely achieved in-plane order probably results from the interdigitation of the pyridine molecules which protrude from the fabricated 2D sheets.

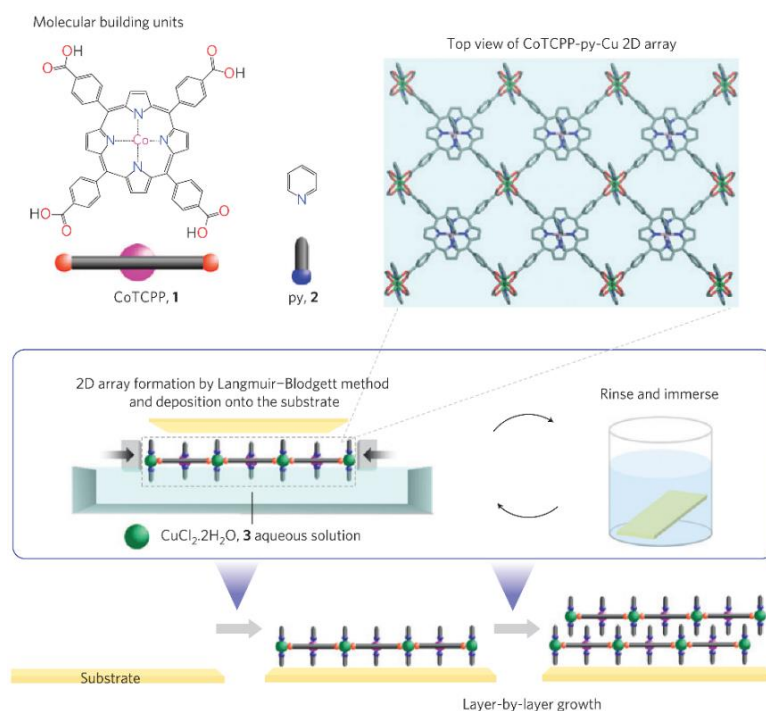


**Figure 1.15** Outline of the Langmuir-Blodgett LbL process. A 2D coordination network is formed at the water-air interface, by reaction of the two ligands with  $\text{Cu}^{2+}$  ions from the water phase. These 2D sheets were then transferred one after the other onto a solid substrate. The layers become aligned to each other due to the protruding pyridine ligands. Taken from Ref. 225.

Employing this method, another structurally similar MOF, NAFS-2,<sup>257</sup> consisting of metal-free carboxylate porphyrin ligands and  $\text{Cu}^{2+}$  ions, was similarly assembled into nanofilms. Moreover, the Kitagawa group reported that using a varied approach, homogeneous SURMOF films were obtained by dipping transfer and ultrasonic exfoliation of a stacked bulk MOF constructed from  $\text{Cu}^{2+}$  and the tcpp linker. Nevertheless, the LB-LbL approach may not be applicable to 3D structured MOFs.

### 1.2.3.7 Evaporation/solvent induced growth of SURMOFs

Evaporation/solvent induced growth of thin layers of MOF crystallites on substrates from precursor solutions containing the metal ions and the organic linkers has been first introduced by Ameloot et al.<sup>227</sup> The key of this particular method is to prepare a precursor solution without the formation of small MOF nuclei. In their seminal paper, the authors revealed that, in the case of HKUST-1, by replacing the standard ethanol/water mixture with dimethyl sulfoxide (DMSO), a particle-free, stable precursor solution could be formed at room temperature as confirmed by dynamic light scattering (DLS) measurements. The formation of HKUST-1 crystals was triggered then by evaporation of the solvent at 100 °C. Upon solvent evaporation, oriented growth of HKUST-1 crystallites preferentially along the [111] direction was observed regardless of the surface chemistry of the substrates (silanol, vinyl, or carboxyl). The group also demonstrated that the solvent evaporation technique could be extended to grow ordered arrays of ZIF-8 and MOF-5.<sup>227</sup>

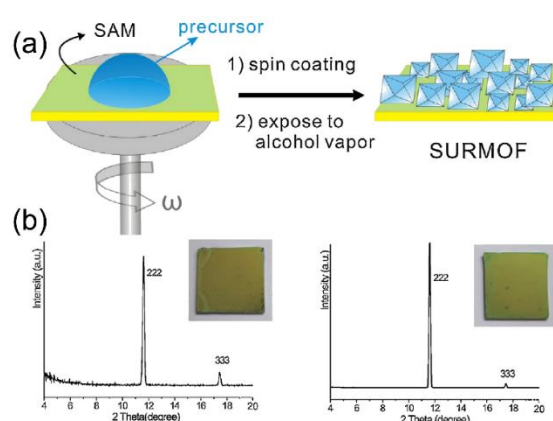


**Figure 1.16** Deposition of dense SURMOFs by solvent induced crystallization. (a) A HKUST-1 precursor solution was spin-coated onto a planar substrate and treated with ethanol vapor (b, left) and methanol vapor (b, right), respectively, to induce oriented crystallization. Adapted from Ref. 62.

Based on the concept of solvent-stabilization, patterns of single submicrometer HKUST-1 crystals were achieved on various SAM-functionalized surfaces by Carbonell et al. utilizing a pen-type lithography method.<sup>83</sup> Furthermore, our group has lately reported the oriented growth of HKUST-1 thin films and patterns by using spin-coating technique<sup>62</sup> followed by a solvent-induced growth. As depicted in Figure 1.16, by spin coating HKUST-1 precursor solution onto substrates, relatively large, uniform films were formed.<sup>62</sup> When the films were exposed to methanol or ethanol vapor, highly [111] oriented crystalline films were obtained. Interestingly, the crystallite orientation of the films is independent of the surface functionalization (-COOH or pyridyl-terminated SAMs). The thickness of the films could be adjusted by controlling the number of spin coating and exposure steps.

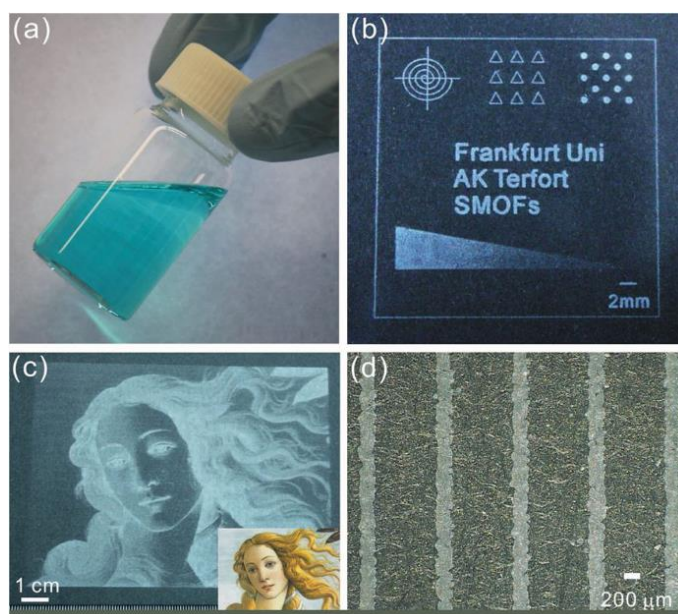


**Figure 1.17** HKUST-1 SURMOF patterns fabricated by the inkjet printing technique. (a) Ink solution; (b), (c) and (d) various patterns. Adapted from Ref. 258.

Well defined HKUST-1 patterns with large areas and high complexity were also realized by inkjet printing (Figure 1.17).<sup>258</sup> For this, the mixture of ethylene glycol and ethanol had to be added to the HKUST-1 precursor solution to adjust the viscosity and surface tension of the solution, making it usable for inkjet printing. Afterwards, the ink was loaded into a typical household inkjet printer and the patterns were controlled by commercial graphics software. By controlling the amount of ink delivered, various patterns could be generated on paper, plastics and textiles. The excess solution could be removed and crystallinity could be improved

by simple immersion into methanol for 30 min. Finally, the crystallinity and chemical identity of the printed films were confirmed by XRD and IRRAS.

#### 1.2.4 Applications of SURMOFs

The vast advantages of SURMOFs, including their homogeneity and the very tight mechanically bonding between the substrate and the MOF crystallites, make them extremely attractive in the practical and specific applications of chemical sensors,<sup>183,259,260</sup> catalytic coatings,<sup>261</sup> adsorption and separation platforms,<sup>243,246,250,262,263</sup> antifouling/antibacterial coatings,<sup>264,265</sup> resistive switching nanodevices,<sup>266</sup> electrochromic/electrochemical devices,<sup>267–272</sup> optical devices,<sup>188,273</sup> electronic devices,<sup>186,274</sup> photovoltaic devices<sup>256</sup> etc..

Sensing and adsorption applications of SURMOFs have been well documented so far. Due to large surface areas combined with the designability of pore size and chemical functionality, high analyte sensitivity and selectivity can be realized.<sup>101</sup> QCM, onto which the SURMOFs can be deposited, open the opportunity to study the adsorption and sensing properties of MOF materials using simple setups. The Bein group deposited HKUST-1 SURMOF onto a QCM substrate and recorded water sorption isotherms.<sup>275</sup> Later, Ameloot et al.<sup>52</sup> demonstrated the electrochemical deposition of HKUST-1 onto QCM electrodes and showed that the deposited HKUST-1 SURMOF can be used as a humidity sensor. Using the direct growth approach, Tu et al. recently deposited a series of ZIFs with different thickness onto QCM electrodes.<sup>276</sup> They found that the fabricated ZIF/QCM devices could be used to detect vapor phase organic compounds including alcohol/water, BTEX compounds (benzene, toluene, ethylbenzene and xylene isomers), and hexane isomers. With the help of QCM technique, the measurements of adsorption kinetics and diffusion coefficients of analytes are possible.<sup>277–279</sup> Zybaylov et al.<sup>278</sup> grew dense HKUST-1 thin films onto QCM sensors and were able to determine the diffusion coefficients of pyridine into the films. A similar study delivered by Uehara et al.<sup>280</sup> indicated that the adsorption kinetics depends on the size of the HKUST-1 nanocrystals for some organic vapors.

The pore orientation of SURMOFs with respect to the surface normal is crucial for the high sensitivity and selectivity in the applications of sensing and adsorption.<sup>243,246,250,262</sup>. Based on

the QCM technique, Liu et al.<sup>243</sup> studied the orientation dependent adsorption of SURMOFs. In their study, highly oriented [Cu<sub>2</sub>(ndc)<sub>2</sub>(dabco)] SURMOFs with different pore openings were chosen as prototypes. The results showed that highly [100] oriented SURMOFs exhibited higher absorption rates towards the analytes (benzene, toluene and *p*-xylene), while SURMOFs with [001] orientation actually hindered the guest molecules from access due to their comparably small pore opening along the [001] direction. The same group also reported the adsorption property of a MOF-on-MOF heterostructure, where a [111] oriented HKUST-1 layer was grown on top of a [001] oriented [Cu<sub>2</sub>(ndc)<sub>2</sub>(dabco)] SURMOF.<sup>250</sup> Furthermore, enantioselective adsorption of an enantiopure SURMOF containing chiral linkers was reported.<sup>246</sup> By utilizing circular dichroism spectroscopy, Gu et al. directly observed the uptake selectivity without the need to extract the guests from a chiral SURMOF.<sup>281</sup> Later, the group extended the study of enantioselective adsorption by using several enantiopure SURMOFs with isorecticular structures and found that the enantioselectivity was significantly influenced by the pore size.<sup>282</sup> Remarkably, as recently demonstrated by the Wöl group, photoswitchable adsorption and optically triggered release (Figure 1.18a) of SURMOFs were also achieved by functionalizing the dicarboxylate linkers or pillars with azobenzene functionalities.<sup>253,262</sup>

Applications of SURMOFs as electronic and photovoltaic devices, which rely on charge transfer or spin transport, are increasingly gaining attention.<sup>186,256,274</sup> For these applications, conductive substrates, such as silicon or gold with inherent electrical contact, are used to deposit SURMOFs. By employing electrochemistry, the charge transport through a HKUST-1 film into an electrolyte was investigated.<sup>192</sup> After loading ferrocene into the pores, the SURMOF could carry a current. Very recently, the Wöl group<sup>191</sup> performed more direct conductivity measurements by replacing the electrolyte by a mercury droplet (Figure 1.18b). They found that, after loading with ferrocene, the resistance of HKUST-1 SURMOFs increased linearly with the film thickness. Combining the experimental results, an incoherent charge-hopping mechanism was proposed by the authors to explain the charge carrier transport. Talin et al.<sup>186</sup> reported that the conductivities of HKUST-1 SURMOFs were greatly improved by loading tetracyanoquinodimethane (TCNQ) into the pores. Guided by theoretical calculations, the authors concluded that in this case the copper paddle-wheel units became coordinated by the TCNQ at apical positions, resulting in a strong electronic coupling between

the guest molecule and the HKUST-1 framework. In photovoltaics, the mobility of both, single charge carriers and charge carrier pairs (excitons), is of utmost importance.<sup>256,283</sup> The Hupp group investigated the transport of the excited states within porphyrin-based SURMOFs via trapping the excitons by a chromophore.<sup>283</sup> They could show that the mobility of the photochemically generated excitons is quite similar to the one in the bulk materials, where the excitons can hop between up to 2000 linkers within their lifetime (4 ns). Recently, Liu et al.<sup>256</sup> reported the fabrication of a prototype of a photovoltaic device based on oriented SURMOF-2 deposited onto conductive and transparent fluorine-doped tin oxide (FTO) electrodes by the spray-assisted LbL method (Figure 1.18c). A high charge carrier mobility and a photo-conversion efficiency of up to 0.45% were observed. The theoretical calculations suggest that the porphyrin-MOFs are actually indirect band-gap semiconductors, what might be the reason for the unexpected high performance of the SURMOF-2 based photovoltaic device.

The optical applications of SURMOFs greatly rely on the optical properties (color, refractive index, fluorescence emission etc.) of the films. Lu et al. firstly fabricated of Fabry-Pérot device (Figure 1.18d) and showed that the color of ZIF films with thicknesses in the micrometer region is mainly determined by their interference properties.<sup>284</sup> The authors demonstrated that the deposited ZIF films could be used to optically monitor the Fabry-Pérot interference peaks as a function of analyte exposure. Moreover, Gu et al. reported the deposition of transparent, homogenous HKUST-1 SURMOFs with well-defined thickness and crystallite orientation by using a dipping robot equipped with an ultrasonic bath.<sup>188</sup> The authors claimed the film quality was greatly improved and suitable for optical applications. Very recently, the concept of the fabrication of ceramic/metal-organic framework multilayers, which can be used for the realization of optical dielectric mirrors and for the investigation of mechanical properties, was demonstrated by the groups of Lotsch and Wölz.<sup>285-287</sup>

Additionally, doping the films with functional guest molecules was proven to be an effective method to enhance the optical properties of SURMOFs.<sup>193,194</sup> The Wölz group revealed that an inorganic dye guest species [Eu(bzac)<sub>3</sub>(bipy)] (bzac = 1-phenyl-1,3-butanedionate, bipy = 2,2'-bipyridine) could be loaded into HKUST-1 SURMOFs by simple immersion of the deposited MOF films into ethanolic solutions of the luminescent molecules.<sup>194</sup> Solid-state absorption spectra suggest that optical excitation can be transferred from the MOF ligands to the Eu atoms



embedded in the pores. This antennae effect provides good potential for further applications of SURMOFs in optical devices. The idea is further extended by Gu et al. for the fabrication of lanthanide coordination compounds (LCCs) encapsulated MOF thin films with high encapsulation efficiency.<sup>193</sup> The authors showed that white light emission could be obtained by tuning the concentration of the LCCs with red, blue and green emission, respectively.

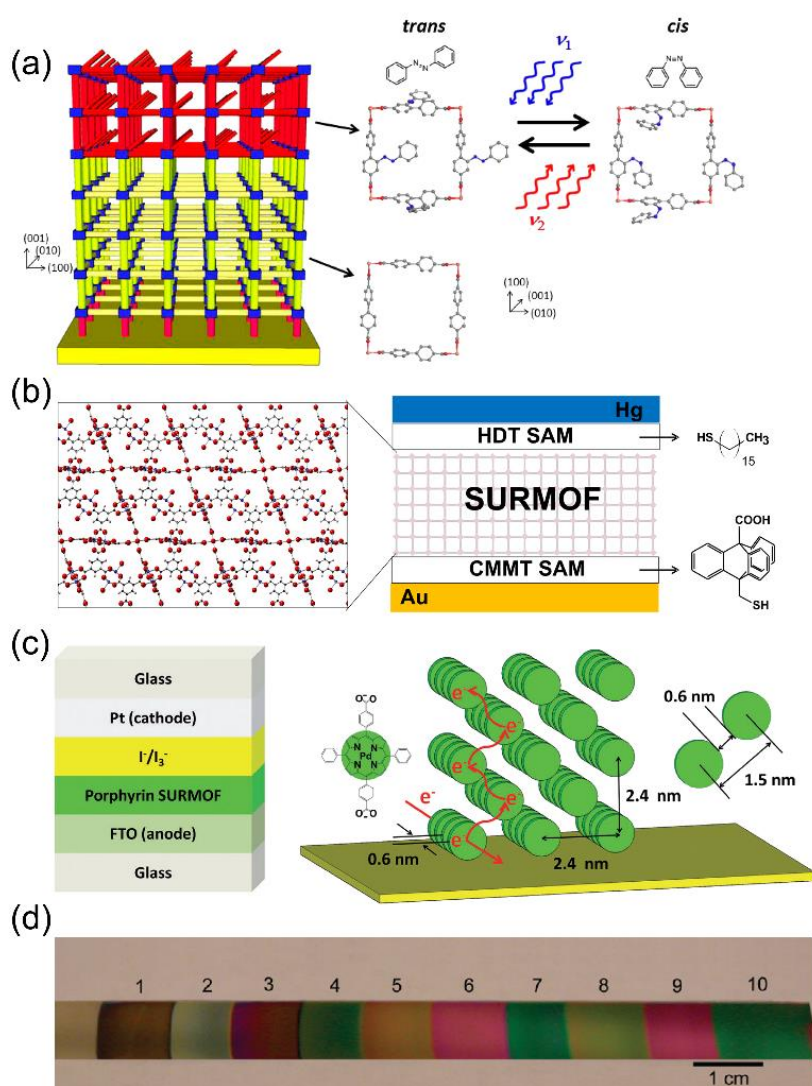


**Figure 1.18** Various applications of SURMOFs: (a) optically triggered release;<sup>253</sup> (b) electric transport device;<sup>191</sup> (c) photovoltaic device;<sup>256</sup> (d) Fabry-Pérot device<sup>284</sup>. Adapted from 191, 253, 256 and 284, respectively.

### 1.3 Common methods for SURMOF characterization

In order to characterize the growth and the properties of SURMOFs, a number of techniques

are employed, including QCM, AFM, SEM, IRRAS and XRD.

QCM can measure mass variation per unit area by measuring the change in frequency of a quartz crystal resonator according to the Sauerbrey equation.<sup>288</sup> In the field of SURMOFs, QCM is often employed to monitor the crystal growth and measure the adsorption capacity of SURMOFs towards gases and volatile organic compounds (VOCs) due to the extremely high sensitivity against mass change.

AFM is a type of scanning probe microscopy (SPM) and it allows the high-magnification observation of a sample's surface topography by scanning the surface with a microscopic tip. In general, three operating modes (contact mode, non-contact mode and tapping mode) can be selected for the measurements of various samples. The surface topography, roughness and film thickness of SURMOFs can be characterized by this technique.

SEM is generally utilized to obtain the information about the sample's surface topography by scanning the sample with a focused beam of electrons. Combining the method with energy-dispersive X-ray spectroscopy (EDS or EDX), the composition of sample can be determined. In this thesis, the crystallite size, morphology, homogeneity and film thickness of SURMOFs are observed by using SEM.

IRRAS is a well-established analytical technique for the characterization of thin films or monolayers on metal surfaces, which provides unique molecular structure and orientation information on the film constituents. The structure and crystallite orientation of SURMOFs can be evaluated by combining different vibrational modes (e.g., asymmetric and symmetric  $\text{-COO}^-$  vibrations for carboxylate-based MOF systems).

XRD is usually employed for the phase identification and crystal structure determination of a crystalline material. For the characterization of crystalline film structures, both out-of-plane and in-plane XRD techniques are utilized and several structure features, such as the orientation and crystallite-size anisotropy, can be obtained. Out-of-plane XRD measurements are mainly used to determine the crystallite orientation of SURMOFs.

## 1.4 Task and outline

MOFs, emerged as novel porous materials, have many potential applications due to their

structural diversity and tunability. Nevertheless, controlled deposition of MOFs onto various surfaces as thin films or coatings is highly demanded to fulfill specific applications in devices. Therefore, this thesis mainly focuses on the controlled growth and the properties of SURMOFs. In order to accomplish the controllable deposition of SURMOFs onto diverse substrates, many protocols have been developed. Among them, stepwise layer-by-layer (LbL) growth (or liquid epitaxial growth, LPE) and spin-coating, were utilized to deposit SURMOFs in this thesis. During the LbL deposition process, several parameters such as crystallite orientation, film thickness, homogeneity, morphology and the distribution of functionalities are needed to be tuned and optimized.

Specifically, in chapter 3, a semi-rigid dicarboxylate linker based  $[\text{Cu}_2(\text{sdb})_2(\text{bipy})]$  SURMOF with low structural symmetry is employed to broaden the applicability of LbL growth method. The growth mechanism of such SURMOFs on both pyridyl- and carboxyl-terminated surfaces is proposed and the pore-orientation dependent uptake capacities of the oriented SURMOFs are evaluated. In chapter 4, the LbL growth of multifunctional SURMOFs containing up to five different carboxylate linkers is attempted using mixed dicarboxylate linkers of the same type but bearing different functionalities. The effect of acidity of the linkers (expressed by their  $pK_a$  values) on the orientational quality and adsorption capacity of the SURMOFs are addressed in detail. Furthermore, chapter 5 describes an approach to realize the application of SURMOFs in electrochemical devices by LbL deposition of SURMOFs containing redox-active species employing  $\text{H}_2(\text{bpdc})$  linker functionalized with ferrocene (Fc) and dimethyl ferrocene ( $\text{Me}_2\text{Fc}$ ) moieties. The charge transfer properties of these SURMOFs are evaluated and interpreted. Additionally, taking advantages of spin-coating and alcohol induced growth of highly oriented HKUST-1 SURMOFs, a series of polyoxometalate (POM) functionalized HKUST-1 SURMOFs (POM@HKUST-1 SURMOFs) with certain crystallite orientation are controllably deposited. The redox properties of the SURMOFs with and without dye loading are addressed in chapter 6.



## 2 Experimental section

### 2.1 Materials and general preparation

All chemicals, which were employed in this thesis, were available commercially and used directly without further purification, except for  $\text{Cu}_2(\text{CD}_3\text{COO})_4 \cdot x\text{D}_2\text{O}$ , 4,4'-sulfonyldibenzoic acid ( $\text{H}_2(\text{sdb})$ ), 2-nitrobenzene-1,4-dicarboxylic acid ( $\text{H}_2(\text{bdc-NO}_2)$ ), the ferrocene (Fc) and dimethyl ferrocene ( $\text{Me}_2\text{Fc}$ ) functionalized 4,4'-biphenyldicarboxylic acid ( $\text{H}_2(\text{bpdc})$ ) linkers ( $\text{H}_2(\text{bpdc-amide-Fc})$  and  $\text{H}_2(\text{bpdc-amide-Me}_2\text{Fc})$ ), (4-(1*H*-pyrazol-4-yl) phenylmethanethiol (PyzP1) and  $(\text{n-Bu}_4\text{N})_4\text{H}(\text{PMO}_{10}\text{V}_2\text{O}_{40})$  (VPMo).  $\text{Cu}_2(\text{CD}_3\text{COO})_4 \cdot x\text{D}_2\text{O}$ , VPMo,  $\text{H}_2(\text{sdb})$  and  $\text{H}_2(\text{bdc-NO}_2)$  were synthesized according to previous reports.<sup>247,289–292</sup> The  $\text{H}_2(\text{bpdc-amide-Fc})$  and  $\text{H}_2(\text{bpdc-amide-Me}_2\text{Fc})$  linkers were synthesized by Julian Scherr from our working group. The syntheses of SAMs, PyzP1 and (4-(4-(4-pyridyl)phenyl)phenyl)methanethiol (PPP1), were performed by Tarek Abu-Husein from our group. The 4'-(mercaptomethyl)-terphenyl-4-carboxylic acid (MTCA) SAM is available in the working group.

*SAM-functionalized substrates:* The gold substrates were manufactured by electron-beam evaporation of 5 nm of Cr and 200 nm of Au onto four-inch Si wafers with [100] orientation. After evaporation, the substrates were cleaned by immersion into a 10 mM 1-hexadecanethiol (HDT) solution in ethanol for 2 h followed by a 2 min treatment in  $\text{H}_2$  plasma. Then, the clean gold substrates were immersed for 48 h in a 0.1 mM PyzP1 solution or a 0.1 mM PPP1 solution or a half saturated MTCA solution in ethanol (some solid MTCA was sonicated in ethanol to obtain a saturated solution, which was, after filtration, diluted with an equal amount of ethanol to avoid precipitation of the MTCA). Since MTCA usually forms bilayers on gold because of hydrogen bond formation, trifluoroacetic acid (TFA) was used to break the hydrogen bonds and thus to remove the second layer. For this, the MTCA-covered substrates were rinsed with ethanol, and then sonicated in a TFA solution (2 drops of TFA in 20 ml ethanol) for 5 min. After rinsing with ethanol and drying in a stream of  $\text{N}_2$ , the substrate was treated in a vacuum chamber at 5 mbar for 30 min to remove the TFA. All substrates were rinsed with ethanol before the stepwise LbL growth.

## 2.2 Experimental details of chapter 3

*Synthesis of [Cu<sub>2</sub>(sdb)<sub>2</sub>(bipy)] bulk crystals:*<sup>293</sup> The synthesis of bulk [Cu<sub>2</sub>(sdb)<sub>2</sub>(bipy)] was similar to the synthesis of [Zn<sub>2</sub>(sdb)<sub>2</sub>(bipy)] reported previously.<sup>294</sup> bipy (0.4 mmol, 62.4 mg, 98%, Alfa Aesar), H<sub>2</sub>(sdb) (0.8 mmol, 245 mg, synthesized according to ref. 289 and 290), and Cu(NO<sub>3</sub>)<sub>2</sub>•3H<sub>2</sub>O (0.8 mmol, 193 mg, 99.5%, ABCR) were dissolved in DMF (Acros Organics, 40 mL). The solution was sealed in a glass vial and heated at 100 °C for 2 days. After cooling, filtration and drying under vacuum, a dark green crystalline powder of [Cu<sub>2</sub>(sdb)<sub>2</sub>(bipy)] was obtained (76% yield). The phase purity was confirmed by the PXRD pattern shown in Figure S8.1.5. A FT-IR spectrum with characteristic vibrations was also recorded to verify the successful synthesis (Figure S8.1.5).

*LbL growth of [Cu<sub>2</sub>(sdb)<sub>2</sub>(bipy)] SURMOFs on gold surfaces:*<sup>293</sup> The LbL deposition was performed in a custom-made temperature controllable glass cell. Programmable peristaltic pumps were used to dose the respective fluids, controlled by a routine written in LabVIEW. The SAM-functionalized substrates in the cell were alternatively exposed to a solution of copper acetate in ethanol (1 mM) for 20 min and to an equimolar H<sub>2</sub>(sdb)/bipy mixture (0.1 mM each, ethanol solution) for 40 min at different temperatures (15-65 °C). Between each step, the substrates were exposed to fresh ethanol for 5 min twice.

## 2.3 Experimental details of chapter 4

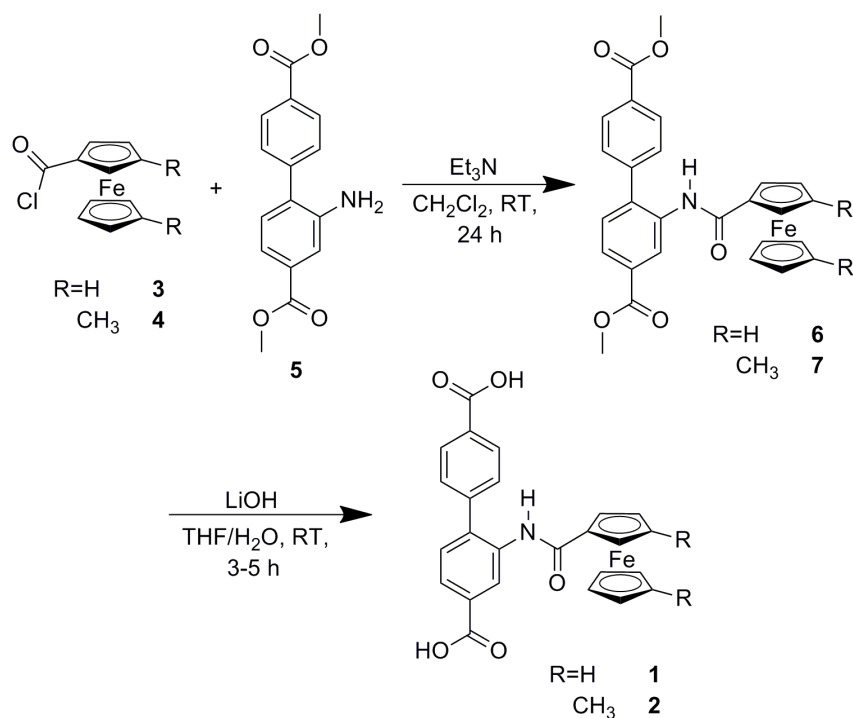
*LbL growth of [Cu<sub>2</sub>L<sub>2</sub>(dabco)] (L = a single kind of dicarboxylate linker) and [Cu<sub>2</sub>Lm<sub>2</sub>(dabco)] (Lm = mixed dicarboxylate linkers) SURMOFs on SAM-functionalized gold surfaces:* The LbL deposition was performed in the same way as described for [Cu<sub>2</sub>(sdb)<sub>2</sub>(bipy)] SURMOFs (section 2.2). Herein, the SAM-functionalized substrates in the cell were alternatively exposed to a solution of copper acetate in ethanol (1 mM) for 15 min and to an equimolar L/dabco or Lm/dabco mixture (L = single kind of linker with a concentration of 0.1 mM; Lm = mixed linkers with a total concentration of 0.1 mM; dabco = 0.1 mM) for 30 min at 60 °C. Between each step, the substrates were exposed to fresh ethanol for 5 min twice.

*Syntheses of bulk [Cu<sub>2</sub>L<sub>2</sub>(dabco)] (L = a single kind of dicarboxylate linker) MOFs:* The syntheses of [Cu<sub>2</sub>L<sub>2</sub>(dabco)] MOFs were all performed in a similar way. The synthesis of

[Cu<sub>2</sub>(bdc)<sub>2</sub>(dabco)] is given as an example. dabco (0.05 mmol, 6 mg, 98%, ABCR) was added to a solution containing H<sub>2</sub>(bdc) (0.1 mmol, 17mg, 99%, Acros Organics) and Cu(NO<sub>3</sub>)<sub>2</sub>•3H<sub>2</sub>O (0.1 mmol, 24 mg, 99.5%, ABCR) in DMF (6 mL, Acros Organics), and the resulting solution was stirred at room temperature for 3 h. Afterwards, the solution was heated to 120 °C in a sealed glass tube for two days. The product was washed with DMF and ethanol and dried at 60 °C in an oven (85% yield). For the synthesis of [Cu<sub>2</sub>(chdc)<sub>2</sub>(dabco)] MOF, the solvent was water instead of DMF.

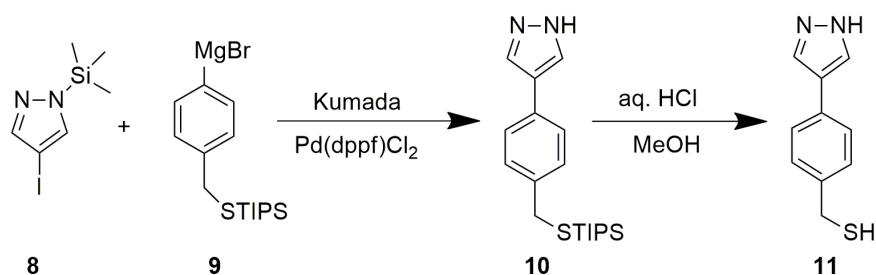
## 2.4 Experimental details of chapter 5

*Synthesis of ferrocene and dimethyl ferrocene functionalized linkers:* H<sub>2</sub>(bpdc-amide-Fc) and H<sub>2</sub>(bpdc-amide-Me<sub>2</sub>Fc) linkers were synthesized by Julian Scherr from our working group. The synthesis sketch is depicted in Scheme 2.1 and details can be found in his master thesis.<sup>295</sup>



**Scheme 2.1** Synthesis route to ferrocene- and dimethylferrocene-functionalized H<sub>2</sub>(bpdc) linkers.

*Synthesis of (4-(1H-pyrazol-4-yl)phenylmethanethiol (PyzP1):* The synthesis of the PyzP1 molecule was performed by Tarek Abu-Husein from our working group. The synthesis route is shown in Scheme 2.2.



**Scheme 2.2** Synthesis of 4-(1*H*-pyrazol-4-yl)phenylmethanethiol (**11**, PyzP1).

The PyzP1 (**11**) was synthesized in a two-step reaction. First, 1-trimethylsilyl-4-iodopyrazole (**8**) was prepared as described in literature.<sup>296</sup> The Kumada coupling of the Grignard reagent **9**, formed from 4-bromobenzyl(triisopropylsilyl (TIPS)) sulfide, with halogen arenes has been optimized in our group.<sup>297</sup> This protocol could be extended to yield the novel compound PyzP1 (**11**).

*Syntheses of bulk [Cu<sub>2</sub>(bpdc-amide-Fc)<sub>2</sub>(dabco)] and [Cu<sub>2</sub>(bpdc-amide-Me<sub>2</sub>Fc)<sub>2</sub>(dabco)]:* The syntheses of bulk [Cu<sub>2</sub>(bpdc-amide-Fc)<sub>2</sub>(dabco)] and [Cu<sub>2</sub>(bpdc-amide-Me<sub>2</sub>Fc)<sub>2</sub>(dabco)] were performed in a similar way using the solvothermal method. H<sub>2</sub>(bpdc-amide-Fc) (0.05 mmol, 23.5 mg) or H<sub>2</sub>(bpdc-amide-Me<sub>2</sub>Fc) (0.05 mmol, 24.8 mg), dabco (0.025 mmol, 2.8 mg, 98%, ABCR), and Cu<sub>2</sub>(OAc)<sub>4</sub>•2H<sub>2</sub>O (0.05 mmol, 9.9 mg, ≥99%, Carl Roth) were dissolved in methanol (VWR, 15 mL). The solution was sealed in a glass vial and heated to 100 °C for 2 days. After cooling, filtration and drying under vacuum, yellow green powders of [Cu<sub>2</sub>(bpdc-amide-Fc)<sub>2</sub>(dabco)] or [Cu<sub>2</sub>(bpdc-amide-Me<sub>2</sub>Fc)<sub>2</sub>(dabco)] was obtained (95% yield for both syntheses). The phase purity was confirmed by the PXRD patterns shown in Figure S8.3.2 and FT-IR spectra were also recorded to verify the successful synthesis (Figure S8.3.2).

*LbL growth of [Cu<sub>2</sub>(bpdc-amide-Fc)<sub>2</sub>(dabco)] (Fc-SURMOF) and [Cu<sub>2</sub>(bpdc-amide-Me<sub>2</sub>Fc)<sub>2</sub>(dabco)] (Me<sub>2</sub>Fc-SURMOF) SURMOFs on gold surfaces:* The LbL deposition was performed in the same way as described for [Cu<sub>2</sub>(sdb)<sub>2</sub>(bipy)] SURMOFs (section 2.2). Herein, the SAM-functionalized substrates in the cell were alternatively exposed to a solution of copper acetate in ethanol (1 mM) for 15 min and to an equimolar L/dabco mixture (L = H<sub>2</sub>(bpdc-amide-Fc) or H<sub>2</sub>(bpdc-amide-Me<sub>2</sub>Fc) with the concentration of 0.1 mM or the 1:1 mixture with the total concentration of 0.1 mM; dabco = 0.1 mM) for 20 min at 60 °C. Between each step, the



substrates were exposed to fresh ethanol for 5 min twice.

*The pore volume evaluation of SURMOFs after functionalization:* The single pore volume of model  $[\text{Cu}_2(\text{bpdc})_2(\text{dabco})]$  system can be evaluated as a cuboid<sup>298</sup>, and the volume can be estimated as:  $V_1 = 12.52 \text{ \AA} \times 12.52 \text{ \AA} \times 7.3 \text{ \AA} \approx 1144 \text{ \AA}^3$ .

After functionalization with ferrocene: Fc moiety could be approximated as a cylinder (6.7 Å height and 6.4 Å diameter) according to Ref. 299,  $V_2 = \pi \times (3.2 \text{ \AA})^2 \times 6.7 \text{ \AA} \approx 216 \text{ \AA}^3$ . As calculated based on crystallographic theory, every functionalized MOF cell contains two Fc moieties. Thus, the total volume of ferrocene moieties  $V_3 = 2 \times V_2 = 432 \text{ \AA}^3$ . The accessible volume in a single pore of Fc-SURMOF is  $V_4 = 1144 \text{ \AA}^3 - 432 \text{ \AA}^3 = 712 \text{ \AA}^3$ .

After functionalization with dimethyl ferrocene:  $\text{Me}_2\text{Fc}$  could also be regarded as a cylinder (6.7 Å height and 10.4 Å diameter) due to the dynamic disorder of methyl groups (the dynamic radius of methyl group is 2.0 Å, Ref. 300). The volume  $V_5 = \pi \times (5.2 \text{ \AA})^2 \times 6.7 \text{ \AA} \approx 569 \text{ \AA}^3$ . Analogously, total volume of  $\text{Me}_2\text{Fc}$  moieties in a single cell is  $V_6 = 2 \times V_5 = 1138 \text{ \AA}^3$ . So the accessible volume in a single pore of  $\text{Me}_2\text{Fc}$ -SURMOF is  $V_7 = 1144 \text{ \AA}^3 - 1138 \text{ \AA}^3 = 6 \text{ \AA}^3$ .

## 2.5 Experimental details of chapter 6

*Preparation of precursor solutions:* HKUST-1 precursor solution was prepared as previously published.<sup>62,227</sup>  $\text{Cu}(\text{NO}_3)_2 \cdot 3\text{H}_2\text{O}$  (1.22 g, 5.24 mmol, 99.5%, ABCR) and 1,3,5-benzenetricarboxylic acid ( $\text{H}_3(\text{btc})$ , 0.58 g, 2.76 mmol, 98%, ABCR) were dissolved in DMSO (5 g, 99.9%, Sigma-Aldrich).

PTA@HKUST-1 and VPMo@HKUST-1 precursors were prepared similarly:  $\text{Cu}(\text{NO}_3)_2 \cdot 3\text{H}_2\text{O}$  (1.22 g, 5.24 mmol, 99.5%, ABCR),  $\text{H}_3(\text{btc})$  (0.58 g, 2.76 mmol, 98%, ABCR) and 1.0 g PTA (Sigma-Aldrich) or 1.0 g VPMo (as-synthesized, see section 2.1) were dissolved in DMSO (5 g, 99.9%, Sigma-Aldrich).

There was a difference for the PMA@HKUST-1 (PMA = phosphomolybdic acid) precursor solution:  $\text{Cu}(\text{NO}_3)_2 \cdot 3\text{H}_2\text{O}$  (1.22 g, 5.24 mmol, 99.5%, ABCR) and 1.0 g PMA (Merck) were dissolved in 3 g of sulfolane to get solution A. Then  $\text{H}_3(\text{btc})$  (0.58 g, 2.76 mmol, 98%, ABCR) was dissolved in 2 g of DMSO to obtain solution B. Finally, solution A was added into solution B under stirring to produce the PMA@HKUST-1 precursor solution.

*Spin coating and methanol vapor induced growth of POM@HKUST-1 SURMOFs:* The spin-coating and growth procedures are similar to the HKUST-1 SURMOF reported by our group.<sup>62</sup> 150  $\mu\text{L}$  of the precursor solution was spin-coated onto the PPP1 SAM-functionalized gold substrates (2 cm  $\times$  2 cm) at 5000 rpm for 15 s (WS-650sz Lite, Laurell). For nucleation from methanol vapor, the substrate was quickly transferred into a desiccator containing some methanol in a glass beaker. Subsequently, the pressure was reduced to 30 mbar for 20 min by means of a membrane pump. Finally the gold substrate was washed with methanol and dried with  $\text{N}_2$ . For nucleation by simple heating, the substrate was quickly transferred into a pre-heated oven (70  $^\circ\text{C}$ ) and kept there for 2 min. The gold substrate was washed with ethanol and dried with  $\text{N}_2$ . To grow thicker HKUST-1 or POM@HKUST-1 SURMOFs, either of these cycles was repeated.

*Dye adsorption and desorption of POM@HKUST-1 SURMOFs:* Dye adsorption experiments were performed as follows: freshly deposited PTA@HKUST-1 SURMOFs were put into 100 ml flasks and then evacuated at room temperature for 30 min. Subsequently, the samples were immersed in ethanolic solutions of dyes (the concentrations were 4 mg/L) at room temperature. After an immersion time of 12 h the samples were removed from the solutions, rinsed with ethanol, and finally dried in a flux of nitrogen gas. In the case of dye desorption, dye loaded PTA@HKUST-1 SURMOFs were soaked into 0.025 M  $\text{NH}_4\text{Cl}$  ethanol-water solution (the volume ratio of ethanol/water was 160) for different times.

## 2.6 Characterization

Powder X-ray diffraction patterns were collected between  $2\theta = 2^\circ$  and  $70^\circ$ , on a STOE theta-theta diffractometer using  $\text{Cu K}\alpha 1$  (1.5418  $\text{\AA}$ ) radiation and a linear position-sensitive detector. Surface X-ray diffraction (SXR) measurements were performed in theta-theta mode, with a step width of  $0.02^\circ$ , and a scan rate of 100 s/step for SURMOFs. Attenuated total reflection (ATR) and IRRA spectra were recorded with a NICOLET 6700 Fourier transform infrared reflection-absorption spectrometer. An ATR unit was employed for the bulk powders. For SURMOFs on gold substrates, a modified smart SAGA unit providing an incidence angle of  $80^\circ$  was utilized and 256 scans were recorded at a resolution of  $4\text{ cm}^{-1}$  from  $600$  to  $4000\text{ cm}^{-1}$ .

at room temperature. SAMs of perdeuterated hexadecanethiol ( $C_{16}D_{33}SH$ ) on gold were used as background samples for the IRRAS measurements. SEM images were recorded on a JEOL JSM 7001F scanning electron microscope at an acceleration voltage of 15 kV. Before SEM observation the samples were sputtered with gold for 40 s using an Edwards S150B sputter coater. AFM measurements were performed on a NanoScope Dimension 3100 atomic force microscope in the contact mode. The simulations of XRD patterns and pore sizes were done by the Mercury software.

*Quantization of the adsorption capacities of highly oriented SURMOFs:* Adsorption capacity measurements of  $[Cu_2(sdb)_2(bipy)]$ , multifunctional  $[Cu_2Lm_2(dabco)]$  and POM@HKUST-1 SURMOFs for VOCs or hazardous gases were performed on QCM25 crystal oscillators (SRS, AT cut, 5 MHz) using a QCM200 controller (SRS). In order to grow SURMOFs on the QCM electrodes, the electrodes were washed with ethanol and cleaned with  $H_2$  plasma followed by immersion into a 0.1 mM PPP1 solution in ethanol for 48 h. Then the SURMOFs were deposited using the stepwise LbL method ( $[Cu_2(sdb)_2(bipy)]$  and  $[Cu_2Lm_2(dabco)]$  SURMOFs) or the spin-coating technique (POM@HKUST-1 SURMOFs) at varied temperatures (15 °C and 50 °C for  $[Cu_2(sdb)_2(bipy)]$  SURMOFs, 60 °C for  $[Cu_2Lm_2(dabco)]$  SURMOFs and room temperature for POM@HKUST-1 SURMOFs). The mass of the SURMOFs on the electrodes was calculated by measuring the change of the oscillation frequency of the crystal ( $\Delta f$ ) before and after the deposition process using the Sauerbrey equation.<sup>288</sup>

For the measurements of VOCs/gases adsorption capacities and selectivities, the QCM devices were mounted into a desiccator. To remove the accommodated guest molecules from the pores, the desiccator was purged with dry  $N_2$  which led to a dramatic increase of frequency. After several minutes, the frequency curve reached a plateau and a stable baseline was obtained. Then the respective VOC vapor was led into the chamber by using dry  $N_2$  as carrier gas (the over pressure of  $N_2$  was 0.2 bar, hazardous gases were directly led into the chamber) and gas uptake was observed by the frequency change. Finally, the desiccator was purged with dry  $N_2$  again to remove the analyte vapor or the hazardous gas.

*Electrochemical measurements:* The cyclic voltammetry (CV) and square-wave voltammetry (SWV) measurements of SURMOFs or dissolved species have been performed under inert gas using a home-made electrochemical cell at room temperature. A three-electrode system was

used where the electrodes were as follows: reference electrode (RE): Ag/AgCl (3 M NaCl, ALS Co., Ltd.); counter electrode (CE): platinum wire (1 mm, ALS Co., Ltd.); working electrode (WE): gold substrate for SURMOFs or gold wire for solutions (3 mm, ALS Co., Ltd.). Before usage, the platinum electrode was cleaned by polishing it on a microcloth polishing pad (ALS Co., Ltd.) with aluminium oxide (0.3  $\mu\text{m}$  particle size) and then the electrode was rinsed with ethanol and Millipore water (18.2  $\text{M}\Omega\cdot\text{cm}$ , 25  $^{\circ}\text{C}$ ). The IviumSoft program was employed to control the measurements and collect the data. As supporting electrolyte, a solution of 0.1 M  $\text{Bu}_4\text{NPF}_6$  in acetonitrile has been used. The HPLC grade acetonitrile was purified through a dried and activated alumina column before use. For the CV measurements of SURMOFs, the area of the working electrode (substrate) was 0.45  $\text{cm}^2$ . For the CV measurements of  $\text{H}_2(\text{bpdc-amide-Fc})$  and  $\text{H}_2(\text{bpdc-amide-Me}_2\text{Fc})$  linkers, saturated solutions were utilized. At least 5 scans have been recorded for each measurement and, for clarity, the third cycle is always represented.

## 3 Temperature dependent crystallographic orientation and growth mechanism of a [Cu<sub>2</sub>(sdb)<sub>2</sub>(bipy)] SURMOF

### 3.1 Introduction

In our efforts to extend the scope of available SURMOF systems, we decided to turn to a new series of [M<sub>2</sub>L<sub>2</sub>P]-type MOFs. These MOFs are based on V-shaped dicarboxylate linkers, such as isophthalate derivatives or 4,4'-sulfonylbiphenyl dicarboxylic acid (H<sub>2</sub>(sdb)),<sup>294,301</sup> which together with the metal SBUs form one-dimensional coordination polymers, which in turn become expanded to two dimensional (2D) sheets by the pillar ligands. Often a second network can interdigitate into the structure, thus reinforcing the 2D sheets. The sheets are held together mostly by van der Waals forces and, as in the case of the sdb ligand, by dipolar interactions between the highly polar sulfone groups.<sup>294,301</sup> These structural features inherently lower the symmetry of the systems, but result in unique guest-molecule adsorption properties arising from the flexible nature of their 2D layer structure.<sup>294</sup> Significantly, deposition of such [M<sub>2</sub>L<sub>2</sub>P] MOFs as functional SURMOFs has not been thoroughly explored. To the best of our knowledge, only one attempt was performed to grow such a MOF, composed of the 5-nitroisophthalate linker and the rigid bipy pillar, onto substrates.<sup>302</sup> However, only micro-sized crystals (3-100 μm) with rather poor homogeneity and orientation were observed on the substrates. Because such [M<sub>2</sub>L<sub>2</sub>P] SURMOFs will enhance profound understanding of the growth mode of SURMOFs and open new applications in adsorption and sensing, it is highly worthy to explore crystallite orientation and homogeneity controlled deposition of such MOFs onto substrates.

In this work, we aim to address the challenges for growing a highly oriented and homogeneous 2D interdigitated, layer-structured [M<sub>2</sub>L<sub>2</sub>P] MOFs onto SAM-functionalized surfaces by the LbL protocol. Particular attention was paid to the deposition-temperature dependent growth modes of SURMOFs. We also demonstrated that these oriented SURMOFs exhibit pore-orientation dependent adsorption capacities with regard to VOCs, suggesting potential applications in VOC sensing.

## 3.2 Results and discussion

### 3.2.1 LbL growth of orientation controlled $[\text{Cu}_2(\text{sdb})_2(\text{bipy})]$ SURMOFs

We chose a orthorhombic  $[\text{Cu}_2(\text{sdb})_2(\text{bipy})]$ <sup>301</sup> MOF system as model, which is constructed by a semi-rigid linker, sdb, and a dinitrogen pillar, bipy, further connected by  $\text{Cu}_2$  SBUs. This MOF is particularly interesting for three reasons: a) Similar to the well-studied tetragonal  $[\text{M}_2\text{L}_2\text{P}]$  MOFs, it contains the paddle-wheel  $\text{Cu}_2$  SBU, which, in principle, allows us to orient this SBU (and thereby also orienting the SURMOF) with its main axis either parallel or orthogonal to the surface normal by coordinating either to monodentate pyridyl groups or bidentate  $-\text{COO}^-$  groups, respectively (Figure S8.1.1). b) In view of crystal structure, the interdigitated 2D layer results in 1D channels along the  $[010]$  direction with two kinds of pore apertures,  $3.3 \text{ \AA} \times 2.5 \text{ \AA}$  and  $6.5 \text{ \AA} \times 5.5 \text{ \AA}$ ; in contrast, there are no pores running along the  $[100]$  and  $[001]$  directions (Figures S8.1.2 and S8.1.3). These 1D channels are of great importance for SURMOFs because it will facilitate guest molecule diffusion when the pore apertures are facing towards the incoming guest molecules, while blocking effects will occur when the pore openings are buried in the film. c) The sulfonyl functional groups in sdb linkers happen to be located along the 1D channel (Figure S8.1.2), meaning that they might play an important role in the adsorption of guest molecules. As can be expected from our previous study of  $[\text{M}_2\text{L}_2\text{P}]$  SURMOFs,<sup>247</sup> the functionality of SAMs and the deposition temperature should be both critical for the oriented growth of SURMOFs. Thus, herein, two SAMs with very high structural quality, PPP1 and MTCA, were chosen to functionalize the surfaces and the LbL deposition was performed at defined temperatures (in the range of 15-65 °C, what is the reachable temperature range in our experimental set-up).

After 40 cycles of LbL deposition were carried out on PPP1 functionalized surfaces, crystalline  $[\text{Cu}_2(\text{sdb})_2(\text{bipy})]$  SURMOFs were successfully grown on SAM functionalized substrates at all deposition temperatures in the range of 15-65 °C, as confirmed by the out-of-plane XRD measurements shown in Figure 3.1a. Surprisingly, the preferred crystallite orientation of  $[\text{Cu}_2(\text{sdb})_2(\text{bipy})]$  SURMOFs was remarkably dependent on the deposition temperature. At low temperatures (below 40 °C), exclusively the (020) diffraction peak was observed, suggesting a perfect oriented growth of the SURMOFs along the  $[010]$  direction. The situation

became complex, when the deposition was performed at temperatures in the range of 40-65 °C. In all cases, besides the (020) diffraction peak, the (002) and (004) diffraction peaks were also present, meaning that the growth of a perfectly oriented SURMOF failed. It is worth noting that, nevertheless, the content of [001] oriented material varied at each temperature and surprisingly, the highest [001] content was obtained at 50 °C (the proportion of (002) peak reaches 95%, see Figure 3.3c), suggesting a significantly preferred [001] oriented growth.

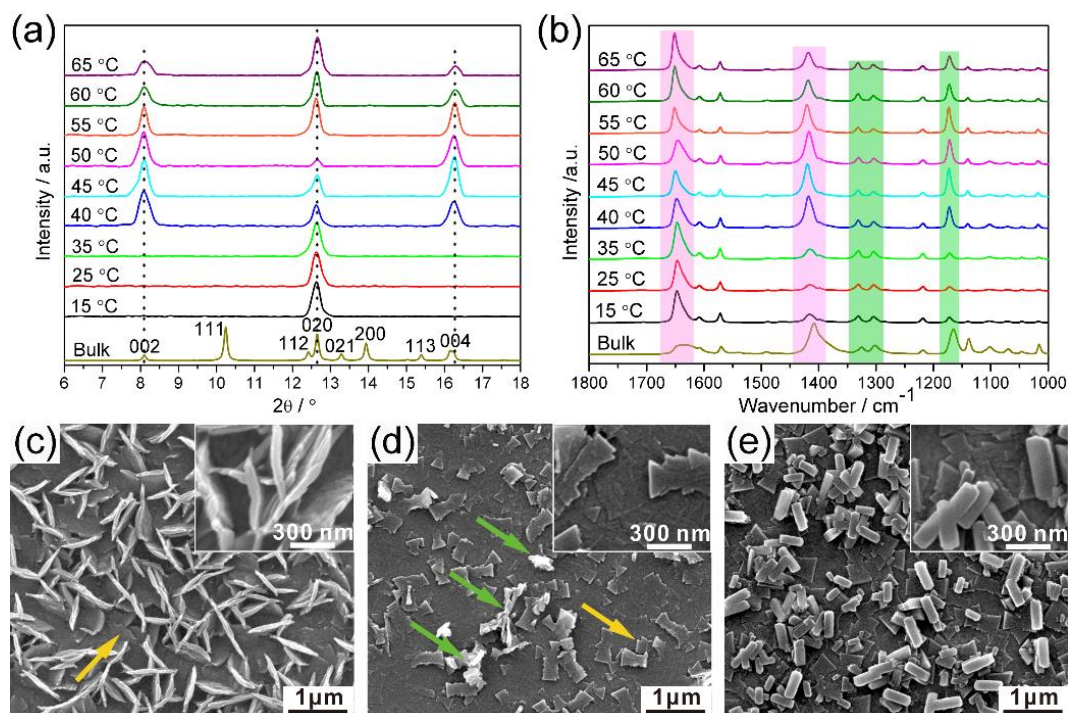


**Figure 3.1** XRD patterns (a) and IRRA spectra (b) of  $[\text{Cu}_2(\text{sdb})_2(\text{bipy})]$  SURMOFs grown on PPP1 surfaces for 40 cycles at different deposition temperatures. The pink and green areas signify carboxylate bands and sulfonyl vibrations, respectively. (c), (d) and (e): SEM images of  $[\text{Cu}_2(\text{sdb})_2(\text{bipy})]$  SURMOFs grown on PPP1 surfaces for 40 cycles at various temperatures. (c) 15 °C; (d) 50 °C; (e) 65 °C.

To further characterize the  $[\text{Cu}_2(\text{sdb})_2(\text{bipy})]$  SURMOFs obtained at different temperatures, IRRAS was employed to confirm the chemical composition and more importantly, to study the orientation behavior of the SURMOFs. According to the IR selection rules for metallic surface,<sup>303</sup> the combination of two carboxylate vibration modes (symmetric and asymmetric -COO<sup>-</sup> vibrations) permits the exact determination of the orientation of the carboxylate groups and thus of the framework with respect to the metal surface. As depicted in Figure 3.1b, IRRA spectra of  $[\text{Cu}_2(\text{sdb})_2(\text{bipy})]$  SURMOFs deposited at temperatures below 40 °C are identical,

showing a pronounced asymmetric  $\text{-COO}^-$  vibration peak located at about  $1650\text{ cm}^{-1}$  (pink rectangle mark in Figure 3.1b), while the symmetric  $\text{-COO}^-$  vibration peak is barely visible. This behavior is in line with our previous observation,<sup>247</sup> where the  $[\text{Cu}_2(\text{f}_4\text{bdc})_2(\text{dabco})]$  SURMOF was grown onto PPP1 surfaces, permitting us to conclude that the Cu-Cu axis of the  $\text{Cu}_2$  SBU was aligned perpendicular to the metal surface, thus further confirming the exclusive  $[010]$  orientation of SURMOFs grown at low temperatures. In contrast, a dramatic increase of peak intensity of the signals of the symmetric  $\text{-COO}^-$  vibration (around  $1420\text{ cm}^{-1}$ , pink column in Figure 3.1b) was observed at the temperature range of  $40\text{--}65\text{ }^\circ\text{C}$ , indicating the appearance of  $[001]$  crystallite orientation. Moreover, the maximum proportion of the symmetric  $\text{-COO}^-$  stretching mode was found in the spectrum recorded of the SURMOF deposited at  $50\text{ }^\circ\text{C}$  (Figure 3.3c), what goes in line with the dominant  $(002)$  diffraction peak observed from XRD results.

Upon close inspection of IRRA spectra, the IR signals of the sulfonyl group (green rectangles in Figure 3.1b) of the sdb linkers show very similar behavior as the  $\text{-COO}^-$  group, with respect to the change of deposition temperature. That is, the intensities of the asymmetric  $\text{-SO}_2$  vibrations at  $1330$  and  $1306\text{ cm}^{-1}$  are almost constant at all deposition temperatures, while very little signal of the symmetric  $\text{-SO}_2$  vibration is observed at low temperatures (below  $40\text{ }^\circ\text{C}$ ), however, the latter significantly increases at  $40\text{ }^\circ\text{C}$  or above. The similarity of the IR signals of the intensity of the  $\text{-COO}^-$  and  $\text{-SO}_2$  groups is a result of both functional groups having the same alignment in the SURMOFs, as illustrated in Figures S8.1.1 and S8.1.2. For example, in a  $[010]$  oriented SURMOF the transition dipole moments of the asymmetric vibrations of  $\text{-SO}_2$  and  $\text{-COO}^-$  groups are both perpendicular to the surface. Therefore, according to the IR selection rule, the asymmetric vibrational peaks of  $\text{-SO}_2$  and  $\text{-COO}^-$  are visible in the IR spectra. On the other hand, the transition dipole moments of the symmetric vibrations of both groups are parallel to the surface and cause the respective vibrational peaks to be absent in the IR spectra. The variations of  $\text{-SO}_2$  groups are well matched with the changes of  $\text{-COO}^-$  vibrations, validating each other, as supported by the almost unchanged intensity ratios (Figure S8.1.4a). In order to investigate the morphology of SURMOFs deposited at various temperatures, SEM images were recorded as shown in Figure 3.1c-e. At first sight, dense films covered by nanosized MOF crystallites were observed on PPP1 surfaces after 40 LbL-deposition cycles.



Nevertheless, the crystallite orientation and size of MOF crystallites remarkably depended on the deposition temperature. At low deposition temperatures (e.g., 15 °C), sheet-like crystallites (~60 nm in thickness) with a uniform vertical alignment were observed (Figure 3.1c), which is in good agreement with the exclusively [010] oriented growth as found by the XRD results. In case of the highest deposition temperature (65 °C, Figure 3.1e), also vertically aligned crystallites were grown on the surface, but the thickness reached about 120 nm. An interesting observation is that these upright-standing crystallites are actually grown on top of flat-lying crystals. Apparently, in the XRD pattern, the (020) diffraction peak originates from those upright-standing crystals while the flat-lying ones contribute the (002) diffraction peak. This suggestion was further confirmed by the data obtained from SURMOF grown at 50 °C. As shown in Figure 3.1d, the SURMOF consists of flat-lying crystallites, which are intergrown to form a dense film, thus a strong (002) diffraction peak was observed in the XRD pattern. Notice that a few mis-oriented crystallites (green arrows) on top of the dense film can be identified, what apparently results in the small (020) peak in the corresponding XRD patterns.

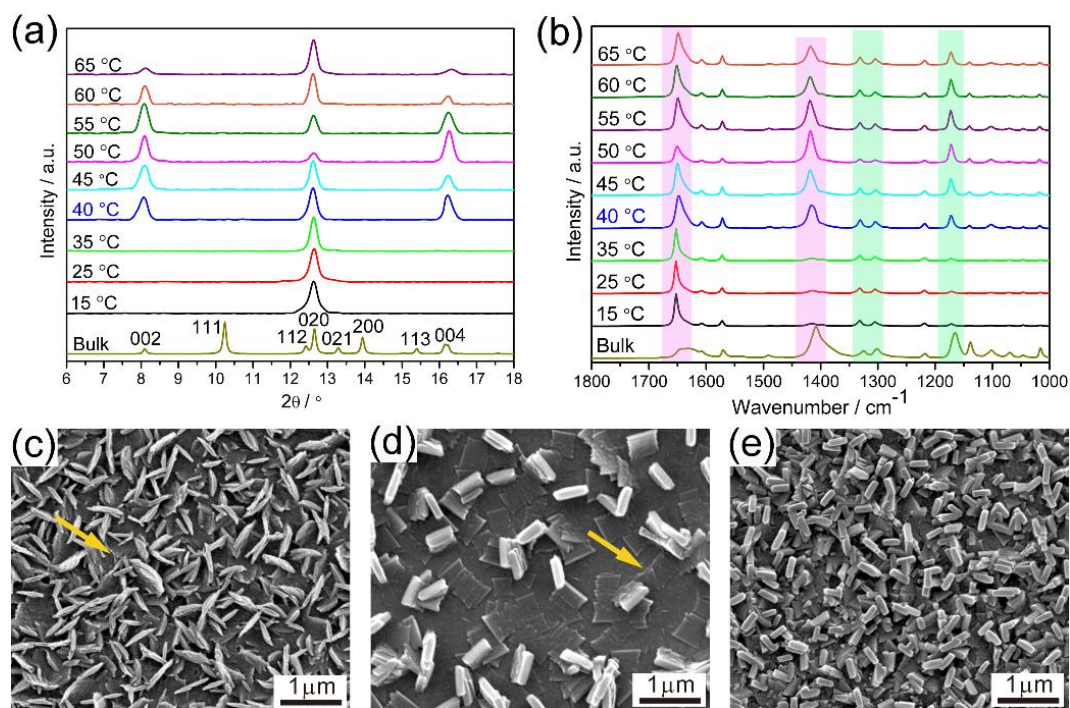


**Figure 3.2** XRD patterns (a) and IRRA spectra (b) of  $[\text{Cu}_2(\text{sdb})_2(\text{bipy})]$  SURMOFs grown on MTCA surfaces for 40 cycles at different deposition temperatures. The pink and green areas signify carboxylate bands and sulfonyl vibrations, respectively. (c), (d) and (e): SEM images of  $[\text{Cu}_2(\text{sdb})_2(\text{bipy})]$  SURMOFs grown on MTCA surfaces for 40 cycles at various temperatures. (c) 15 °C; (d) 50 °C; (e) 65 °C.

As generally accepted, SAMs with different functional groups can greatly tailor the crystallite orientation of SURMOFs.<sup>201,216,246</sup> Surprisingly, in the case of  $[\text{Cu}_2(\text{sdb})_2(\text{bipy})]$  SURMOFs grown on MTCA SAMs (-COOH termination), the very same temperature-dependent orientation as in the case of SURMOFs grown on PPP1 surfaces was observed, as indicated by the XRD, IRRAS and SEM results depicted in Figure 3.2 and the intensity ratios of the  $-\text{SO}_2/-\text{COO}^-$  vibrational signals shown in Figure S8.1.4b. That is, low deposition temperatures (below 40 °C) result in [010] oriented SURMOFs, while high temperatures (40-65 °C) cause SURMOF growth with a mixture of orientations. The best defined [001] oriented growth was obtained by deposition at 50 °C (see Figure 3.3d). The SEM micrographs of SURMOFs grown on MTCA surfaces are also quite similar to the ones grown on PPP1 surfaces (Figure 3.2c-e). To the best of our knowledge, this is the first example for which the growth of SURMOFs by LbL method is only dependent on the deposition temperature, and not on the surface chemistry of the substrates.

### 3.2.2 First-layer study and growth mechanism of $[\text{Cu}_2(\text{sdb})_2(\text{bipy})]$ SURMOFs

In order to better understand the deposition-temperature dependent growth of  $[\text{Cu}_2(\text{sdb})_2(\text{bipy})]$  SURMOFs, and in particular, the relationship between the orientation of the very first layer and the final SURMOF, we turned to studying the structure of the initial layer by IRRA spectroscopy. For this, the IRRA spectra were recorded after each deposition step. Here, the  $\text{Cu}_2(\text{OAc})_4$  was replaced by the perdeuterated one ( $\text{Cu}_2(\text{CD}_3\text{COO})_4$ ) due to the overlap of the symmetric  $-\text{COO}^-$  vibration and the vibration of the  $-\text{CH}_3$  groups in  $\text{Cu}_2(\text{OAc})_4$ .<sup>247</sup> The observations of 0.5 cycle (immersed only in  $\text{Cu}_2(\text{CD}_3\text{COO})_4$  solution and then rinsed) on both, PPP1 and MTCA surfaces, were consistent with our former results<sup>247</sup> and omitted here. The representative IRRA spectra after 1 cycle growth (first dipping the substrates into the metal precursor solution, followed by a rinsing step, then immersion into the ligand solution, and finally another rinsing step) at different deposition temperatures are presented in Figure 3.3. Astonishingly, after immersion into the ligand solution (completing the first cycle), the situation was totally different from the  $[\text{Cu}_2(\text{f4bdc})_2(\text{dabco})]$  system:<sup>247</sup> Almost identical IRRA spectra were observed on both, PPP1 and MTCA surfaces, for  $[\text{Cu}_2(\text{sdb})_2(\text{bipy})]$  SURMOFs

at each deposition temperature, clearly indicating that temperature dominates the growth of SURMOF. A drastic change of the IRRA spectra, regarding the relative intensity of the asymmetric and symmetric  $\text{-COO}^-$  and  $\text{-SO}_2$  peaks, both occurred at 40 °C, which indicates that the strong change in structure/orientation already occurs in the first layer.

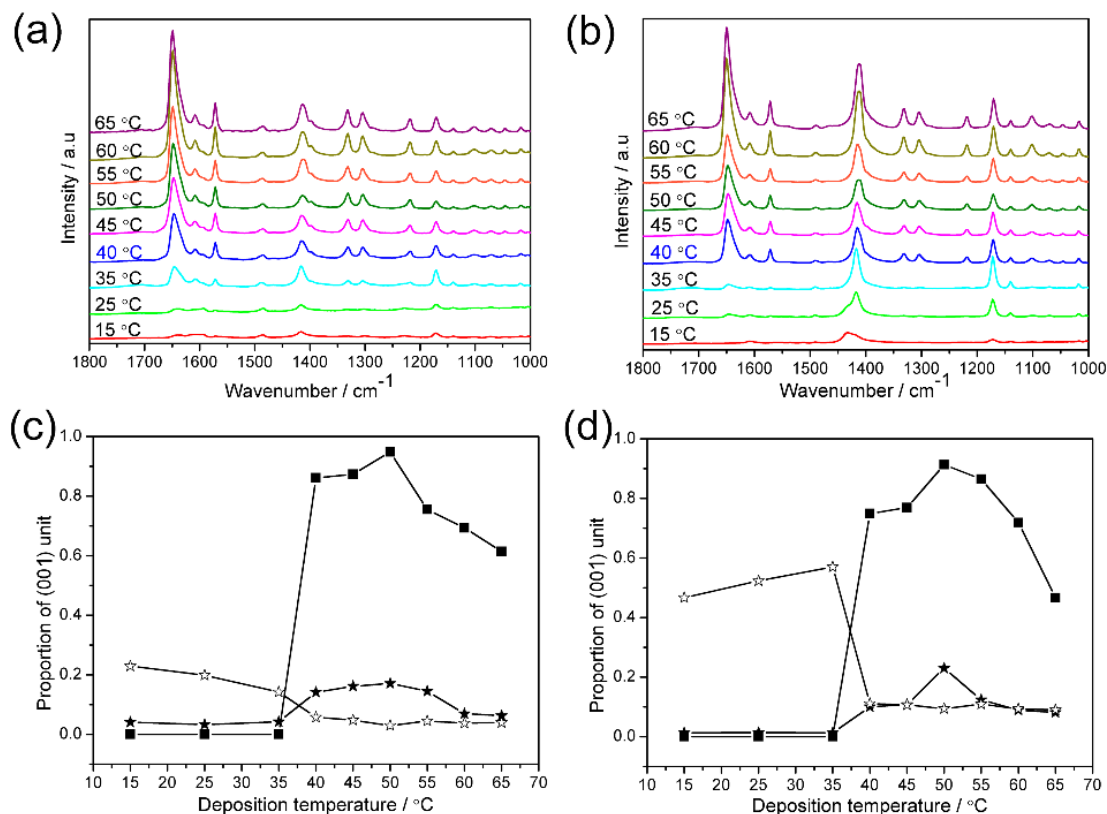


**Figure 3.3** IRRA spectra of  $[\text{Cu}_2(\text{sdb})_2(\text{bipy})]$  grown on PPP1 (a) and MTCA (b) surfaces after 1 cycle at various temperatures; (c) and (d) Corresponding temperature-dependent orientational composition (filled squares: XRD data of multilayers; filled stars: IRRAS data of multilayers; open stars: IRRAS data of the system after 1 cycle).

To quantify the effect of the temperature on the orientation, the proportion of crystallites with [001] orientation was calculated by data from XRD and IRRA results, since the crystallite orientation is unambiguously connected to the orientation of the Cu<sub>2</sub> SBU. The calculation models were adopted from our former publication<sup>247</sup> and the results are shown in Figure 3.3c and d. A series of interesting observations can be made from those results. First of all, on both SAMs, the proportion of [001] oriented crystallites shows a very similar pattern with respect to deposition temperature, meaning instead of surface chemistry, temperature is responsible

for the crystallite orientation. Secondly, either on PPP1 or MTCA SAM, the proportion of [001] oriented material, calculated from the multilayer IRRAS and XRD data, also produces very similar results, validating each other. At low temperatures (below 40 °C), on both surfaces, the proportion of [001] oriented crystallites was very low (below 5%). A maximum percentage of [001] crystallite orientation was observed at 50 °C. With further increase of the deposition temperature to 65 °C, this percentage slightly decreases. Nevertheless, the proportion of [001] oriented MOF calculated from IRRAS data of the first layer shows a completely inverted behavior (Figure 3.3c and d): at low temperature, the [001] orientation is preferred, while at higher temperatures the SURMOF layer is predominantly [010] oriented. The transition temperature is again, as in the “bulk” case (40 cycles) between 35 and 40 °C.

All in all, the observations of [Cu<sub>2</sub>(sdb)<sub>2</sub>(bipy)] SURMOFs after one and 40 cycles suggest a rather complex SURMOF growth picture. We propose that the observed orientational behavior is explained by the interplay of two phenomena, which have been typically disregarded for the growth of SURMOFs, although well recognized in other areas of surface chemistry: minimization of surface energies and (Ostwald) ripening.<sup>293</sup> A recent publication<sup>304</sup> suggests that the LbL growth follows the Volmer-Weber mechanism, in which the surface growth is not dominated by nucleation but by crystal growth, so that a limited number of crystals form instead of a closed film. In conjunction with the minimization of surface energies, it can be expected that crystals form in a way such that the most energetic surfaces (surface area times surface energy) come into contact with the substrate surface. In case of the orthorhombic [Cu<sub>2</sub>(sdb)<sub>2</sub>(bipy)] MOF, the (001) surface exposing the highly dipolar -SO<sub>2</sub> groups is also the largest crystal face, at least at temperatures below 55 °C (compare Figure 3.1c, d). This crystal shape is a result of a slower growth along the [001] direction, in particular in comparison with the one in the [010] direction. Based on these observations, the temperature-dependent behavior of the system can be explained in the following manner: At low temperatures, crystals with different orientation nucleate at the surface, with the [001] ones dominating because of the minimization of surface energy (Figure 3.4, center left). While this behavior violates the well-established template effects of the groups exposed by the SAMs, different coordinative modes can be imagined in addition to pure van der Waals effects (see Figure S8.1.1). Because of the preferred growth in the [001] and [100] direction, the crystals with [001] orientation

intergrow, thus effectively blocking their further development (green arrows in Figures 3.1 and 3.4). After this, the few crystals with a [010] orientation take up most of the material during the following deposition cycles (Figure 3.4, lower left), thus leading to the growth of the observed upright platelets (Figure 3.1c).

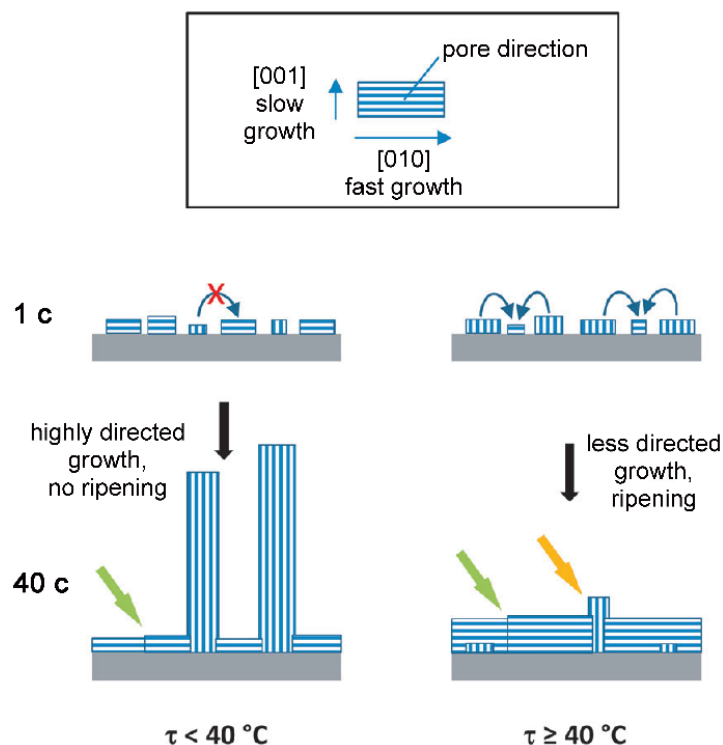


**Figure 3.4** Summary of the observed growth mechanism. In the beginning of the deposition, crystals form in a Volmer-Weber growth mode. While at high temperatures template effects play a role at this phase, at low temperature surface energy minimization predominates. At later growth stages, higher temperatures promote ripening in conjunction with minimization of surface energies leading to reorientation. In contrast, at temperatures below 40 °C, the dominant orientational species is determined by differences in growth rates. The arrows point out the same phenomena as found in Figure 3.1.

At 40 °C, the crystal lattice energy can be overcome, so that recrystallization (ripening) can occur under the deposition conditions. As has been shown earlier,<sup>247</sup> higher temperatures facilitate the mono-coordination at the apical site of the Cu<sub>2</sub> SBU at the SAM surface, thus promoting nucleation of SURMOFs crystallites with [010] orientation. Because of the efficient coordination, these crystals are still flat (Figure 3.4, center right), but upon further deposition of material it should result in upright plates as in the case of the low-temperature deposits. This large-surface situation is nevertheless suppressed by the Ostwald ripening process, which

leads to recrystallization during the deposition process and favors the formation of lying-down, [001] oriented crystals (Figure 3.1d). Because of the higher temperatures, growth in the [001] direction is less hampered, thus permitting an efficient SURMOF growth.

This hypothesis is supported by micrographs recorded at the different surfaces and different temperatures after deposition of one cycle (see Figure S8.1.9). Independent of the surface chemistry and the temperature, all the surfaces show the crystals typical for the Volmer-Weber growth. Regardless of their orientation, all these crystals lie flat on the surfaces with aspect ratios (width/height) between four and ten (see Table S8.1.1). The main difference is a higher crystal density in the systems deposited at higher temperatures (55 °C).

In the regime of the highest temperatures, the discrimination between growth velocities is even less pronounced, so that the crystals become less plate-like. This change of shape reduces the differences in the energetic situation, which in conjunction with the increased entropy, as can be seen, for example, by the change of ligand conformation mentioned above, leads to less ordered SURMOF systems.

### 3.2.3 Pore-orientation dependent adsorption capacities of volatile organic compounds (VOCs)

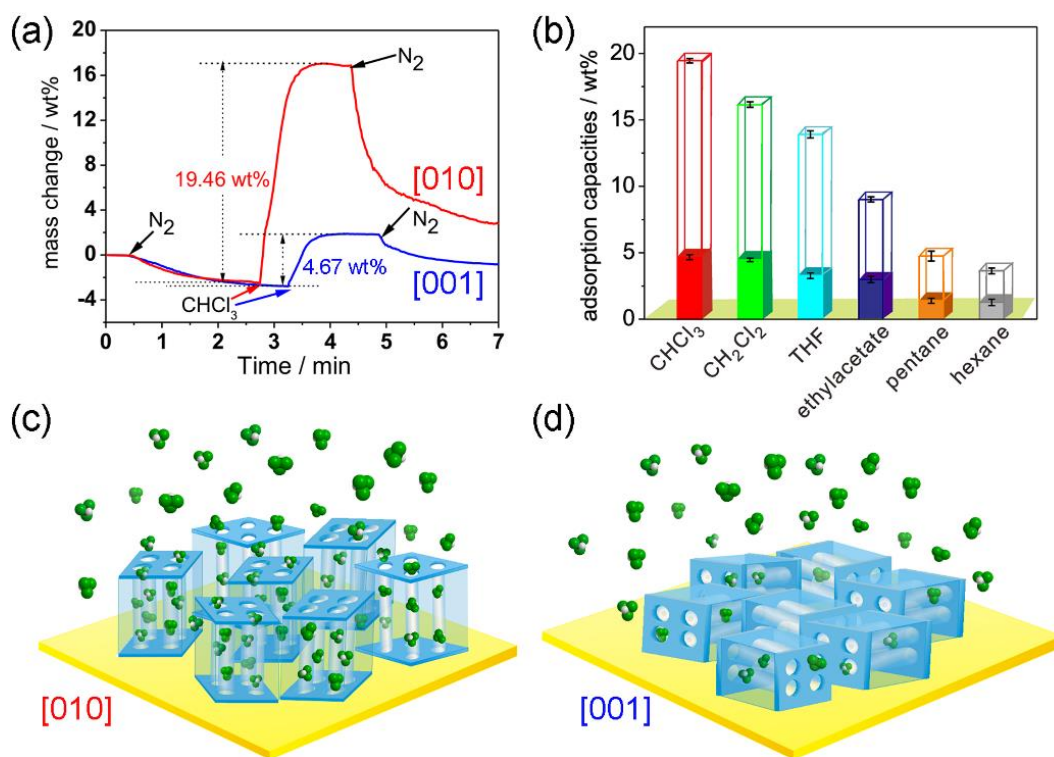
One of the most interesting features of oriented SURMOFs is that the pore orientation is highly controllable. It has already been demonstrated that the pore-orientation dependent adsorption of guest molecules can be tuned by simply controlling the SURMOF orientation with respect to the substrates.<sup>243,302</sup> In our case, the  $[\text{Cu}_2(\text{sdb})_2(\text{bipy})]$  SURMOFs are ideal candidates to investigate the pore-orientation dependent adsorption of VOCs since it contains only 1D -SO<sub>2</sub> functionalized pores. To do this, highly [010] and preferably [001] oriented  $[\text{Cu}_2(\text{sdb})_2(\text{bipy})]$  SURMOFs (denoted as SURMOF<sub>010</sub> and SURMOF<sub>001</sub>), were deposited at temperatures of 15 °C and 50 °C, respectively, onto PPP1 functionalized gold-coated QCM sensors due to their extremely high sensitivity against mass change.<sup>278,280</sup> As revealed by SEM images shown in Figure S8.1.6, both desired SURMOFs are highly homogeneous and dense coatings (note that the white spots are actually [010] oriented crystallites), which are particularly suited for adsorption-capacity measurements.

Figure 3.5 demonstrates the adsorption/desorption isotherms of chloroform for SURMOF<sub>010</sub>

and SURMOF<sub>001</sub> at room temperature. The activation of the SURMOFs can be simply achieved by purging with pure N<sub>2</sub> and in both cases a loss of 2.5 wt% solvent (ethanol) was found. However, when the activated samples were exposed to a stream of N<sub>2</sub> carrier gas containing chloroform molecules, a huge difference of adsorption curve was observed for [010] and [001] oriented SURMOFs. In the case of SURMOF<sub>010</sub>, a total uptake of 19.5 wt% for chloroform was observed. As can be seen in the crystal structure (Figures S8.1.2 and S8.1.3), the 1D pores are oriented along the [010] direction, meaning that SURMOF<sub>010</sub> provides pore openings directly facing the incoming chloroform stream. Therefore, a high uptake is expected due to the free access of chloroform molecules into SURMOF<sub>010</sub> without spatial limitation. Moreover, the polar sulfonyl functional groups located in the pores could also contribute to the efficient adsorption for the polar chloroform molecules due to the strong interaction between the -SO<sub>2</sub> groups and the chloroform molecules. This strong interaction was also evident by the fact that the mass of the SURMOFs did not return to the original activated state by re-purging with N<sub>2</sub>. On the other hand, only 4.7 wt% uptake of chloroform was observed for SURMOF<sub>001</sub>. As suggested by the crystal structure (Figure S8.1.3), there are no pore openings in the [001] direction, thus access of guest molecules from this direction should actually be hindered. In other words, the perfect SURMOF<sub>001</sub> should, theoretically, not adsorb any guest molecules at all. Nevertheless, as indicated by XRD, IRRAS and SEM results, some [010] mis-oriented crystallites in SURMOF<sub>001</sub> are present, which might be responsible for the observed small uptake. Moreover, the high resolution SEM image in Figure 3.1d also suggest that though dense plate-like [001] oriented crystallites form a dense film, there are several plate-like crystals which are higher than the surrounding crystals, causing exposed (010) facets at the respective boundaries, which then allow for the adsorption of guest molecules. The adsorption equilibrium for both samples was achieved within 2 minutes corresponding to a rapid dynamic adsorption. The above processes regarding the adsorption of chloroform into SURMOFs are depicted in Figure 3.5c and d.

As can be seen in Figure 3.5b and Figure S8.1.7, the SURMOF<sub>010</sub> take up almost four times the mass of any guest molecule as compared to the SURMOF<sub>001</sub>. This behavior can also be easily explained by the fact that in the former case the pore openings are exposed towards the ambient, while the respective crystal surfaces of the [001] oriented crystals block each other,

as has been discussed above. This distinction can be made by comparing the uptake kinetics of the two systems. Therefore, we measured the diffusion coefficients (see Figure S8.1.8) of chloroform in SURMOF<sub>010</sub> and SURMOF<sub>001</sub> by fitting the adsorption isotherms with an exponential decay function and neglecting the surface barriers, as described in previous studies.<sup>278,279,305</sup> The values of diffusion coefficients for SURMOF<sub>010</sub> and SURMOF<sub>001</sub> are  $4.41 \times 10^{-15} \text{ m}^2/\text{s}$  and  $4.44 \times 10^{-15} \text{ m}^2/\text{s}$ , respectively, which within 1% are the same, implying that the adsorption capacities are exclusively determined by intracrystalline diffusion.<sup>305</sup> These data clearly demonstrates that the quality of both the pores and their openings are independent of the orientation, and thus the deposition temperature.



**Figure 3.5** (a) Adsorption/desorption isotherms of chloroform for SURMOF<sub>010</sub> (red line) and SURMOF<sub>001</sub> (blue line) at room temperature; (b) Adsorption capacities of SURMOF<sub>010</sub> (empty boxes) and SURMOF<sub>001</sub> (filled boxes) for VOCs at room temperature; (c) and (d) Schematic adsorption processes of SURMOF<sub>010</sub> and SURMOF<sub>001</sub> for chloroform (the green objects represent chloroform molecules and the white tubes depict the pores).

### 3.3 Conclusions

In conclusion, we have demonstrated that, besides surface template (defined by the functional



groups of SAMs), deposition temperature in the LbL procedure is a key parameter to control the crystallite orientation in orthorhombic  $[\text{Cu}_2(\text{sdb})_2(\text{bipy})]$  SURMOFs. Temperature induced ripening processes and the tendency for the minimization of surface energies can out-compete the template effects. Either on monodentate pyridyl- or bidentate carboxyl-terminated surfaces, exclusively  $[010]$  oriented  $[\text{Cu}_2(\text{sdb})_2(\text{bipy})]$  SURMOFs are obtained at low temperatures (below  $40\text{ }^\circ\text{C}$ ). In contrast, high deposition temperatures ( $40\text{-}65\text{ }^\circ\text{C}$ ) result in a mixture of orientations in SURMOFs owing to temperature-induced ripening processes and the tendency for the minimization of surface energies. A maximum of the preferred  $[001]$  oriented growth of SURMOFs (95% distribution of  $[001]$  crystallite orientation) can be achieved at  $50\text{ }^\circ\text{C}$ . To take advantage of the extremely high sensitivity of the QCM technique,  $[010]$  and  $[001]$  oriented SURMOFs were deposited onto QCM gold electrodes. The study of adsorption capacities of oriented SURMOFs for a series of VOCs suggests that the quality of both the pores and their openings are independent of the orientation, and thus the deposition temperature. Because all the pore openings of a  $[010]$  oriented SURMOF are directly facing the incoming guest molecules, a high adsorption capacity is expected, particularly for small and polar guest molecules due to their free entering and strong interaction with polar  $-\text{SO}_2$  groups located in the pores. In view of SURMOFs serving as platforms for adsorption and sensing of VOCs, the highly oriented  $[\text{Cu}_2(\text{sdb})_2(\text{bipy})]$  SURMOFs are expected to be excellent candidates.



## 4 Multifunctional SURMOFs: The effects of linker acidity ( $pK_a$ ) on the orientational quality

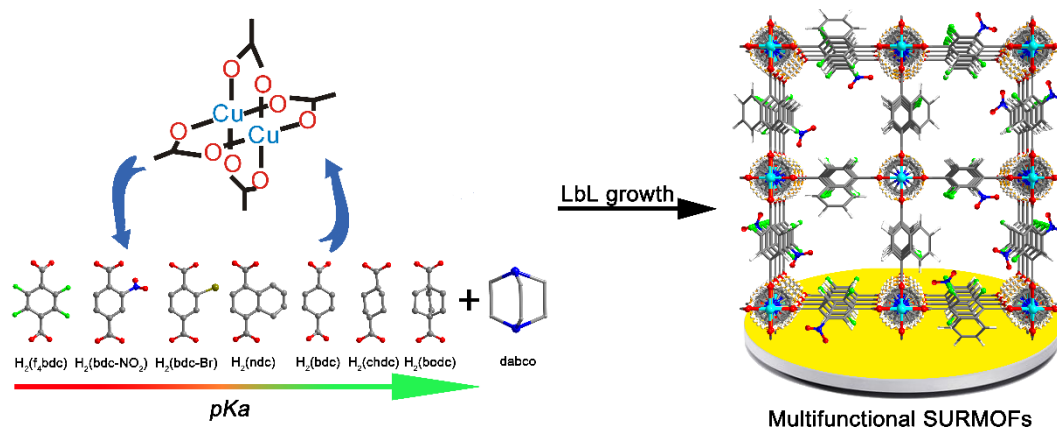
### 4.1 Introduction

The functionality of SURMOFs is crucial for many applications.<sup>246,253,262</sup> Nevertheless, the incorporation of multivariate functionalities into oriented SURMOFs, yielding multivariate/multifunctional SURMOFs (denoted as MTV-SURMOFs) without significantly changing the crystal structure, still remains challenging. Inspired by the sequential solvothermal synthesis of multivariate/multifunctional bulk MOFs (MTV-MOFs) by using mixed linkers with similar structures but bearing two or more types of functionality,<sup>306–309</sup> we are aiming to grow highly oriented MTV-SURMOFs combining the mixed-linker strategy with the LbL growth. Notably, nevertheless, the LbL deposition of such MTV-SURMOFs using the mixed-linker strategy has not been investigated thus far.

In order to accomplish the effective incorporation of functionalities into SURMOFs, we have turned our attention to the tetragonal  $[M_2L_2P]$  MOF system. The  $[M_2L_2P]$  system is an ideal model for the construction of MTV-SURMOFs with mixed linkers since the dicarboxylate linkers can be easily replaced by linkers of the same type.<sup>184,201,251,252</sup> However, the controlled spatial arrangement of the mixed linkers which relates to the orientation of MTV-SURMOFs imposes a real challenge. As mentioned before, many applications of SURMOFs require a precise control of the direction of the pore openings, which depends on highly oriented growth of the MOF crystallites with regard to substrates. This is also true for the MTV-SURMOFs. An recent in-depth study<sup>247</sup> of LbL growth of a  $[Cu_2(f_4bdc)_2(dabco)]$  SURMOF shows that in fact an interplay of surface chemistry, deposition temperature, and first layer order determines the orientation and crystal quality of SURMOFs, suggesting a complicated LbL growth mode of tetragonal  $[M_2L_2P]$  SURMOFs although only a single kind of dicarboxylate linker was involved. Since MTV-SURMOFs contain more than one kind of carboxylate linker, it could be expected that a more complicated set of rules applies.

In this work, we decided to investigate the oriented growth of a series of  $[M_2Lm_2P]$  SURMOFs, where  $Lm$  represents a mixture of dicarboxylate linkers, each bearing single or multiple functionalities (Scheme 4.1). Our previous work<sup>247</sup> indicated that, both surface chemistry and

deposition temperature, play significant roles for the crystallite orientation of SURMOFs. In order to understand how other intrinsic factors, such as the  $pK_a$  values of dicarboxylate linkers, affect the orientation of MTV-SURMOFs, we used the same conditions (the same surface chemistry and deposition temperature) for the growth of MTV-SURMOFs with different types and mixing ratios of dicarboxylate linkers. For this, a pyridyl-terminated SAM, PPP1, and a deposition temperature of 60 °C were applied and kept constant since highly [001] oriented  $[M_2L_2P]$  SURMOFs have been grown under these conditions.<sup>247</sup>



**Scheme 4.1** Schematic illustration of the LbL growth of  $[Cu_2Lm_2(dabco)]$  SURMOFs with multivariate functionalities and pore structures through a mixed-linker approach.

A key to the successful growth of mixed-linker SURMOFs is that the chosen linkers,  $L_m$ , are able to form MOFs with isorecticular structures and the same dimensions. The derivatives of 1,4-benzenedicarboxylic acid ( $H_2(bdc)$ ) are excellent candidates because of their ability in forming isorecticular MOFs. The acidity of  $H_2(bdc)$  derivatives, which is described by the  $pK_a$  values of the corresponding molecules, greatly depends on the functional groups. In order to demonstrate the  $pK_a$  effect on the orientational quality of  $[M_2Lm_2P]$  SURMOFs, in this work, bicycle [2.2.2]octane-1,4-dicarboxylic acid ( $H_2(bodc)$ ,  $pK_a^1 = 4.49$ ), trans-1,4-cyclohexanedicarboxylic acid ( $H_2(chdc)$ ,  $pK_a^1 = 4.18$ <sup>310</sup>),  $H_2(bdc)$  ( $pK_a^1 = 3.51$ <sup>311,312</sup>),  $H_2(ndc)$  ( $pK_a^1 = 2.97$ <sup>310</sup>), 2-bromobenzene-1,4-dicarboxylic acid ( $H_2(bdc-Br)$ ,  $pK_a^1 = 2.44$ ), 2-nitrobenzene-1,4-dicarboxylic acid ( $H_2(bdc-NO_2)$ ,  $pK_a^1 = 1.79$ <sup>312</sup>) and  $H_2(f_4bdc)$  ( $pK_a^1 = 1.42$ <sup>313</sup>) were chosen as dicarboxylate linkers and dabco was chosen as dinitrogen pillar ligand. By coordinating to the  $Cu_2$  paddle-wheel SBU,  $[Cu_2Lm_2(dabco)]$  SURMOFs can be obtained with

various ratios of Lm, as shown in Scheme 4.1. We advance a hypothesis regarding the linker  $pK_a$  effect on the orientational quality of MTV-SURMOFs deposited from different linker mixtures. We also show that the MTV-SURMOFs exhibit tunable adsorption capacities towards VOCs, suggesting the potential application in VOC sensing.

## 4.2 Results and discussion

### 4.2.1 Linker $pK_a$ effect on $[\text{Cu}_2\text{L}_2(\text{dabco})]$ SURMOFs containing a single kind of linker

We first determined the ability of the single linkers to form isorecticular  $[\text{Cu}_2\text{L}_2(\text{dabco})]$  (L = a single kind of dicarboxylate linker) SURMOFs because of the large difference of  $pK_a$  values of the chosen linkers. The XRD and IRRAS results (Figure 4.1) indicate that indeed all of the chosen linkers are able to form isorecticular  $[\text{Cu}_2\text{L}_2(\text{dabco})]$  SURMOFs. However, we found that the  $pK_a$  values of the linkers greatly affect the orientational quality of the  $[\text{Cu}_2\text{L}_2(\text{dabco})]$  SURMOFs, though the same surface chemistry and deposition temperature were used. For example, linkers possessing relatively high  $pK_a$  values ( $\text{H}_2(\text{ndc})$ ,  $\text{H}_2(\text{bdc})$  and  $\text{H}_2(\text{chdc})$ ) result in exclusively [001] oriented  $[\text{Cu}_2\text{L}_2(\text{dabco})]$  SURMOFs. However, if the linker  $pK_a$  value is too high ( $\text{H}_2(\text{bodc})$ ), the  $[\text{Cu}_2(\text{bodc})_2(\text{dabco})]$  SURMOF becomes mix-oriented (with 4.9% of [100] mis-orientation, Figure S8.2.1). In the case of  $[\text{Cu}_2\text{L}_2(\text{dabco})]$  SURMOFs built from dicarboxylate linkers with low  $pK_a$  values ( $\text{H}_2(\text{f}_4\text{bdc})$  and  $\text{H}_2(\text{bdc-NO}_2)$ ), layers with a less defined orientation were obtained as indicated by the presence of a (100) diffraction peak in out-of-plane XRD results. The reason of the  $pK_a$  dependent orientational quality of the  $[\text{Cu}_2\text{L}_2(\text{dabco})]$  SURMOFs can be mainly ascribed to the different coordination ability of the linkers, which is caused by different  $pK_a$  values. The linkers with high  $pK_a$  values usually cause stronger coordination ability to the  $\text{Cu}_2$  SBU, forming stronger Cu-L bonds. Therefore, the  $\text{Cu}_2$  SBUs are arranged in order by the strong Cu-L bonds during the LbL growth on pyridyl-terminated surfaces and the  $[\text{Cu}_2\text{L}_2(\text{dabco})]$  SURMOFs with perfect [001] orientation were obtained. However, when the linker  $pK_a$  value is too high, it is difficult to be deprotonated and the coordination between  $\text{Cu}_2$  SBU and linker becomes weak, which might influence the arrangement of  $\text{Cu}_2$  SBU (the Cu-Cu axis of  $\text{Cu}_2$  SBU is perpendicular/ parallel to the surface, corresponding to the [001]/ [100] orientation of SURMOFs on pyridyl-terminated surface),

resulting in mix-oriented SURMOF. In contrast, the low  $pK_a$  linkers with higher acidity are easier deprotonated but result in less nucleophilic carboxylate ions which coordinate less effectively to the  $\text{Cu}_2$  SBU. Therefore, the reduced coordination ability of the low  $pK_a$  linkers might affect the orientation of  $\text{Cu}_2$  SBU, resulting in the SURMOFs with unexpected [100] orientation.

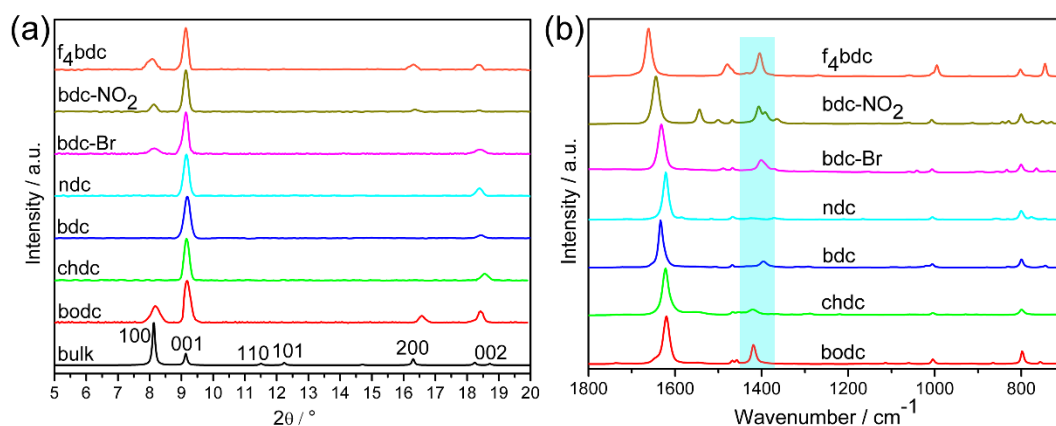


**Figure 4.1** XRD patterns (a) and IRRA spectra (b) of  $[\text{Cu}_2\text{L}_2(\text{dabco})]$  ( $\text{L}$  = a single kind of dicarboxylate linker) SURMOFs grown at  $60\text{ }^\circ\text{C}$  on PPP1 surfaces. The blue column signifies the area, where symmetric  $-\text{COO}^-$  vibrations are expected.

This suggestion was further supported by the IRRA spectra depicted in Figure 4.1b. According to the IR selection rules in the vicinity of metallic surface,<sup>303</sup> two carboxylate vibrational modes (asymmetric and symmetric  $-\text{COO}^-$  stretchings) permit the exact determination of the orientation of the carboxylate group, and thus the orientation of the  $\text{Cu}_2$  SBU. In general, for the tetragonal  $[\text{M}_2\text{L}_2\text{P}]$  SURMOFs, a perfect [001] crystallite orientation will cause only the asymmetric  $-\text{COO}^-$  to be visible in the IRRA spectrum, while the symmetric  $-\text{COO}^-$  signal is invisible. A reversed behavior is expected for the [100] oriented SURMOFs. In the case of the  $[\text{Cu}_2\text{L}_2(\text{dabco})]$  SURMOFs consisting of linkers with high  $pK_a$  values, only the respective asymmetric  $-\text{COO}^-$  vibration ( $\sim 1625\text{ cm}^{-1}$ ) was observed in the IRRA spectra (the small peaks located around  $1400\text{ cm}^{-1}$  for  $[\text{Cu}_2(\text{bdc})_2(\text{dabco})]$  and  $[\text{Cu}_2(\text{chdc})_2(\text{dabco})]$  SURMOFs can be assigned to C-C stretchings due to the structure properties of respective linkers), suggesting that the main axes of the  $\text{Cu}_2$  SBUs are perpendicularly aligned to the SAM-functionalized surface, as expected for highly [001] oriented SURMOFs. In contrast, the symmetric  $-\text{COO}^-$

signals became conspicuous (around  $1400\text{ cm}^{-1}$ , marked by sky-blue column in Figure 4.1b) when  $\text{H}_2(\text{bodc})$  linker or the linkers with low  $pK_a$  values were employed for the construction of  $[\text{Cu}_2\text{L}_2(\text{dabco})]$  SURMOFs. This is in line with the appearance of the small (100) diffraction peak in the XRD patterns (Figure 4.1a). The XRD and IRRAS studies of the  $[\text{Cu}_2\text{L}_2(\text{dabco})]$  SURMOFs allow us to conclude that when the  $pK_a$  value of the dicarboxylate linker falls below a certain value (2.7, estimated according to Figure S8.2.1) or raises above a certain value (4.3, estimated according to Figure S8.2.1), mis-oriented  $[\text{Cu}_2\text{L}_2(\text{dabco})]$  crystallites (in our case, with unexpected [100] orientation) occur. The content of misoriented [100] crystallites was calculated according to our previous paper.<sup>247</sup> The results show that the variation of the content of [100] orientation (Table S8.2.1 and Figure S8.2.1) is well consistent with the XRD and IRRAS results.

#### 4.2.2 Linker $pK_a$ effect on $[\text{Cu}_2\text{Lm}_2(\text{dabco})]$ SURMOFs containing two linkers

Now we turn our attention to the more complicate  $[\text{M}_2\text{Lm}_2\text{P}]$  SURMOFs consisting of two mixed dicarboxylate linkers. In order to simplify the  $[\text{M}_2\text{Lm}_2\text{P}]$  system, we first deposited the  $[\text{Cu}_2\text{Lm}_2(\text{dabco})]$  SURMOFs from binary mixtures of dicarboxylate linkers in an equimolar ratio. As illustrated in Figure 4.2a, c and e, all the  $[\text{Cu}_2\text{Lm}_2(\text{dabco})]$  SURMOFs, which are built from two dicarboxylate linkers, are crystalline with similar parameters for the (001) planes as the  $[\text{Cu}_2(\text{f}_4\text{bdc})_2(\text{dabco})]$  tetragonal system. Notably,  $[\text{Cu}_2\text{Lm}_2(\text{dabco})]$  SURMOFs deposited from  $\text{H}_2(\text{ndc})$ - $\text{H}_2(\text{chdc})$ ,  $\text{H}_2(\text{chdc})$ - $\text{H}_2(\text{bdc})$  and  $\text{H}_2(\text{ndc})$ - $\text{H}_2(\text{bdc})$  mixtures all show exclusive [001] crystallite orientation (see Figure 4.2a). This correlates well with the fact that the single-linker  $[\text{Cu}_2\text{L}_2(\text{dabco})]$  SURMOFs, which are respectively built from each of these three dicarboxylate linkers, all exhibit the exclusive [001] orientation due to the high  $pK_a$  values. Therefore, the mixing of these three high  $pK_a$  linkers does not affect the crystallite orientation of the corresponding  $[\text{Cu}_2\text{Lm}_2(\text{dabco})]$  MTV-SURMOFs. In contrast, when any of the three linkers was mixed with the  $\text{H}_2(\text{bdc-NO}_2)$  linker, the orientational quality of the obtained  $[\text{Cu}_2\text{Lm}_2(\text{dabco})]$  SURMOFs could mostly not be maintained. Only the  $[\text{Cu}_2(\text{bdc-NO}_2+\text{ndc})_2(\text{dabco})]$  SURMOF shows exclusive [001] crystallite orientation, while the other two  $[\text{Cu}_2\text{Lm}_2(\text{dabco})]$  SURMOFs also contain [100] oriented crystallites (Figure 4.2c). A

similar effect was observed when the  $H_2(f_4\text{bdc})$  linker was mixed with any of the other four dicarboxylate linkers. The resulting  $[\text{Cu}_2\text{Lm}_2(\text{dabco})]$  SURMOFs all show a mixture of orientations (Figure 4.2e).

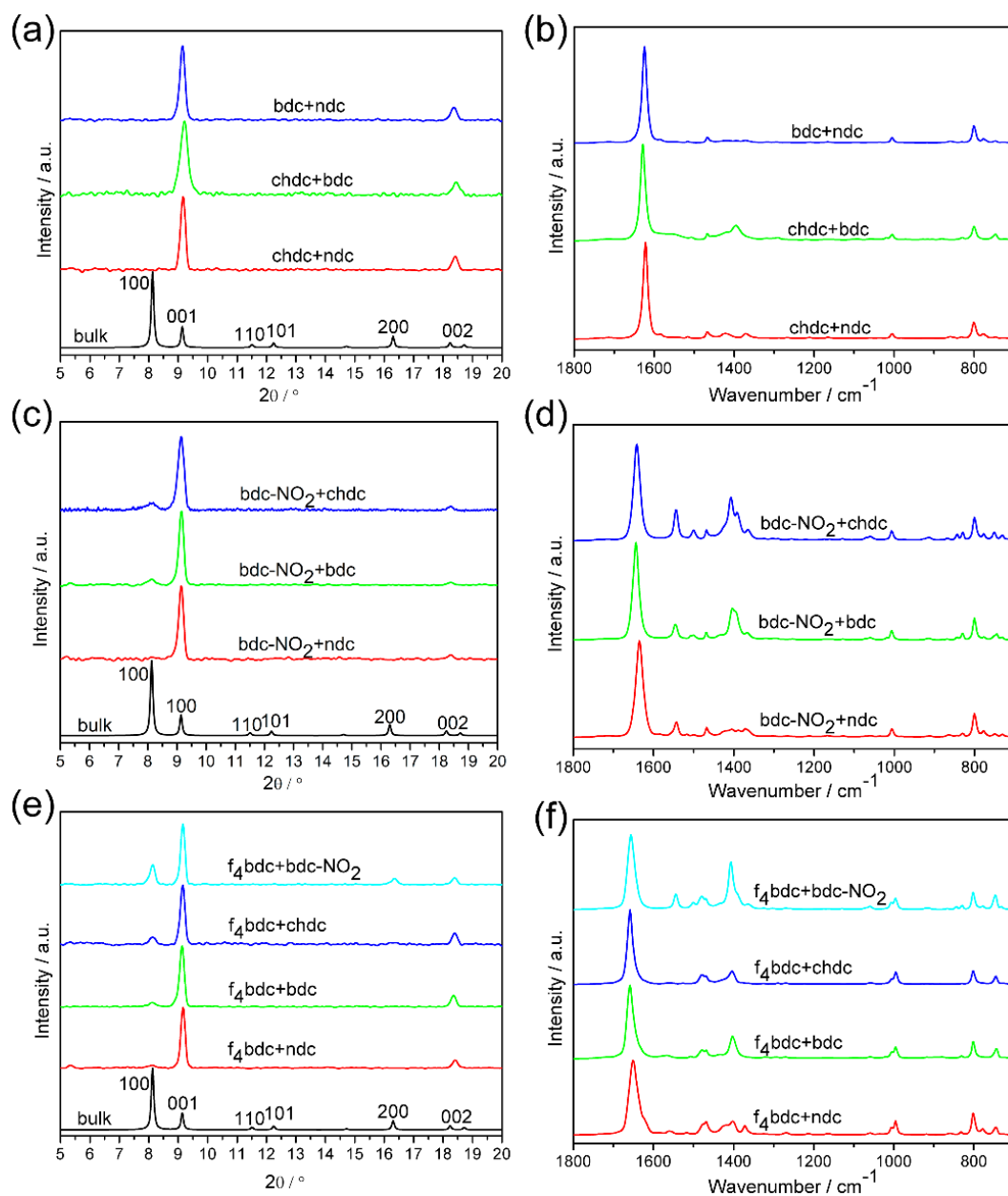


**Figure 4.2** XRD patterns (a, c, e) and IRRA spectra (b, d, f) of  $[\text{Cu}_2\text{Lm}_2(\text{dabco})]$  ( $\text{Lm}$  = mixtures of two linkers) SURMOFs grown at 60 °C on PPP1 surfaces (the molar ratios of the linkers are all 1:1).

The IRRA spectra (Figure 4.2b, d and f) further confirm that the orientational quality of the  $[\text{Cu}_2\text{Lm}_2(\text{dabco})]$  SURMOFs containing two dicarboxylate linkers largely depends on the  $pK_a$  values of the involved linkers. The visible vibration signals of functional groups belonging to the corresponding dicarboxylate linkers shown in Figure S8.2.4-8.2.13 (such as  $746\text{ cm}^{-1}$  for



H<sub>2</sub>(bdc) linker, 776 cm<sup>-1</sup> for H<sub>2</sub>(ndc) linker, sky-blue column in Figure S8.2.4, S8.2.5 and S8.2.6; 1544 cm<sup>-1</sup> for H<sub>2</sub>(bdc-NO<sub>2</sub>) linker, sky-blue column in Figure S8.2.7-8.2.10) all support the successful incorporation of both linkers in each of the [Cu<sub>2</sub>Lm<sub>2</sub>(dabco)] SURMOFs. Similarly, the *pK<sub>a</sub>* effect on the crystallite orientation of the [Cu<sub>2</sub>Lm<sub>2</sub>(dabco)] SURMOFs can be further supported by the variational intensity of symmetric -COO<sup>-</sup> signals which usually are representatives for [100] orientation in tetragonal [M<sub>2</sub>L<sub>2</sub>P] SURMOFs.<sup>247</sup> As shown in Figure 4.2b, in all the three spectra, the barely visible symmetric -COO<sup>-</sup> vibrations (~1400 cm<sup>-1</sup>) are well consistent with the highly [001] oriented [Cu<sub>2</sub>Lm<sub>2</sub>(dabco)] SURMOFs if Lm are linker mixtures of (bdc+ndc), (chdc+bdc) and (chdc+ ndc). When [100] oriented crystallites were present, the signals of symmetric -COO<sup>-</sup> vibrations (~1400 cm<sup>-1</sup>) showed up in the corresponding IRRA spectra of [Cu<sub>2</sub>Lm<sub>2</sub>(dabco)] SURMOFs (Figure 4.2d and 4.2f). For example, symmetric -COO<sup>-</sup> vibrations were observed in the spectra of [Cu<sub>2</sub>Lm<sub>2</sub>(dabco)] SURMOFs where Lm were (bdc-NO<sub>2</sub>+chdc) and (f<sub>4</sub>bdc+bdc-NO<sub>2</sub>) due to the high content of [100] oriented crystallites in both SURMOFs. These results indicate that by utilizing the mixed-linker approach, [Cu<sub>2</sub>Lm<sub>2</sub>(dabco)] MTV-SURMOFs can be grown on PPP1 surfaces and the [001] orientational quality can be controlled by employing different binary mixtures of dicarboxylate linkers with different *pK<sub>a</sub>* values.

In order to quantitatively evaluate the effect of the linker *pK<sub>a</sub>* on the orientational quality of [Cu<sub>2</sub>Lm<sub>2</sub>(dabco)] SURMOFs containing two linkers, the content of [100] oriented crystallites was recorded employing the method which we used before.<sup>247</sup> According to Table S8.2.1, we found that for H<sub>2</sub>(bdc-NO<sub>2</sub>) and H<sub>2</sub>(f<sub>4</sub>bdc) based [Cu<sub>2</sub>Lm<sub>2</sub>(dabco)] SURMOFs the content of the unexpected [100] orientation increases with increasing *pK<sub>a</sub>* values of the accompanying dicarboxylate linkers (from H<sub>2</sub>(ndc) to H<sub>2</sub>(chdc), Table S8.2.1). However, the [Cu<sub>2</sub>(f<sub>4</sub>bdc+bdc-NO<sub>2</sub>)<sub>2</sub>(dabco)] SURMOF exhibited an even higher content of the unwanted [100] oriented crystallites than the SURMOFs formed from the single linkers. This phenomenon might be ascribed to an interplay of the low *pK<sub>a</sub>* values of the single linkers and the interactions between the two linkers. For instance, linkers with low *pK<sub>a</sub>* values have better deprotonation ability but worse coordination ability to the Cu<sub>2</sub> SBU. Moreover, if the electron-withdrawing groups are mixed with the electron-rich moieties, the interactions between the two linkers will be more significant and the [001] orientational quality of MTV-SURMOFs will become better.

To further quantify the  $pK_a$  effects of the binary mixtures and explore the relationship between the orientational quality and the effects, the shifts of the asymmetric  $-\text{COO}^-$  signals in the  $[\text{Cu}_2\text{Lm}_2(\text{dabco})]$  MTV-SURMOFs with respect to the parent  $[\text{Cu}_2\text{L}_2(\text{dabco})]$  SURMOFs were calculated by comparing the peak positions in the corresponding IRRA spectra. The linker  $pK_a$  effects on the quality of [001] orientation might be more significant if the asymmetric  $-\text{COO}^-$  vibrations in the  $[\text{Cu}_2\text{Lm}_2(\text{dabco})]$  SURMOFs are closer to the average value of the respective parent asymmetric  $-\text{COO}^-$  signals in  $[\text{Cu}_2\text{L}_2(\text{dabco})]$  SURMOFs. As depicted in Figure S8.2.4-8.2.13, all the asymmetric  $-\text{COO}^-$  vibrations in the  $[\text{Cu}_2\text{Lm}_2(\text{dabco})]$  SURMOFs are much closer to the parent  $[\text{Cu}_2\text{L}_2(\text{dabco})]$  SURMOFs containing the low  $pK_a$  linkers, meaning that the linkers with low  $pK_a$  values play a major role in the orientational quality of the  $[\text{Cu}_2\text{Lm}_2(\text{dabco})]$  MTV-SURMOFs.

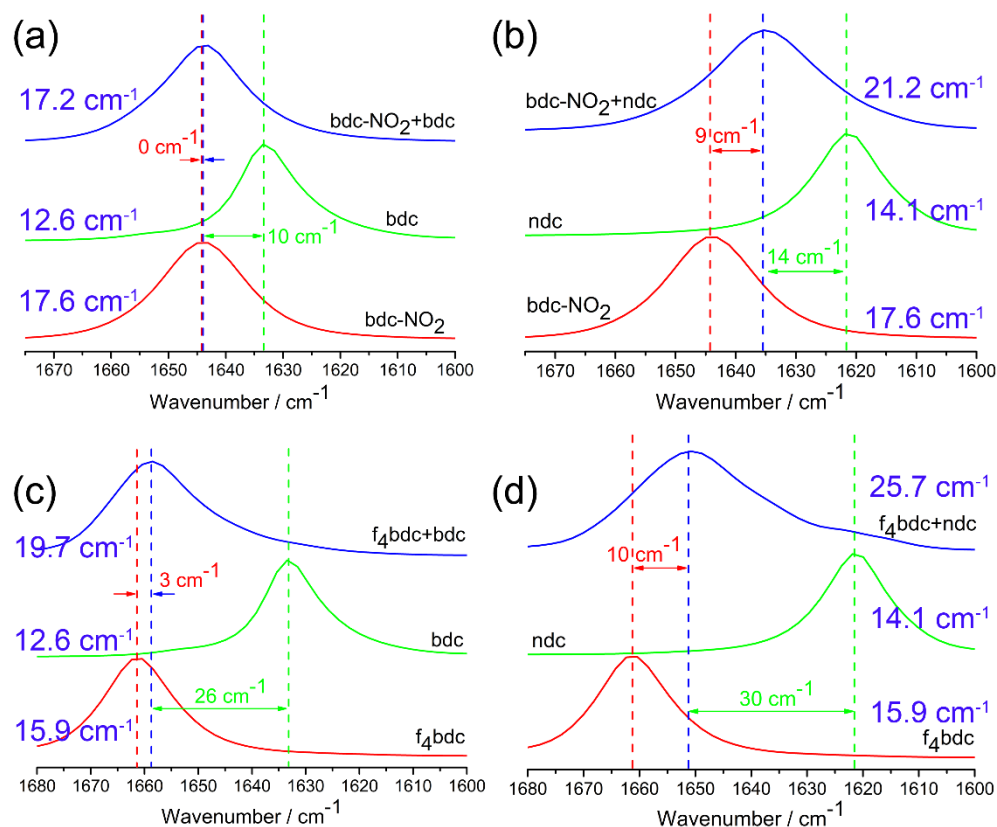


**Figure 4.3** Magnified IRRA spectra of  $[\text{Cu}_2\text{Lm}_2(\text{dabco})]$  SURMOFs showing shifts of asymmetric  $-\text{COO}^-$  vibrations (green and red numbers) compared to parent  $[\text{Cu}_2\text{L}_2(\text{dabco})]$  SURMOFs, while the blue numbers represent full width at half maximum of the asymmetric  $-\text{COO}^-$  vibrations. (a)  $[\text{Cu}_2(\text{bdc-NO}_2+\text{bdc})_2(\text{dabco})]$ ; (b)  $[\text{Cu}_2(\text{bdc-NO}_2+\text{ndc})_2(\text{dabco})]$ ; (c)  $[\text{Cu}_2(\text{f}_4\text{bdc}+\text{bdc})_2(\text{dabco})]$ ; (d)  $[\text{Cu}_2(\text{f}_4\text{bdc}+\text{ndc})_2(\text{dabco})]$ .

As demonstrated in Figure 4.3a and b, compared to  $[\text{Cu}_2(\text{bdc-NO}_2)_2(\text{dabco})]$  SURMOF, the shifts of asymmetric  $-\text{COO}^-$  vibrations are 0 and  $9\text{ cm}^{-1}$  for  $[\text{Cu}_2(\text{bdc-NO}_2+\text{bdc})_2(\text{dabco})]$  and  $[\text{Cu}_2(\text{bdc-NO}_2+\text{ndc})_2(\text{dabco})]$ , respectively, meaning that the linkers with low  $pK_a$  values play a major role in the orientational quality of  $[\text{Cu}_2\text{Lm}_2(\text{dabco})]$  SURMOFs. Thus, the  $[\text{Cu}_2(\text{bdc-NO}_2+\text{ndc})_2(\text{dabco})]$  SURMOF shows a better [001] orientational quality (with perfect [001] orientation) than that of the  $[\text{Cu}_2(\text{bdc-NO}_2+\text{bdc})_2(\text{dabco})]$  SURMOF (with 2.7% of [100] crystallite orientation). A similar effect can be observed for  $\text{H}_2(\text{f}_4\text{bdc})$  based  $[\text{Cu}_2\text{Lm}_2(\text{dabco})]$  SURMOFs (Figure 4.3c and d). Due to the difference of asymmetric  $-\text{COO}^-$  vibrations shifts ( $3\text{ cm}^{-1}$  and  $10\text{ cm}^{-1}$ , respectively) resulted from the different effects of  $(\text{f}_4\text{bdc}+\text{bdc})$  and  $(\text{f}_4\text{bdc}+\text{ndc})$  mixtures, the content of [100] oriented crystallites in  $[\text{Cu}_2(\text{f}_4\text{bdc}+\text{ndc})_2(\text{dabco})]$  SURMOF is much lower than that in  $[\text{Cu}_2(\text{f}_4\text{bdc}+\text{bdc})_2(\text{dabco})]$  SURMOF (Table S8.2.1). However, if two dicarboxylate linkers with relatively low  $pK_a$  values are mixed together, for example,  $\text{H}_2(\text{f}_4\text{bdc})$ - $\text{H}_2(\text{bdc-NO}_2)$  mixture, due to the worse coordination ability to the  $\text{Cu}_2$  SBU, much more disorder is generated and the [001] orientational quality of the  $[\text{Cu}_2(\text{f}_4\text{bdc}+\text{bdc-NO}_2)_2(\text{dabco})]$  SURMOF becomes worse as indicated by the highest content of mis-oriented [100] crystallites observed in the SURMOF (Table S8.2.1).

#### 4.2.3 Linker $pK_a$ effect on $[\text{Cu}_2\text{Lm}_2(\text{dabco})]$ SURMOFs containing more linkers

Moreover, utilizing the mixed-linker approach, highly oriented  $[\text{Cu}_2\text{Lm}_2(\text{dabco})]$  SURMOFs consisting of up to five linkers can be obtained by mixing the respective dicarboxylate linkers in the LbL growth process. As clearly illustrated in Figure 4.4a, interestingly,  $[\text{Cu}_2\text{Lm}_2(\text{dabco})]$  SURMOFs containing three, four and five linkers all exhibit exclusive [001] orientation even if a mixture of three linkers with low  $pK_a$  values, for example,  $\text{H}_2(\text{bdc-NO}_2)$ ,  $\text{H}_2(\text{f}_4\text{bdc})$  and  $\text{H}_2(\text{ndc})$ , is employed during the LbL growth. The reason might be mainly ascribed to the linker  $pK_a$  effects which has been observed in the binary linker mixtures. The corresponding IRRA spectra shown in Figure 4.4b are almost identical and exhibit almost invisible symmetric  $-\text{COO}^-$  vibrations (green column), further confirming the exclusive [001] crystallite orientation. Additionally, all the spectra show characteristic vibrations from the corresponding linkers, such as  $776\text{ cm}^{-1}$  for  $\text{H}_2(\text{ndc})$  linker,  $746\text{ cm}^{-1}$  for  $\text{H}_2(\text{bdc})$  and  $\text{H}_2(\text{f}_4\text{bdc})$  linkers (sky-blue

column) and  $1544\text{ cm}^{-1}$  for  $\text{H}_2(\text{bdc-NO}_2)$  (pink column) in Figure 4.4b, demonstrating the well incorporation of three, four and five functionalities. Analogously, the shifts of asymmetric  $-\text{COO}^-$  vibrations could be used to distinguish the three spectra. As shown in Figure S8.2.14, with increasing number of the mixed dicarboxylate linkers, the asymmetric  $-\text{COO}^-$  vibration shifts gradually to lower wavenumbers, which close to the intermediate value of the five  $[\text{Cu}_2\text{L}_2(\text{dabco})]$  SURMOFs. The result indicates promisingly that, in principle, highly  $[001]$  oriented  $[\text{Cu}_2\text{Lm}_2(\text{dabco})]$  SURMOFs can be obtained, which could incorporate more functionalities by simply adding more dicarboxylate linkers of the same type but with different functionalities into the growth solution. Apparently, the individual  $pK_a$  values do not play a role in this case.

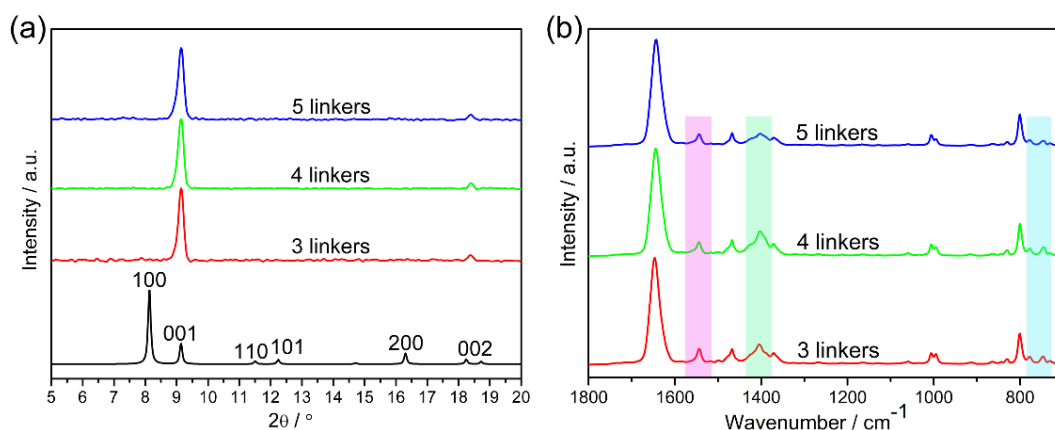


**Figure 4.4** XRD patterns (a) and IRRA spectra (b) of  $[\text{Cu}_2\text{Lm}_2(\text{dabco})]$  SURMOFs with 3 (red), 4 (green) and 5 (blue) dicarboxylate linkers grown at  $60\text{ }^\circ\text{C}$  on PPP1 surfaces (3 linkers =  $\text{H}_2(\text{f}_4\text{bdc}) + \text{H}_2(\text{bdc-NO}_2) + \text{H}_2(\text{ndc})$ ; 4 linkers =  $\text{H}_2(\text{f}_4\text{bdc}) + \text{H}_2(\text{bdc-NO}_2) + \text{H}_2(\text{ndc}) + \text{H}_2(\text{bdc})$ ; 5 linkers =  $\text{H}_2(\text{f}_4\text{bdc}) + \text{H}_2(\text{bdc-NO}_2) + \text{H}_2(\text{ndc}) + \text{H}_2(\text{bdc}) + \text{H}_2(\text{chdc})$ ). The green column signifies symmetric  $-\text{COO}^-$  vibrations, while the pink and sky-blue columns indicate the characteristic vibrations of linkers (see details in corresponding text).

#### 4.2.4 Effect of the linker ratio in $[\text{Cu}_2\{(\text{bdc})_x+(\text{f}_4\text{bdc})_{1-x}\}_2(\text{dabco})]$ ( $0 \leq x \leq 1$ ) SURMOFs on the orientation

Importantly, the orientational quality of the  $[\text{Cu}_2\text{Lm}_2(\text{dabco})]$  SURMOFs could also be tuned by altering the ratio of the mixed dicarboxylate linkers. Figure 4.5a displays the out-of-plane XRD patterns of  $[\text{Cu}_2\{(\text{bdc})_x+(\text{f}_4\text{bdc})_{1-x}\}_2(\text{dabco})]$  ( $x$  is a fraction of bdc linker and the value is between 0 and 1) SURMOFs grown from  $\text{H}_2(\text{bdc})$ - $\text{H}_2(\text{f}_4\text{bdc})$  mixtures with different molar

ratios. Obviously, the content of [100] oriented crystallites (Table S8.2.2, marked by pink color in Figure 4.5a) increased with increasing content of  $f_4\text{bdc}$  linker (with low  $pK_a$  value). Notably, however, the SURMOF grown only from  $\text{H}_2(f_4\text{bdc})$  linker (no addition of  $\text{H}_2\text{bdc}$ ) had a lower content of [100] mis-orientation than the ones grown from the mixtures containing 40% and 20%  $\text{H}_2(\text{bdc})$  linker (Table S8.2.2). This interesting variation of the content of [100] orientation might be mainly ascribed to the overall  $pK_a$  effects of  $\text{H}_2(f_4\text{bdc})$ - $\text{H}_2(\text{bdc})$  mixtures with different ratios as demonstrated by the shape changes of the characteristic vibrations (C-H and C-F vibrations) shown in the IRRA spectra (Figure 4.5b, gray column). When the percentage of  $\text{H}_2(f_4\text{bdc})$  in the mixture is low (e.g., lower than 50%), the orientation of SURMOFs is dominated by the bdc linker, that is the [001] crystallite orientation. When the molar ratio of  $\text{H}_2(f_4\text{bdc})/\text{H}_2(\text{bdc})$  changes from 1:1 (50% bdc) to 4:1 (20% bdc), the  $\text{H}_2(f_4\text{bdc})$  linker directs the orientation of the SURMOFs and causes an increase of the [100] mis-oriented crystallites. When there is no  $\text{H}_2(\text{bdc})$  linker (100%  $f_4\text{bdc}$ ) in the LbL growth solution, the effects between the two linkers does not exist anymore and therefore, the SURMOF only presents the  $pK_a$  effect of the  $\text{H}_2(f_4\text{bdc})$  on the orientation.

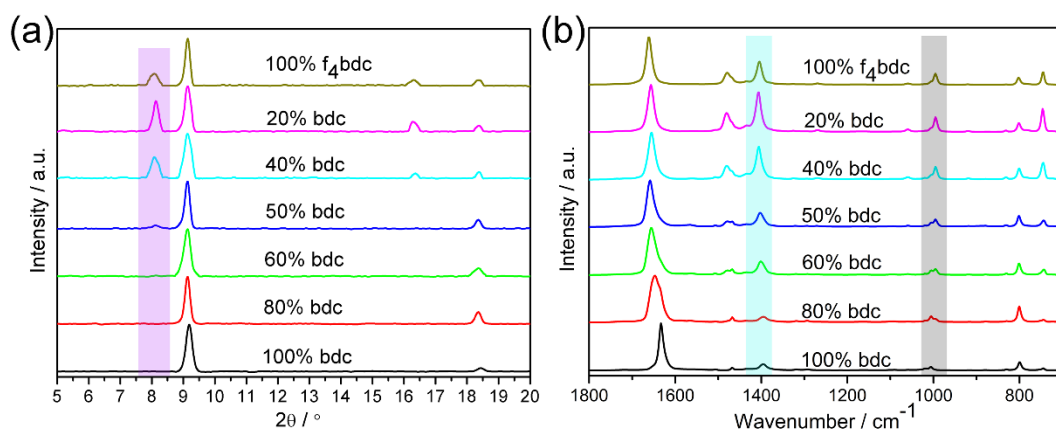


**Figure 4.5** XRD patterns (a) and IRRA spectra (b) of  $[\text{Cu}_2\{(\text{bdc})_x+(\text{f}_4\text{bdc})_{1-x}\}_2(\text{dabco})]$  ( $0 \leq x \leq 1$ ) SURMOFs grown at  $60^\circ\text{C}$  on PPP1 surfaces. The pink column shows the content variation of [100] orientation. The cyan column signifies the symmetric  $-\text{COO}^-$  vibrations, while the gray column indicates the characteristic vibrations of C-H and C-F.

The IRRA spectra of  $[\text{Cu}_2\{(\text{bdc})_x+(\text{f}_4\text{bdc})_{1-x}\}_2(\text{dabco})]$  ( $0 \leq x \leq 1$ ) SURMOFs deposited from the  $\text{H}_2(f_4\text{bdc})$ - $\text{H}_2(\text{bdc})$  mixtures with different molar ratios are depicted in Figure 4.5b. In line with

XRD results, IRRA spectra of SURMOFs with a mixture of orientations show both symmetric ( $\sim 1400\text{ cm}^{-1}$ , marked by cyan column) and asymmetric  $-\text{COO}^-$  ( $1630\text{-}1660\text{ cm}^{-1}$ ) vibration peaks, while the symmetric  $-\text{COO}^-$  peak is barely seen in the highly [001] oriented SURMOFs. It is worth noting that the asymmetric  $-\text{COO}^-$  peaks of mixed-linker SURMOFs are all located between the SURMOFs deposited either from  $\text{H}_2(\text{bdc})$  or  $\text{H}_2(\text{f}_4\text{bdc})$  linker (Figure S8.2.15), which further indicates that indeed both linkers were successfully incorporated into the MTV-SURMOFs.

#### 4.2.5 Adsorption capacities of $[\text{Cu}_2\{(\text{bdc})_x+(\text{f}_4\text{bdc})_{1-x}\}_2(\text{dabco})]$ ( $0 \leq x \leq 1$ ) SURMOFs

The adsorption capacities of  $[\text{Cu}_2\{(\text{bdc})_x+(\text{f}_4\text{bdc})_{1-x}\}_2(\text{dabco})]$  SURMOFs with different molar ratios of linkers were evaluated by a QCM utilizing benzene ( $\text{C}_6\text{H}_6$ ) and hexafluorobenzene ( $\text{C}_6\text{F}_6$ ) as probe molecules. Theoretically,  $[\text{Cu}_2\{(\text{bdc})_x+(\text{f}_4\text{bdc})_{1-x}\}_2(\text{dabco})]$  SURMOFs with higher content of bdc should be more attractive for the  $\text{C}_6\text{F}_6$  molecules, while the high content of  $\text{f}_4\text{bdc}$  linker in the SURMOFs would result in more efficient adsorption for  $\text{C}_6\text{H}_6$  due to the Ar-H/Ar-F interaction. Despite the varied molar ratios of linkers, films of similar density were observed for all the  $[\text{Cu}_2\{(\text{bdc})_x+(\text{f}_4\text{bdc})_{1-x}\}_2(\text{dabco})]$  ( $0 \leq x \leq 1$ ) SURMOFs, as illustrated by the SEM images, which are recorded in Figure S8.2.16, making them excellent candidates for VOCs adsorption/desorption measurements. As demonstrated in Figure 4.6a, the adsorption capacities of  $[\text{Cu}_2\{(\text{bdc})_x+(\text{f}_4\text{bdc})_{1-x}\}_2(\text{dabco})]$  SURMOFs for  $\text{C}_6\text{H}_6$  and  $\text{C}_6\text{F}_6$  both increase with increasing content of bdc linker, meaning the adsorption capacities could be tuned by varying the molar ratios of the linkers. All the SURMOFs present overall higher adsorption capacities for  $\text{C}_6\text{H}_6$  than  $\text{C}_6\text{F}_6$  and the adsorption capacities of both compounds reach the maximum for  $[\text{Cu}_2(\text{bdc})_2(\text{dabco})]$  SURMOF. These different adsorption capacities are mainly attributed to an interplay of the different van der Waals diameters of the probe molecules ( $5.35\text{ \AA}$  for  $\text{C}_6\text{H}_6$ <sup>314</sup> and  $5.91\text{ \AA}$  for  $\text{C}_6\text{F}_6$ <sup>315</sup>), the different pore sizes of the  $[\text{Cu}_2\{(\text{bdc})_x+(\text{f}_4\text{bdc})_{1-x}\}_2(\text{dabco})]$  SURMOFs and the Ar-H/Ar-F interaction. Firstly, the  $\text{C}_6\text{H}_6$  molecules are smaller than  $\text{C}_6\text{F}_6$ , and thus the pores are more accessible for the smaller  $\text{C}_6\text{H}_6$  molecules and thus leads to higher adsorption capacities for all the SURMOFs. Secondly, the pore sizes of  $[\text{Cu}_2(\text{bdc})_2(\text{dabco})]$  and  $[\text{Cu}_2(\text{f}_4\text{bdc})_2(\text{dabco})]$  along the *c* axis ([001] direction) are  $7.4\text{ \AA} \times 7.4$

Å and  $6.3 \text{ Å} \times 6.3 \text{ Å}$ , respectively (Figure S8.2.17) as explicitly illustrated in previous publications.<sup>298,316</sup> Therefore, the  $[\text{Cu}_2(\text{bdc})_2(\text{dabco})]$  SURMOF exhibits maximal adsorption capacity of both test compounds due to the larger [001] oriented pore volume. In addition, the pore volumes of  $[\text{Cu}_2\{(\text{bdc})_x+(\text{f}_4\text{bdc})_{1-x}\}_2(\text{dabco})]$  ( $0 \leq x \leq 1$ ) SURMOFs are highly tunable by varying the ratios of mixed dicarboxylate linkers as already experimentally testified on a Zn-pillared MOF by Walton and coworkers.<sup>313</sup> Specifically, the effective pore diameters of  $[\text{Cu}_2\{(\text{bdc})_x+(\text{f}_4\text{bdc})_{1-x}\}_2(\text{dabco})]$  ( $0 \leq x \leq 1$ ) SURMOFs along the *c* axis increase with an increasing content of *bdc* linker (Figure 4.6b) and therefore the adsorption capacities for both compounds gradually increases. Finally, the Ar-H/Ar-F interaction in the adsorption capacities can be demonstrated by the differential (denoted as capacity ratios of either  $\text{C}_6\text{H}_6$  to  $\text{C}_6\text{F}_6$  or  $\text{C}_6\text{F}_6$  to  $\text{C}_6\text{H}_6$ ) shown in Figure S8.2.18. The capacity ratios of  $\text{C}_6\text{F}_6$  to  $\text{C}_6\text{H}_6$  gradually increase with increasing content of *bdc* linker, clearly indicating that the  $[\text{Cu}_2\{(\text{bdc})_x+(\text{f}_4\text{bdc})_{1-x}\}_2(\text{dabco})]$  ( $0 \leq x \leq 1$ ) SURMOFs with higher content of *bdc* linker are more attractive for the  $\text{C}_6\text{F}_6$  molecules. These data clearly demonstrate that the content of dicarboxylate linkers in the  $[\text{Cu}_2\text{Lm}_2(\text{dabco})]$  MTV-SURMOFs plays a major role in the adsorption capacities towards VOCs.

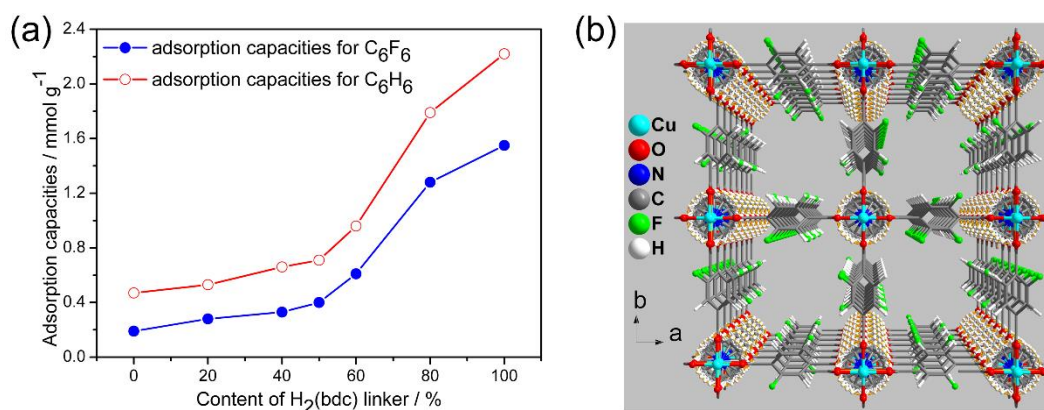


**Figure 4.6** (a) Adsorption capacities of  $[\text{Cu}_2\{(\text{bdc})_x+(\text{f}_4\text{bdc})_{1-x}\}_2(\text{dabco})]$  ( $0 \leq x \leq 1$ ) SURMOFs towards  $\text{C}_6\text{H}_6$  (empty circles) and  $\text{C}_6\text{F}_6$  (filled circles) at room temperature; (b) Multivariate pore environments of  $[\text{Cu}_2\{(\text{bdc})_x+(\text{f}_4\text{bdc})_{1-x}\}_2(\text{dabco})]$  SURMOFs with different molar ratios of linkers; white: H; green: F.

### 4.3 Conclusions

In conclusion, we have demonstrated the  $pK_a$  values of dicarboxylate linkers greatly affect the orientational quality of tetragonal  $[\text{M}_2\text{L}_2\text{P}]$  SURMOFs. Highly [001] oriented  $[\text{Cu}_2\text{L}_2(\text{dabco})]$

SURMOFs can be obtained by the LbL deposition from high  $pK_a$  linkers on pyridyl-terminated surfaces, while dicarboxylate linkers with low  $pK_a$  values result in mis-oriented SURMOFs (with unexpected [100] crystallite orientation). Based on the  $pK_a$  effect on the orientational quality of the  $[\text{Cu}_2\text{L}_2(\text{dabco})]$  SURMOFs, highly oriented  $[\text{Cu}_2\text{Lm}_2(\text{dabco})]$  MTV-SURMOFs containing up to five different dicarboxylate linkers are achieved by combining a simple mixed-linker approach with the LbL growth. The orientational quality of the  $[\text{Cu}_2\text{Lm}_2(\text{dabco})]$  SURMOFs is controlled by the categories, quantities and molar ratios of mixed linkers with different  $pK_a$  values, depending on the interactions between/among dicarboxylate linkers. Exclusively [001] oriented  $[\text{Cu}_2\text{Lm}_2(\text{dabco})]$  MTV-SURMOFs are obtained when the growth nutrient solution contains two linkers of relatively high  $pK_a$  values or more than two kinds of dicarboxylate linkers (then the  $pK_a$  values of the linkers do not matter). While the mixtures with the high content of low  $pK_a$  linkers result in the mis-oriented  $[\text{Cu}_2\text{Lm}_2(\text{dabco})]$  MTV-SURMOFs with unexpected [100] orientations. Finally, it was demonstrated that the adsorption capacities of  $[\text{Cu}_2\text{Lm}_2(\text{dabco})]$  MTV-SURMOFs are tunable by varying the molar ratio of the linkers in a binary mixture as indicated for the  $[\text{Cu}_2\{(\text{bdc})_x+(\text{f}_4\text{bdc})_{1-x}\}_2(\text{dabco})]$  ( $0 \leq x \leq 1$ ) SURMOF system.



## 5 LbL deposition and pore-size limited charge transfer of SURMOFs containing redox-active species

### 5.1 Introduction

Considering the fact that the vast majority of MOFs are insulators, the application of MOFs in electronic or electrochemical devices is extremely challenging. The common way for realizing electrical conductivity in MOFs is to introduce functional units into the accessible pores. For example, electrical conductivity has been achieved in HKUST-1 by introducing redox-active molecules (ferrocene<sup>191,192</sup> or TCNQ<sup>186</sup>) into the pores. Nevertheless, this method usually has the disadvantages that the amount of functional molecules and electrical conductivity are difficult to control and tune. As an alternative strategy, the “bottom-up” approach involving the judicious selection of metal nodes and the functionalization of organic linkers has been demonstrated as an effective method to increase the intrinsic conductivity of MOFs. With this approach, Dincă and coworkers recently developed a series of conductive MOFs such as  $M_2(\text{tftb})$  ( $M = \text{Mn, Co, Zn}$  and  $\text{Cd}$ ; tftb = tetrathiafulvalene tetrabenzoate),  $M_3(\text{hitp})_2$  ( $M = \text{Cu}$  and  $\text{Ni}$ ; hitp = 2,3,6,7,10,11-hexaiminotriphenylene) and  $M_2(\text{debdc})$  ( $M = \text{Fe}$  and  $\text{Mn}$ ; debdc = 2,5-disulfhydrylbenzene-1,4-dicarboxylate) shown in Figure 5.1.<sup>317–321</sup>

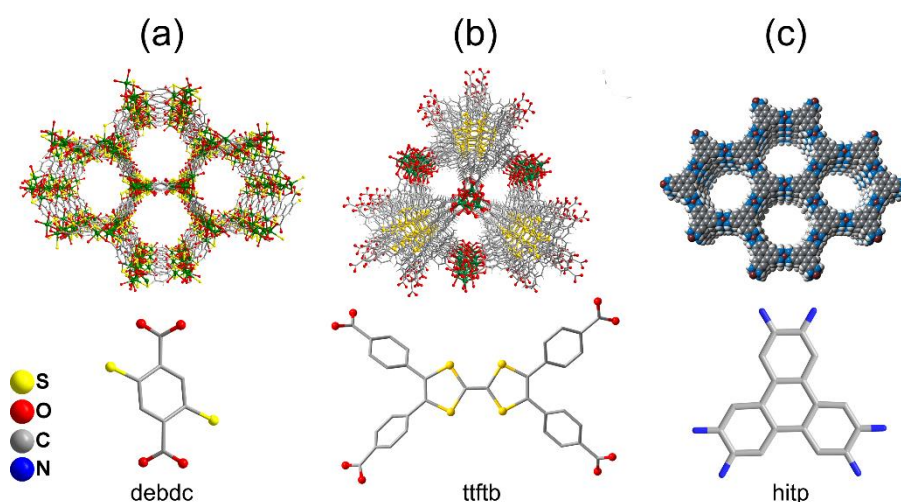
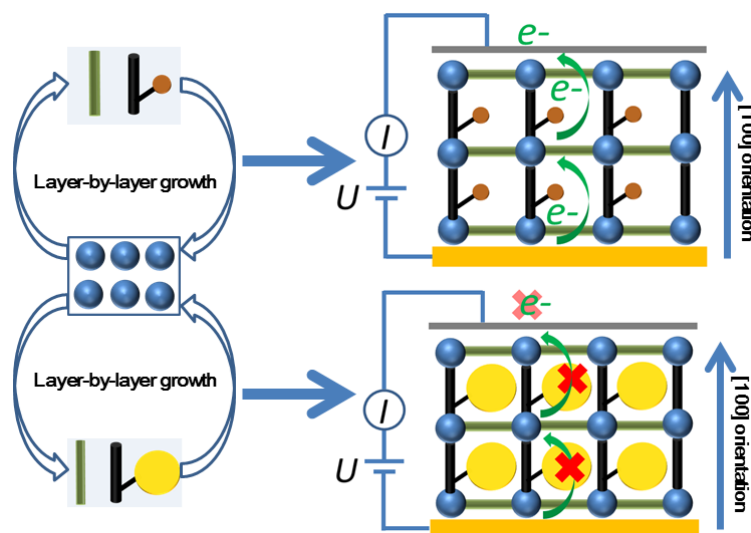


**Figure 5.1** Conductive MOF structures. (a)  $M_2(\text{debdc})$ ; (b)  $M_2(\text{tftb})$  and (c)  $M_3(\text{hitp})_2$ .

In addition, redox-active MOFs containing NDI (1,4,5,8-naphthalenetetracarboxylic diimide), porphyrin and pyrene cores are reported for the applications in electrochromic and

electrochemical devices.<sup>174,267–272</sup> Moreover, based on ferrocene moieties, the Kitagawa group recently reported a kind of 2D redox-active framework using 1,1'-ferrocenedicarboxylic acid as organic linker.<sup>322</sup>

Herein, combining the LbL growth protocol with the “bottom-up” approach, we carried out the investigations on the oriented growth and the electrochemical properties of the  $[M_2L_2P]$  SURMOFs containing redox-active species deposited from the organic linkers functionalized with ferrocene (Fc) and dimethyl ferrocene ( $Me_2Fc$ ) moieties (Scheme 5.1). A novel pyrazole-terminated SAM ((4-(1*H*-pyrazol-4-yl) phenylmethanethiol, PyzP1) was employed to adjust the surface chemistry and govern the nucleation and growth of the SURMOFs. In order to obtain crystalline films with tunable crystallite orientation and to achieve rational design and covalent functionalization of the dicarboxylate linkers, the tetragonal  $[Cu_2(bpdc)_2(dabco)]$  system was chosen as a lead structure due to its relatively high phase stability (up to 513 K) and large pores for the accommodation of Fc and  $Me_2Fc$  moieties.<sup>298</sup> Two moieties (Fc and  $Me_2Fc$ ) with similar electrochemical properties (Figure S8.3.1) but different van der Waals diameters were selected to control and adjust the accessible pore volume and thus the charge transfer properties of SURMOFs. Cyclic voltammetry (CV) was used to characterize the charge transfer by employing  $Bu_4NPF_6$  dissolved in acetonitrile as an inert electrolyte and Fc and  $Me_2Fc$  functionalized organic linkers as suitable inner-sphere redox systems.



**Scheme 5.1** Schematic illustration of LbL growth and charge transfer tuning of SURMOFs functionalized with ferrocene (Fc) and dimethyl ferrocene ( $Me_2Fc$ ) moieties (blue balls: Cu SBUs; green bars: dabco; brown circles: Fc moieties; yellow circles:  $Me_2Fc$  moieties).

## 5.2 Results and discussion

### 5.2.1 LbL growth of $[\text{Cu}_2(\text{bpdc-amide-Fc})_2(\text{dabco})]$ (Fc-SURMOF) and $[\text{Cu}_2(\text{bpdc-amide-Me}_2\text{Fc})_2(\text{dabco})]$ ( $\text{Me}_2\text{Fc-SURMOF}$ ) SURMOFs

The redox-species containing SURMOFs were LbL grown onto pyrazole-terminated surfaces at 60 °C (see details in section 2.4) and the orientation of the SURMOFs was inspected by out-of-plane X-ray diffraction. As shown in Figure 5.2a, compared to the simulated XRD pattern from  $[\text{Cu}_2(\text{bpdc})_2(\text{dabco})]$  system, the ferrocene moiety functionalized SURMOF ( $[\text{Cu}_2(\text{bpdc-amide-Fc})_2(\text{dabco})]$ , Fc-SURMOF) is highly crystalline and oriented along the [100] direction on PzP1 surfaces. As expected, the Fc-SURMOF has a tetragonal crystal structure as indicated by the comparable XRD patterns of bulk  $[\text{Cu}_2(\text{bpdc-amide-Fc})_2(\text{dabco})]$  and  $[\text{Cu}_2(\text{bpdc})_2(\text{dabco})]$  MOF (Figure S8.3.2). In addition, the perfect [100] orientation of MOF crystallites means that the Fc moieties are regularly arranged inside the tetragonal framework, prompting the charge transfer through the oriented pores (Scheme 5.1). Surprisingly, if the dimethyl ferrocene functionalized dicarboxylate linker ( $\text{H}_2(\text{bpdc-amide-Me}_2\text{Fc})$ ) was employed, three additional diffraction peaks, (101), (210) and (310), appear in the resultant SURMOF ( $[\text{Cu}_2(\text{bpdc-amide-Me}_2\text{Fc})_2(\text{dabco})]$ ,  $\text{Me}_2\text{Fc-SURMOF}$ , Figure 5.2a).  $\text{Me}_2\text{Fc-SURMOF}$  exhibits the dominant [100] orientation, further confirmed by the almost identical IRRA spectra of Fc- and  $\text{Me}_2\text{Fc-SURMOFs}$  shown in Figure 5.2b. The SEM observation (Figure 5.2c and d) demonstrates that the crystallites in both SURMOFs possess similar morphologies and are densely packed to form homogeneous films which are essential for the electrochemical measurements. In Fc-SURMOF, the uniform crystallites stand upright on the substrate and exhibit exclusively the [100] orientation, while there are some mis-oriented crystallites in the  $\text{Me}_2\text{Fc-SURMOF}$ , which lead to the mixed orientations.

Unfortunately, the attempts to adjust the crystallite orientation of Fc- and  $\text{Me}_2\text{Fc-SURMOFs}$  were not successful by employing carboxyl- or pyridyl-terminated SAMs such as MTCA and PPP1 for the tetragonal  $[\text{M}_2\text{L}_2\text{P}]$  system.<sup>247,323</sup> If MTCA SAM was utilized under 60 °C, only amorphous materials were obtained, while Fc-SURMOF exhibited preferred [100] orientation when PPP1 SAM was employed under the same condition (Figure S8.3.3a). Interestingly, the observation is different from the previous reports<sup>246,247</sup> that the tetragonal  $[\text{M}_2\text{L}_2\text{P}]$  system

usually exhibits [001] orientation on PPP1 surfaces. The reason is probably the larger volume of the ferrocene moiety compared to the dabco pillar, which makes the [001] oriented alignment impossible on the PPP1 surface. So the Fc-SURMOF also shows a [100] crystallite orientation on pyridyl-terminated surface. Nevertheless, only loosely packed thin films were obtained on PPP1 surfaces (Figure S8.3.3b) for Fc-SURMOF, which were not suitable for CV measurements. Thus, the pyrazole-terminated PyzP1 SAM was essential to obtain the closely packed and well-oriented thin films of Fc-SURMOF. The packing density and orientation difference of the SURMOFs can be mainly ascribed to the different nucleation and template effects caused by different functionalities and structural properties of the chosen SAMs on substrates. As shown in Figure S8.3.4, after immersion of PyzP1 SAM into  $\text{Cu}_2(\text{OAc})_4$  ethanol solution (half cycle), the intensity of the symmetric  $-\text{COO}^-$  vibration at around  $1440\text{ cm}^{-1}$  is much stronger than that after the deposition of  $\text{Cu}_2(\text{OAc})_4$  on PPP1 SAM, meaning that the  $\text{Cu}_2$  SBU is probably coordinated to both N atoms in the pyrazole group which might contribute to the perfect [100] orientation and high packing density of crystallites.

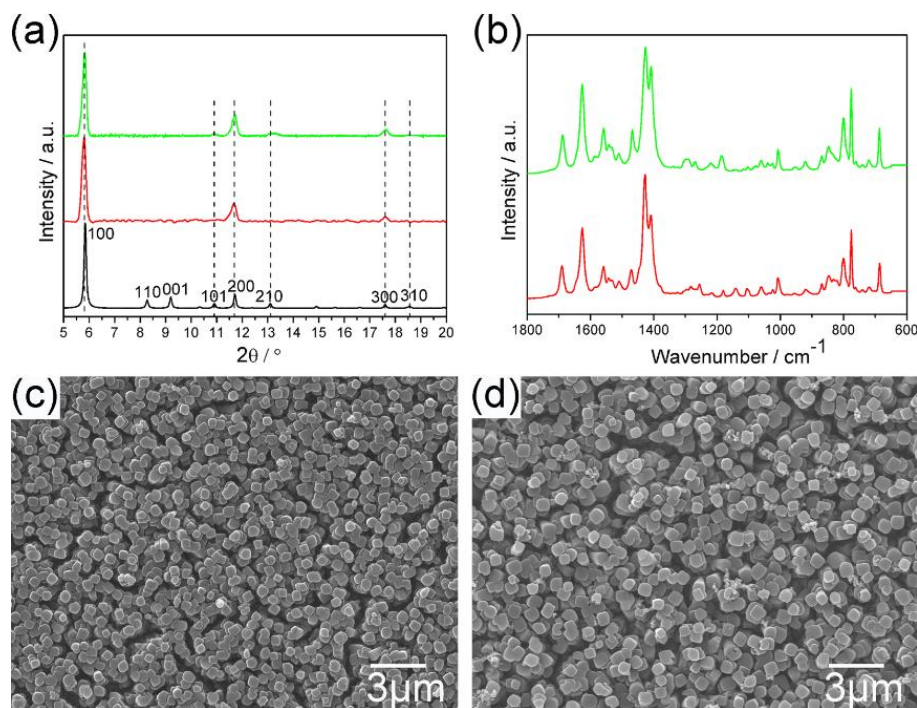


**Figure 5.2** XRD patterns (a) and IRRA spectra (b) of Fc- and  $\text{Me}_2\text{Fc-SURMOFs}$  grown at  $60\text{ }^\circ\text{C}$  on PyzP1 surfaces (black: simulated XRD pattern from  $[\text{Cu}_2(\text{bpdc})_2(\text{dabco})]$  tetragonal system; red: Fc-SURMOF, 40 deposition cycles; green:  $\text{Me}_2\text{Fc-SURMOF}$ , 40 deposition cycles); (c) and (d) SEM images of Fc-SURMOF (c) and  $\text{Me}_2\text{Fc-SURMOF}$  (d).

### 5.2.2 Charge transfer properties of Fc- and Me<sub>2</sub>Fc-SURMOFs

The CV measurements of the SURMOFs illustrated in Figure 5.3 exhibit a vast difference. For the Fc-SURMOF, the CVs present a remarkable current density ( $115 \mu\text{A}/\text{cm}^2$ ) and a well-defined pair of redox peaks at  $E_{pa} = 0.69\text{V}$  and  $E_{pc} = 0.61\text{V}$  versus Ag/AgCl, assigned to the ferrocene/ferrocenium redox process, which is analogous to the observations for ferrocene-modified SURGEL coatings<sup>324</sup> and a Zn-MOF<sup>322</sup> for which 1,1'-ferrocene dicarboxylic acid was employed as a linker. This means that the ferrocene moieties in the highly oriented Fc-SURMOF are reversibly oxidized and reduced inside the [100] oriented pores, what can also be seen in the solution CV curves of H<sub>2</sub>(bpdc-amide-Fc) linker in the same electrolyte (Figure S8.3.1). The peak separation of 80 mV in the SURMOF CVs is close to the theoretical value expected for a Nernstian diffusion limited redox reaction.<sup>325</sup> Moreover, the peak current density shows a linear dependence on the square root of the scan rate (Figures 5.3b and S8.3.5) which also indicates that the charge transfer of the redox process is controlled by the diffusion of charge carriers in the Fc-SURMOF, as described by the Randles-Sevcik equation.<sup>325–327</sup> Therefore, we infer that the current density is probably limited by the diffusion of counter-anions in the [100] ordered pores since the crystallites are highly oriented on the electrode surface, still possessing accessible porosity after introduction of the Fc moiety as supported by the evaluation of the pore volume (see section 2.4). This observation is similar to the aforementioned report for a Zn-MOF<sup>322</sup> but different from the report of crystalline HKUST-1 SURMOF,<sup>192</sup> where the electron hopping transfer through the Fc molecules was contributed to the electrochemical reaction. In addition, the CV measurement of the residual electrolyte solution confirms that there was no dissolution of the H<sub>2</sub>(bpdc-amide-Fc) linker, further validating that the redox reaction was attributed to the ferrocene moieties incorporated in the framework. Importantly, the Fc-SURMOF turned out to be stable during the CV measurements as attested by no significant crystallinity loss after the measurements (Figure S8.3.6).

However, a striking change in the electrochemical properties occurred for Me<sub>2</sub>Fc-SURMOF as almost no faradaic current was observed (Figure 5.3a). Moreover, a CV curve recorded using a ferrocene-containing electrolyte did show almost no faradaic current demonstrating that the Me<sub>2</sub>Fc-SURMOF is a closely packed insulating crystalline thin film (Figure S8.3.7).

The less accessible pore volume due to the presence of the Me<sub>2</sub>Fc moiety (see section 2.4) probably prevents the diffusion of counteranions through the framework and hence hinders the charge transfer.

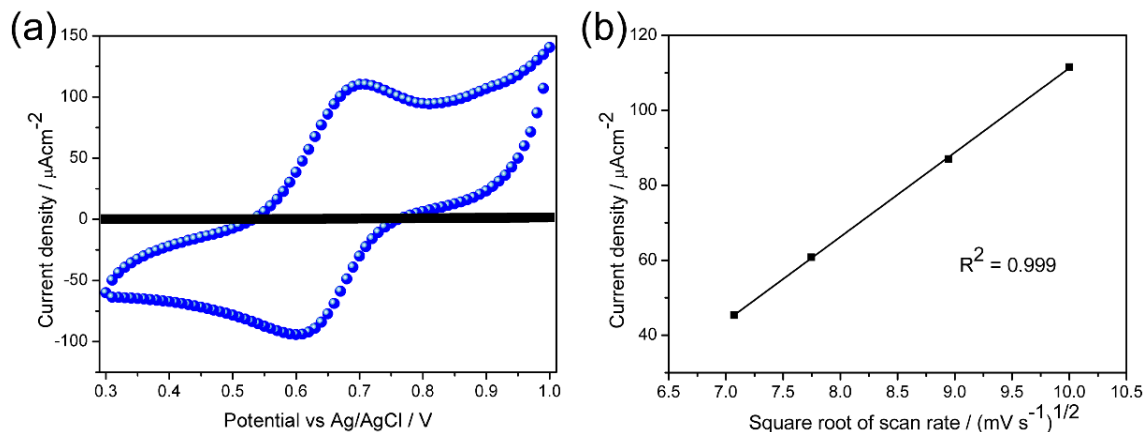


**Figure 5.3** (a) CVs of Fc- and Me<sub>2</sub>Fc-SURMOFs measured in 0.1 M Bu<sub>4</sub>NPF<sub>6</sub> in MeCN (scan rate: 100 mV/s; blue: Fc-SURMOF, 40 deposition cycles; black: Me<sub>2</sub>Fc-SURMOF, 40 deposition cycles); (b) The linear dependence of the current density vs the square root of the scan rates for Fc-SURMOF.

In order to further verify the diffusion limitation of charge transfer, the behaviors of very thin layers of Fc- and Me<sub>2</sub>Fc-SURMOFs were studied. In both cases, the redox peaks gradually become defined with increasing number of deposition cycles (from 1 to 3 cycles) as indicated in Figure 5.4. Interestingly, the peak currents (both anodic and cathodic) decrease linearly for Fc-SURMOF, while they decrease disorderly for Me<sub>2</sub>Fc-SURMOF with increasing number of deposition cycles. Considering that no crystallites are formed after 3-cycle growth (Figures S8.3.8 and S8.3.9), the LbL deposited redox-active linkers are attributed to the defined redox peaks. At the same time, the thicker film and thus the longer diffusion path with increasing number of deposition cycles causes the decrease of peak currents. Surprisingly, when the crystallites are formed on the surfaces, the CVs of Fc- and Me<sub>2</sub>Fc-SURMOFs show a vast difference (Figures S8.3.10 and S8.3.11). The CV curve of Fc-SURMOF exhibits defined redox peaks, while almost no faradaic current could be observed for Me<sub>2</sub>Fc-SURMOF, further confirming the pore-size limited charge transfer.

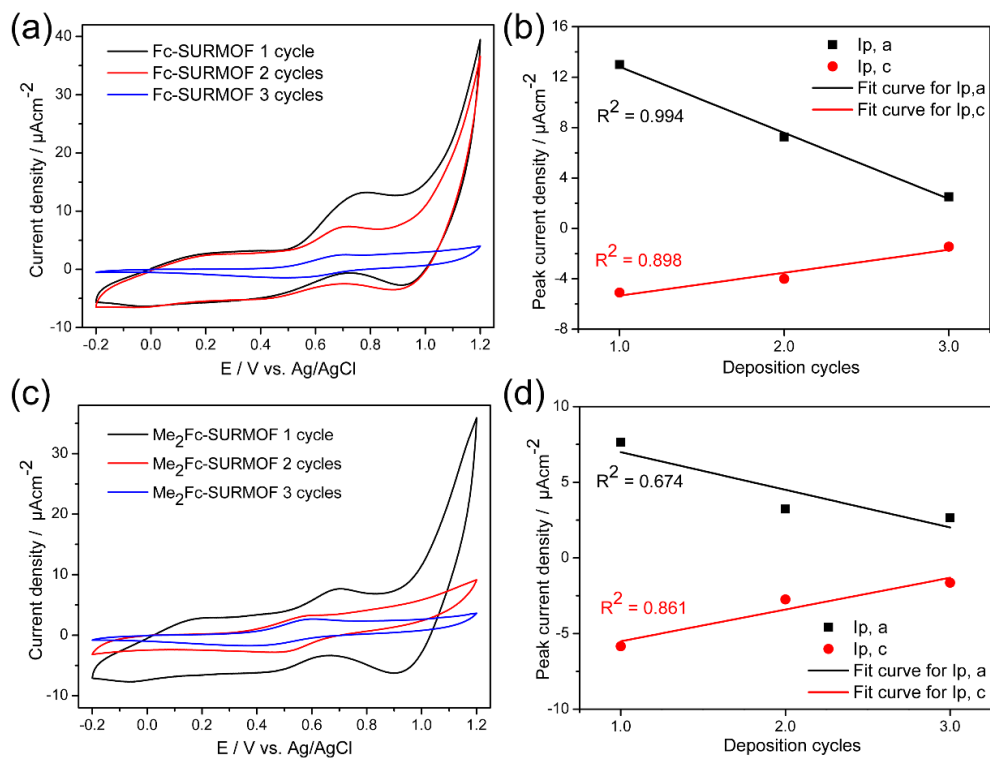


**Figure 5.4** Cyclic voltammograms of Fc-SURMOF (a) and Me<sub>2</sub>Fc-SURMOF (c) after different deposition cycles in 0.1 M Bu<sub>4</sub>NPF<sub>6</sub> in MeCN (scan rate: 100 mV/s); (b) and (d) Corresponding linear fit of the peak current vs the deposition cycles for Fc-SURMOF (b) and Me<sub>2</sub>Fc-SURMOF (d).

### 5.2.3 Electrochemical property tuning of the SURMOFs containing redox-active species

To illustrate the electrochemical tunability of the SURMOFs containing redox-active species, further CV experiments were carried out on different SURMOFs. As depicted in Figure 5.5c, a mixed-component SURMOF ([Cu<sub>2</sub>(bpdC-amide-Fc+bpdC-amide-Me<sub>2</sub>Fc)<sub>2</sub>(dabco)], mix-SURMOF, with a linker molar ratio of 1:1) with preferred [100] orientation and closely packed crystallites (see Figure S8.3.12) exhibits a medium current density (66  $\mu\text{A}/\text{cm}^2$ ) and a larger potential separation of 336 mV, compared to the pure Fc-SURMOF, which means the redox process is suppressed and only quasi-reversible. This might be due to the disordered charge transfer paths in the mix-SURMOF caused by the incorporation of the bulky H<sub>2</sub>(bpdC-amide-Me<sub>2</sub>Fc) linker. When the MOF-on-MOF strategy was applied, interesting behaviors were attained despite both MOF-on-MOF samples showed very high crystallinity and preferred [100] crystallite orientation (Figure 5.5a and b). The CV curve of Me<sub>2</sub>Fc-SURMOF on Fc-SURMOF sample clearly describes a mixed electrochemical behavior with a relatively low

current density ( $\sim 12 \mu\text{A}/\text{cm}^2$ ) and an irreversible redox process (Figure 5.5d, gray open circles). This observation reveals that only ferrocene moieties inside the bottom framework which are in proximity to the SAM@metal/SURMOF interface were oxidized and reduced since the upper layer was already demonstrated as an insulating crystalline layer. Surprisingly, no faradic current was recorded when the MOF layer order was inverted (Figure 5.5d, gray filled circles). The insulating  $\text{Me}_2\text{Fc}$ -SURMOF layer, which totally cuts off the charge transfer from the metal electrode to the upper ferrocene moieties, is supposed to be the reason. Thus the counteranions could not diffuse through the  $\text{Me}_2\text{Fc}$ -SURMOF layer and no faradic current was recorded. The above results clearly demonstrate that the electrochemical properties of the SURMOFs can be efficiently altered by the deposition of mix-SURMOF and MOF-on-MOF heterostructures.

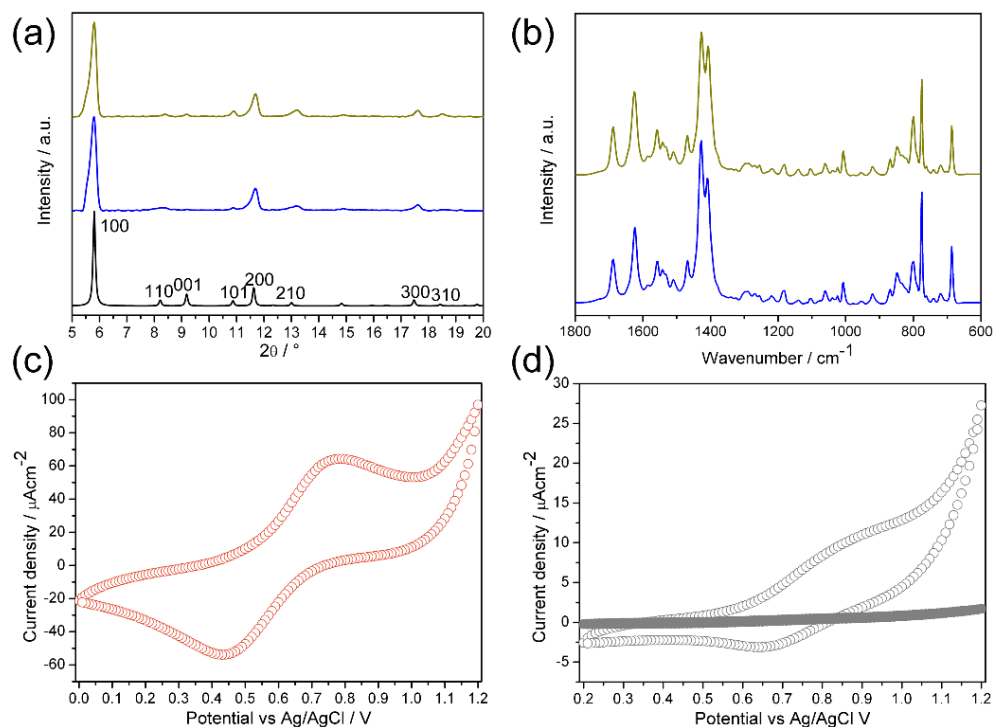


**Figure 5.5** XRD patterns (a) and IRRA spectra (b) of MOF-on-MOF SURMOFs grown at  $60^\circ\text{C}$  on PyzP1 surfaces (blue: 40 cycles of  $\text{Me}_2\text{Fc}$ -SURMOF on top of 40 cycles of Fc-SURMOF; yellow green: 40 cycles of Fc-SURMOF on top of 40 cycles of  $\text{Me}_2\text{Fc}$ -SURMOF). (c) and (d) CV curves of mix-SURMOF (c, 40 cycles, grown at  $60^\circ\text{C}$  on PyzP1 surfaces and the linker molar ratio is 1:1) and MOF-on-MOF SURMOFs (d, gray open circles: 40 cycles of  $\text{Me}_2\text{Fc}$ -SURMOF on top of 40 cycles of Fc-SURMOF; gray filled circles: 40 cycles of Fc-SURMOF on top of 40 cycles of  $\text{Me}_2\text{Fc}$ -SURMOF) in  $0.1 \text{ M Bu}_4\text{NPF}_6$  in MeCN (scan rate:  $100 \text{ mV/s}$ ).



### 5.3 Conclusions

In conclusion, we have demonstrated the LbL growth of a novel, exclusively [100] oriented ferrocene functionalized SURMOF (Fc-SURMOF) onto pyrazole-terminated surface. The Fc-SURMOF exhibits excellent electrochemical properties due to the reversible oxidation and reduction of ferrocene moieties. A diffusion controlled mechanism was proposed and the diffusion of counteranions in the accessible [100] oriented pores was regarded to limit the current. Interestingly, the electrochemical properties of the  $[\text{Cu}_2(\text{bpdc})_2(\text{dabco})]$  SURMOF could be successfully tuned by adjusting the accessible porosity of the framework employing bulky  $\text{Me}_2\text{Fc}$  moiety to functionalize the SURMOF. The resultant  $\text{Me}_2\text{Fc}$ -SURMOF with preferred [100] orientation was found to be a closely packed insulating crystalline layer since the counteranions could not diffuse through this layer and no extensive charge transfer was observed. Furthermore, the insulating  $\text{Me}_2\text{Fc}$ -SURMOF layer could be further employed to tune the electrochemical properties of mix-SURMOF and MOF-on-MOF heterostructures. Mix-SURMOF exhibits a medium current density and a larger potential separation, while the MOF-on-MOF heterostructures show totally inverse electrochemical behaviors.



## **6 Polyoxometalate loaded HKUST-1 (POM@HKUST-1) SURMOFs: POM dependent crystallite orientation and electrochemical application**

### 6.1 Introduction

Polyoxometalates (POMs) are a class of compounds constructed by three or more transition metal oxyanions, which possess abundant coordination sites on the oxygen-rich surface.<sup>328,329</sup> The intrinsic chemical properties of Keggin-type POMs, such as strong acidity and excellent redox properties, allow them for the application in a variety of scientific fields including catalysis, electronics and magnetics.<sup>328,330–333</sup> Nevertheless, the disadvantages of bulk POMs often limit their application, for example, in catalysis, because of the relatively small surface areas (typically  $<10\text{ m}^2\text{g}^{-1}$ ) of bulk POMs which usually hinder the access of reactants and thus lower the catalytic efficiency.

Recently, MOFs with high crystallinity and surface areas have been demonstrated to be suitable host matrices to encapsulate various POMs for specific applications, such as electrocatalysis and proton conductance.<sup>334–339</sup> However, in order to realize the applications, the POM encapsulated MOF powders are usually pressed into pellets (proton conductance) or deposited onto electrode surfaces (in the application of electrocatalysis) which usually lowers the electron transport efficiency and thus the properties. Bearing this in mind, highly oriented SURMOFs should be ideal supports to overcome the disadvantages.

Since HKUST-1 has been well established as a matrix for the encapsulation of a series of Keggin-type POMs,<sup>337</sup> in this work, we aimed to deposit POM-functionalized HKUST-1 SURMOFs (denoted as POM@HKUST-1 SURMOFs) by combining spin-coating with alcohol induced growth, which has exhibited advantages in the oriented growth of HKUST-1 SURMOFs because the film thickness and crystallite size could be tuned by simply controlling the number of spin-coating cycles and the vapor treatment time.<sup>62</sup> To this end, three different kinds of Keggin-type POMs, phosphotungstic acid (PTA), phosphomolybdic acid (PMA) and the tetrabutylammonium (TBA) salt of vanadium-substituted phosphomolybdate ( $((n\text{-Bu}_4\text{ N})_4\text{H}(\text{PMo}_{10}\text{V}_2\text{O}_{40}))$ , VPMo) were selected for the encapsulation. With the help of methanol vapor,

the three POMs were successfully encapsulated into the oriented HKUST-1 SURMOFs without leaching. Due to excellent catalytic and redox properties of Keggin POMs, POM@HKUST-1 SURMOFs open the opportunity of the application as electrocatalysts in the electrochemical devices. In addition, PTA@HKUST-1 SURMOF permits a selective adsorption of a cationic dye, methylene blue (MB), in contrast to two other cationic dyes, rhodamine B (RhB) and methyl violet (MV). Moreover, the MB filled PTA@HKUST-1 SURMOF shows enhanced electrochemical properties compared to the PTA@HKUST-1 SURMOF, demonstrating that the highly oriented POM@HKUST-1 SURMOFs are effective platforms for the loading of redox-active dyes for electrochemical applications.

## 6.2 Results and discussion

### 6.2.1 Growth and orientation tuning of POM@HKUST-1 SURMOFs

Figure 6.1 depicts out-of-plane XRD patterns of highly oriented POM@HKUST-1 SURMOFs on PPP1 surfaces. As can be seen in the Figure, PTA and PMA functionalized HKUST-1 SURMOFs exclusively orient along the [111] direction, showing (111), (222) and (333) diffraction peaks. The relative intensity of (111) and (222) diffraction peaks in PTA@HKUST-1 SURMOF is well in accordance with the simulated XRD pattern (Figure 6.1b and e). However, the relative intensity of those two peaks in PMA@HKUST-1 SURMOF exhibits a discrepancy compared to the simulated pattern (Figure 6.1c and f). Surprisingly, the VPMo@HKUST-1 SURMOF demonstrates a different crystallite orientation than the PTA@HKUST-1 SURMOF although the precursors are prepared in the same way (see section 2.5). With the addition of VPMo into the precursor, the SURMOF becomes highly oriented along the [100] direction. Compared to the simulated HKUST-1 pattern (Figure 6.1a), the intensity of (400) diffraction peak in the VPMo@HKUST-1 SURMOF becomes stronger (Figure 6.1g), indicating well-ordered incorporation of the VPMo POM into the HKUST-1 SURMOF. The orientation difference might be mainly ascribed to the special template effect of VPMo-POM. Due to the low solubility of VPMo in alcohols,<sup>292</sup> the VPMo precipitates much faster than the HKUST-1 crystallites and may serve as hard template for the [100] oriented growth of VPMo@HKUST-1 SURMOF.

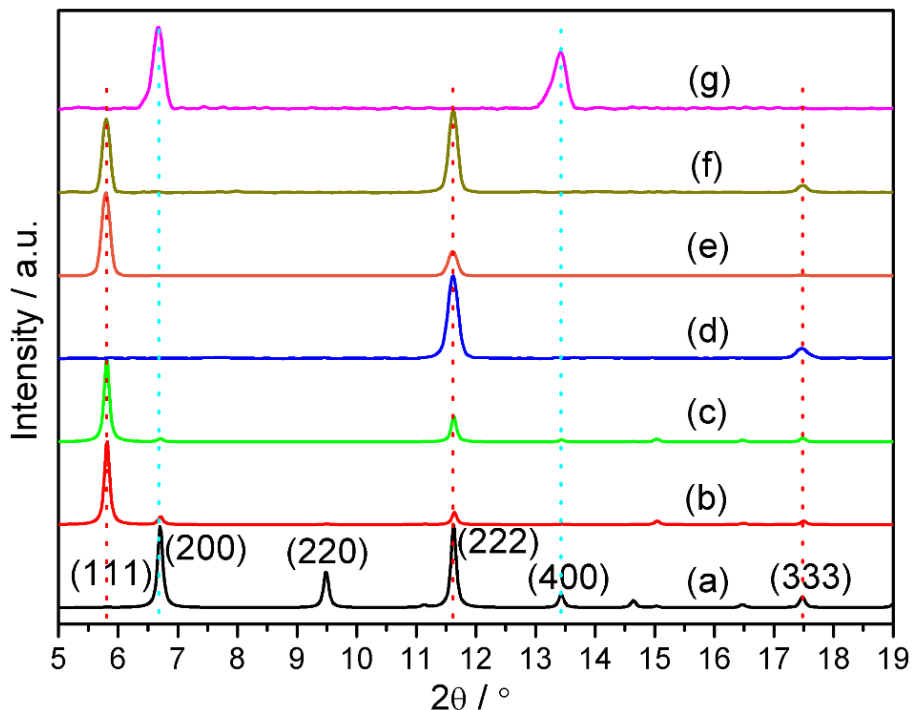


**Figure 6.1** Simulated XRD patterns of HKUST-1 (a), PTA@HKUST-1 (b), PMA@HKUST-1 (c) and out-of-plane XRD patterns of HKUST-1 (d), PTA@HKUST-1 (e), PMA@HKUST-1 (f), VPMo@ HKUST-1 (g) SURMOFs fabricated by combining spin coating (10 cycles) with methanol vapor induced growth at room temperature on PPP1 surfaces. The XRD pattern of VPMo@ HKUST-1 could not be simulated since the X-ray structure is not known yet.

The IRRA spectra of POM@HKUST-1 SURMOFs are depicted in Figure 6.2. Compared to the spectra of pure bulk POMs, we can see that the five characteristic POM vibrations<sup>292</sup> all appear in the IRRA spectra of POM@HKUST-1 SURMOFs (completely rinsed by ethanol and MeCN) as marked in the region I, II and III, which confirms that the Keggin-type POMs are well incorporated into HKUST-1 SURMOFs during the one-step methanol vapor induced growth process. Additionally, the IRRA spectra of the POM@HKUST-1 SURMOFs are all comparable to the one of pure HKUST-1 SURMOF which illustrates that the methanol vapor induced growth happened in all cases. As reported before,<sup>9</sup> HKUST-1 has two kinds of pore openings with the same ratio. The large pores with a diameter of 0.9 nm are quite suitable for the accommodation of the POMs due to a good match of sizes, while the small pockets with 0.46-nm-diameter windows cannot accommodate any POMs. The incorporation content of POMs was estimated by Total Reflection X-Ray Fluorescence Spectroscopy (TXRF). For

PTA@HKUST-1 SURMOF, the ratio of  $\text{Cu}^{2+}/\text{W}^{6+}$  is 1/1.14 (Table S8.4.1), which is close to the stoichiometric ratio of 1, demonstrating that there is a nearly full encapsulation of PTA units into the larger pores (see the model in Figure S8.4.1) in accordance with a previous report on bulk PTA@HKUST-1 material.<sup>337</sup>

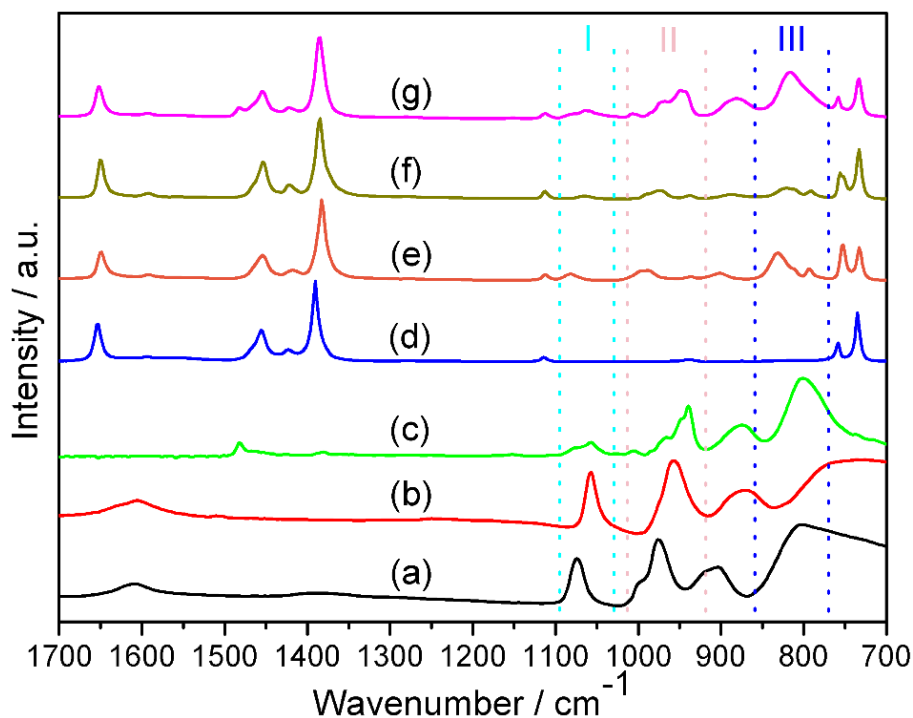


**Figure 6.2** FT-IR spectra of PTA (a), PMA (b), VPMo (c) and IRRA spectra of HKUST-1 (d), PTA@HKUST-1 (e), PMA@HKUST-1 (f), VPMo@HKUST-1 (g) SURMOFs fabricated by combining spin coating (10 cycles) and methanol vapor induced growth at room temperature on PPP1 surfaces. The regions of I, II and III signify the five characteristic POM vibrations.

### 6.2.2 Adsorption capacities and redox properties of POM@HKUST-1 SURMOFs

The adsorption capacities of POM@HKUST-1 SURMOFs for hazardous gases were evaluated by QCM due to its high sensitivity against mass change.<sup>246,258,260</sup> As shown in Figure 6.3, PTA@HKUST-1 SURMOF shows the highest uptake for ammonia and the lowest uptake for HCl. As already demonstrated by the TXRF measurements (Table S8.4.1), in PTA@HKUST-1 SURMOF, the large pores are occupied by the PTA molecules (around 50% of all the pores are occupied), only the small pores are free for the accommodation of guest molecules. Accordingly, the uptake of guest molecules should theoretically be halved in comparison to

the pure HKUST-1 SURMOF. Surprisingly, we find that only the uptake of HCl is halved, while the adsorption capacity of Cl<sub>2</sub> is almost the same as that of HKUST-1 reported in our previous publication.<sup>258</sup> The result indicates that PTA@HKUST-1 SURMOF exhibits higher selectivity towards chlorine and ammonia after functionalization with the Keggin-type PTA as compared to pure HKUST-1 SURMOFs. Moreover, the redox properties of POM@HKUST-1 SURMOFs were characterized by CV measurements. As depicted in Figure S8.4.2, after functionalization with corresponding POMs, new redox peaks appear in the CV curves of VPMo@HKUST-1 and PTA@HKUST-1 SURMOFs indicating the potential application of SURMOFs in electrochemical devices. For instance, VPMo@HKUST-1 SURMOF can be utilized as electrocatalyst to oxidize ascorbic acid (Figure S8.4.3) as supported by the threefold increase of the peak current after addition of ascorbic acid into the electrolyte during a SWV experiment.

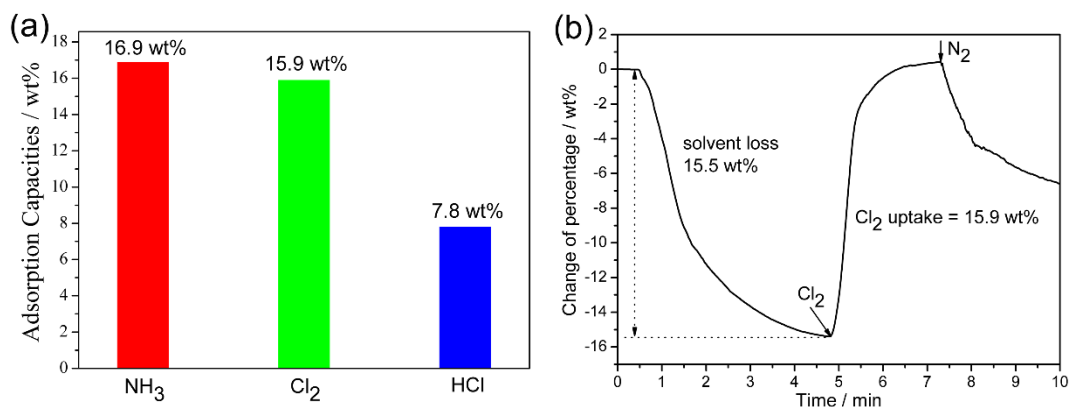


**Figure 6.3** (a) Adsorption capacities of PTA@HKUST SURMOF on QCM sensor for various gases; (b) Typical curve of PTA@HKUST SURMOF for Cl<sub>2</sub> adsorption.

### 6.2.3 Selective methylene blue (MB) dye loading and enhanced electrochemical properties of POM@HKUST-1 SURMOFs

POM functionalized MOFs have been documented as a highly effective dye scavenger.<sup>153,340</sup> Taken this into account, the application of POM@HKUST-1 SURMOFs was also evaluated by adsorption of cationic dyes. As shown in Figure 6.4, PTA@HKUST-1 SURMOF exhibits much better adsorption efficiency than the pure HKUST-1 SURMOFs as supported by the UV-Vis spectra and the color change. In addition, the adsorption capacities of PTA@HKUST-1

SURMOF towards the three dyes show a difference. After 12 h, the adsorption percentage (calculated by the integral of UV-Vis spectra of the dye solutions before and after SURMOF immersion) of MB can reach 100% (Figure 6.4b), while the adsorption percent of MV and RhB is 95% and 90%, respectively (Figure 6.4c and d).

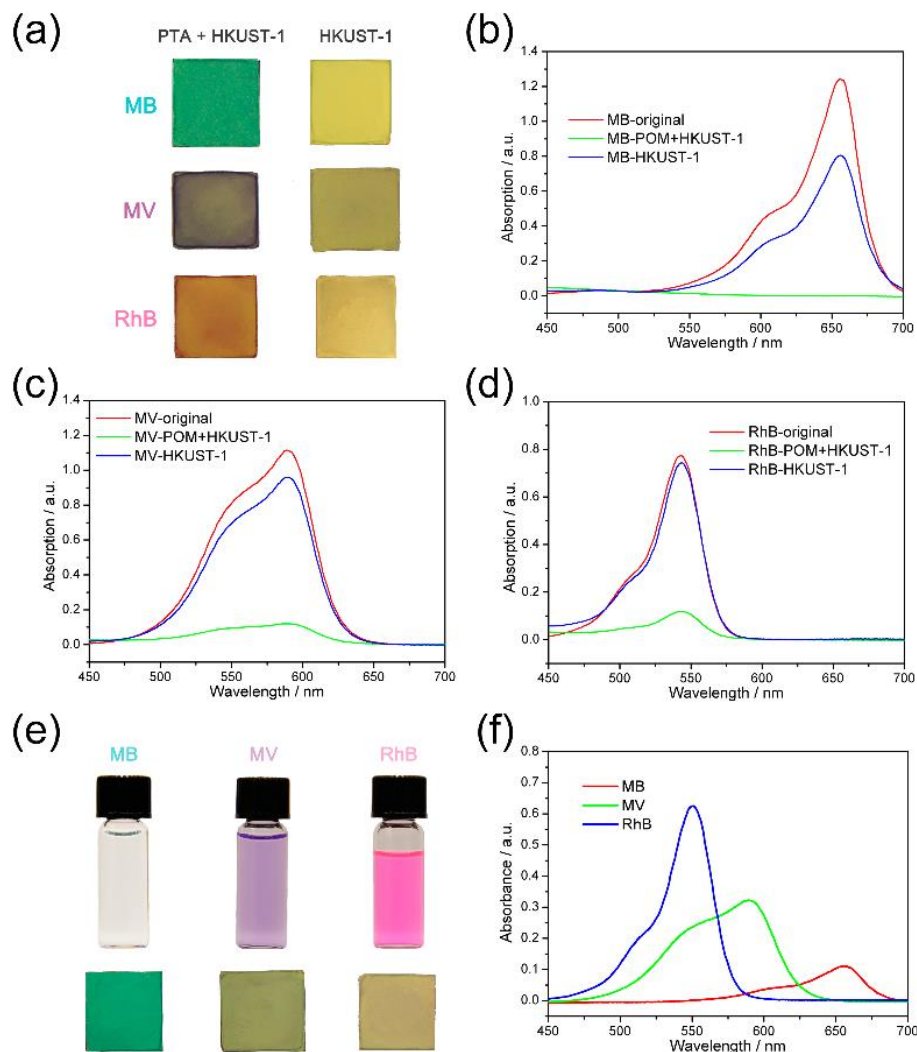


**Figure 6.4** (a) Color differences of PTA@HKUST-1 (left) and HKUST-1 (right) SURMOFs after being soaked in the ethanolic solutions of MB, MV and RhB (the concentrations were 4 mg/L); (b), (c) and (d) Corresponding UV-Vis spectra of the solutions; (e) Color differences of cationic dye loaded PTA@HKUST-1 SURMOFs after soaking in 0.025 M NH<sub>4</sub>Cl ethanol-water solution (the volume ratio of ethanol/water is 160); (f) Corresponding UV-Vis spectra of the solutions.

Surprisingly, desorption of the three dyes also varied (Figure 6.4e and f). After being soaked in 0.025 M NH<sub>4</sub>Cl ethanol-water solution (the volume ratio of ethanol/water is 160), the



desorption of RhB is the fastest and nearly all the dye molecules are desorbed within 1 min, while it takes at least 30 min for MV and the MB molecules are almost not desorbed even after 24 h (Figure 6.4e). The different effects on dye adsorption/ desorption of POM@HKUST-1 SURMOFs can mainly ascribed to the structure properties of POMs and dye molecules. Firstly, POMs are a kind of hydrophilic metal-oxo cluster compounds. Incorporation of POMs improves the hydrophilic property of SURMOF and allows the free access of the hydrophilic dye molecules.<sup>340</sup> Secondly, the negatively charged POMs, which are encapsulated in the neutral framework, can strongly interact with the positive charges of cationic dyes. Therefore, the PTA@HKUST-1 SURMOF with reduced pore volume exhibits a higher dye uptake capacity than the HKUST-1 SURMOF with its large pores. However, adsorption capacity and desorption properties of PTA@HKUST-1 SURMOF are mainly determined by the molecular size of the dye molecules. MB molecules are small enough for free access, while the large molecular volumes of MV and RhB molecules result in a steric hindrance between dye molecules and the active adsorption sites on PTA@HKUST-1 SURMOF. Therefore, the PTA@HKUST-1 SURMOF illustrates a selective adsorption of MB over the other two cationic dyes (MV and RhB). As illustrated in Figure S8.4.4, PTA@HKUST-1 SURMOF shows selective adsorption of MB and MV from MB-MV-RhB and MV-RhB mixtures, respectively. Similarly, almost no desorption of MB dye molecules was observed for the MB loaded PTA@HKUST-1 SURMOF, which indicates that the PTA@HKUST-1 SURMOF can selectively hold the MB dye molecules inside the oriented pores.

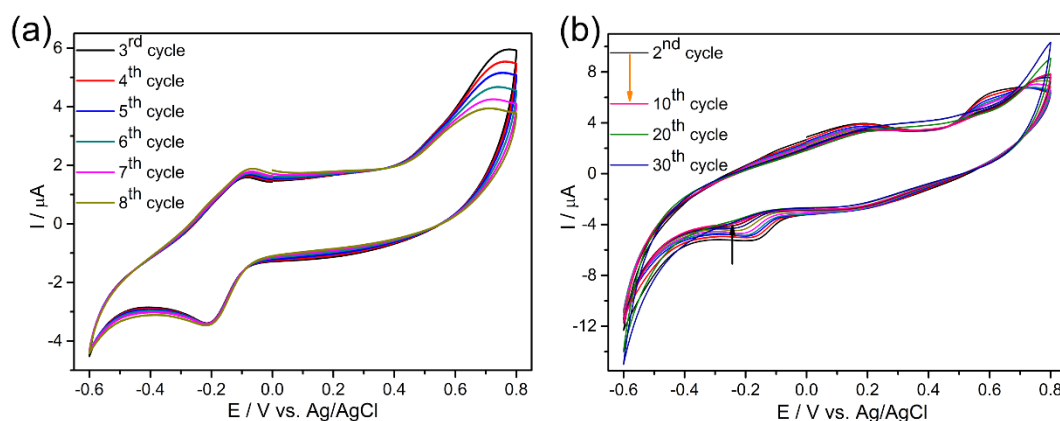


**Figure 6.5** CV measurements of PTA@HKUST-1 SURMOF loaded with MB dye without (a) and with (b) UV irradiation measured in 0.1 M  $\text{Bu}_4\text{NPF}_6$  in MeCN (scan rate: 100 mV/s).

Inspired by the strong interaction between PTA@HKUST-1 SURMOF and MB dye, the redox properties of MB loaded PTA@HKUST-1 SURMOF were studied. As indicated in Figure 6.5a, the CVs of PTA@HKUST-1 SURMOF with MB loading show defined redox peaks at around -0.22 V and -0.08 V which belong to the MB molecules (Figure S8.4.5). Furthermore, there is no MB leaching even after 10 cycles, illustrating the binding between the SURMOF and MB dye is very strong. In contrast, if the CV measurements are performed under UV irradiation, the MB molecules are released gradually during the measurements (Figure 6.5b) due to the degradation effect of PTA-POM under UV light. Moreover, after release of the MB molecules, the PTA@HKUST-1 SURMOF can be reused for MB loading indicating the reusability of SURMOF platform for dye loading

### 6.3 Conclusions

In conclusion, we have shown that highly oriented POM@HKUST-1 SURMOFs with high efficiency of POM loading were fabricated combining the spin-coating technique and methanol vapor induced growth. The crystallite orientation of the SURMOFs could be tuned by altering the category of POM and no POM leaching was observed. The POM@HKUST-1 SURMOFs demonstrated the potential application as electrocatalyst in electrochemical devices due to the excellent redox property of Keggin-type POMs. In addition, the POM@HKUST-1 SURMOFs could also be employed as an ideal platform for the selective loading of MB dye with high efficiency as demonstrated by PTA@HKUST-1 SURMOF. Remarkably, the MB dye could not be desorbed by ion exchange because of the strong binding between the dye molecules and the framework. Additionally, MB loaded PTA@HKUST-1 SURMOF showed reliable redox properties under inert condition, further illustrating the potential application of SURMOF in electrochemical devices. Moreover, MB dye could be released by UV irradiation during the CV measurements.

## 7 Summary

This thesis mainly discusses the LbL and spin-coating controlled deposition and potential application of SURMOFs. Various parameters during the growth process, such as surface chemistry, deposition temperature and functionalities, were finely tuned to fabricate highly oriented SURMOFs with high quality. Moreover, several applications of SURMOFs, such as chemical and electrochemical sensing were explored.

By employing a semi-rigid dicarboxylate linker of H<sub>2</sub>(sdb), the applicability of LbL protocol was successfully broadened to a 2D interdigitated [M<sub>2</sub>L<sub>2</sub>P] system with low symmetry. The novel growth mode of [Cu<sub>2</sub>(sdb)<sub>2</sub>(bipy)] SURMOFs on SAM-functionalized surfaces was demonstrated. Instead of the surface template, the effects of temperature-induced ripening and minimization of surface energies dominate the growth of SURMOFs. Low temperatures (below 40 °C) usually cause the growth of highly oriented [Cu<sub>2</sub>(sdb)<sub>2</sub>(bipy)] SURMOFs with exclusive [010] orientation either on monodentate pyridyl- or bidentate carboxyl-terminated surfaces, while SURMOFs with a mixture of [010] and [001] orientations are obtained at high temperatures (40-65 °C). In addition, the pore-orientation dependent adsorption capacities of such oriented SURMOFs were evaluated by QCM. The results demonstrate that the quality of both the pores and their openings are independent of the crystallite orientation, and thus the deposition temperature.

Combining the LbL growth with the mixed-linker approach, MTV-SURMOFs containing up to five dicarboxylate linkers were successfully deposited onto pyridyl-terminated surfaces. The linker *pK<sub>a</sub>* effect on the orientation of multifunctional [Cu<sub>2</sub>Lm<sub>2</sub>(dabco)] SURMOFs was systematically investigated. Through controlling the categories, quantities and molar ratios of mixed linkers, the quality of [001] orientation in [Cu<sub>2</sub>Lm<sub>2</sub>(dabco)] SURMOFs was precisely controlled. The linker mixtures with relatively high *pK<sub>a</sub>* values promote the growth of exclusively [001] oriented [Cu<sub>2</sub>Lm<sub>2</sub>(dabco)] SURMOFs, whereas mis-oriented SURMOFs (with unexpected [100] orientation) are obtained when the growth solutions contain linkers with lower *pK<sub>a</sub>* values. Additionally, by varying the molar ratios of linkers in the H<sub>2</sub>(bdc)-H<sub>2</sub>(f<sub>4</sub>bdc) ligand mixture, the adsorption capacities and selectivities of [Cu<sub>2</sub>{(bdc)<sub>x</sub>+(f<sub>4</sub>bdc)<sub>1-x</sub>}]<sub>2</sub>(dabco) (0 ≤ x ≤ 1) SURMOFs towards benzene and hexafluorobenzene were tunable.

Through the functionalization of the H<sub>2</sub>(bpdc) linker with Fc and Me<sub>2</sub>Fc moieties, highly oriented SURMOFs containing redox-active species were stepwise LbL deposited onto the pyrazole-terminated surfaces. Interestingly, the pyrazole termination was found to be the key for the high crystallinity and the exclusive [100] orientation of [Cu<sub>2</sub>(bpdc-amide-Fc)<sub>2</sub>(dabco)] SURMOF (Fc-SURMOF). Nevertheless, further investigation is needed for understanding the mechanism. Due to the reversible oxidation and reduction of Fc moieties in the oriented pores, the exclusively [100] oriented Fc-SURMOF exhibits excellent electrochemical properties, while no apparent charge transfer could be observed for the [Cu<sub>2</sub>(bpdc-amide-Me<sub>2</sub>Fc)<sub>2</sub>(dabco)] SURMOF (Me<sub>2</sub>Fc-SURMOF). Based on these results, a pore-size dependent charge transfer mechanism was proposed and the diffusion of counteranions in the exclusively [100] oriented pores was regarded to limit the current. Moreover, the electrochemical properties of mix-SURMOF and MOF-on-MOF heterostructures were successfully tuned by employing the insulating Me<sub>2</sub>Fc-SURMOF crystalline layer.

When replacing the LbL deposition protocol by spin-coating, a series of POM@HKUST-1 SURMOFs with certain crystallite orientation were grown onto pyridyl-terminated surfaces combined with methanol induced growth. No POM leaching was observed and the crystallite orientation of the POM@HKUST-1 SURMOFs could be tuned by altering the POM category. Due to the excellent redox properties of Keggin-type POMs, the POM@HKUST-1 SURMOFs could be employed in the electrochemical devices. Furthermore, with the loading of methylene blue (MB) into the PTA@HKUST-1 SURMOF, the redox properties were greatly enhanced and no dye release was observed during the CV measurements. In contrast, under UV irradiation, the MB dye becomes released during the CV measurements and the recovered SURMOF can be reused for dye loading.

## 8 Appendix

### 8.1 Appendix of chapter 3

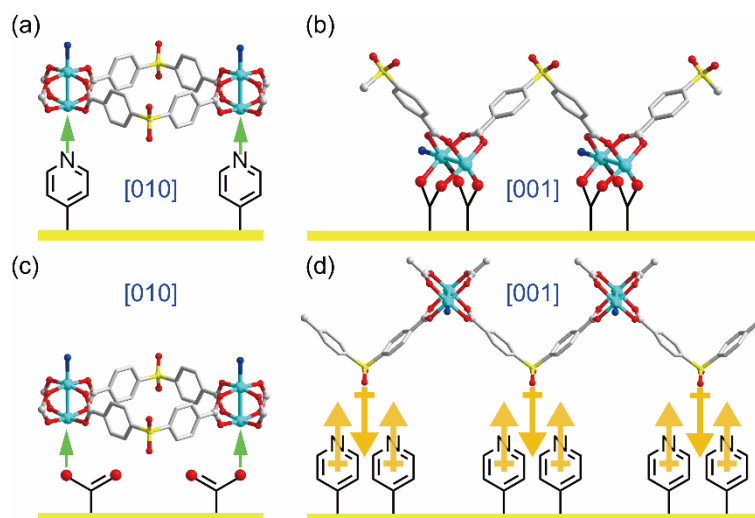


**Figure S8.1.1** Possible binding modes for  $[\text{Cu}_2(\text{sdb})_2(\text{bipy})]$  onto pyridyl-terminated (a, d) and carboxyl-terminated SAMs (b, c). The green arrows show coordinative binding, while the orange arrows suggest dipolar interactions as driving forces.

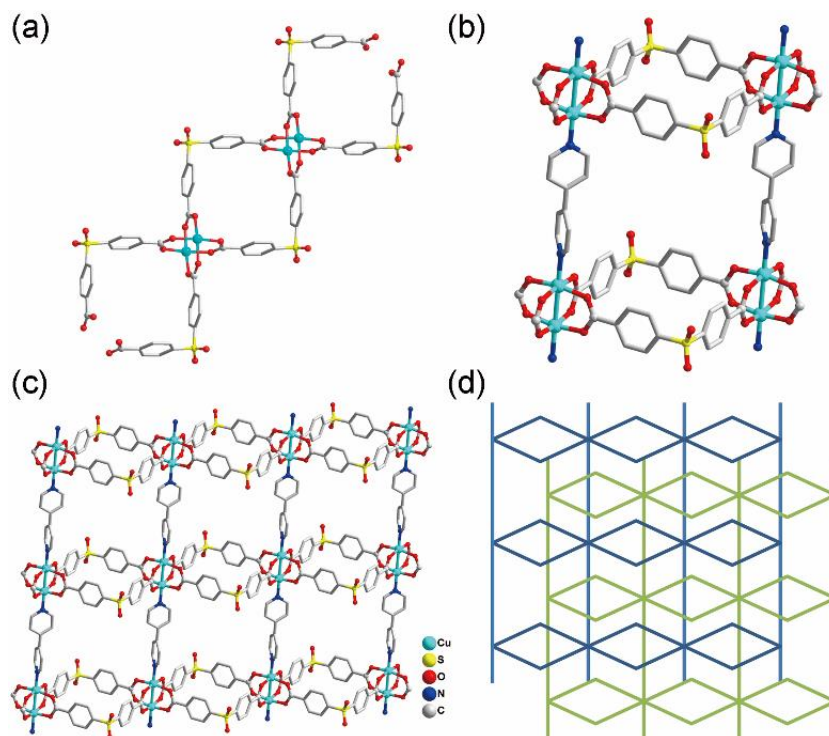


**Figure S8.1.2** Crystallographic structure of  $[\text{Cu}_2(\text{sdb})_2(\text{bipy})]$ ; (a) 1D double chain; (b) coordination unit; (c) 2D sheet and (d) interdigitated framework.

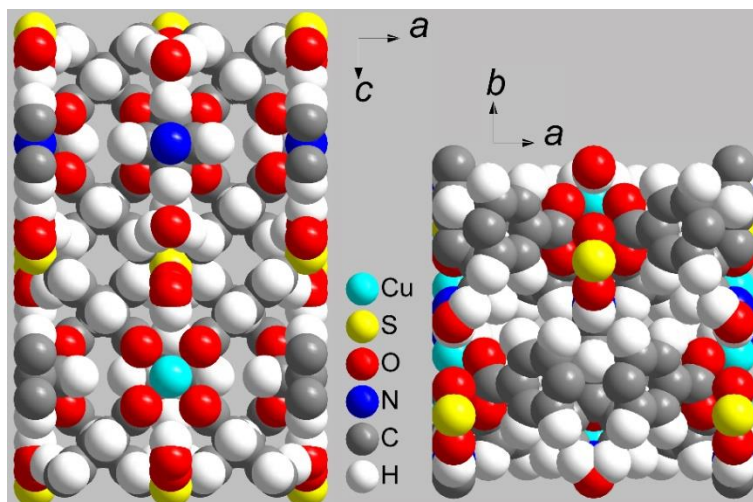


**Figure S8.1.3** Space-filling modes of  $[\text{Cu}_2(\text{sdb})_2(\text{bipy})]$  MOF system along the  $[010]$  (left) and the  $[001]$  (right) directions.

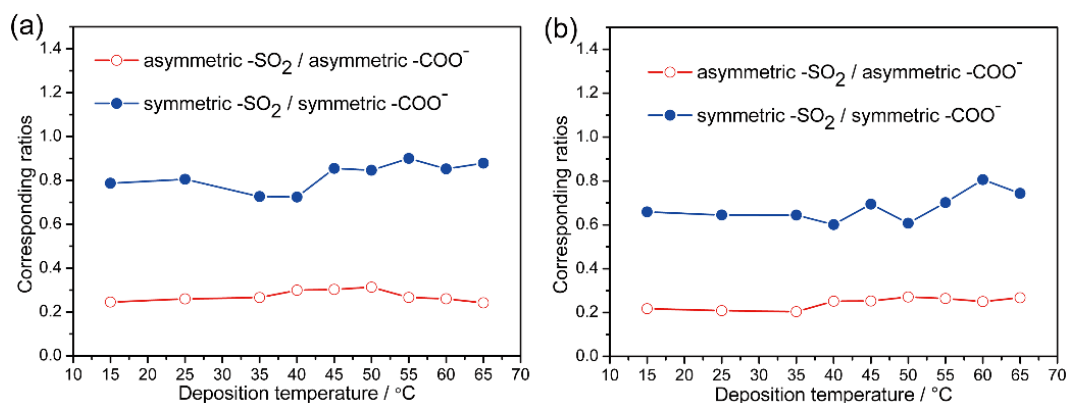


**Figure S8.1.4** Intensity ratios of asymmetric  $-\text{SO}_2$  to asymmetric  $-\text{COO}^-$  and symmetric  $-\text{SO}_2$  to symmetric  $-\text{COO}^-$ , respectively, for 40 cycles SURMOFs grown on PPP1 (a) and MTCA (b) surfaces.

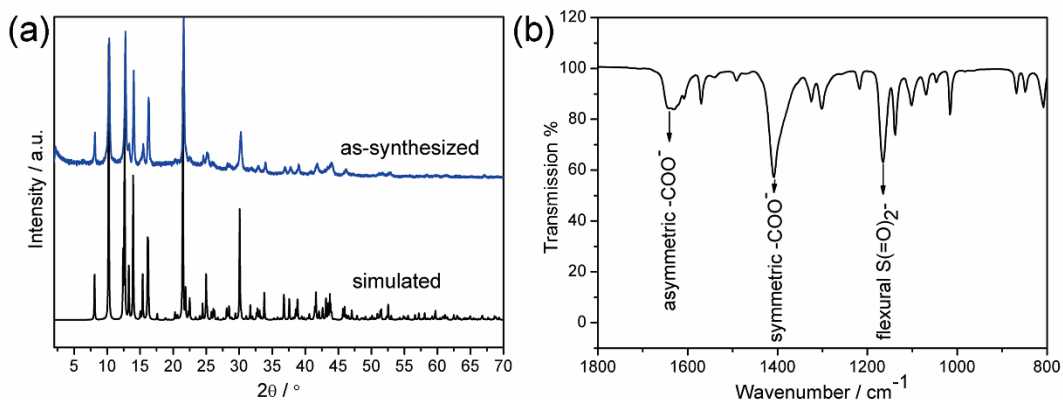


**Figure S8.1.5** (a) XRD powder pattern of bulk  $[\text{Cu}_2(\text{sdb})_2(\text{bipy})]$  MOF; (b) bulk FT-IR spectrum of  $[\text{Cu}_2(\text{sdb})_2(\text{bipy})]$  MOF, recorded with an ATR unit.

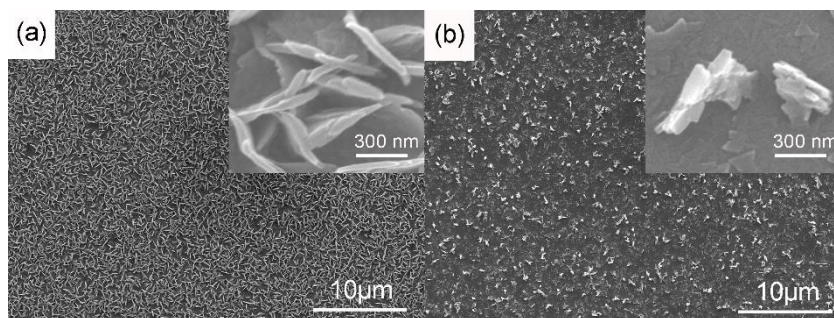


**Figure S8.1.6** SEM images of SURMOF<sub>010</sub> (a) and SURMOF<sub>001</sub> (b) thin films on PPP1 functionalized QCM electrodes.

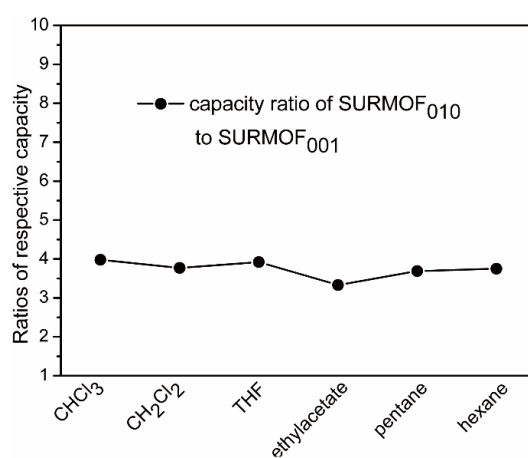


**Figure S8.1.7** Adsorption capacity ratios of SURMOF<sub>010</sub> to SURMOF<sub>001</sub> towards various VOCs.

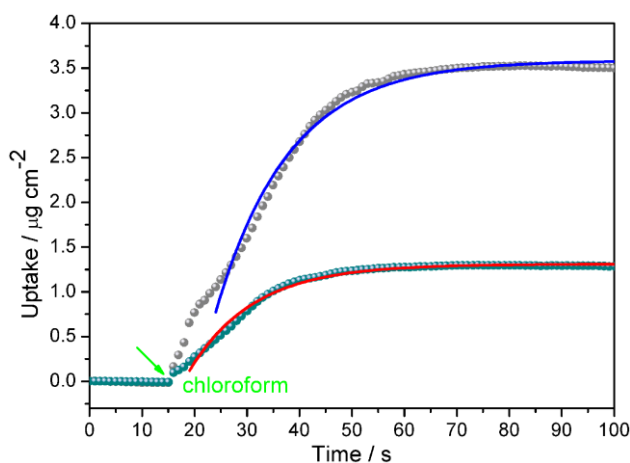


**Figure S8.1.8** Chloroform uptake by SURMOF<sub>010</sub> (gray line) and SURMOF<sub>001</sub> (navy blue line); the blue line and red line are the corresponding fits with the exponential decay function ( $m(t)=m_{eq}(1-\exp(-t/\tau))^{305}$ ), respectively. Where a time constant of  $\tau = l^2/3D + 1/\alpha$ ,  $l$  denotes the film thickness,  $D$  is the (transport) diffusivity,  $\alpha$  is surface permeability,  $m_{eq}$  is the equilibrium loading and  $t$  is the time. Neglecting the surface barriers, the diffusion coefficient ( $D$ ) can be estimated.

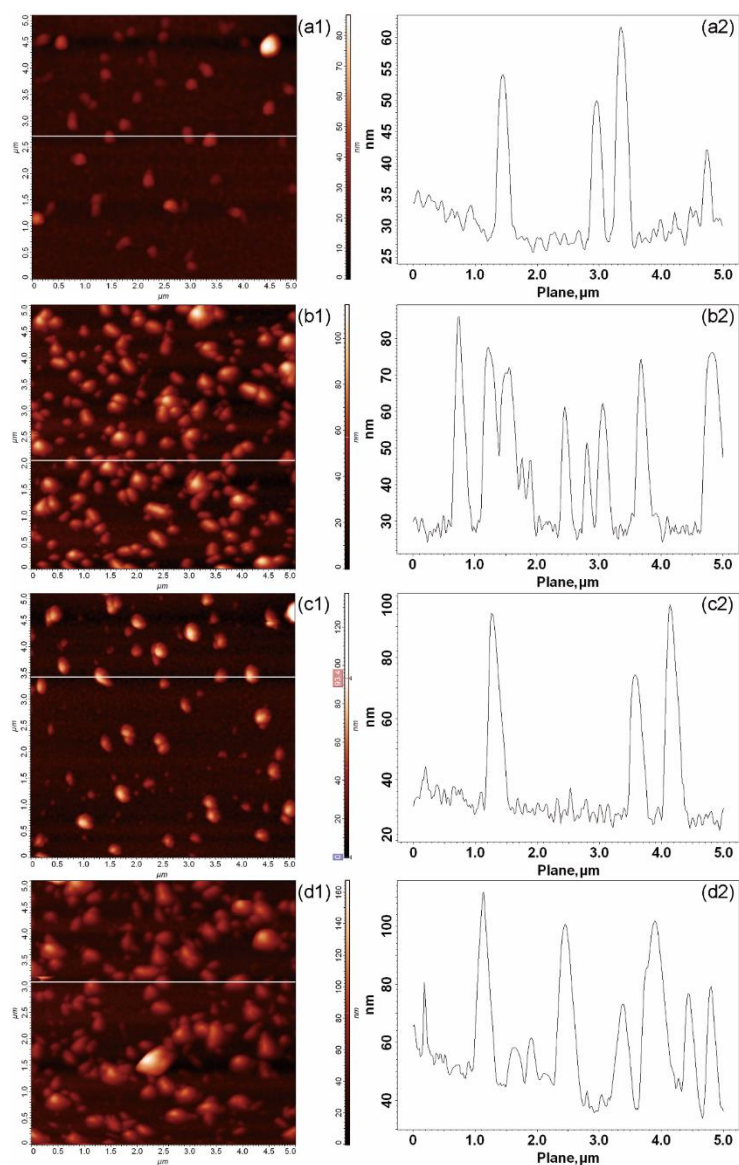


**Figure S8.1.9** Representative AFM data (images and line scans) for the SURMOFs deposited for 1 cycle onto PPP1 SAM at 15 °C (a), PPP1 SAM at 55 °C (b), MTCA SAM at 15 °C (c), and MTCA SAM at 55 °C (d). Representative line scans are given in (a2)-(d2), the results are statistically summarized in Table S8.1.1.

**Table S8.1.1** Average width-to-height of the crystals formed after the first deposition cycle as determined by AFM (Figure S8.1.9). The numbers in parentheses gives the numbers of crystals used for the statistics.

Temperature	Surface Chemistry	
	MTCA	PPP1
15 °C	$4.6 \pm 1.5$ (8)	$10 \pm 4$ (6)
55 °C	$4.2 \pm 0.9$ (11)	$4.2 \pm 1.0$ (14)



## 8.2 Appendix of chapter 4

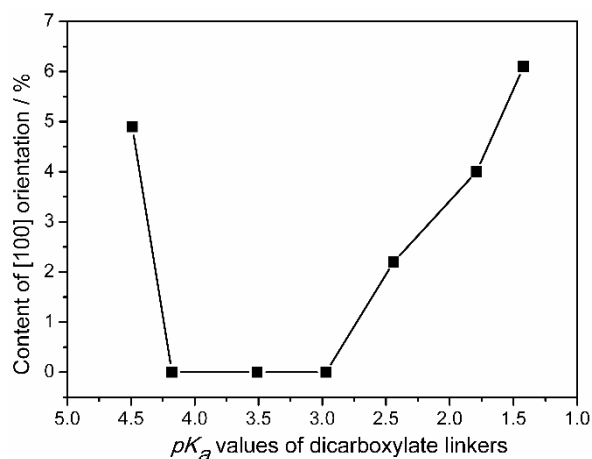


**Figure S8.2.1** The [100] orientation content as a function of linker  $pK_a$  values for single-linker containing  $[\text{Cu}_2\text{L}_2(\text{dabco})]$  SURMOFs grown at 60 °C on PPP1 surfaces as calculated from XRD data.

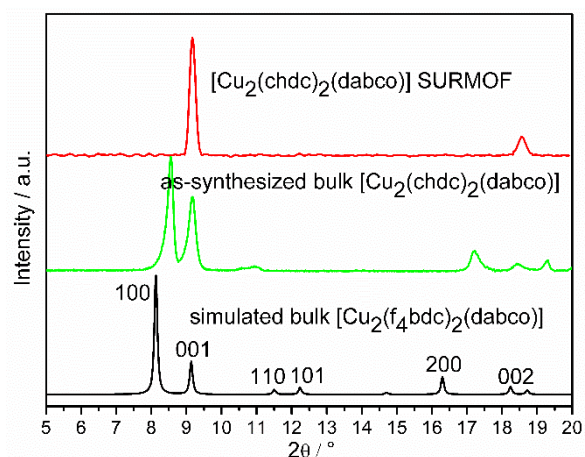


**Figure S8.2.2** XRD patterns of  $[\text{Cu}_2(\text{chdc})_2(\text{dabco})]$  bulk powder and SURMOF.

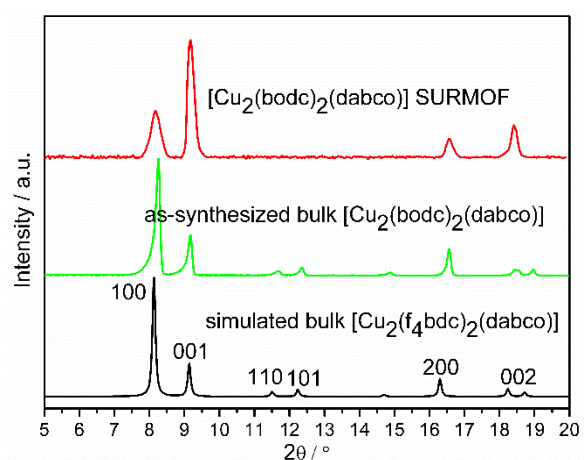


**Figure S8.2.3** XRD patterns of  $[\text{Cu}_2(\text{bodc})_2(\text{dabco})]$  bulk powder and SURMOF.

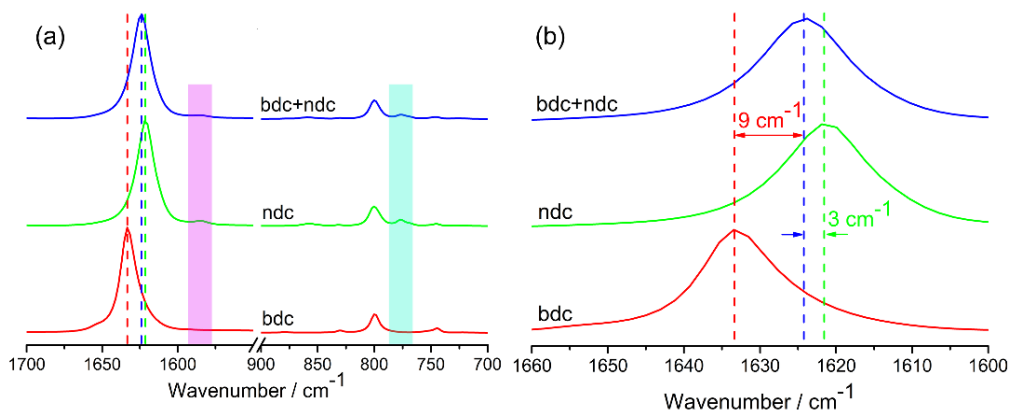


**Figure S8.2.4** IRRA spectra of  $[\text{Cu}_2(\text{bdc}+\text{ndc})_2(\text{dabco})]$ ,  $[\text{Cu}_2(\text{bdc})_2(\text{dabco})]$  and  $[\text{Cu}_2(\text{ndc})_2(\text{dabco})]$  SURMOFs.

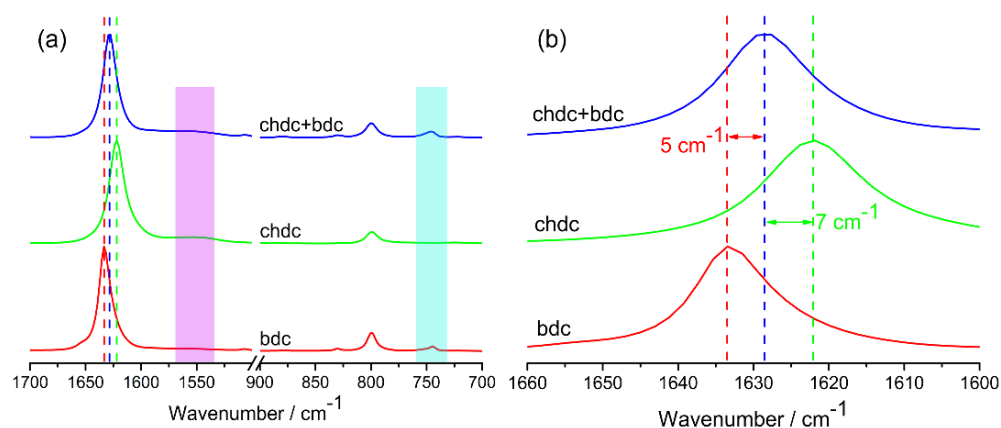


**Figure S8.2.5** IRRA spectra of  $[\text{Cu}_2(\text{chdc}+\text{bdc})_2(\text{dabco})]$ ,  $[\text{Cu}_2(\text{chdc})_2(\text{dabco})]$  and  $[\text{Cu}_2(\text{bdc})_2(\text{dabco})]$  SURMOFs.

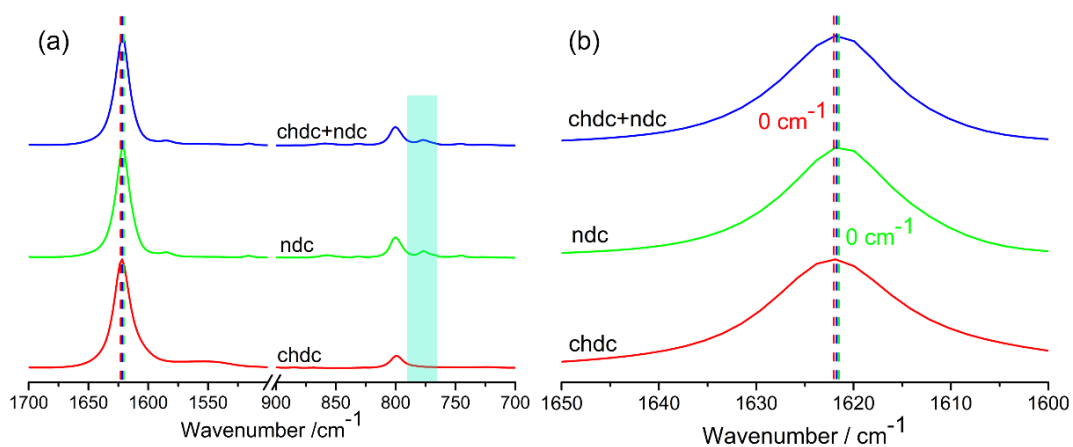


**Figure S8.2.6** IRRA spectra of  $[\text{Cu}_2(\text{chdc}+\text{ndc})_2(\text{dabco})]$ ,  $[\text{Cu}_2(\text{chdc})_2(\text{dabco})]$  and  $[\text{Cu}_2(\text{ndc})_2(\text{dabco})]$  SURMOFs.

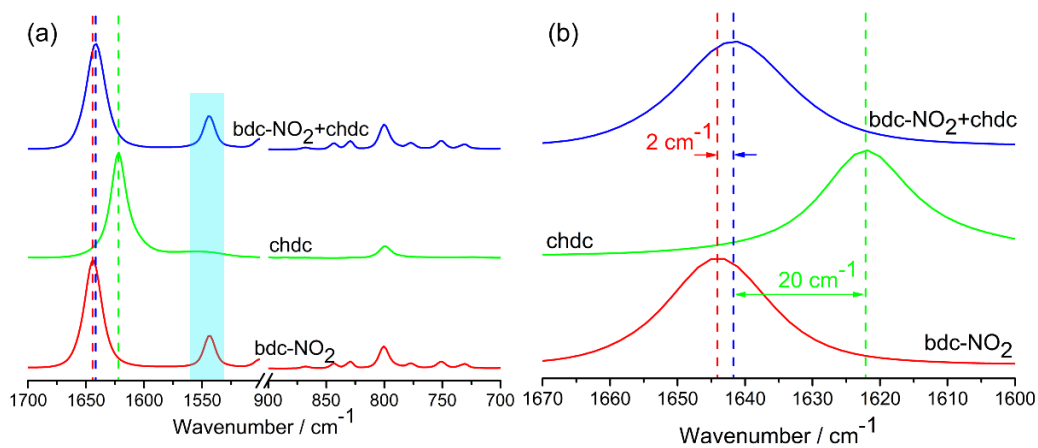


**Figure S8.2.7** IRRA spectra of  $[\text{Cu}_2(\text{bdc-NO}_2+\text{chdc})_2(\text{dabco})]$ ,  $[\text{Cu}_2(\text{bdc-NO}_2)_2(\text{dabco})]$  and  $[\text{Cu}_2(\text{chdc})_2(\text{dabco})]$  SURMOFs.

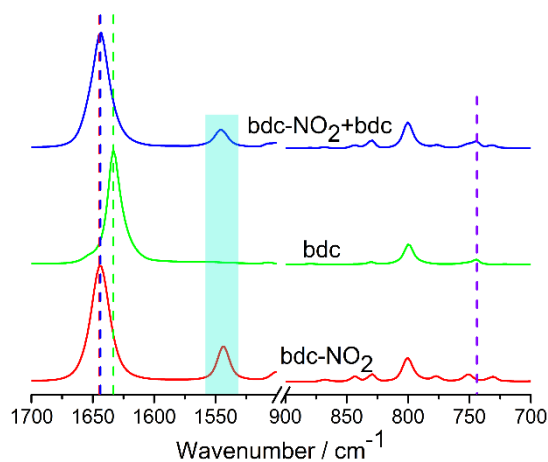


**Figure S8.2.8** IRRA spectra of  $[\text{Cu}_2(\text{bdc-NO}_2+\text{bdc})_2(\text{dabco})]$ ,  $[\text{Cu}_2(\text{bdc-NO}_2)_2(\text{dabco})]$  and  $[\text{Cu}_2(\text{bdc})_2(\text{dabco})]$  SURMOFs.

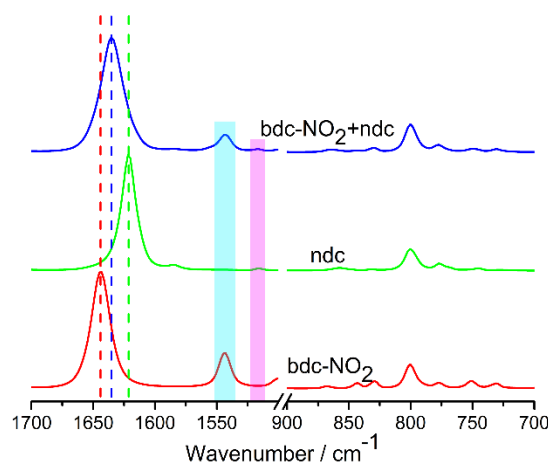


**Figure S8.2.9** IRRA spectra of  $[\text{Cu}_2(\text{bdc-NO}_2+\text{ndc})_2(\text{dabco})]$ ,  $[\text{Cu}_2(\text{bdc-NO}_2)_2(\text{dabco})]$  and  $[\text{Cu}_2(\text{ndc})_2(\text{dabco})]$  SURMOFs.

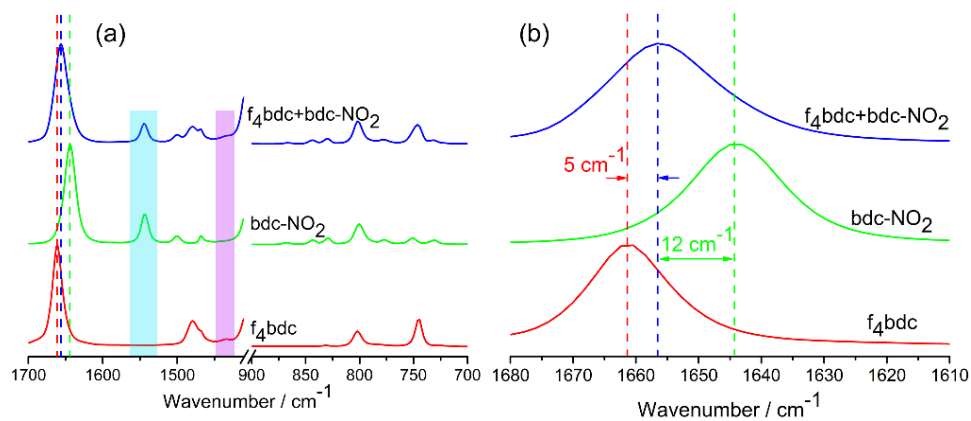


**Figure S8.2.10** IRRA spectra of  $[\text{Cu}_2(\text{f}_4\text{bdc}+\text{bdc-NO}_2)_2(\text{dabco})]$ ,  $[\text{Cu}_2(\text{f}_4\text{bdc})_2(\text{dabco})]$  and  $[\text{Cu}_2(\text{bdc-NO}_2)_2(\text{dabco})]$  SURMOFs.

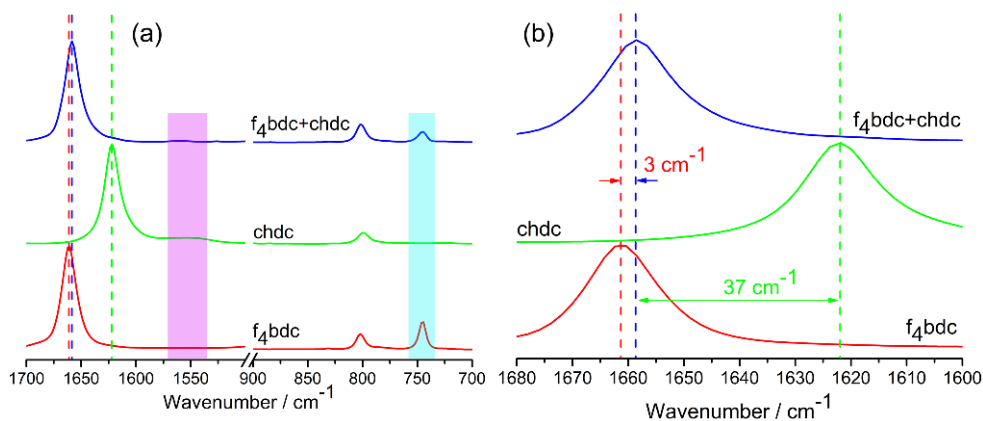


**Figure S8.2.11** IRRA spectra of  $[\text{Cu}_2(\text{f}_4\text{bdc}+\text{chdc})_2(\text{dabco})]$ ,  $[\text{Cu}_2(\text{f}_4\text{bdc})_2(\text{dabco})]$  and  $[\text{Cu}_2(\text{chdc})_2(\text{dabco})]$  SURMOFs.

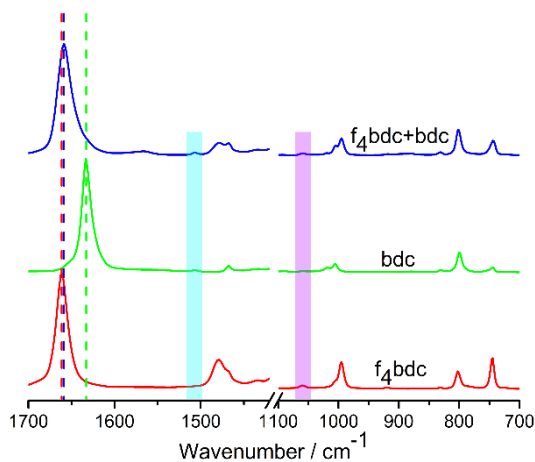


**Figure S8.2.12** IRRA spectra of  $[\text{Cu}_2(\text{f}_4\text{bdc}+\text{bdc})_2(\text{dabco})]$ ,  $[\text{Cu}_2(\text{f}_4\text{bdc})_2(\text{dabco})]$  and  $[\text{Cu}_2(\text{bdc})_2(\text{dabco})]$  SURMOFs.

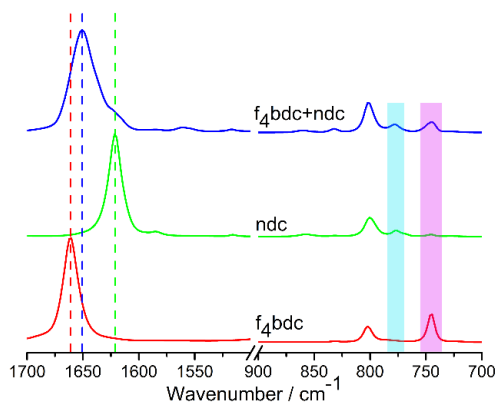


**Figure S8.2.13** IRRA spectra of  $[\text{Cu}_2(\text{f}_4\text{bdc}+\text{ndc})_2(\text{dabco})]$ ,  $[\text{Cu}_2(\text{f}_4\text{bdc})_2(\text{dabco})]$  and  $[\text{Cu}_2(\text{ndc})_2(\text{dabco})]$  SURMOFs.

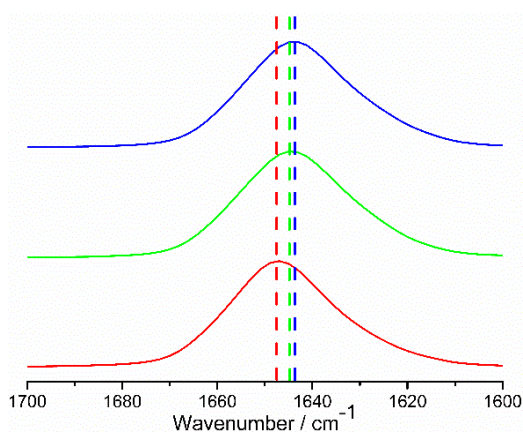


**Figure S8.2.14** Magnified IRRA spectra of  $[\text{Cu}_2\text{Lm}_2(\text{dabco})]$  SURMOFs with 3 (red), 4 (green) and 5 (blue) dicarboxylate linkers grown at  $60\text{ }^\circ\text{C}$  on PPP1 surfaces (3 linkers =  $\text{H}_2(\text{f}_4\text{bdc}) + \text{H}_2(\text{bdc-NO}_2) + \text{H}_2(\text{ndc})$ ; 4 linkers =  $\text{H}_2(\text{f}_4\text{bdc}) + \text{H}_2(\text{bdc-NO}_2) + \text{H}_2(\text{ndc}) + \text{H}_2(\text{bdc})$ ; 5 linkers =  $\text{H}_2(\text{f}_4\text{bdc}) + \text{H}_2(\text{bdc-NO}_2) + \text{H}_2(\text{ndc}) + \text{H}_2(\text{bdc}) + \text{H}_2(\text{chdc})$ ).

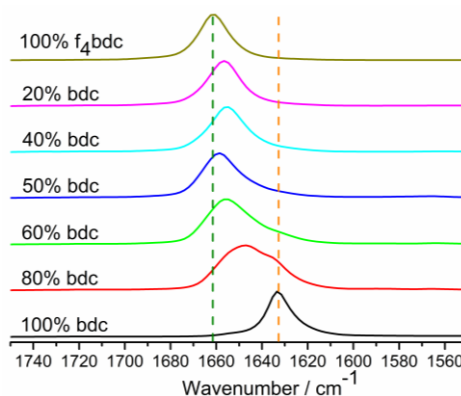


**Figure S8.2.15** Magnified IRRA spectra of  $[\text{Cu}_2\{(\text{bdc})_x+(\text{f}_4\text{bdc})_{1-x}\}_2(\text{dabco})]$  ( $0 \leq x \leq 1$ ) SURMOFs grown at  $60\text{ }^\circ\text{C}$  on PPP1 surfaces.

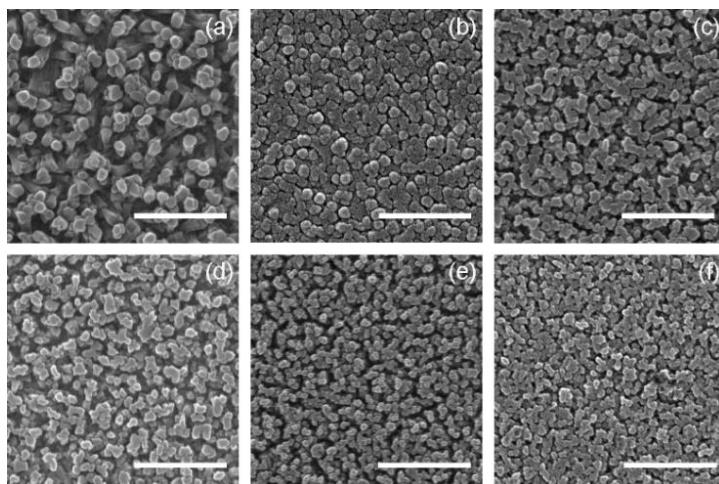


**Figure S8.2.16** SEM images of  $[\text{Cu}_2\{(\text{bdc})_x+(\text{f}_4\text{bdc})_{1-x}\}_2(\text{dabco})]$  ( $0 \leq x \leq 1$ ) SURMOFs with varied linker molar ratios grown at  $60^\circ\text{C}$  on PPP1 surfaces. (a) 100% bdc; (b) 80% bdc; (c) 60% bdc; (d) 50% bdc; (e) 40% bdc and (f) 20% bdc; scale bar:  $1\ \mu\text{m}$ .

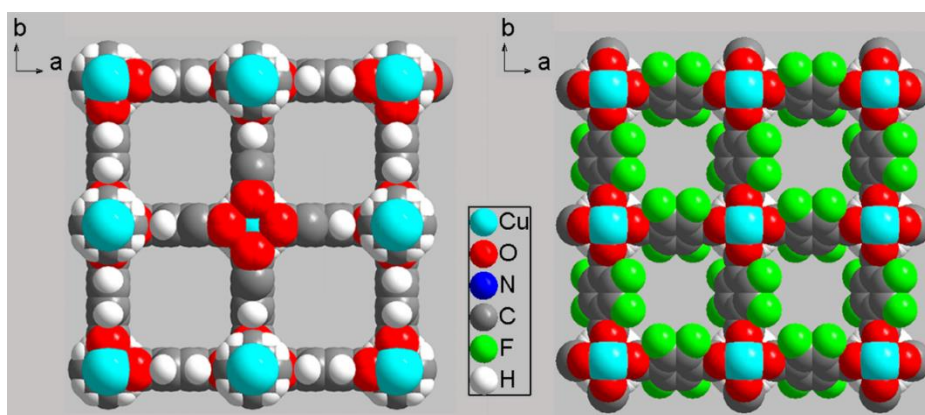


**Figure S8.2.17** Space-filling models of  $[\text{Cu}_2(\text{bdc})_2(\text{dabco})]$  (left) and  $[\text{Cu}_2(\text{f}_4\text{bdc})_2(\text{dabco})]$  (right) along  $c$  axis.

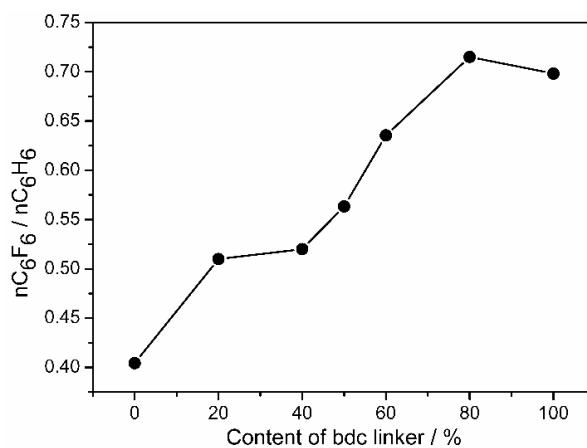


**Figure S8.2.18** Capacity ratios of  $\text{C}_6\text{F}_6$  to  $\text{C}_6\text{H}_6$  in  $[\text{Cu}_2\{(\text{bdc})_x+(\text{f}_4\text{bdc})_{1-x}\}_2(\text{dabco})]$  ( $0 \leq x \leq 1$ ) SURMOFs.

**Table S8.2.1** Content of [100] oriented crystallites (%) in single-linker containing [Cu<sub>2</sub>L<sub>2</sub>(dabco)] SURMOFs and [Cu<sub>2</sub>Lm<sub>2</sub>(dabco)] SURMOFs containing two mixed linkers (with a molar ratio of 1:1) grown at 60 °C on PPP1 surfaces as calculated from XRD data.

	bdc (4.49)	chdc (4.18)	bdc (3.51)	ndc (2.97)	bdc-Br (2.44)	bdc-NO <sub>2</sub> (1.79)	f <sub>4</sub> bdc (1.42)
bdc (4.49)	4.9	--	--	--	--	--	--
chdc (4.18)	--	0.0	0.0	0.0	--	2.9	3.7
bdc (3.51)	--	0.0	0.0	0.0	--	2.7	2.2
ndc (2.97)	--	0.0	0.0	0.0	--	0.0	1.8
bdc-Br (2.44)	--	--	--	--	2.2	--	--
bdc-NO <sub>2</sub> (1.79)	--	2.9	2.7	0.0	--	4.0	8.0
f <sub>4</sub> bdc (1.42)	--	3.7	2.2	1.8	--	8.0	6.1

**Table S8.2.2** Content of [100] oriented crystallites (%) in [Cu<sub>2</sub>{(bdc)<sub>x</sub>+(f<sub>4</sub>bdc)<sub>1-x</sub>}]<sub>2</sub>(dabco)] (0 ≤ x ≤ 1) SURMOFs with different linker ratios grown at 60 °C on PPP1 surfaces as calculated from XRD data.

100% bdc	80% bdc	60% bdc	50% bdc	40% bdc	20% bdc	0% bdc
0	0	0	2.2	8.8	11.9	6.1

## 8.3 Appendix of chapter 5

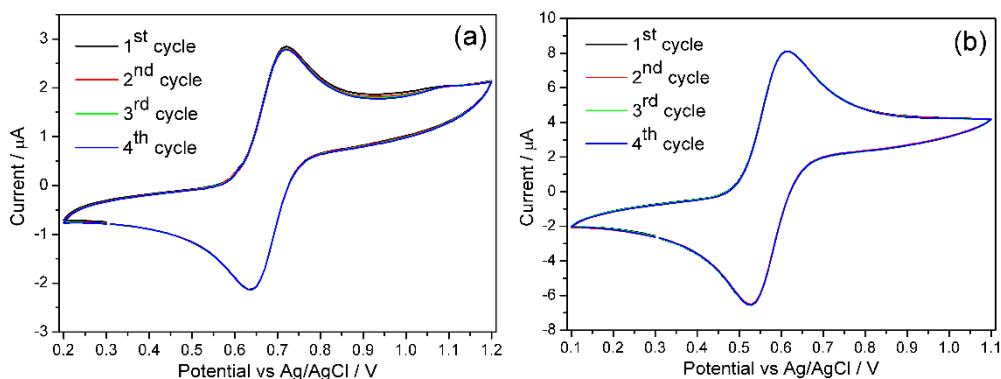


**Figure S8.3.1** CV measurements of the  $H_2(bpdc\text{-amide-Fc})$  (a) and  $H_2(bpdc\text{-amide-Me}_2Fc)$  (b) linkers in 0.1 M  $Bu_4NPF_6$  in MeCN (scan rate: 100 mV/s).

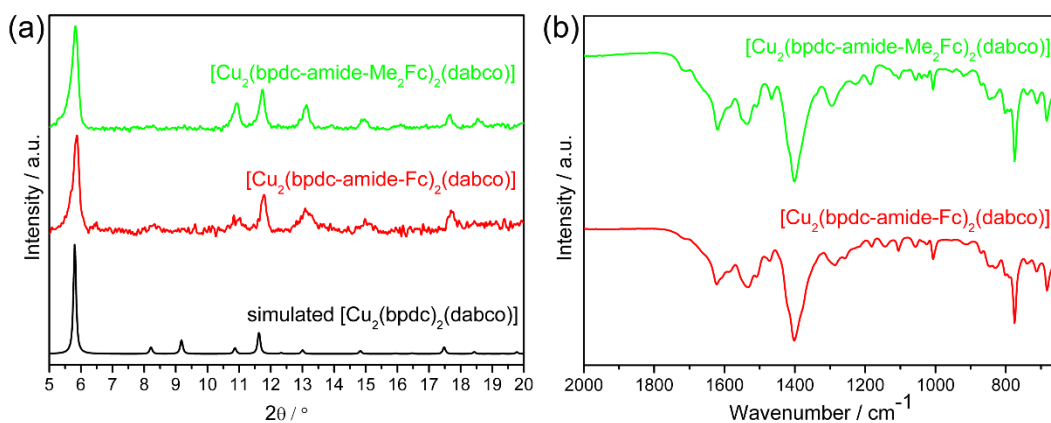


**Figure S8.3.2** XRD patterns (a) and FT-IR spectra (b) of bulk  $[Cu_2(bpdc\text{-amide-Fc})_2(dabco)]$  and  $[Cu_2(bpdc\text{-amide-Me}_2Fc)_2(dabco)]$  MOFs.

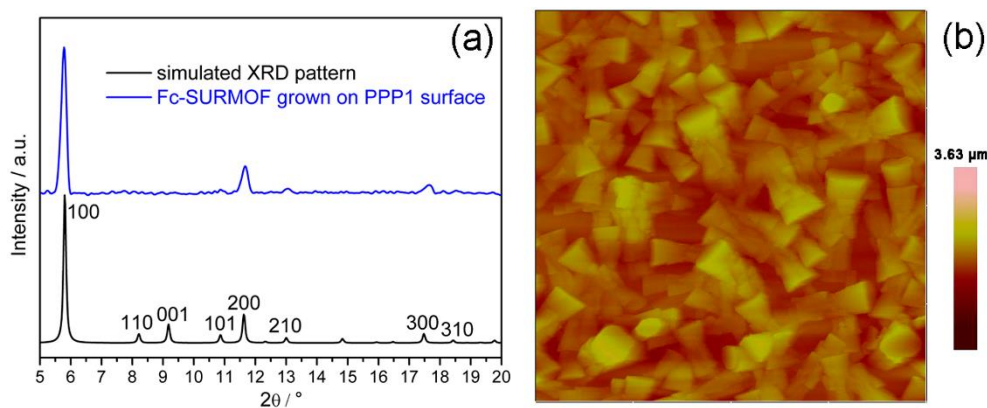


**Figure S8.3.3** XRD pattern (a) and AFM image (b) of Fc-SURMOF (40 cycles) grown at 60 °C on PPP1 surface.



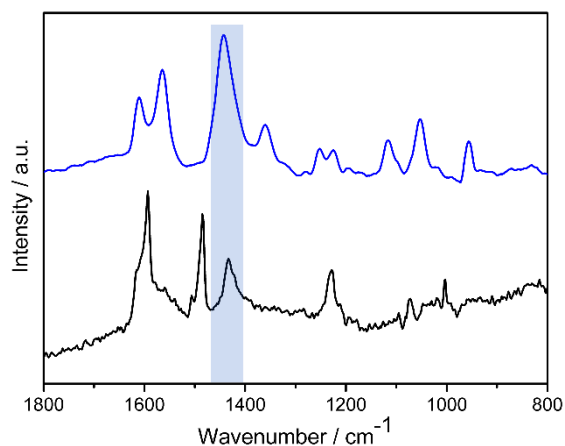


**Figure S8.3.4** IRRA spectra of half-cycle Fc-SURMOF (SAM functionalized substrates are only immersed into  $\text{Cu}_2(\text{OAc})_4$  solution) on PPP1 SAM (black) and PyzP1 SAM (blue) at 60 °C. Blue column signifies the symmetric  $-\text{COO}^-$  vibrations.

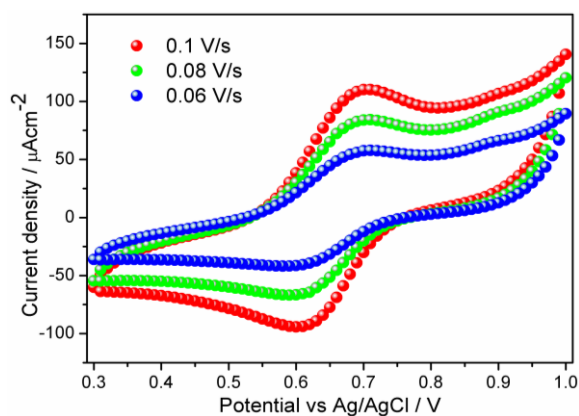


**Figure S8.3.5** Cyclic voltammograms of Fc-SURMOF (grown at 60 °C on PyzP1 surface) at different scan rates in 0.1 M  $\text{Bu}_4\text{NPF}_6$  in MeCN.

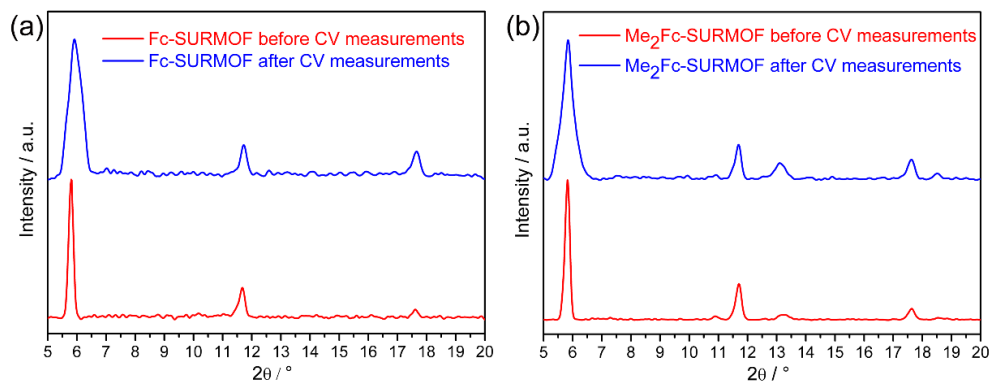


**Figure S8.3.6** Out-of-plane XRD patterns of Fc-SURMOF (a) and  $\text{Me}_2\text{Fc-SURMOF}$  (b) before and after CV measurements.

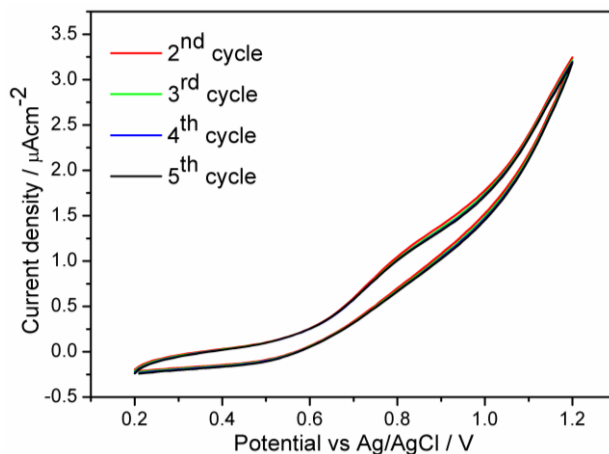


**Figure S8.3.7** CV measurement of  $\text{Me}_2\text{Fc-SURMOF}$  in  $0.1 \text{ M Bu}_4\text{NPF}_6$  added with saturated ferrocene in MeCN (scan rate:  $100 \text{ mV/s}$ ).

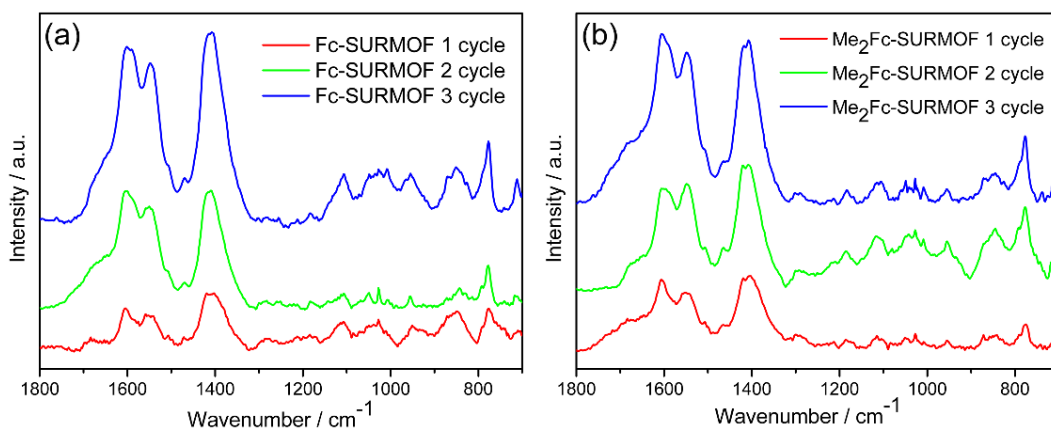


**Figure S8.3.8** IRRA spectra of Fc-SURMOF (a) and  $\text{Me}_2\text{Fc-SURMOF}$  (b) after different deposition cycles grown at  $60 \text{ }^\circ\text{C}$  on PyzP1 surfaces.

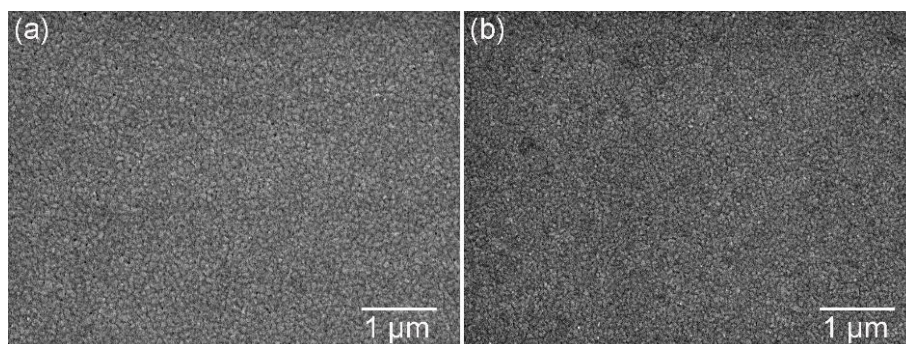


**Figure S8.3.9** SEM images of Fc-SURMOF (a) and  $\text{Me}_2\text{Fc-SURMOF}$  (b) after 3 deposition cycles grown at  $60 \text{ }^\circ\text{C}$  on PyzP1 surfaces showing the crystallinity of gold surface.

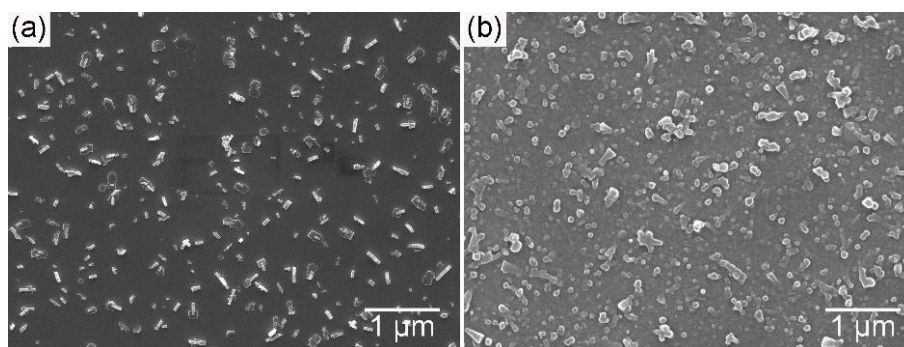


**Figure S8.3.10** SEM images of Fc-SURMOF (left) and Me<sub>2</sub>Fc-SURMOF (right) after 10 deposition cycles grown at 60 °C on PyzP1 surfaces.

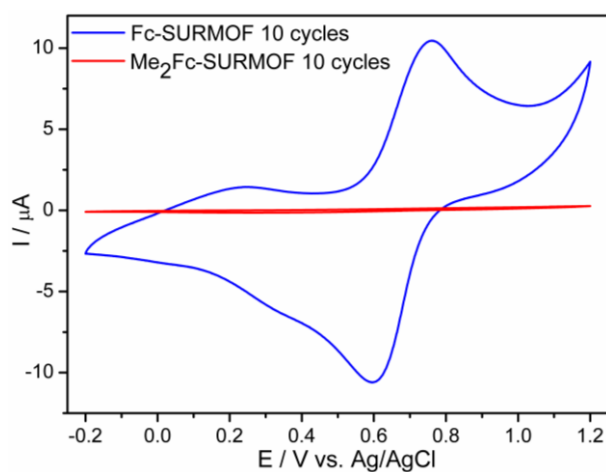


**Figure S8.3.11** CV curves of Fc- and Me<sub>2</sub>Fc-SURMOF after 10 cycle growth in 0.1 M Bu<sub>4</sub>NPF<sub>6</sub> in MeCN (scan rate: 100 mV/s).

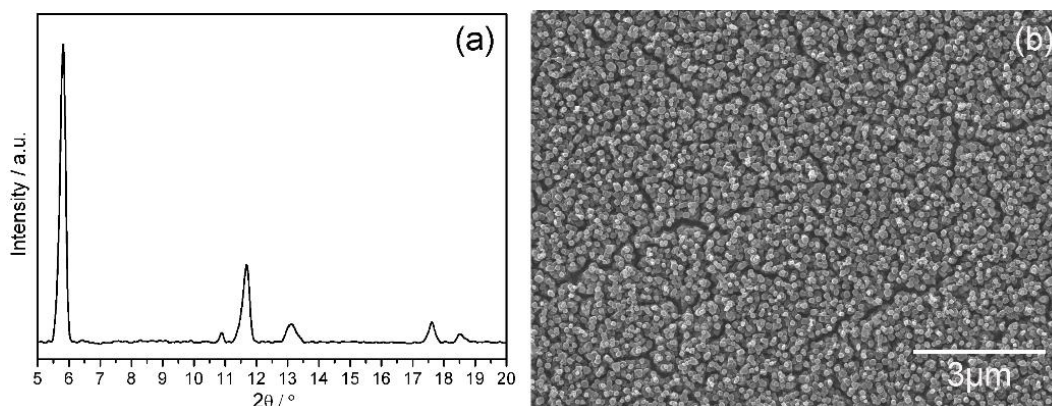


**Figure S8.3.12** XRD pattern (a) and SEM image (b) of mix-SURMOF grown at 60 °C on PyzP1 surface.

## 8.4 Appendix of chapter 6

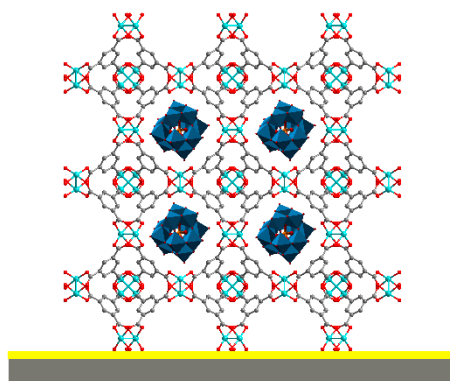


**Figure S8.4.1** The model of the encapsulation of Keggin POMs inside the large pores of HKUST-1 SURMOF.

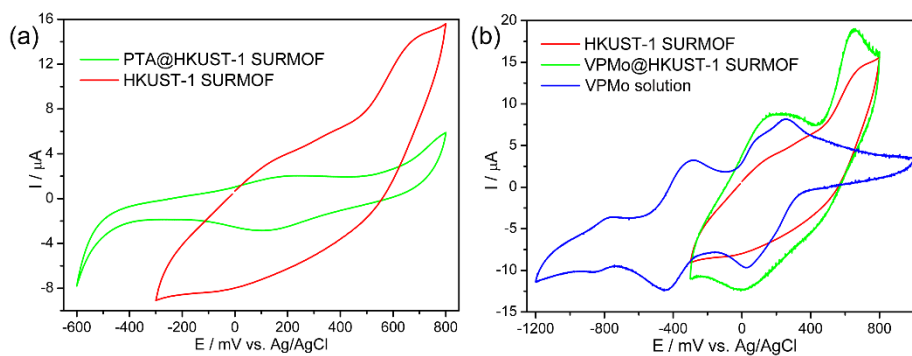


**Figure S8.4.2** CV curves of PTA@HKUST-1 SURMOF (a) and VPMo@HKUST-1 SURMOF (b) in 0.1 M Bu<sub>4</sub>NPF<sub>6</sub> in MeCN (scan rate: 100 mV/s).

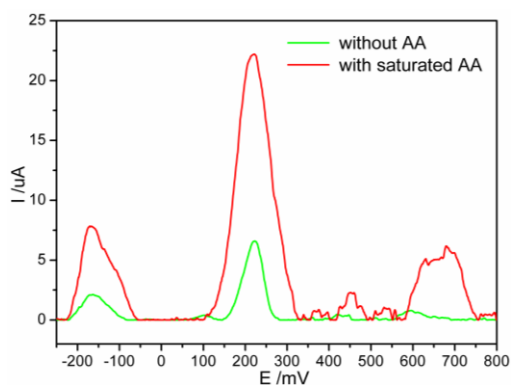


**Figure S8.4.3** Square wave scans of VPMo@HKUST-1 SURMOF in 0.1 M Bu<sub>4</sub>NPF<sub>6</sub> in MeCN with (red line) and without (green line) saturated ascorbic acid (AA). The pulse amplitude was 10 mV; the potential step was 1 mV and the frequency was 50 Hz.



**Figure S8.4.4** Color differences of dye selectively loaded PTA@HKUST-1 SURMOFs (left: the SURMOF is selectively loaded with MB after immersion into MB-MV-RhB mixture; right: the SURMOF is selectively loaded with MV after immersion into MV-RhB mixture) after being soaked in 0.025 M  $\text{NH}_4\text{Cl}$  ethanol-water solution (the volume ratio of ethanol/water is 160).

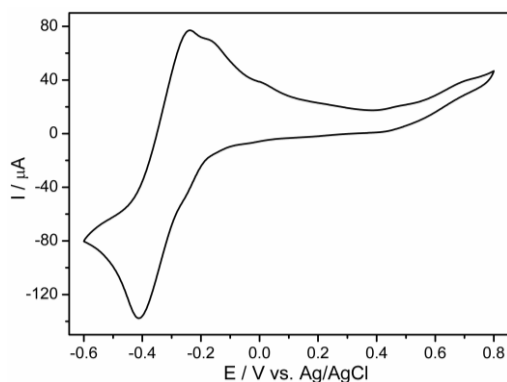


**Figure S8.4.5** CV measurement of MB dye in 0.1 M  $\text{Bu}_4\text{NPF}_6$  in MeCN (scan rate: 100 mV/s).

**Table S8.4.1** Trace element analyses of PTA@HKUST-1 SURMOFs (two samples were deposited under same conditions) based on TXRF measurements.

Element	Line	Concentration-1 / %	Concentration-2 / %
Cu	K12	41.474	41.480
W	L1	47.133	47.140
Au	L1	11.332	11.334

## 8.5 List of abbreviations

Å	Angstrom ( $1 \text{ \AA} = 10^{-10} \text{ m}$ )
AES	Auger electron spectroscopy
AFM	atomic force microscopy
APTES	3-aminopropyltriethoxysilane
ATR	attenuated total reflection infrared spectroscopy
azo-bpdc	2-azobenzene-4,4'-biphenyldicarboxylate
bbc	4,4',4''-(benzene-1,3,5-triyl-tris(benzene-4,1-diyl)) tribenzoate
bdc	1,4-benzenedicarboxylate
bdc-BME	2,5-bis(2-methoxyethoxy)-1,4-benzene dicarboxylate
bdc-NH <sub>2</sub>	2-amino-1,4-benzenedicarboxylate
bdc-NO <sub>2</sub>	2-nitrobenzene-1,4-dicarboxylate
bipy	4,4'-bipyridine
bpdc	4,4'-biphenyl dicarboxylate
bptc	3,3',5,5'-biphenyltetracarboxylate
btb	4,4',4''-benzene-1,3,5-triyl-tribenzoate
btc	1,3,5-benzenetricarboxylate
bte	4,4',4''-[benzene-1,3,5-triyl-tris(ethyne-2,1-diyl)]tribenzoate
Bu	butyl
Bu <sub>4</sub> NPF <sub>6</sub>	tetra(n-butyl)ammonium hexafluorophosphate
bzac	l-phenyl-1,3- butanedionate
CAU	Christian-Albrechts-University
CAU-1	$[(\text{Al}_4(\text{OH})_2)(\text{bdc-NH}_2)_3]$
chdc	trans-1,4-cyclohexane-dicarboxylate
CV	cyclic voltammetry
dabco	1,4-diazabicyclo[2.2.2]octane
debdc	2,5-disulfhydrylbenzene-1,4-dicarboxylate
dhbdc	2,5-dihydroxy-1,4-benzenedicarboxylate
DLS	dynamic light scattering

---

DMF	dimethylformamide
DMSO	dimethyl sulfoxide
DNA	deoxyribonucleic acid
EDS/EDX	energy-dispersive X-ray spectroscopy
f <sub>4</sub> bdc	tetrafluorobenzene-1,4-dicarboxylate
Fc	ferrocene
Me <sub>2</sub> Fc	dimethyl ferrocene
FT-IR	Fourier transform infrared spectroscopy
FTO	fluorine-doped tin oxide
HDT	1-hexadecanethiol
hitp	2,3,6,7,10,11-hexaiminotriphenylene
HKUST	Hongkong University of Science and Technology
HKUST-1	[Cu <sub>3</sub> (btc) <sub>2</sub> ]
HREELS	high resolution electron energy loss spectroscopy
htb	4,4',4''-(1,3,4,6,7,9,9b-heptaazaphenalene-2,5,8-triyl)tribenzoate
IRMOF	isorecticular MOF
IRMOF-3	[(Zn <sub>4</sub> O)(bdc-NH <sub>2</sub> ) <sub>3</sub> ]
IRMOF-74	isorecticular MOF-74
IRRAS	infrared reflection-absorption spectroscopy
LB	Langmuir-Blodgett
LbL	layer-by-layer
LCCs	lanthanide coordination compounds
LPE	liquid-phase epitaxy
μCP	microcontact printing
MB	methylene blue
MIL	Material Institut Lavoiser
MIL-53	[Fe <sub>3</sub> O(bdc) <sub>3</sub> ]
MIL-88A	[Fe <sub>3</sub> O(fumarate) <sub>3</sub> ]
MIL-88B-NH <sub>2</sub>	[Fe <sub>3</sub> O(bdc-NH <sub>2</sub> ) <sub>3</sub> ]
MIL-101-Cr	[Cr <sub>3</sub> O(bdc) <sub>3</sub> ]

mM	mmol/L
MOFs	metal-organic frameworks
MOF-5	$[(Zn_4O)(bdc)_3]$
MOF-14	$[Cu_3(btb)_2]$
MOF-74	$[Zn_2(dhbdc)]$
MOF-177	$[(Zn_4O)(btb)_2]$
MOF-180	$[(Zn_4O)(bte)_2]$
MOF-200	$[(Zn_4O)(bbc)_2]$
MOF-210	$[(Zn_4O)_3(bte)_4(bpdc)_3]$
MOF-399	$[Cu_3(bbc)_2]$
MOF-505	$[Cu_2(bptc)]$
MTCA	4'-(mercaptomethyl)terphenyl-4-carboxylic acid
MTV-MOF	multivariate/multifunctional MOF
MTV-SURMOF	multivariate/multifunctional SURMOF
MV	methyl violet
NAFS-1	$[Cu(Co-tcpp)(bipy)]$
NAFS-2	$[Cu(tcpp)(bipy)]$
ndc	1,4-naphthalenedicarboxylate
NDI	1,4,5,8-naphthalenetetracarboxylic diimide
NMR	nuclear magnetic resonance
NU	Northwestern University
NU-100	$[Cu_3\{1,3,5\text{-tris}[(1,3\text{-carboxylate-5-(4-(ethynyl)phenyl))ethynyl]\text{-benzene}\}]$
PCPs	porous coordination polymers
$Pd(dppf)Cl_2$	[1,1'-bis(diphenylphosphino)ferrocene]palladium dichloride
PEG	polyethylene glycol
$pK_a$	ionization constant
PMA	phosphomolybdic acid
POM	polyoxometalate
PPF	porphyrin paddlewheel framework
PPF-5	$[Co_2(Pd-tcpp)(bipy)_3]$



---

PPP1	(4-(4-(4-pyridyl)phenyl)phenyl)-methanethiol
PSM	postsynthetic modification
PTA	phosphotungstic acid
PyzP1	(4-(1 <i>H</i> -pyrazol-4-yl))phenylmethanethiol
QCM	quartz crystal microbalance
RhB	rhodamine B
SAMs	self-assembled monolayers
SBU	secondary building unit
sdb	4,4'-sulfonylbiphenyl dicarboxylate
SEM	scanning electron microscopy
SFG	sum frequency generation
STM	scanning tunneling microscopy
SURMOFs	surface-mounted metal-organic frameworks
SURMOF-2	[M <sub>2</sub> L <sub>2</sub> ] M = Zn <sup>2+</sup> or Cu <sup>2+</sup> ; L = dicarboxylate linker
SWV	square wave voltammetry
tatb	4,4',4''- <i>s</i> -triazine-2,4,6-triyltribenzoate
tatab	4,4',4''- <i>s</i> -triazine-1,3,5-triyltri- <i>p</i> -aminobenzoate
TBA	tetrabutylammonium
TCNQ	tetracyanoquinodimethane
tcpp	5,10,15,20-tetrakis(4-carboxyphenyl) porphyrin
t <sup>2</sup> dc	thieno[3,2- <i>b</i> ]thiophene-2,5-dicarboxylate
TFA	trifluoroacetic acid
TIPS	triisopropylsilyl
ttca	triphenylene-2,6,10-tricarboxylate
ttfb	tetrathiafulvalene tetrabenzoate
TXRF	total reflection X-ray fluorescence spectrometry
UiO	University of Oslo
UiO-66-NH <sub>2</sub>	[(Zr <sub>6</sub> O <sub>4</sub> )(bdc-NH <sub>2</sub> ) <sub>6</sub> ]
UMCM	University of Michigan Crystalline Material
UMCM-2	[(Zn <sub>4</sub> O)(btb) <sub>4</sub> (t <sup>2</sup> dc) <sub>2</sub> ]

UPS	ultraviolet photoelectron spectroscopy
UV-Vis	ultraviolet-visible spectroscopy
VOCs	volatile organic compounds
VPMo	(n-Bu <sub>4</sub> N) <sub>4</sub> H(PMo <sub>10</sub> V <sub>2</sub> O <sub>40</sub> )
XANES	X-ray absorption near edge structure
XRD	X-ray diffraction
XPS	X-ray photoelectron spectroscopy
ZIFs	zeolitic imidazolate frameworks
ZIF-8	[Zn(2-methylimidazole) <sub>2</sub> ]
ZIF-22	[Zn(5-azabenzimidazole) <sub>2</sub> ]
ZIF-90	[Zn(imidazole-2-carboxaldehyde) <sub>2</sub> ]

## 9 References

- 1 S. L. James, *Chem. Soc. Rev.*, 2003, **32**, 276–288.
- 2 O. M. Yaghi, M. O’Keeffe, N. W. Ockwig, H. K. Chae, M. Eddaoudi and J. Kim, *Nature*, 2003, **423**, 705–714.
- 3 G. Férey, *Chem. Soc. Rev.*, 2008, **37**, 191–214.
- 4 H. C. Zhou, J. R. Long and O. M. Yaghi, *Chem. Rev.*, 2012, **112**, 673–674.
- 5 H. Furukawa, K. E. Cordova, M. O’Keeffe and O. M. Yaghi, *Science*, 2013, **341**, 974–986.
- 6 H. C. Zhou and S. Kitagawa, *Chem. Soc. Rev.*, 2014, **43**, 5415–5418.
- 7 O. K. Farha, I. Eryazici, N. C. Jeong, B. G. Hauser, C. E. Wilmer, A. A. Sarjeant, R. Q. Snurr, S. T. Nguyen, A. Ö. Yazaydin and J. T. Hupp, *J. Am. Chem. Soc.*, 2012, **134**, 15016–15021.
- 8 J. R. Long and O. M. Yaghi, *Chem. Soc. Rev.*, 2009, **38**, 1213–1214.
- 9 S. S. Y. Chui, S. M. F. Lo, J. P. Charmant, A. G. Orpen and I. D. Williams, *Science*, 1999, **283**, 1148–1150.
- 10 K. S. Park, Z. Ni, A. P. Côté, J. Y. Choi, R. Huang, F. J. Uribe-Romo, H. K. Chae, M. O’Keeffe and O. M. Yaghi, *Proc. Natl. Acad. Sci.*, 2006, **103**, 10186–10191.
- 11 H. Li, M. Eddaoudi, M. O’Keeffe and O. M. Yaghi, *Nature*, 1999, **402**, 276–279.
- 12 G. Férey, C. Mellot-Draznieks, C. Serre, F. Millange, J. Dutour, S. Surblé and I. Margiolaki, *Science*, 2005, **309**, 2040–2042.
- 13 H. B. Jeazet, T. Koschine, C. Staudt, K. Raetzke and C. Janiak, *Membranes*, 2013, **3**, 331–353.
- 14 D. J. Tranchemontagne, J. L. Mendoza-Cortés, M. O’Keeffe and O. M. Yaghi, *Chem. Soc. Rev.*, 2009, **38**, 1257–1283.
- 15 S. Kitagawa, R. Kitaura and S. Noro, *Angew. Chem. Int. Ed.*, 2004, **43**, 2334–2375.
- 16 J. J. Perry Iv, J. A. Perman and M. J. Zaworotko, *Chem. Soc. Rev.*, 2009, **38**, 1400–1417.
- 17 M. O’Keeffe and O. M. Yaghi, *Chem. Rev.*, 2012, **112**, 675–702.
- 18 M. Li, D. Li, M. O’Keeffe and O. M. Yaghi, *Chem. Rev.*, 2013, **114**, 1343–1370.
- 19 J. Kim, B. Chen, T. M. Reineke, H. Li, M. Eddaoudi, D. B. Moler, M. O’Keeffe and O. M. Yaghi, *J. Am. Chem. Soc.*, 2001, **123**, 8239–8247.
- 20 M. Eddaoudi, J. Kim, D. Vodak, A. Sudik, J. Wachter, M. O’Keeffe and O. M. Yaghi, *Proc. Natl. Acad. Sci.*, 2002, **99**, 4900–4904.

- 21 H. Li, M. Eddaoudi, T. L. Groy and O. M. Yaghi, *J. Am. Chem. Soc.*, 1998, **120**, 8571–8572.
- 22 Y. Diskin-Posner, S. Dahal and I. Goldberg, *Angew. Chem. Int. Ed.*, 2000, **39**, 1288–1292.
- 23 H. K. Chae, M. Eddaoudi, J. Kim, S. I. Hauck, J. F. Hartwig, M. O’Keeffe and O. M. Yaghi, *J. Am. Chem. Soc.*, 2001, **123**, 11482–11483.
- 24 M. Eddaoudi, J. Kim, N. Rosi, D. Vodak, J. Wachter, M. O’Keeffe and O. M. Yaghi, *Science*, 2002, **295**, 469–472.
- 25 H. Furukawa, Y. B. Go, N. Ko, Y. K. Park, F. J. Uribe-Romo, J. Kim, M. O’Keeffe and O. M. Yaghi, *Inorg. Chem.*, 2011, **50**, 9147–9152.
- 26 H. X. Deng, S. Grunder, K. E. Cordova, C. Valente, H. Furukawa, M. Hmadeh, F. Gándara, A. C. Whalley, Z. Liu, S. Asahina, H. Kazumori, M. O’Keeffe, O. Terasaki, J. F. Stoddart and O. M. Yaghi, *Science*, 2012, **336**, 1018–1023.
- 27 N. L. Rosi, J. Kim, M. Eddaoudi, B. Chen, M. O’Keeffe and O. M. Yaghi, *J. Am. Chem. Soc.*, 2005, **127**, 1504–1518.
- 28 H. K. Chae, D. Y. Siberio-Pérez, J. Kim, Y. Go, M. Eddaoudi, A. J. Matzger, M. O’Keeffe and O. M. Yaghi, *Nature*, 2004, **427**, 523–527.
- 29 H. Furukawa, N. Ko, Y. B. Go, N. Aratani, S. B. Choi, E. Choi, A. Ö. Yazaydin, R. Q. Snurr, M. O’Keeffe, J. Kim and O. M. Yaghi, *Science*, 2010, **329**, 424–428.
- 30 X. S. Wang, S. Q. Ma, D. F. Sun, S. Parkin and H. C. Zhou, *J. Am. Chem. Soc.*, 2006, **128**, 16474–16475.
- 31 X. S. Wang, S. Q. Ma, D. Q. Yuan, J. W. Yoon, Y. K. Hwang, J. S. Chang, X. P. Wang, M. R. Jørgensen, Y. S. Chen and H. C. Zhou, *Inorg. Chem.*, 2009, **48**, 7519–7521.
- 32 D. F. Sun, S. Q. Ma, Y. X. Ke, D. J. Collins and H. C. Zhou, *J. Am. Chem. Soc.*, 2006, **128**, 3896–3897.
- 33 S. Q. Ma, D. F. Sun, M. Ambrogio, J. A. Fillinger, S. Parkin and H. C. Zhou, *J. Am. Chem. Soc.*, 2007, **129**, 1858–1859.
- 34 K. Koh, A. G. Wong-Foy and A. J. Matzger, *J. Am. Chem. Soc.*, 2009, **131**, 4184–4185.
- 35 M. Sindoro, N. Yanai, A. Y. Jee and S. Granick, *Acc. Chem. Res.*, 2013, **47**, 459–469.
- 36 E. A. Flügel, A. Ranft, F. Haase and B. V. Lotsch, *J. Mater. Chem.*, 2012, **22**, 10119–10133.
- 37 N. Stock and S. Biswas, *Chem. Rev.*, 2012, **112**, 933–969.
- 38 T. R. Cook, Y. R. Zheng and P. J. Stang, *Chem. Rev.*, 2012, **113**, 734–777.
- 39 B. Seoane, S. Castellanos, A. Dikhtiarenko, F. Kapteijn and J. Gascon, *Coord. Chem. Rev.*, 2016, **307**,

- 147–187.
- 40 M. Giménez-Marqués, T. Hidalgo, C. Serre and P. Horcajada, *Coord. Chem. Rev.*, 2016, **307**, 342–360.
- 41 Z. H. Xiang, D. P. Cao, X. H. Shao, W. C. Wang, J. W. Zhang and W. Z. Wu, *Chem. Eng. Sci.*, 2010, **65**, 3140–3146.
- 42 N. A. Khan, I. J. Kang, H. Y. Seok and S. H. Jung, *Chem. Eng. J.*, 2011, **166**, 1152–1157.
- 43 Z. Ni and R. I. Masel, *J. Am. Chem. Soc.*, 2006, **128**, 12394–12395.
- 44 N. A. Khan, E. Haque and S. H. Jung, *Phys. Chem. Chem. Phys.*, 2010, **12**, 2625–2631.
- 45 Z. Q. Li, L. G. Qiu, T. Xu, Y. Wu, W. Wang, Z. Y. Wu and X. Jiang, *Mater. Lett.*, 2009, **63**, 78–80.
- 46 L. G. Qiu, Z. Q. Li, Y. Wu, W. Wang, T. Xu and X. Jiang, *Chem. Commun.*, 2008, 3642–3644.
- 47 T. Friščić, D. G. Reid, I. Halasz, R. S. Stein, R. E. Dinnebier and M. J. Duer, *Angew. Chem. Int. Ed.*, 2010, **49**, 712–715.
- 48 A. Pichon and S. L. James, *CrystEngComm*, 2008, **10**, 1839–1847.
- 49 A. Pichon, A. Lazuen-Garay and S. L. James, *CrystEngComm*, 2006, **8**, 211–214.
- 50 A. Martinez Joaristi, J. Juan-Alcañiz, P. Serra-Crespo, F. Kapteijn and J. Gascon, *Cryst. Growth Des.*, 2012, **12**, 3489–3498.
- 51 M. Y. Li and M. Dinca, *J. Am. Chem. Soc.*, 2011, **133**, 12926–12929.
- 52 R. Ameloot, L. Stappers, J. Fransaer, L. Alaerts, B. F. Sels and D. E. De Vos, *Chem. Mater.*, 2009, **21**, 2580–2582.
- 53 K. M. Taylor, A. Jin and W. B. Lin, *Angew. Chem. Int. Ed.*, 2008, **47**, 7722–7725.
- 54 L. B. Sun, J. R. Li, J. Park and H. C. Zhou, *J. Am. Chem. Soc.*, 2012, **134**, 126–129.
- 55 L. Hu, P. Zhang, Q. W. Chen, H. Zhong, X. Y. Hu, X. R. Zheng, Y. Wang and N. Yan, *Cryst. Growth Des.*, 2012, **12**, 2257–2264.
- 56 M. L. Pang, A. J. Cairns, Y. L. Liu, Y. Belmabkhout, H. C. Zeng and M. Eddaoudi, *J. Am. Chem. Soc.*, 2012, **134**, 13176–13179.
- 57 W. J. Rieter, K. M. Taylor, H. Y. An, W. L. Lin and W. B. Lin, *J. Am. Chem. Soc.*, 2006, **128**, 9024–9025.
- 58 J. Della Rocca and W. B. Lin, *Eur. J. Inorg. Chem.*, 2010, **2010**, 3725–3734.
- 59 H. L. Guo, Y. Z. Zhu, S. Wang, S. Q. Su, L. Zhou and H. J. Zhang, *Chem. Mater.*, 2012, **24**, 444–450.
- 60 M. H. Pham, G. T. Vuong, F. G. Fontaine and T. O. Do, *Cryst. Growth Des.*, 2011, **12**, 1008–1013.
- 61 A. Umemura, S. Diring, S. Furukawa, H. Uehara, T. Tsuruoka and S. Kitagawa, *J. Am. Chem. Soc.*,

- 2011, **133**, 15506–15513.
- 62 J. L. Zhuang, D. Ceglarek, S. Pethuraj and A. Terfort, *Adv. Funct. Mater.*, 2011, **21**, 1442–1447.
- 63 X. P. Sun, S. J. Dong and E. K. Wang, *J. Am. Chem. Soc.*, 2005, **127**, 13102–13103.
- 64 M. Oh and C. A. Mirkin, *Nature*, 2005, **438**, 651–654.
- 65 X. D. Xu, R. G. Cao, S. Jeong and J. Cho, *Nano Lett.*, 2012, **12**, 4988–4991.
- 66 N. Yanai, M. Sindoro, J. Yan and S. Granick, *J. Am. Chem. Soc.*, 2013, **135**, 34–37.
- 67 J. Cravillon, R. Nayuk, S. Springer, A. Feldhoff, K. Huber and M. Wiebcke, *Chem. Mater.*, 2011, **23**, 2130–2141.
- 68 T. Tsuruoka, S. Furukawa, Y. Takashima, K. Yoshida, S. Isoda and S. Kitagawa, *Angew. Chem. Int. Ed.*, 2009, **48**, 4739–4743.
- 69 W. Cho, H. J. Lee and M. Oh, *J. Am. Chem. Soc.*, 2008, **130**, 16943–16946.
- 70 A. Carné-Sánchez, I. Imaz, M. Cano-Sarabia and D. Maspocho, *Nat. Chem.*, 2013, **5**, 203–211.
- 71 J. Reboul, S. Furukawa, N. Horike, M. Tsotsalas, K. Hirai, H. Uehara, M. Kondo, N. Louvain, O. Sakata and S. Kitagawa, *Nat. Mater.*, 2012, **11**, 717–723.
- 72 S. Furukawa, J. Reboul, S. Diring, K. Sumida and S. Kitagawa, *Chem. Soc. Rev.*, 2014, **43**, 5700–5734.
- 73 H. J. Lee, W. Cho and M. Oh, *Chem. Commun.*, 2012, **48**, 221–223.
- 74 C. H. Kuo, Y. Tang, L. Y. Chou, B. T. Sneed, C. N. Brodsky, Z. P. Zhao and C. K. Tsung, *J. Am. Chem. Soc.*, 2012, **134**, 14345–14348.
- 75 S. Aguado, J. Canivet and D. Farrusseng, *J. Mater. Chem.*, 2011, **21**, 7582–7588.
- 76 S. Sorribas, B. Zornoza, C. Tólez and J. Coronas, *Chem. Commun.*, 2012, **48**, 9388–9390.
- 77 P. Pachfule, B. K. Balan, S. Kurungot and R. Banerjee, *Chem. Commun.*, 2012, **48**, 2009–2011.
- 78 J. Huo, M. Marcello, A. Garai and D. Bradshaw, *Adv. Mater.*, 2013, **25**, 2717–2722.
- 79 L. Peng, J. L. Zhang, J. S. Li, B. X. Han, Z. M. Xue, B. B. Zhang, J. H. Shi and G. Y. Yang, *J. Colloid Interface Sci.*, 2014, **416**, 198–204.
- 80 S. Cao, G. Gody, W. Zhao, S. Perrier, X. Y. Peng, C. Ducati, D. Y. Zhao and A. K. Cheetham, *Chem. Sci.*, 2013, **4**, 3573–3577.
- 81 M. Jahan, Q. Bao, J. X. Yang and K. P. Loh, *J. Am. Chem. Soc.*, 2010, **132**, 14487–14495.
- 82 K. M. Choi, H. J. Jeon, J. K. Kang and O. M. Yaghi, *J. Am. Chem. Soc.*, 2011, **133**, 11920–11923.
- 83 C. Carbonell, I. Imaz and D. Maspocho, *J. Am. Chem. Soc.*, 2011, **133**, 2144–2147.
- 84 M. R. Lohe, M. Rose and S. Kaskel, *Chem. Commun.*, 2009, 6056–6058.

- 85 W. W. Zhan, Q. Kuang, J. Z. Zhou, X. J. Kong, Z. X. Xie and L. S. Zheng, *J. Am. Chem. Soc.*, 2013, **135**, 1926–1933.
- 86 H. Y. Lu and S. P. Zhu, *Eur. J. Inorg. Chem.*, 2013, **2013**, 1294–1300.
- 87 M. Faustini, J. Kim, G. Y. Jeong, J. Y. Kim, H. R. Moon, W. S. Ahn and D. P. Kim, *J. Am. Chem. Soc.*, 2013, **135**, 14619–14626.
- 88 R. Ameloot, F. Vermoortele, W. Vanhove, M. B. Roeffaers, B. F. Sels and D. E. De Vos, *Nat. Chem.*, 2011, **3**, 382–387.
- 89 Y. Y. Fu, C. X. Yang and X. P. Yan, *Chem. Commun.*, 2013, **49**, 7162–7164.
- 90 R. Ostermann, J. Cravillon, C. Weidmann, M. Wiebcke and B. M. Smarsly, *Chem. Commun.*, 2011, **47**, 442–444.
- 91 K. Khaletskaya, J. Reboul, M. Meilikhov, M. Nakahama, S. Diring, M. Tsujimoto, S. Isoda, F. Kim, K. Kamei, R. A. Fischer, S. Kitagawa and S. Furukawa, *J. Am. Chem. Soc.*, 2013, **135**, 10998–11005.
- 92 E. F. de Melo, N. da C. Santana, K. G. B. Alves, G. F. de S. C. P. de Melo, M. O. Rodrigues and S. A. Júnior, *J. Mater. Chem. C*, 2013, **1**, 7574–7581.
- 93 J. L. Rowsell and O. M. Yaghi, *Angew. Chem. Int. Ed.*, 2005, **44**, 4670–4679.
- 94 D. J. Collins and H. C. Zhou, *J. Mater. Chem.*, 2007, **17**, 3154–3160.
- 95 L. J. Murray, M. Dincă and J. R. Long, *Chem. Soc. Rev.*, 2009, **38**, 1294–1314.
- 96 Y. H. Hu and L. Zhang, *Adv. Mater.*, 2010, **22**, 117–130.
- 97 M. P. Suh, H. J. Park, T. K. Prasad and D. W. Lim, *Chem. Rev.*, 2011, **112**, 782–835.
- 98 N. L. Rosi, J. Eckert, M. Eddaoudi, D. T. Vodak, J. Kim, M. O’Keeffe and O. M. Yaghi, *Science*, 2003, **300**, 1127–1129.
- 99 K. Sumida, D. L. Rogow, J. A. Mason, T. M. McDonald, E. D. Bloch, Z. R. Herm, T. H. Bae and J. R. Long, *Chem. Rev.*, 2011, **112**, 724–781.
- 100 J. R. Li, Y. G. Ma, M. C. McCarthy, J. Sculley, J. M. Yu, H. K. Jeong, P. B. Balbuena and H. C. Zhou, *Coord. Chem. Rev.*, 2011, **255**, 1791–1823.
- 101 L. E. Kreno, K. Leong, O. K. Farha, M. Allendorf, R. P. Van Duyne and J. T. Hupp, *Chem. Rev.*, 2011, **112**, 1105–1125.
- 102 V. Stavila, R. Parthasarathi, R. W. Davis, F. El Gabaly, K. L. Sale, B. A. Simmons, S. Singh and M. D. Allendorf, *ACS Catal.*, 2015, **6**, 55–59.
- 103 J. W. Liu, L. F. Chen, H. Cui, J. Y. Zhang, L. Zhang and C. Y. Su, *Chem. Soc. Rev.*, 2014, **43**, 6011–

- 6061.
- 104 T. Zhang and W. B. Lin, *Chem. Soc. Rev.*, 2014, **43**, 5982–5993.
- 105 D. Cunha, M. Ben Yahia, S. Hall, S. R. Miller, H. Chevreau, E. Elkaïn, G. Maurin, P. Horcajada and C. Serre, *Chem. Mater.*, 2013, **25**, 2767–2776.
- 106 J. Della Rocca, D. M. Liu and W. B. Lin, *Acc. Chem. Res.*, 2011, **44**, 957–968.
- 107 J. L. Rowsell and O. M. Yaghi, *J. Am. Chem. Soc.*, 2006, **128**, 1304–1315.
- 108 O. K. Farha, A. Ö. Yazaydın, I. Eryazici, C. D. Malliakas, B. G. Hauser, M. G. Kanatzidis, S. T. Nguyen, R. Q. Snurr and J. T. Hupp, *Nat. Chem.*, 2010, **2**, 944–948.
- 109 W. Zhou, H. Wu and T. Yildirim, *J. Am. Chem. Soc.*, 2008, **130**, 15268–15269.
- 110 X. S. Wang, S. Q. Ma, P. M. Forster, D. Q. Yuan, J. Eckert, J. J. López, B. J. Murphy, J. B. Parise and H. C. Zhou, *Angew. Chem. Int. Ed.*, 2008, **47**, 7263–7266.
- 111 X. Lin, I. Telepeni, A. J. Blake, A. Dailly, C. M. Brown, J. M. Simmons, M. Zoppi, G. S. Walker, K. M. Thomas, T. J. Mays, P. Hubberstey, N. R. Champness and M Schröder, *J. Am. Chem. Soc.*, 2009, **131**, 2159–2171.
- 112 Y. G. Lee, H. R. Moon, Y. E. Cheon and M. P. Suh, *Angew. Chem. Int. Ed.*, 2008, **47**, 7741–7745.
- 113 D. M. D’Alessandro, B. Smit and J. R. Long, *Angew. Chem. Int. Ed.*, 2010, **49**, 6058–6082.
- 114 S. Bourrelly, P. L. Llewellyn, C. Serre, F. Millange, T. Loiseau and G. Férey, *J. Am. Chem. Soc.*, 2005, **127**, 13519–13521.
- 115 A. R. Millward and O. M. Yaghi, *J. Am. Chem. Soc.*, 2005, **127**, 17998–17999.
- 116 P. L. Llewellyn, S. Bourrelly, C. Serre, A. Vimont, M. Daturi, L. Hamon, G. De Weireld, J. S. Chang, D. Y. Hong, Y. Kyu Hwang, S. H. Jung and G Férey, *Langmuir*, 2008, **24**, 7245–7250.
- 117 S. R. Caskey, A. G. Wong-Foy and A. J. Matzger, *J. Am. Chem. Soc.*, 2008, **130**, 10870–10871.
- 118 D. Britt, H. Furukawa, B. Wang, T. G. Glover and O. M. Yaghi, *Proc. Natl. Acad. Sci.*, 2009, **106**, 20637–20640.
- 119 J. J. Gassensmith, H. Furukawa, R. A. Smaldone, R. S. Forgan, Y. Y. Botros, O. M. Yaghi and J. F. Stoddart, *J. Am. Chem. Soc.*, 2011, **133**, 15312–15315.
- 120 T. G. Glover, G. W. Peterson, B. J. Schindler, D. Britt and O. Yaghi, *Chem. Eng. Sci.*, 2011, **66**, 163–170.
- 121 D. Britt, D. Tranchemontagne and O. M. Yaghi, *Proc. Natl. Acad. Sci.*, 2008, **105**, 11623–11627.
- 122 U. Mueller, M. Schubert, F. Teich, H. Puetter, K. Schierle-Arndt and J. Pastre, *J. Mater. Chem.*, 2006,



- 16**, 626–636.
- 123 A. U. Czaja, N. Trukhan and U. Müller, *Chem. Soc. Rev.*, 2009, **38**, 1284–1293.
- 124 S. Horike, D. Umeyama and S. Kitagawa, *Acc. Chem. Res.*, 2013, **46**, 2376–2384.
- 125 M. Yoon, K. Suh, S. Natarajan and K. Kim, *Angew. Chem. Int. Ed.*, 2013, **52**, 2688–2700.
- 126 A. Shigematsu, T. Yamada and H. Kitagawa, *J. Am. Chem. Soc.*, 2011, **133**, 2034–2036.
- 127 C. Montoro, P. Ocón, F. Zamora and J. A. Navarro, *Chem. Eur. J.*, 2015, **54**, 7234–7254.
- 128 J. M. Taylor, K. W. Dawson and G. K. Shimizu, *J. Am. Chem. Soc.*, 2013, **135**, 1193–1196.
- 129 X. Meng, S. Y. Song, X. Z. Song, M. Zhu, S. N. Zhao, L. L. Wu and H. J. Zhang, *Chem. Commun.*, 2015, **51**, 8150–8152.
- 130 T. Yamada, M. Sadakiyo and H. Kitagawa, *J. Am. Chem. Soc.*, 2009, **131**, 3144–3145.
- 131 M. Sadakiyo, T. Yamada and H. Kitagawa, *J. Am. Chem. Soc.*, 2014, **136**, 13166–13169.
- 132 R. Ameloot, M. Aubrey, B. M. Wiers, A. P. Gómora-Figueroa, S. N. Patel, N. P. Balsara and J. R. Long, *Chem. Eur. J.*, 2013, **19**, 5533–5536.
- 133 T. N. Tu, N. Q. Phan, T. T. Vu, H. L. Nguyen, K. E. Cordova and H. Furukawa, *J. Mater. Chem. A*, 2016, **4**, 3638–3641.
- 134 H. W. Zhang and P. K. Shen, *Chem. Rev.*, 2012, **112**, 2780–2832.
- 135 J. A. Hurd, R. Vaidhyanathan, V. Thangadurai, C. I. Ratcliffe, I. L. Moudrakovski and G. K. Shimizu, *Nat. Chem.*, 2009, **1**, 705–710.
- 136 B. M. Wiers, M. L. Foo, N. P. Balsara and J. R. Long, *J. Am. Chem. Soc.*, 2011, **133**, 14522–14525.
- 137 W. X. Chen, H. R. Xu, G. L. Zhuang, L. S. Long, R. B. Huang and L. S. Zheng, *Chem. Commun.*, 2011, **47**, 11933–11935.
- 138 J. Lee, O. K. Farha, J. Roberts, K. A. Scheidt, S. T. Nguyen and J. T. Hupp, *Chem. Soc. Rev.*, 2009, **38**, 1450–1459.
- 139 M. Yoon, R. Srirambalaji and K. Kim, *Chem. Rev.*, 2011, **112**, 1196–1231.
- 140 A. Corma, H. Garcia and F. X. Llabrés i Xamena, *Chem. Rev.*, 2010, **110**, 4606–4655.
- 141 A. Henschel, K. Gedrich, R. Kraehnert and S. Kaskel, *Chem. Commun.*, 2008, 4192–4194.
- 142 O. K. Farha, A. M. Shultz, A. A. Sarjeant, S. T. Nguyen and J. T. Hupp, *J. Am. Chem. Soc.*, 2011, **133**, 5652–5655.
- 143 A. M. Shultz, O. K. Farha, D. Adhikari, A. A. Sarjeant, J. T. Hupp and S. T. Nguyen, *Inorg. Chem.*, 2011, **50**, 3174–3176.

- 144 S. Hasegawa, S. Horike, R. Matsuda, S. Furukawa, K. Mochizuki, Y. Kinoshita and S. Kitagawa, *J. Am. Chem. Soc.*, 2007, **129**, 2607–2614.
- 145 Y. D. Zang, J. Shi, F. M. Zhang, Y. J. Zhong and W. D. Zhu, *Catal. Sci. Technol.*, 2013, **3**, 2044–2049.
- 146 F. Schröder, D. Esken, M. Cokoja, M. W. van den Berg, O. I. Lebedev, G. Van Tendeloo, B. Walaszek, G. Buntkowsky, H. H. Limbach, B. Chaudret and others, *J. Am. Chem. Soc.*, 2008, **130**, 6119–6130.
- 147 B. Z. Yuan, Y. Y. Pan, Y. W. Li, B. L. Yin and H. F. Jiang, *Angew. Chem. Int. Ed.*, 2010, **49**, 4054–4058.
- 148 A. Aijaz, A. Karkamkar, Y. J. Choi, N. Tsumori, E. Rönnebro, T. Autrey, H. Shioyama and Q. Xu, *J. Am. Chem. Soc.*, 2012, **134**, 13926–13929.
- 149 A. M. Shultz, O. K. Farha, J. T. Hupp and S. T. Nguyen, *J. Am. Chem. Soc.*, 2009, **131**, 4204–4205.
- 150 S. Takaishi, E. J. DeMarco, M. J. Pellin, O. K. Farha and J. T. Hupp, *Chem. Sci.*, 2013, **4**, 1509–1513.
- 151 X. S. Wang, M. Chrzanowski, C. Kim, W. Y. Gao, L. Wojtas, Y. S. Chen, X. P. Zhang and S. Q. Ma, *Chem. Commun.*, 2012, **48**, 7173–7175.
- 152 L. Meng, Q. G. Cheng, C. Kim, W. Y. Gao, L. Wojtas, Y. S. Chen, M. J. Zaworotko, X. P. Zhang and S. Q. Ma, *Angew. Chem. Int. Ed.*, 2012, **51**, 10082–10085.
- 153 C. Zou, Z. J. Zhang, X. Xu, Q. H. Gong, J. Li and C. D. Wu, *J. Am. Chem. Soc.*, 2012, **134**, 87–90.
- 154 C. Zou, T. F. Zhang, M. H. Xie, L. J. Yan, G. Q. Kong, X. L. Yang, A. Ma and C. D. Wu, *Inorg. Chem.*, 2013, **52**, 3620–3626.
- 155 M. H. Xie, X. L. Yang, Y. B. He, J. Zhang, B. L. Chen and C. D. Wu, *Chem. Eur. J.*, 2013, **19**, 14316–14321.
- 156 D. W. Feng, Z. Y. Gu, J. R. Li, H. L. Jiang, Z. W. Wei and H. C. Zhou, *Angew. Chem. Int. Ed.*, 2012, **51**, 10307–10310.
- 157 D. W. Feng, W. C. Chung, Z. W. Wei, Z. Y. Gu, H. L. Jiang, Y. P. Chen, D. J. Darensbourg and H. C. Zhou, *J. Am. Chem. Soc.*, 2013, **135**, 17105–17110.
- 158 M. Müller, S. Hermes, K. Köhler, M. W. van den Berg, M. Muhler and R. A. Fischer, *Chem. Mater.*, 2008, **20**, 4576–4587.
- 159 H. L. Jiang, B. Liu, T. Akita, M. Haruta, H. Sakurai and Q. Xu, *J. Am. Chem. Soc.*, 2009, **131**, 11302–11303.
- 160 D. Esken, S. Turner, O. I. Lebedev, G. Van Tendeloo and R. A. Fischer, *Chem. Mater.*, 2010, **22**, 6393–6401.

- 161 S. Proch, J. Herrmannsdörfer, R. Kempe, C. Kern, A. Jess, L. Seyfarth and J. Senker, *Chem. Eur. J.*, 2008, **14**, 8204–8212.
- 162 E. V. Ramos-Fernandez, C. Pieters, B. van der Linden, J. Juan-Alcañiz, P. Serra-Crespo, M. Verhoeven, H. Niemantsverdriet, J. Gascon and F. Kapteijn, *J. Catal.*, 2012, **289**, 42–52.
- 163 C. Wang, K. E. deKrafft and W. B. Lin, *J. Am. Chem. Soc.*, 2012, **134**, 7211–7214.
- 164 Z. M. Zhang, T. Zhang, C. Wang, Z. K. Lin, L. S. Long and W. B. Lin, *J. Am. Chem. Soc.*, 2015, **137**, 3197–3200.
- 165 Z. C. Hu, B. J. Deibert and J. Li, *Chem. Soc. Rev.*, 2014, **43**, 5815–5840.
- 166 S. Sanda, S. Parshamoni, S. Biswas and S. Konar, *Chem. Commun.*, 2015, **51**, 6576–6579.
- 167 S. Khatua, S. Goswami, S. Biswas, K. Tomar, H. S. Jena and S. Konar, *Chem. Mater.*, 2015, **27**, 5349–5360.
- 168 Y. J. Cui, F. L. Zhu, B. L. Chen and G. D. Qian, *Chem. Commun.*, 2015, **51**, 7420–7431.
- 169 K. Müller-Buschbaum, F. Beuerle and C. Feldmann, *Microporous Mesoporous Mater.*, 2015, **216**, 172–199.
- 170 M. J. Dong, M. Zhao, S. Ou, C. Zou and C. D. Wu, *Angew. Chem. Int. Ed.*, 2014, **53**, 1575–1579.
- 171 Y. Li, S. S. Zhang and D. T. Song, *Angew. Chem. Int. Ed.*, 2013, **52**, 710–713.
- 172 Y. J. Cui, H. Xu, Y. F. Yue, Z. Y. Guo, J. C. Yu, Z. X. Chen, J. K. Gao, Y. Yang, G. D. Qian and B. L. Chen, *J. Am. Chem. Soc.*, 2012, **134**, 3979–3982.
- 173 M. Kurmoo, *Chem. Soc. Rev.*, 2009, **38**, 1353–1379.
- 174 W. Liu and X. B. Yin, *TrAC Trends Anal. Chem.*, 2016, **75**, 86–96.
- 175 A. Morozan and F. Jaouen, *Energy Environ. Sci.*, 2012, **5**, 9269–9290.
- 176 D. Bradshaw, A. Garai and J. Huo, *Chem. Soc. Rev.*, 2012, **41**, 2344–2381.
- 177 A. Bédard and R. A. Fischer, *Chem. Rev.*, 2011, **112**, 1055–1083.
- 178 O. Shekhah, J. Liu, R. A. Fischer and C. Wöll, *Chem. Soc. Rev.*, 2011, **40**, 1081–1106.
- 179 H. L. Jiang and Q. Xu, *Chem. Commun.*, 2011, **47**, 3351–3370.
- 180 R. Makiura and H. Kitagawa, *Eur. J. Inorg. Chem.*, 2010, **2010**, 3715–3724.
- 181 D. Zacher, R. Schmid, C. Wöll and R. A. Fischer, *Angew. Chem. Int. Ed.*, 2011, **50**, 176–199.
- 182 D. Zacher, O. Shekhah, C. Wöll and R. A. Fischer, *Chem. Soc. Rev.*, 2009, **38**, 1418–1429.
- 183 L. Heinke, M. Tu, S. Wannapaiboon, R. A. Fischer and C. Wöll, *Microporous Mesoporous Mater.*, 2015, **216**, 200–215.

- 184 J. L. Zhuang, A. Terfort and C. Wöll, *Coord. Chem. Rev.*, 2016, **307**, 391–424.
- 185 B. Liu and R. A. Fischer, *Sci. China Chem.*, 2011, **54**, 1851–1866.
- 186 A. A. Talin, A. Centrone, A. C. Ford, M. E. Foster, V. Stavila, P. Haney, R. A. Kinney, V. Szalai, F. El Gabaly, H. P. Yoon, F. Léonard, and M. D. Allendorf, *Science*, 2014, **343**, 66–69.
- 187 S. Bundschuh, O. Kraft, H. K. Arslan, H. Gliemann, P. G. Weidler and C. Wöll, *Appl. Phys. Lett.*, 2012, **101**, 101910.
- 188 Z. G. Gu, A. Pfriem, S. Hamsch, H. Breitwieser, J. Wohlgemuth, L. Heinke, H. Gliemann and C. Wöll, *Microporous Mesoporous Mater.*, 2015, **211**, 82–87.
- 189 M. E. Silvestre, M. Franzreb, P. G. Weidler, O. Shekhah and C. Wöll, *Adv. Funct. Mater.*, 2013, **23**, 1210–1213.
- 190 Z. B. Wang, J. X. Liu, B. Lukose, Z. G. Gu, P. G. Weidler, H. Gliemann, T. Heine and C. Wöll, *Nano Lett.*, 2014, **14**, 1526–1529.
- 191 J. X. Liu, T. Wächter, A. Irmeler, P. G. Weidler, H. Gliemann, F. Pauly, V. Mugnaini, M. Zharnikov and C. Wöll, *ACS Appl. Mater. Interfaces*, 2015, **7**, 9824–9830.
- 192 A. Dragässer, O. Shekhah, O. Zybaylo, C. Shen, M. Buck, C. Wöll and D. Schlottwein, *Chem. Commun.*, 2012, **48**, 663–665.
- 193 Z. G. Gu, Z. Chen, W. Q. Fu, F. Wang and J. Zhang, *ACS Appl. Mater. Interfaces*, 2015, **7**, 28585–28590.
- 194 H. C. Streit, M. Adlung, O. Shekhah, X. Stammer, H. K. Arslan, O. Zybaylo, T. Ladnorg, H. Gliemann, M. Franzreb, C. Wöll and C. Wickleder, *ChemPhysChem*, 2012, **13**, 2699–2702.
- 195 A. Ulman, *Chem. Rev.*, 1996, **96**, 1533–1554.
- 196 J. C. Love, L. A. Estroff, J. K. Kriebel, R. G. Nuzzo and G. M. Whitesides, *Chem. Rev.*, 2005, **105**, 1103–1170.
- 197 C. Vericat, M. E. Vela, G. Benitez, P. Carro and R. C. Salvarezza, *Chem. Soc. Rev.*, 2010, **39**, 1805–1834.
- 198 F. Schreiber, *J. Phys. Condens. Matter*, 2004, **16**, 881–900.
- 199 S. Hermes, F. Schröder, R. Chelmowski, C. Wöll and R. A. Fischer, *J. Am. Chem. Soc.*, 2005, **127**, 13744–13745.
- 200 O. Shekhah, H. Wang, S. Kowarik, F. Schreiber, M. Paulus, M. Tolan, C. Sternemann, F. Evers, D. Zacher, R. A. Fischer and C. Wöll, *J. Am. Chem. Soc.*, 2007, **129**, 15118–15119.

- 201 D. Zacher, K. Yussenko, A. Bédard, S. Henke, M. Molon, T. Ladnorg, O. Shekhah, B. Schüpbach, T. de los Arcos, M. Meilikhov, A. Terfort, C. Wöl and R. A. Fischer, *Chem. Eur. J.*, 2011, **17**, 1448–1455.
- 202 B. D. Gates, Q. B. Xu, M. Stewart, D. Ryan, C. G. Willson and G. M. Whitesides, *Chem. Rev.*, 2005, **105**, 1171–1196.
- 203 L. H. Dubois and R. G. Nuzzo, *Annu. Rev. Phys. Chem.*, 1992, **43**, 437–463.
- 204 P. A. Lewis, Z. J. Donhauser, B. A. Mantooth, R. K. Smith, L. A. Bumm, K. F. Kelly and P. S. Weiss, *Nanotechnology*, 2001, **12**, 231.
- 205 O. Cavalleri, A. Hirstein, J. P. Bucher and K. Kern, *Thin Solid Films*, 1996, **284**, 392–395.
- 206 G. E. Poirier, *Chem. Rev.*, 1997, **97**, 1117–1128.
- 207 S. Subramanian and S. Sampath, *Anal. Bioanal. Chem.*, 2007, **388**, 135–145.
- 208 N. Ballav, H. Thomas, T. Winkler, A. Terfort and M. Zharnikov, *Angew. Chem. Int. Ed.*, 2009, **48**, 5833–5836.
- 209 D. Samanta and A. Sarkar, *Chem. Soc. Rev.*, 2011, **40**, 2567–2592.
- 210 G. Brunoro, A. Frignani, A. Colledan and C. Chiavari, *Corros. Sci.*, 2003, **45**, 2219–2231.
- 211 Y. T. Wang, Y. X. Zhou, J. Sokolov, B. Rigas, K. Levon and M. Rafailovich, *Biosens. Bioelectron.*, 2008, **24**, 162–166.
- 212 T. J. Huang, B. Brough, C. M. Ho, Y. Liu, A. H. Flood, P. A. Bonvallet, H. R. Tseng, J. F. Stoddart, M. Baller and S. Magonov, *Appl. Phys. Lett.*, 2004, **85**, 5391–5393.
- 213 L. Venkataraman, J. E. Klare, I. W. Tam, C. Nuckolls, M. S. Hybertsen and M. L. Steigerwald, *Nano Lett.*, 2006, **6**, 458–462.
- 214 J. A. Rogers and R. G. Nuzzo, *Mater. Today*, 2005, **8**, 50–56.
- 215 S. Takeuchi, W. R. DiLuzio, D. B. Weibel and G. M. Whitesides, *Nano Lett.*, 2005, **5**, 1819–1823.
- 216 O. Shekhah, H. Wang, D. Zacher, R. A. Fischer and C. Wöl, *Angew. Chem. Int. Ed.*, 2009, **48**, 5038–5041.
- 217 S. R. Venna and M. A. Carreon, *J. Am. Chem. Soc.*, 2010, **132**, 76–78.
- 218 H. L. Guo, G. S. Zhu, I. J. Hewitt and S. L. Qiu, *J. Am. Chem. Soc.*, 2009, **131**, 1646–1647.
- 219 A. Schoedel, C. Scherb and T. Bein, *Angew. Chem. Int. Ed.*, 2010, **49**, 7225–7228.
- 220 E. Biemmi, C. Scherb and T. Bein, *J. Am. Chem. Soc.*, 2007, **129**, 8054–8055.
- 221 Y. S. Li, H. Bux, A. Feldhoff, G. L. Li, W. S. Yang and J. Caro, *Adv. Mater.*, 2010, **22**, 3322–3326.
- 222 Y. S. Li, F. Y. Liang, H. Bux, A. Feldhoff, W. S. Yang and J. Caro, *Angew. Chem. Int. Ed.*, 2010, **49**,

- 548–551.
- 223 O. Shekhah, H. Wang, M. Paradinas, C. Ocal, B. Schüpbach, A. Terfort, D. Zacher, R. A. Fischer and C. Wöl, *Nat. Mater.*, 2009, **8**, 481–484.
- 224 H. K. Arslan, O. Shekhah, J. Wohlgemuth, M. Franzreb, R. A. Fischer and C. Wöl, *Adv. Funct. Mater.*, 2011, **21**, 4228–4231.
- 225 R. Makiura, S. Motoyama, Y. Umemura, H. Yamanaka, O. Sakata and H. Kitagawa, *Nat. Mater.*, 2010, **9**, 565–571.
- 226 Y. Yoo and H. K. Jeong, *Chem Commun*, 2008, **21**, 2441–2443.
- 227 R. Ameloot, E. Gobechiya, H. Uji-i, J. A. Martens, J. Hofkens, L. Alaerts, B. F. Sels and D. E. De Vos, *Adv. Mater.*, 2010, **22**, 2685–2688.
- 228 P. Horcajada, C. Serre, D. Grosso, C. Boissiere, S. Perruchas, C. Sanchez and G. Férey, *Adv. Mater.*, 2009, **21**, 1931–1935.
- 229 A. Demessence, P. Horcajada, C. Serre, C. Boissière, D. Grosso, C. Sanchez and G. Férey, *Chem. Commun.*, 2009, 7149–7151.
- 230 J. Reboul, S. Furukawa, N. Horike, M. Tsotsalas, K. Hirai, H. Uehara, M. Kondo, N. Louvain, O. Sakata and S. Kitagawa, *Nat. Mater.*, 2012, **11**, 717–723.
- 231 J. Gascon, S. Aguado and F. Kapteijn, *Microporous Mesoporous Mater.*, 2008, **113**, 132–138.
- 232 M. Arnold, P. Kortunov, D. J. Jones, Y. Nedellec, J. Kärgler and J. Caro, *Eur. J. Inorg. Chem.*, 2007, **2007**, 60–64.
- 233 S. Hermes, D. Zacher, A. Baunemann, C. Wöl and R. A. Fischer, *Chem. Mater.*, 2007, **19**, 2168–2173.
- 234 D. Zacher, A. Baunemann, S. Hermes and R. A. Fischer, *J. Mater. Chem.*, 2007, **17**, 2785–2792.
- 235 A. S. Huang, H. Bux, F. Steinbach and J. Caro, *Angew. Chem. Int. Ed.*, 2010, **49**, 4958–4961.
- 236 A. S. Huang, W. Dou and J. Caro, *J. Am. Chem. Soc.*, 2010, **132**, 15562–15564.
- 237 D. Van Gough, T. N. Lambert, D. R. Wheeler, M. A. Rodriguez, M. T. Brumbach, M. D. Allendorf and E. D. Spoeerke, *ACS Appl. Mater. Interfaces*, 2014, **6**, 1509–1514.
- 238 D. Käfer, G. Witte, P. Cyganik, A. Terfort and C. Wöl, *J. Am. Chem. Soc.*, 2006, **128**, 1723–1732.
- 239 C. Scherb, A. Schödel and T. Bein, *Angew. Chem. Int. Ed.*, 2008, **47**, 5777–5779.
- 240 F. M. Hinterholzinger, S. Wuttke, P. Roy, T. Preuß, A. Schaate, P. Behrens, A. Godt and T. Bein, *Dalton Trans.*, 2012, **41**, 3899–3901.
- 241 F. Hinterholzinger, C. Scherb, T. Ahnfeldt, N. Stock and T. Bein, *Phys. Chem. Chem. Phys.*, 2010, **12**,

- 4515–4520.
- 242 O. Shekhah, *Materials*, 2010, **3**, 1302–1315.
- 243 B. Liu, M. Tu and R. A. Fischer, *Angew. Chem. Int. Ed.*, 2013, **52**, 3402–3405.
- 244 O. Shekhah, R. Swaidan, Y. Belmabkhout, M. du Plessis, T. Jacobs, L. J. Barbour, I. Pinnau and M. Eddaoudi, *Chem. Commun.*, 2014, **50**, 2089–2092.
- 245 O. Shekhah and M. Eddaoudi, *Chem. Commun.*, 2013, **49**, 10079–10081.
- 246 B. Liu, O. Shekhah, H. K. Arslan, J. X. Liu, C. Wöll and R. A. Fischer, *Angew. Chem. Int. Ed.*, 2012, **51**, 807–810.
- 247 J. L. Zhuang, M. Kind, C. M. Grytz, F. Farr, M. Diefenbach, S. Tussupbayev, M. C. Holthausen and A. Terfort, *J. Am. Chem. Soc.*, 2015, **137**, 8237–8243.
- 248 H. Chun, D. N. Dybtsev, H. Kim and K. Kim, *Chem. Eur. J.*, 2005, **11**, 3521–3529.
- 249 O. Shekhah, K. Hirai, H. Wang, H. Uehara, M. Kondo, S. Diring, D. Zacher, R. A. Fischer, O. Sakata, S. Kitagawa, S. Furukawa and C. Wöll, *Dalton Trans.*, 2011, **40**, 4954–4958.
- 250 M. Tu and R. A. Fischer, *J. Mater. Chem. A*, 2014, **2**, 2018–2022.
- 251 B. Liu, M. Tu, D. Zacher and R. A. Fischer, *Adv. Funct. Mater.*, 2013, **23**, 3790–3798.
- 252 B. Liu, M. Y. Ma, D. Zacher, A. Bédard, K. Yussenko, N. Metzler-Nolte, C. Wöll and R. A. Fischer, *J. Am. Chem. Soc.*, 2011, **133**, 1734–1737.
- 253 L. Heinke, M. Cakici, M. Dommaschk, S. Grosjean, R. Herges, S. Bräse and C. Wöll, *ACS Nano*, 2014, **8**, 1463–1467.
- 254 M. Meilikhov, S. Furukawa, K. Hirai, R. A. Fischer, and S. Kitagawa, *Angew. Chem. Int. Ed.*, 2013, **52**, 341–345.
- 255 J. X. Liu, B. Lukose, O. Shekhah, H. K. Arslan, P. Weidler, H. Gliemann, S. Bräse, S. Grosjean, A. Godt, X. L. Feng, K. Müllen, I. B. Magdau, T. Heine and C. Wöll, *Sci. Rep.*, 2012, **2**, 921.
- 256 J. Liu, W. Zhou, J. Liu, I. Howard, G. Kilibarda, S. Schlabach, D. Coupry, M. Addicoat, S. Yoneda, Y. Tsutsui and others, *Angew. Chem. Int. Ed.*, 2015, **54**, 7441–7445.
- 257 S. Motoyama, R. Makiura, O. Sakata and H. Kitagawa, *J. Am. Chem. Soc.*, 2011, **133**, 5640–5643.
- 258 J. L. Zhuang, D. Ar, X. J. Yu, J. X. Liu and A. Terfort, *Adv. Mater.*, 2013, **25**, 4631–4635.
- 259 W. J. Li, S. Y. Gao, T. F. Liu, L. W. Han, Z. J. Lin and R. Cao, *Langmuir*, 2013, **29**, 8657–8664.
- 260 M. D. Allendorf, R. J. Houk, L. Andruszkiewicz, A. A. Talin, J. Pikarsky, A. Choudhury, K. A. Gall and P. J. Hesketh, *J. Am. Chem. Soc.*, 2008, **130**, 14404–14405.

- 261 S. Aguado, J. Canivet and D. Farrusseng, *Chem. Commun.*, 2010, **46**, 7999–8001.
- 262 Z. B. Wang, S. Grosjean, S. Bräse and L. Heinke, *ChemPhysChem*, 2015, **16**, 3779–3783.
- 263 W. W. Qin, M. E. Silvestre, G. Brenner-Weiss, Z. B. Wang, S. Schmitt, J. Hübner and M. Franzreb, *Sep. Purif. Technol.*, 2015, **156**, 249–258.
- 264 W. Li, S. Zhou, S. Gao, S. Chen, M. Huang and R. Cao, *Adv. Mater. Interfaces*, 2015, **2**, 1400405.
- 265 M. P. A. Sancet, M. Hanke, Z. Wang, S. Bauer, C. Azucena, H. K. Arslan, M. Heinle, H. Gliemann, C. Wöll and A. Rosenhahn, *Biointerphases*, 2013, **8**, 29.
- 266 Z. B. Wang, D. Nminibapiel, P. Shrestha, J. X. Liu, W. Guo, P. G. Weidler, H. Baumgart, C. Wöll and E. Redel, *ChemNanoMat*, 2016, **2**, 67–73.
- 267 I. Hod, W. Bury, D. M. Gardner, P. Deria, V. Roznyatovskiy, M. R. Wasielewski, O. K. Farha and J. T. Hupp, *J. Phys. Chem. Lett.*, 2015, **6**, 586–591.
- 268 C. R. Wade, M. Y. Li and M. Dincă, *Angew. Chem. Int. Ed.*, 2013, **52**, 13377–13381.
- 269 I. Hod, M. D. Sampson, P. Deria, C. P. Kubiak, O. K. Farha and J. T. Hupp, *ACS Catal.*, 2015, **5**, 6302–6309.
- 270 C. W. Kung, T. C. Wang, J. E. Mondloch, D. Fairen-Jimenez, D. M. Gardner, W. Bury, J. M. Klingsporn, J. C. Barnes, R. Van Duyne, J. F. Stoddart and others, *Chem. Mater.*, 2013, **25**, 5012–5017.
- 271 S. R. Ahrenholtz, C. C. Epley and A. J. Morris, *J. Am. Chem. Soc.*, 2014, **136**, 2464–2472.
- 272 C. W. Kung, T. H. Chang, L. Y. Chou, J. T. Hupp, O. K. Farha and K. C. Ho, *Electrochem. Commun.*, 2015, **58**, 51–56.
- 273 J. X. Liu, E. Redel, S. Walheim, Z. B. Wang, V. Oberst, J. X. Liu, S. Heissler, A. Welle, M. Moosmann, T. Scherer, M. Bruns, H. Gliemann and C. Wöll, *Chem. Mater.*, 2015, **27**, 1991–1996.
- 274 V. Stavila, A. A. Talin and M. D. Allendorf, *Chem. Soc. Rev.*, 2014, **43**, 5994–6010.
- 275 E. Biemmi, A. Darga, N. Stock and T. Bein, *Microporous Mesoporous Mater.*, 2008, **114**, 380–386.
- 276 M. Tu, S. Wannapaiboon, K. Khaletskaya and R. A. Fischer, *Adv. Funct. Mater.*, 2015, **25**, 4470–4479.
- 277 W. C. Zhou, C. Wöll and L. Heinke, *Materials*, 2015, **8**, 3767–3775.
- 278 O. Zybaylo, O. Shekhah, H. Wang, M. Tafipolsky, R. Schmid, D. Johannsmann and C. Wöll, *Phys. Chem. Chem. Phys.*, 2010, **12**, 8093–8098.
- 279 L. Heinke and C. Wöll, *Phys. Chem. Chem. Phys.*, 2013, **15**, 9295–9299.
- 280 H. Uehara, S. Diring, S. Furukawa, Z. Kalay, M. Tsotsalas, M. Nakahama, K. Hirai, M. Kondo, O. Sakata and S. Kitagawa, *J. Am. Chem. Soc.*, 2011, **133**, 11932–11935.



- 281 Z. G. Gu, J. B ü rck, A. Bihlmeier, J. X. Liu, O. Shekhah, P. G. Weidler, C. Azucena, Z. B. Wang, S. Heissler, H. Gliemann, W. Klopper, A. S. Ulrich and C W ö l, *Chem. Eur. J.*, 2014, **20**, 9879–9882.
- 282 Z. G. Gu, S. Grosjean, S. Br ä e, C. W ö l and L. Heinke, *Chem. Commun.*, 2015, **51**, 8998–9001.
- 283 M. C. So, S. Jin, H. J. Son, G. P. Wiederrecht, O. K. Farha and J. T. Hupp, *J. Am. Chem. Soc.*, 2013, **135**, 15698–15701.
- 284 G. Lu and J. T. Hupp, *J. Am. Chem. Soc.*, 2010, **132**, 7832–7833.
- 285 F. M. Hinterholzinger, A. Ranft, J. M. Feckl, B. R ö hle, T. Bein and B. V. Lotsch, *J. Mater. Chem.*, 2012, **22**, 10356–10362.
- 286 A. Ranft, F. Niekkel, I. Pavlichenko, N. Stock and B. V. Lotsch, *Chem. Mater.*, 2015, **27**, 1961–1970.
- 287 J. P. Best, J. Michler, J. X. Liu, Z. B. Wang, M. Tsotsalas, X. Maeder, S. R ö se, V. Oberst, J. X. Liu, S. Walheim, H. Gliemann, P. G. Weidler, E. Redel and C. W ö l, *Appl. Phys. Lett.*, 2015, **107**, 101902.
- 288 G. Sauerbrey, *Z. F ü r Phys.*, 1959, **155**, 206–222.
- 289 K. P. Li, J. L. Qu, B. Xu, Y. H. Zhou, L. J. Liu, P. Peng and W. J. Tian, *New J. Chem.*, 2009, **33**, 2120–2127.
- 290 S. H. Hsiao and C. P. Yang, *J. Polym. Sci. Part Polym. Chem.*, 1990, **28**, 2501–2508.
- 291 M. Ghaemy and H. Mighani, *Chin. Chem. Lett.*, 2009, **20**, 800–804.
- 292 S. Himeno and N. Ishio, *J. Electroanal. Chem.*, 1998, **451**, 203–209.
- 293 X. J. Yu, J. L. Zhuang, J. Scherr, T. Abu-Husein and A. Terfort, *Angew. Chem. Int. Ed.*, 2016, **55**, 8348–8352.
- 294 Y. Hijikata, S. Horike, M. Sugimoto, M. Inukai, T. Fukushima and S. Kitagawa, *Inorg. Chem.*, 2013, **52**, 3634–3642.
- 295 Julian Scherr, Synthese Ferrocen-haltiger Bausteine für elektroaktive metallorganische Netzwerke. Masterarbeit, Goethe-Universität Frankfurt 2014.
- 296 A. Y. Volkonskii, E. M. Kagramanova, N. D. Kagramanov and N. D. Chkanikov, *Russ. Chem. Bull.*, 2012, **61**, 2001–2003.
- 297 T. Abu-Husein, S. Schuster, D. A. Egger, M. Kind, T. Santowski, A. Wiesner, R. Chiechi, E. Zojer, A. Terfort and M. Zharnikov, *Adv. Funct. Mater.*, 2015, **25**, 3943–3957.
- 298 K. Seki and W. Mori, *J. Phys. Chem. B*, 2002, **106**, 1380–1385.
- 299 Y. Odagaki, K. Hirotsu, T. Higuchi, A. Harada and S. Takahashi, *J Chem Soc Perkin Trans 1*, 1990, 1230–1231.

- 300 J. K. Badenhoop and F. Weinhold, *J. Chem. Phys.*, 1997, **107**, 5422–5432.
- 301 W. J. Zhuang, C. Y. Sun and L. P. Jin, *Polyhedron*, 2007, **26**, 1123–1132.
- 302 K. Hirai, K. Sumida, M. Meilikhov, N. Louvain, M. Nakahama, H. Uehara, S. Kitagawa and S. Furukawa, *J. Mater. Chem. C*, 2014, **2**, 3336–3344.
- 303 R. G. Greenler, *J. Chem. Phys.*, 1966, **44**, 310–315.
- 304 M. L. Ohnsorg, C. K. Beaudoin and M. E. Anderson, *Langmuir*, 2015, **31**, 6114–6121.
- 305 L. Heinke, Z. G. Gu and C. Wöll, *Nat. Commun.*, 2014, **5**, 4562.
- 306 S. Yuan, W. G. Lu, Y. P. Chen, Q. Zhang, T. F. Liu, D. W. Feng, X. Wang, J. S. Qin and H. C. Zhou, *J. Am. Chem. Soc.*, 2015, **137**, 3177–3180.
- 307 H. X. Deng, C. J. Doonan, H. Furukawa, R. B. Ferreira, J. Towne, C. B. Knobler, B. Wang and O. M. Yaghi, *Science*, 2010, **327**, 846–850.
- 308 H. Furukawa, U. Müller and O. M. Yaghi, *Angew. Chem. Int. Ed.*, 2015, **54**, 3417–3430.
- 309 Y. B. He, B. Li, M. O’Keeffe and B. L. Chen, *Chem. Soc. Rev.*, 2014, **43**, 5618–5656.
- 310 A. C. Kathalikkattil, S. Damodaran, K. K. Bisht and E. Suresh, *J. Mol. Struct.*, 2011, **985**, 361–370.
- 311 J. Otton and S. Ratton, *J. Polym. Sci. Part Polym. Chem.*, 1991, **29**, 377–391.
- 312 M. Hojo, Y. Kondo, K. Zei, K. Okamura, Z. Chen and M. Kobayashi, *Bull. Chem. Soc. Jpn.*, 2014, **87**, 98–109.
- 313 H. Jasuja, N. C. Burtch, Y. Huang, Y. Cai and K. S. Walton, *Langmuir*, 2013, **29**, 633–642.
- 314 L. D. Spicer and B. S. Rabinovitch, *J. Phys. Chem.*, 1970, **74**, 2445–2448.
- 315 J. C. Choe and M. S. Kim, *Bull. Korean Chem. Soc.*, 1986, **7**, 275.
- 316 R. Kitaura, F. Iwahori, R. Matsuda, S. Kitagawa, Y. Kubota, M. Takata and T. C. Kobayashi, *Inorg. Chem.*, 2004, **43**, 6522–6524.
- 317 S. S. Park, E. R. Hontz, L. Sun, C. H. Hendon, A. Walsh, T. Van Voorhis and M. Dincă, *J. Am. Chem. Soc.*, 2015, **137**, 1774–1777.
- 318 D. Sheberla, L. Sun, M. A. Blood-Forsythe, S. Er, C. R. Wade, C. K. Brozek, A. Aspuru-Guzik and M. Dincă, *J. Am. Chem. Soc.*, 2014, **136**, 8859–8862.
- 319 M. G. Campbell, D. Sheberla, S. F. Liu, T. M. Swager and M. Dincă, *Angew. Chem. Int. Ed.*, 2015, **54**, 4349–4352.
- 320 L. Sun, T. Miyakai, S. Seki and M. Dincă, *J. Am. Chem. Soc.*, 2013, **135**, 8185–8188.
- 321 L. Sun, C. H. Hendon, M. A. Minier, A. Walsh and M. Dincă, *J. Am. Chem. Soc.*, 2015, **137**, 6164–

- 6167.
- 322 K. Hirai, H. Uehara, S. Kitagawa and S. Furukawa, *Dalton Trans.*, 2012, **41**, 3924–3927.
- 323 J. L. Zhuang, J. Friedel and A. Terfort, *Beilstein J. Nanotechnol.*, 2012, **3**, 570–578.
- 324 V. Mugnaini, M. Tsotsalas, F. Bebensee, S. Grosjean, A. Shahnas, S. Bräse, J. Lahann, M. Buck and C. Wöl, *Chem. Commun.*, 2014, **50**, 11129–11131.
- 325 A. J. Bard, L. R. Faulkner, J. Leddy and C. G. Zoski, *Electrochemical methods: fundamentals and applications*, Wiley New York, 1980, vol. 2.
- 326 K. Itaya, I. Uchida and V. D. Neff, *Acc. Chem. Res.*, 1986, **19**, 162–168.
- 327 M. Strømme, G. A. Niklasson and C. G. Granqvist, *Solid State Commun.*, 1995, **96**, 151–154.
- 328 A. Dolbecq, E. Dumas, C. R. Mayer and P. Mialane, *Chem. Rev.*, 2010, **110**, 6009–6048.
- 329 M. T. Pope and A. Müller, *Angew. Chem. Int. Ed.*, 1991, **30**, 34–48.
- 330 M. Sadakane and E. Steckhan, *Chem. Rev.*, 1998, **98**, 219–238.
- 331 X. López, C. Bo and J. M. Poblet, *J. Am. Chem. Soc.*, 2002, **124**, 12574–12582.
- 332 C. L. Hill, *Chem. Rev.*, 1998, **98**, 1–2.
- 333 O. A. Kholdeeva and R. I. Maksimovskaya, *J. Mol. Catal. Chem.*, 2007, **262**, 7–24.
- 334 R. M. Yu, X. F. Kuang, X. Y. Wu, C. Z. Lu and J. P. Donahue, *Coord. Chem. Rev.*, 2009, **253**, 2872–2890.
- 335 D. Y. Du, J. S. Qin, S. L. Li, Z. M. Su and Y. Q. Lan, *Chem. Soc. Rev.*, 2014, **43**, 4615–4632.
- 336 D. M. Fernandes, A. D. Barbosa, J. Pires, S. S. Balula, L. Cunha-Silva and C. Freire, *ACS Appl. Mater. Interfaces*, 2013, **5**, 13382–13390.
- 337 C. Y. Sun, S. X. Liu, D. D. Liang, K. Z. Shao, Y. H. Ren and Z. M. Su, *J. Am. Chem. Soc.*, 2009, **131**, 1883–1888.
- 338 F. J. Ma, S. X. Liu, C. Y. Sun, D. D. Liang, G. J. Ren, F. Wei, Y. G. Chen and Z. M. Su, *J. Am. Chem. Soc.*, 2011, **133**, 4178–4181.
- 339 Y. W. Liu, X. Yang, J. Miao, Q. Tang, S. M. Liu, Z. Shi and S. X. Liu, *Chem. Commun.*, 2014, **50**, 10023–10026.
- 340 A. X. Yan, S. Yao, Y. G. Li, Z. M. Zhang, Y. Lu, W. L. Chen and E. B. Wang, *Chem. Eur. J.*, 2014, **20**, 6927–6933.



## 10 Curriculum Vitae

### Personal Data

---

Date of Birth                      12<sup>th</sup>, October, 1986  
Nationality                        Chinese  
Marital Status                    Married

### Education

---

**Sep. 2005 – Jun. 2009**            **Bachelor of Engineering**  
School of Materials Science and Engineering, Zhengzhou University, China  
Title: Synthesis of ZnO nanostructures  
Supervisor: Prof. Dr. Hongxia Lu

**Sep. 2009 – Jun. 2012**            **Master of Engineering**  
School of Materials Science and Engineering, Zhengzhou University, China  
Title: Synthesis and photocatalytic properties of ZnSn(OH)<sub>6</sub> and ZnSn(OH)<sub>6</sub>/ZnO micro/nanostructures  
Supervisor: Prof. Dr. Hongxia Lu

**Sep. 2012 – Mar. 2016**            **PhD of Science**  
Institute for Inorganic and Analytical Chemistry, University of Frankfurt, Germany  
Title: Controlled growth and application of highly oriented surface-mounted metal-organic frameworks (SURMOFs)  
Supervisor: Prof. Dr. Andreas Terfort

### Awards

---

**2007**                                    Excellent College Student, Zhengzhou University  
**2008**                                    The 2<sup>nd</sup> rank of Annual Scholarship, Zhengzhou University  
**2009**                                    The 3<sup>rd</sup> rank of Annual Scholarship, Zhengzhou University  
**2011**                                    Ten Top Student, Zhengzhou University  
**2011**                                    Excellent Graduate Student, Zhengzhou University  
**2011**                                    Outstanding Student Leader, Zhengzhou University  
**2012**                                    Graduate of Merit/Triple A Student, Zhengzhou University  
**2012**                                    Excellent Graduate Student, Henan Province  
**2012**                                    Graduate of Merit/Triple A Student, Henan Province  
**2009 - 2012**                        The 1<sup>st</sup> rank of Annual Scholarship for Graduate, Zhengzhou University



## 11 Acknowledgements

Many people have offered me valuable help during the last three and half years. Without them, this thesis would not have been accomplished.

First and foremost, I am sincerely grateful to my supervisor Prof. Dr. Andreas Terfort, who took me in his research group and offered great support during my PhD study. He is open-minded, tolerant and very nice. It is a real pleasure to work with him. I really appreciate his approach of not spoon feeding his students and let them have full scientific freedom to do research. But he is always available for guidance and advice when I meet difficulties in the research. I think joining his group was the best thing happened to me back in 2012 and I feel tremendously lucky to have him as my PhD supervisor. His enthusiasm, professionalism and passion for science have deeply influenced me and undoubtedly will benefit me forever. Outside of the work, he is friendly to every group member. He has given me a lot of experience about life and social interaction. I am quite sure that my learnings from him about how to be a better person will fetch me success in my future endeavors too.

Then, I would like to acknowledge China Scholarship Council (CSC) for giving me the wonderful opportunity to carry out this research under the supervision of Prof. Dr. Andreas Terfort and providing me the financial support in the starting 36 months. The further financial support during the extension period provided by Prof. Dr. Andreas Terfort is also highly appreciated.

Most importantly, I am also grateful to the former and current group members, Dr. Jinliang Zhuang, Dr. Frederic Farr, Dr. Britta Kämpken, Dr. Theresa Weber, Dr. Matthias Berger, Kathrin Barbe, Dr. Martin Kind, Tarek Abu-Husein, Julian Scherr, Sebastian Schneider, Dr. Zibin Zhang, Yiming Xian, Zeping Wang, Christoph Partes, Christina Schulze, Matthias Füsser, Michael Gärtner, Felix Klockmann, Felix Neumeyer, Gordon Keitl, Marc Zeplichal, Hannelore Bovermann-Naumann, Ulrich Koch, Claudia Rittmeyer, Thaleia Vavaleskou and Dr. Larissa Zherlitsyna. It is my pleasure to work with you guys. Jinliang, behaving like my second supervisor, I am particularly thankful for the help in teaching me experimental skills and sharing life experience in Frankfurt. Tarek, thanks for always being so nice to me like my

old brother, teaching me a lot of German culture and helping me overcome many issues in my personal life. Moreover, the PPP1 and PzP1 molecules, which are synthesized by you, are so awesome. Julian, my buddy, thank you so much for your great ideas, ferrocene and dimethyl ferrocene functionalized H<sub>2</sub>(bpdc) linkers and help in my work. I still remember we had a lot of fun in Dresden. Martin, he always gave me valuable suggestions on my research. It is very memorable for me to chat with you while drinking a beer. Sebastian, he did a lot of CV measurements for me. My special thanks go to Thaleia. She took many AFM and SEM images for me. Moreover, I have learned plenty skills in managing these equipments from her. Michael and Yiming, I couldn't find better labmates than you guys. It was so helpful to work with you. Many thanks to our secretary Mrs. Bovermann-Naumann for her nice assistance in registration, E-mails and so on. Thank our new secretary Mr. Koch for the nice E-mails and helps. In particular, I am grateful to Martin, Sebastian, Julian and Zibin again, who proof read my thesis. Outside of the Terfort research group, my warm thanks are addressed to our cooperation partners. I thank Dr. Lothar Fink, Edith Alig, Dr. Jinxuan Liu (Prof. Christof Wöll's group, Karlsruhe Institute of Technology) for providing XRD measurements and Dr. Torsten Henning and Diana Leichner (Justus Liebig University) for the SEM measurements.

Besides, I have to thank Zhengzhou University (ZZU), CSC and the Chinese Embassy in Germany for their assistance in extending my PhD study duration. Moreover, my sincere thanks go to Prof. Dr. Hongxia Lu and Jingyi Du in ZZU for their kind care and warm encouragement. I also thank all my friends in Frankfurt. They brought so much joy to me and we had great time together.

Finally, I would like to express my gratitude to my family for all their love and support. My parents, their sacrifices constantly inspire me to make progresses. My wife, Man He, always stands by my side and she is my impetus to move forward. Luckily, with their love and support, I could concentrate my mind and work through these years.



## **12 Erklärung über frühere Promotionsverfahren und Eidesstattliche Versicherung**

### ERKLÄRUNG

Ich erkläre, dass ich mich bisher keiner Doktorprüfung unterzogen habe.

Frankfurt am Main, den

---

Xiujun Yu

### Eidesstattliche Versicherung

Ich erkläre hiermit an Eides Statt, dass ich die vorgelegte Dissertation über die Titel

### **Controlled Growth and Application of Highly Oriented Surface-Mounted Metal-Organic Frameworks (SURMOFs)**

selbständig angefertigt und mich anderer Hilfsmittel als der in ihr angegebenen nicht bedient habe, insbesondere, dass alle Entlehnungen aus anderen Schriften mit Angabe der betreffenden Schrift gekennzeichnet sind.

Ich versichere, nicht die Hilfe einer kommerziellen Promotionsvermittlung in Anspruch genommen zu haben.

Frankfurt am Main, den

---

Xiujun Yu